Crystal Structure and Phase Transitions in Various Functional Perovskites

Charlotte A.L. Dixon

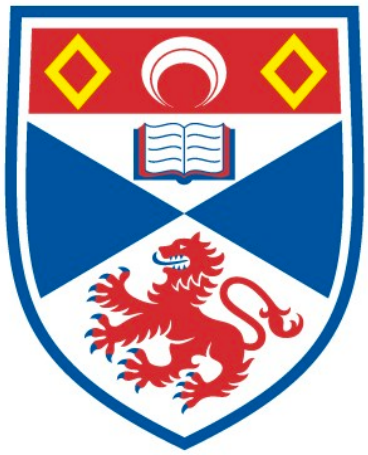

This thesis is submitted in partial fulfilment for the degree of PhD at the University of St Andrews

Date of submission

August 2017

1. Candidate's declarations:

I, Charlotte Dixon hereby certify that this thesis, which is approximately 60,000 words in length, has been written by me, and that it is the record of work carried out by me, or principally by myself in collaboration with others as acknowledged, and that it has not been submitted in any previous application for a higher degree.

I was admitted as a research student in August, 2013 and as a candidate for the degree of PhD in [August, 2014]; the higher study for which this is a record was carried out in the University of St Andrews between 2013 and 2017.

Date …….. signature of candidate ……

2. Supervisor's declaration:

I hereby certify that the candidate has fulfilled the conditions of the Resolution and Regulations appropriate for the degree of …… in the University of St Andrews and that the candidate is qualified to submit this thesis in application for that degree.

Date …….. signature of supervisor ……

3. Permission for publication: (*to be signed by both candidate and supervisor*)

In submitting this thesis to the University of St Andrews I understand that I am giving permission for it to be made available for use in accordance with the regulations of the University Library for the time being in force, subject to any copyright vested in the work not being affected thereby. I also understand that the title and the abstract will be published, and that a copy of the work may be made and supplied to any bona fide library or research worker, that my thesis will be electronically accessible for personal or research use unless exempt by award of an embargo as requested below, and that the library has the right to migrate my thesis into new electronic forms as required to ensure continued access to the thesis. I have obtained any third-party copyright permissions that may be required in order to allow such access and migration, or have requested the appropriate embargo below.

The following is an agreed request by candidate and supervisor regarding the publication of this thesis:

Embargo on all printed and electronic copies for the same fixed period of 2 years on the following ground:
Publication would preclude future publication.

Date …….. signature of candidate ……

signature of supervisor ……

Abstract

There has been specific interest over the past decade in the discovery and development of new piezoelectric and ferroelectric materials for the use in functional devices, specifically with the aim of replacing the widespread use of $PbZr_xTi_{1-x}O_3$.

The work detailed in this thesis focuses on the structural characterisation and thermal behaviour of several perovskites possessing interesting physical characteristics, such as ferroelectricity or magnetism. Structural evolution and phase behaviour is characterised using Rietveld refinement techniques on high resolution powder neutron diffraction data. Additional analytical techniques such as symmetry mode analysis, permittivity measurements and second harmonic generation measurements are also often exploited.

The work on the $Li_xNa_{1-x}NbO_3$ system demonstrated a susceptibility to softening of the T_4 octahedral tilt mode up to a composition of at least $x = 0.12$, indicating that the LNN-*X* solid solution could yield a number of unique perovskite structures. A rationale for how this T_4 mode varies across the composition range is offered. The higher doped composition at a value of $x = 0.20$, displays even more intriguing structural behaviour with the adoption of not one but two variants of the very rare $a^+a^+c^-$ Glazer tilt system.

A detailed bond length/bond angle analysis as a function of temperature is used to rationalise the nature of the octahedral distortion that drives the $c > a$ crossover in the rare earth orthoferrite $LaFeO_3$. Symmetry mode analysis is exploited to assist in the structural comparison to the related compound $Bi_{0.5}La_{0.5}FeO_3$, highlighting the anomalous behaviour it exhibits as a result of magnetoelectric coupling effects.

The nature of the paraelectric – ferroelectric transition in the layered perovskite-like Dion Jacobson phase, $CsBi_{0.6}La_{0.4}Nb_2O_7$ is identified as a direct "avalanche" type transition, making it an example of a hybrid improper ferroelectric. Ferroelectricity in this case does not occur as a result of traditional second-order Jahn-Teller distortions, but is achieved *via* a mechanism known as trilinear coupling. Experimental analysis is important in understanding the intricacies of this trilinear coupling mechanism. Symmetry mode analysis of $CsBi_{0.6}La_{0.4}Nb_2O_7$ shows that two zone boundary primary order parameters (M_2^+ and M_5^-) associated with octahedral tilting condense simultaneously, and couple to a zone centre ferroelectric distortion mode (Γ_4^-). The similar temperature dependency for the two octahedral tilt modes excludes the presence of an intermediary phase, suggesting that the trilinear coupling in this layered phase is strong.

Detailed structural characterisations such as those highlighted in this thesis are of fundamental importance as they can identify new design-led approaches to functional materials.

Acknowledgements

I would firstly like to give a special thankyou to my supervisor, Professor Philip Lightfoot, for giving me the opportunity to work in a fantastic group, and for taking the time to ensure that I got to this stage in one piece, with results! It has been a tremendous help to have a supervisor who is always willing and interested to look at and discuss results at every step of the way.

I would also like to thank all past and present members of the Lightfoot group for making my time in the group so enjoyable and creating a wonderful work atmosphere. I would like to thank Dr. Lucy Clark in particular, for all her help and support throughout the past two years, and for always being there to listen. In addition, I would like to thank Daniel Firth and Simon Vornholt for keeping things fun throughout my time in St Andrews.

I would also like to thank Mr. Jason McNulty for his patience when I have wanted to carry out yet another dielectric experiment, and for his help with regard to troubleshooting problems and explaining the ins and outs of the instruments and measurements taken.

During the course of my PhD I have been fortunate enough to have made several trips to the ISIS neutron spallation source. I would like to thank the beamline scientists, Dr. Kevin Knight, Dr. Alexandra Gibbs and Dr. Aziz Daoud-Aladine for their kind assistance and helpful guidance and comments on the experiments.

I must also thank my parents, Heather and Ian Dixon, who have truly supported me in everything I aim to achieve. For being proud of me but not pushing me, giving me the freedom to take the path I choose. I would also like to thank my paternal grandparents, Harold and Joan Dixon for their kindness and support.

I would finally like to dedicate this to my late grandmother, Violet Moore, who wanted nothing more than to see my thesis finished, and who kept a copy of my first paper in the living room, showing anyone willing to look. Someone who always fought my corner and had the firm belief I could achieve anything I set my mind to, even when I didn't. So, this is for her.

Contents

1 Introduction

1.1 The Perovskite Structure – Background and History

The ABX_3 perovskite structure has proven to be one of the most versatile structure types in materials chemistry, adopted for a wide range of chemical compositions with various interesting crystal symmetries and functional properties. To date perovskites have demonstrated superconducting[1, 2], ferroelectric[3-5] and multiferroic[6] properties to name only a few. For this reason perovskites can be found in a wide range of useful electronic devices such as fuel cells[7], solar cells[8], data storage devices[9], and sensors[10, 11]. Their unique ability to incorporate almost any element of the periodic table make perovskites the focus of much research, with a search using the term "perovskite" in Web of Science® yielding 57,982 results on the topic, with 5,658 research papers published in 2016 alone.

The first perovskite structure was discovered by Gustav Rose in 1839 in the Ural Mountains of Russia. This was in the form of the mineral $CaTiO_3$. The mineral was given the name "Perovskite" (which is now used as a more general term for the structure type) after the Russian scientist A. von Perovskji (1792-1856)[12]. Originally, the structure type did not generate a great deal of interest. The work of V.M. Goldschmidt focused on a large number of synthetic perovskites in the years 1924-26, characterising their unit cells using X-ray diffraction at a time when the technique was still in its inception. The lattice parameters deduced in his early work on perovskites have proven to be impressively accurate today. The first full characterisation of the 3D crystal structure was achieved by Helen D. Megaw in her work on $BaTiO_3$, again using X-ray diffraction techniques[13]. The rapid increase

in the interest of the structure for materials chemists came with the observation of the incredibly high dielectric constant, κ, exhibited in $BaTiO_3$ by Wainer and Solomon[14] in the early 1940s, leading to its wide use as an insulating material in capacitors. The next significant event in the history of perovskites came with the suggestion by Von Hippel that the reason for the high dielectric constant of $BaTiO_3$ was due to ferroelectricity[15, 16]. This was confirmed independently by Ginsberg[17], Megaw[18], and Blattner, Matthias and Merz[19]. The discovery of the first ferroelectric perovskite was of great importance as it was the first example of a ferroelectric structure that contained no hydrogen bonds and also possessed more than one ferroelectric phase[20]. Moving forward 40 years, the Nobel prize was awarded to Bednorz and Muller for their work on the High-T_C superconductor $Ba_xLa_{2-x}CuO_4$[21]. This discovery sparked an intense upsurge in perovskite-based research.

Currently, much of the research on perovskites is devoted to the discovery of new polar, dielectric materials with comparable relative permittivity values to replace the industry standard, PZT ($PbZr_xTi_{1-x}O_3$)[22-25]. Despite its highly desirable properties including high dielectric and piezoelectric constants[26], the wide spread use of PZT in devices such as ultrasound transducers, and actuators[5] is associated with high levels of pollution. This eventually led to EU legislature in 2003 which demanded that the use of PZT in electronic devices be completely "phased-out" and substituted by lead-free alternatives[27, 28]. Alkali niobate perovskites have so far emerged as some of the most promising candidates[29-32], with much of the work of this thesis focused on the structural characterisation of phase transitions in select compositions of the $Li_xNa_{1-x}NbO_3$ solid solution. The more recent discovery of a new class of "hybrid-improper ferroelectrics" in the layered perovskite-like Aurivillius and Dion-Jacobson phases could potentially herald a new era in perovskite ferroelectric materials with further important consequences in the fields of multiferroics and magnetoelectric coupling[33].

1.2 Crystallography

1.2.1 Crystal symmetry

The primary focus of this work is the determination of crystalline structure and symmetry of various perovskite phases, therefore in this section some of the fundamental crystallography concepts are introduced. Crystalline structures are defined as those that display long range periodic order involving a regular arrangement of atoms in three-dimensional space. The smallest repeating arrangement of these atoms is used to describe the translational symmetry of the structure and is referred to as the unit cell. The unit cell is defined by 6 individual parameters consisting of, unit cell lengths *a*, *b* and *c*, and angles α, β, and γ.

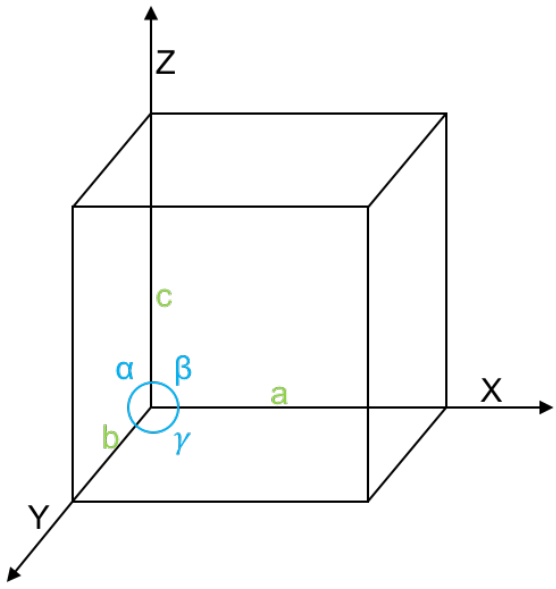

Figure 1.1 Schematic of unit cell dimensions, showing cell lengths *a*, *b* and *c* and angles α, β and γ.

There are 7 unique, symmetry-dictated ways in which these parameters can be related to one another, thus making up the 7 crystal systems detailed in Table 1.1.

Table 1.1 The seven crystal systems. The ≠ sign indicates two entities are not necessarily equal to one another.

Crystal System		Unit cell	Essential symmetry elements
Cubic	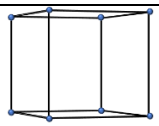	$a = b = c$, $\alpha = \beta = \gamma = 90°$	Four 3-fold axes
Tetragonal	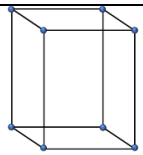	$a = b \neq c$, $\alpha = \beta = \gamma = 90°$	One 4-fold axis
Hexagonal	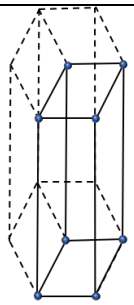	$a = b \neq c$, α, $\beta = 90°$ $\gamma = 120°$	One 6-fold axis
Trigonal*	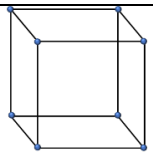	$a = b = c$, $\alpha = \beta = \gamma \neq 90°$	One 3-fold axis
Orthorhombic	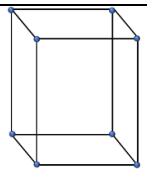	$a \neq b \neq c$, $\alpha = \beta = \gamma = 90°$	Three perpendicular 2-fold axes/ or mirror plane
Monoclinic	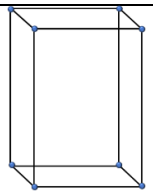	$a \neq b \neq c$, $\alpha = \gamma = 90°$ $\beta \neq 90°$	2-fold rotational axes/ or mirror planes
Triclinic	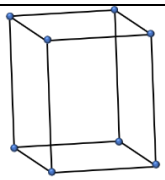	$a \neq b \neq c$, $\alpha \neq \beta \neq \gamma \neq 90°$	None

* A second special case of trigonal symmetry is the rhombohedral lattice, in which $\gamma = 120°$

Whilst the unit cell provides a basis for the lattice motif, describing atoms as fractional coordinates along the cell lengths *a*, *b* and *c*, and increasing or changing the number and position of the lattice points creates several different types of crystal lattice: primitive (P), body-centred (I), face-centred (F) and C-centred (C).

Combination of the seven types of crystal system with the four types of lattice (P, I, F and C shown in Figure 1.2) generates 14 Bravais lattices, detailed in Table 1.2 below.

Table 1.2 The 14 Bravais lattices that result from each possible combination of unit cell and lattice type.

Crystal System	Bravais Lattice
Cubic	P, I, F
Tetragonal	P, I
Hexagonal	P
Trigonal/ Rhombohedral	P/R*
Orthorhombic	P, I, F, C (A or B)
Monoclinic	P, C
Triclinic	P

* The symbol R is used to represented the centred rhombohedral cell.

Point group symmetry elements result in 32 individual crystallographic point groups. When combined with the Bravais lattices and additional translational symmetry elements this results in 230 unique space group symmetries in three-dimensional space. The various symmetry elements that are used to denote the symmetry of these 230 space groups are detailed in the following section.

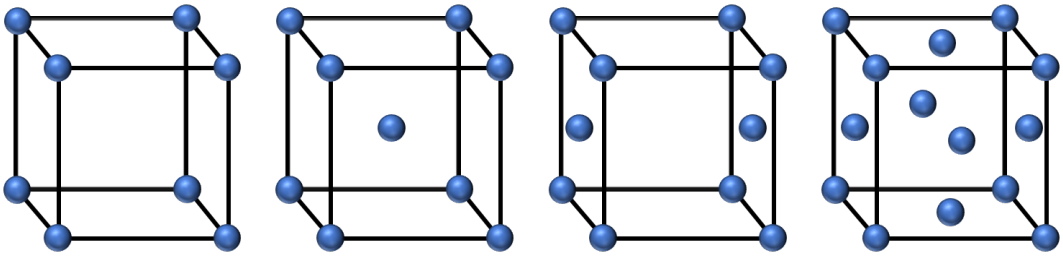

Figure 1.2 From left to right, Primitive (P), Body centred (I), C-centred (C) and Face centred (F) lattice types.

1.2.2 Symmetry operations

Whilst numerous unique symmetry operations can be performed on a crystal, they can be categorised into three main classes: rotation, reflection and inversion. These point symmetry operations are defined as operations the crystal can undergo whilst remaining unchanged.

As a rule, if rotation through an angle less than 360 ° leaves the lattice unchanged, the axis through which it was rotated is described as having rotational symmetry. The degree of this rotational symmetry is linked to the magnitude of the angle through which the lattice must be rotated to remain unchanged, or the number of times that an object can be rotated about its axis unchanged before returning to its starting position (360 °/*n*). For example, a four-fold rotation axis, denoted simply by the number 4, indicates that the crystal lattice displays four-fold symmetry around that axis such that a rotation through 90 ° does not change the structure.

Reflections occur across a mirror plane; therefore all positions are translated to equivalent positions on the opposite side of the mirror plane *e.g.* (*x*, *y*, *z* -> -*x*, *y*, *z*).

The inversion symmetry operation indicates a centre of symmetry relating to all lattice points in the unit cell so that if each point was moved through the inversion centre by an equal amount the lattice would remain unchanged. An inversion centre at the origin of the lattice is denoted with a $\bar{1}$ and results in a translation of *x*, *y*, *z* to -*x*, -*y*, -*z*. Inversions on an axis of rotational symmetry or rotoinversions lead to improper symmetry, these are denoted as $\bar{2}$, $\bar{3}$, $\bar{4}$ and $\bar{6}$. A conventional crystal cannot possess 5-fold rotation symmetry.

Apart from the three classes of point group symmetry elements, there are additional translational elements, screw axes and glide planes. A screw axis describes a simultaneous rotation and translation. Again, due to the symmetry restrictions imposed by the three-dimensional lattice, only 1, 2, 3, 4, and 6 rotations are allowed. The subscript associated with the screw axis notations denotes the fraction along the axis the lattice point translates. For example, a screw axis denoted as 2_1 describes a two-fold rotation with a simultaneous translation by ½ along the unit cell length.

Glide planes describe reflection through a mirror plane with a simultaneous translation parallel to the plane. Glide planes are indicated by the letters *a*, *b*, *c*, *n* and *d*. The letter symbols *a*, *b* and *c* describe reflection through a mirror plane followed by translation by ½ of the cell length of the cell axis specified by the letter. The *n*-glide translates the object diagonally upon reflection through the mirror plane, *i.e.* translation by ½ along two of the unit cell lengths. A *d*-glide is similar to the *n*-glide, but translates the lattice point by ¼, diagonally.

Out of the 32 crystallographic point groups only 10 of these are polar (polar point groups are needed for ferroelectric materials). For a space group to be polar it must be derived from one of the polar point groups, by further consideration of translational symmetry elements: it must possess at least one axis that is not perpendicular to a 2-fold axis or mirror plane *e.g. P*4*mm* or *R*3c (*i.e.* must possess at least one anisotropic axis).

1.2.3 Miller planes

A useful representation of the crystal lattice is as a set of individual planes, which can relate the crystal lattice to points in the diffraction pattern. The planes are known as Miller planes and are described by three indices *h*, *k*, *l* relating to the unit cell vectors *a*, *b* and *c*. The value of the Miller index is the reciprocal of fractional coordinate at which it intercepts the corresponding cell length *i.e.* the Miller plane (100) intercepts the *a* unit cell vector at the origin and runs parallel to both the *b* and *c* unit cell vector, whilst a Miller plane that intersects halfway along the *a*-axis only is identified as the (200) plane. Diagonal Miller planes such as (110) intercept the *a* and *b* unit cell lengths at the origin and run parallel to *c*. These Miller indices are utilised when indexing the spots in the diffraction pattern generated by the crystal lattice (see Chapter 3, Section 3.3 on Ewald's sphere and the reciprocal lattice). Examples of the (100) and (110) Miller planes are shown in Figure 1.3.

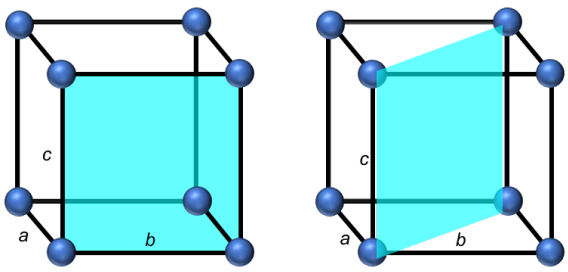

Figure 1.3 Representation of Miller planes (100) and (110) at *a*,0,0 and *a*, *b*, 0.

1.3 The Perovskite Structure

Perovskites are mixed metal compounds of the formula ABX_3, where A is typically a large group I or group II cation or lanthanide, B is typically a smaller transition metal cation and X is typically oxide or less frequently a halide anion. The structure involves a three-dimensional network of corner-sharing BO_6 octahedra set amongst a primitive lattice of A-site cations. The A- and B-site cations are 12 and 6 coordinate to oxygen respectively. A representation of the ideal cubic perovskite structure is shown in Figure 1.4.

As discussed previously in section 1.1 the perovskite structure can accommodate almost any element in the periodic table, leading to its exotic chemistry and properties. Whilst the ideal structure is cubic (often referred to as the aristotype structure) with a close packed arrangement of corner-sharing BO_6 octahedra, varying the size ratio of the A and B cations leads to distorted phases with lower symmetry (*hetto*types). In addition to changes in composition, distorted phases can be induced by variations in the temperature[34] or pressure[35] of the system. It is these lower symmetry distorted phases that often result in the interesting physical properties. The metric which evaluates the degree of size mismatch between the A and B cations, often providing a predictor for the crystal system a compound will adopt was developed by Goldschmidt and is commonly referred to as Goldschmidt's tolerance factor[36] (Equation 1.1).

$$t = \frac{R_A + R_X}{\sqrt{2}(R_B + R_X)} \qquad \text{Equation 1.1}$$

where R_A is the radius of the A-site cation, R_X is the radius of the anionic species and R_B is the radius of the B-site cation.

The perovskite structure-type forms for a tolerance factor range of $0.78 < t < 1.05$[37].

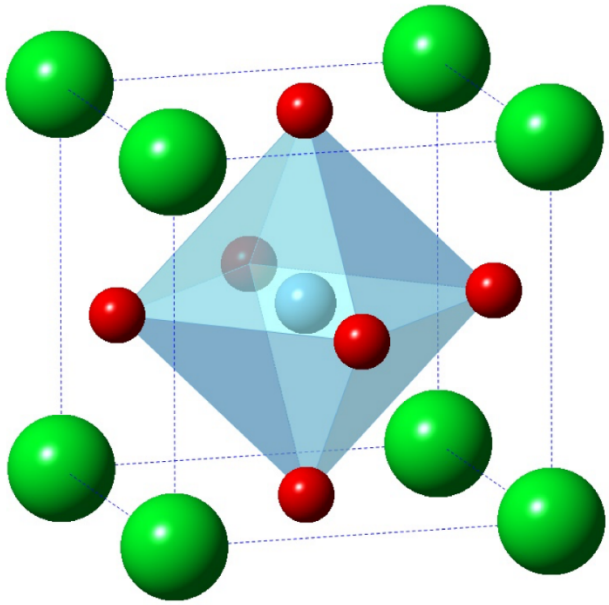

Figure 1.4 Representation of the idealised cubic ABX_3 perovskite structure. The larger A-site cations are shown in green and situated at the corners of the unit cell. The smaller B-site cation is placed at the body centre and is shown in blue. X anions are located at face centre positions and shown in red.

1.4 Distortions from the ideal cubic structure

Perovskites can distort in three ways; these include tilts of the BO_6 octahedral units, A-site cation displacements and/or distortion of the octahedra. Of these, the predominant factor that governs the resulting space group symmetry of the distorted phase is tilting of the octahedra. It was Glazer[38, 39] and Megaw[40] who were the first to suggest this link between lower symmetry structures and

octahedral tilting. The introduction of a size mismatch between the A- and B- site cations is the driving force for this tilting, which takes place to maximise bonding at the A-site for values where $t < 0.985$[41, 42]. For lower tolerance factor values this octahedral tilting is often accompanied by co-operative A-site displacements. In compositions where $t > 1$, B-site displacements typically occur (which occasionally give rise to ferroelectricity) to maximise B-O bonding interactions. The final distortion type, in which the BO_6 octahedral units distort, is more rarely seen but can occur as a secondary effect to compensate for underbonding at apical oxygen sites, often in co-operation with A-site displacements.

Work by Reaney *et al*. provided insight into the link between tolerance factor and the type of octahedral tilting exhibited by the structure. Through a systematic survey of the tilt systems adopted by various perovskites with varying *t*, they reported that for $0.985 < t < 1.06$ no tilting was observed and a perovskite with cubic symmetry formed at room temperature. For $0.964 < t < 0.985$, typically only out-of-phase tilts were observed (normally of rhombohedral symmetry), and for $t < 0.964$ a combination of in-phase and out-of-phase tilts were observed (normally of orthorhombic symmetry)[41].

In addition to size considerations the electronic configuration of the A- and B-sites often plays a critical role, particularly with regard to the physical properties of the resulting compound, with selectivity in the choice of A and B cation potentially inducing magnetism or ferroelectricity. The crystal-chemical origins of these effects in perovskites are discussed further in sections 1.8 and 1.11 respectively.

Both ion-size mismatch and changes to electronic configuration can be introduced by partial substitution at the A- and B-sites for different species *via* chemical doping. This must be carried out whilst maintaining overall electroneutrality of the structure. Creation of a solid solution of the formula $A_{1-x}A'_xBO_3$ can often allow for

manipulation of the crystal structure and the chemical and physical properties by varying the value of *x*. This is a widely exploited approach in perovskite chemistry. The Hume-Rothery rules[43] state that a solid solution can be stabilised to accommodate a cation size difference of ~ 15 %.

1.5 Octahedral Tilting Distortions

Seminal work by Glazer[38, 39] identified 23 unique tilt systems that arise when each possible tilt configuration of a 2 × 2 x 2 block of corner-linked octahedra in three dimensional space is considered. These 23 tilt combinations were further simplified by Howard and Stokes to just 15[44]. A list of these tilt systems and their corresponding space group symmetries is given in Table 1.3. In Glazer notation tilts are described in terms of component tilts about each of the three "pseudo-cubic" axes. Due to the corner-sharing connectivity of the BO_6 octahedra, tilting of a specific axis in one direction determines the direction of the tilt in directions perpendicular to this axis, and consequently leading to an effective doubling of the axis perpendicular to the tilt. Successive octahedra along the original tilting axis, however, are not bound by the corner-sharing connectivity and are free to tilt in the same or opposite direction. When two adjacent octahedra along a singular axis tilt in the same direction this is referred to as an "in-phase" tilt. Conversely, an "out-of-phase" tilt occurs when two adjacent octahedra tilt in opposite directions along an axis. A simple representation highlighting the effect of these two types of octahedral tilting is shown in Figure 1.5. To classify these unique tilt systems, Glazer developed a new notation which takes into account both magnitude and direction of the tilt. Tilt magnitudes are described by the lower case letter *a*, *b* or *c*. Two tilts of equal magnitude are therefore assigned the same letter, e.g. *aac* describes a system in which the tilts about the *a*- and *b*-axes

are equal. The direction of the tilt is denoted with the symbols + or - for in-phase and out-of-phase tilts respectively. An axis around which no tilting occurs is indicated with a superscript 0. When two axes are each described by in-phase tilts or one in-phase and one-out-of-phase tilt, this indicates that the two axes are normal to each other. Two out-of-phase tilts indicate two axes that are inverted toward one another. For example, the $R\bar{3}c$ space group ($a^-a^-a^-$) setting has three axes that are inclined toward one another by equal amounts.

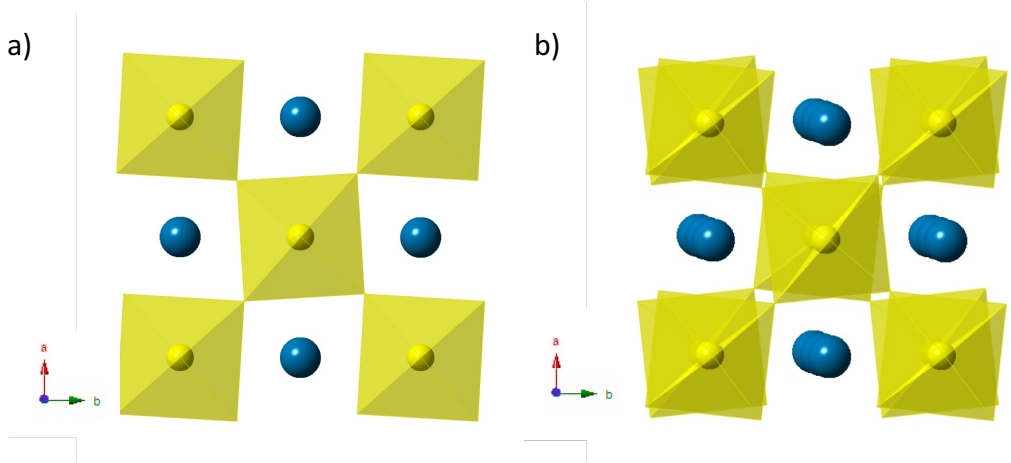

Figure 1.5 Schematics of typical perovskite tilt systems with a) highlighting the effect of an in-phase tilt along the *c*-axis ($a^0a^0c^+$ in Glazer notation) and b) highlighting the effect of an out-of-phase tilt along the *c*-axis ($a^0a^0c^-$).

Table 1.3 The 15 unique tilt systems and their corresponding space group symmetries as described by Howard and Stokes[44]. The space group symmetries are listed in terms of descending symmetry through a series of in-phase and out-of-phase octahedral tilts from cubic $Pm\bar{3}m$.

Glazer tilt system[45]	Space Group Symmetry
$a^0a^0a^0$	$Pm\bar{3}m$
$a^+a^+a^+$	$Im\bar{3}$
$a^0b^+b^+$	$I4/mmm$
$a^0a^0c^+$	$P4/mbm$
$a^0a^0c^-$	$I4/mcm$
$a^0b^-b^-$	$Imma$
$a^-a^-a^-$	$R\bar{3}c$
$a^+b^+c^+$	$Immm$
$a^+a^+c^-$	$P4_2/nmc$
$a^0b^+c^-$	$Cmcm$
$a^+b^-b^-$	$Pnma$
$a^0b^-c^-$	$C2/m$
$a^-b^-b^-$	$C2/c$
$a^+b^-c^-$	$P2_1/m$
$a^-b^-c^-$	$P\bar{1}$

1.6 Difference Reflections

These deviations from the ideal cubic structure to the lower symmetry *hetto*types are evidenced in the diffraction profiles generated by the crystalline superlattice structure. This may occur as the characteristic splitting of specific peaks due to the distorted unit cell metrics (*i.e.* when $a \neq b \neq c$ no longer applies, as a consequence

of octahedral tilting distortions). Furthermore, the appearance of additional peaks (commonly referred to as difference reflections) arising from the extended superlattice are often observed in the diffraction pattern. Identification of these peaks is sometimes challenging, but necessary, in order to unambiguously identify the symmetry of the distorted phase.

The origin of these difference reflections lies in the approximate doubling of unit cell axes perpendicular to those about which octahedral tilts are present (as described previously). Extra reflections are produced, which lie at half the value of those of the original cubic lattice in reciprocal space. These extra reflections can be indexed (based on a $2_{ap} \times 2_{ap} \times 2_{ap}$ supercell) with odd values for some Miller indices, in contrast to those arising from the cubic subcell which have strictly even values for *h*, *k* and *l*. Usefully, the + and – tilts produce difference reflections with unique patterns of Miller indices. In-phase tilts give rise to reflections with odd-odd-even Miller indices, based on a doubled unit cell metric, whilst out-of-phase tilts result in odd-odd-odd reflections. Glazer established a set of guidelines for identifying the tilting origin of the various types of difference reflections (Table 1.4).

Table 1.4 Rules established by Glazer[39] identifying the relationship between type of octahedral tilt and the Miller indices of the resulting difference reflections.

Tilt type	Miller index pattern	Extra conditions
a^+	even-odd-odd	$k \neq l$
b^+	odd-even-odd	$h \neq l$
c^+	odd-odd-even	$h \neq k$
a^-	odd-odd-odd	$k \neq l$
b^-	odd-odd-odd	$h \neq l$
c^-	odd-odd-odd	$h \neq k$

In addition to patterns in the Miller index values, further identifiers are found for + and – tilts as they condense at specific locations in the Brillouin zone of the cubic aristotype structure. This results in characteristic peaks for each type of tilt at specific d-spacings or 2θ values in the diffraction pattern. For + tilts, reflections are produced at reciprocal lattice points corresponding to one face-centred position in real space. In the reciprocal lattice the reflections are located at, for example, ($\boldsymbol{k}$ = ½, ½, 0) for a c^+ tilt, commonly referred to as the M-point. For – tilts, the resulting Bragg reflections correspond to all face-centred points. The location of the reflection in the reciprocal lattice this corresponds to is ($\boldsymbol{k}$ = ½, ½, ½), also known as the R-point. Throughout this work the identification of M- and R-point peaks is used as a guide when assigning the space group symmetry of emergent phases and identifying phase transitions in the various systems studied.

1.7 Symmetry Modes and the Reciprocal Lattice

An alternative way of considering the various distortions that may manifest to bring about a lower symmetry phase is in terms of their symmetry-adapted modes. In this approach distorted structures are referenced as a set of structural degrees of freedom resulting from the phase transition from the aristotype or higher symmetry phase. Symmetry modes present in the aristotype that are permitted in the lower symmetry phase must be identified. The structural distortion to the lower symmetry phase is then described as the sum of the contributions of the active individual symmetry modes. In this manner, trends in atomic displacements or macroscopic strains can be described as vectors. For this, irreducible representations of the distortions are extremely useful as their basis vectors can easily be selected to be normal to one another, including those of additional *irreps*. In this manner *irreps.* not only allow formation of a complete

basis set but offer unique descriptions of the distortions, allowing for scrutiny of individual distortion modes in a completely decorrelated manner. This is valuable when wanting to understand the structural effects propagated by individual distortion modes, especially with regard to the emergence of a new phase. For example, a distorted structure with *P*4/*mbm* symmetry ($a^0a^0c^+$) is related to the parent $Pm\bar{3}m$ structure *via* an in-phase octahedral rotation that is described by the irreducible representation, M_3^+. A space group *irrep.* is defined by those distortions that are associated with the ***k***-point superlattice reflections. While many phase transitions can be described by a single *irrep.*, some transitions can only be achieved by the combination of multiple *irreps.* and are therefore necessarily described by reducible representations[46].

These individual distortion modes that bring about structural changes in real space are related to reflections in the diffraction profile in reciprocal space. The two basic types of octahedral tilt therefore occur at specific ***k***-points in reciprocal space. As highlighted in the previous section the + and – tilts occur at (***k*** = ½, ½, 0) and (***k*** = ½, ½, ½) respectively. These tilts can be recast as the M_3^+ and R_4^+ symmetry modes (Figure 1.6), using the notation of Miller and Love[47]. These ***k***-positions in reciprocal space are described in relation to the origin of the Brillouin zone located at the centre of the reciprocal cubic cell. Therefore, in the reciprocal lattice M points are located midway along the cell edge (½, ½, 0) and R points are located on the corners (½, ½, ½). Other, more complex, octahedral tilts comprising of a sequence of + and – tilts such as the T_4 mode present in Phases P, R and S of $NaNbO_3$ (see Chapter 4) are also uniquely described in this approach (the T-line is located between R- and M-points at (***k*** = ½, ½, γ)). A schematic of the cubic Brillouin zone, highlighting the location of specific symmetry modes is shown in Figure 1.7.

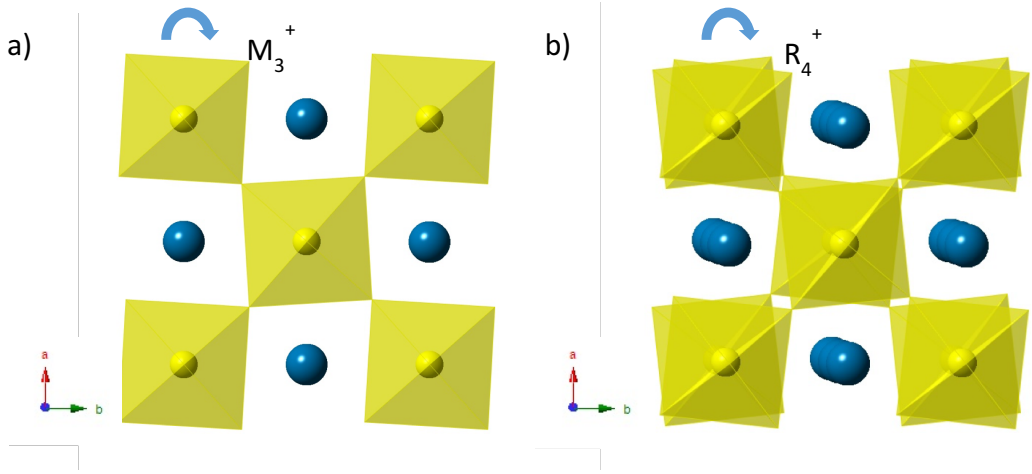

Figure 1.6 Adaptation of Figure 1.5, rethought in terms of the symmetry modes M_3^+ and R_4^+ which represent + and – tilts respectively. In a tilt system such as $a^0a^0c^+$, the M_3^+ mode acts around the *c*-axis. The view looking down the *c*-axis, shown in a), highlights the overlapping octahedra which result. In the $a^0a^0c^-$ the action of the R_4^+ mode acts about *c*, and results in the staggered octahedra shown in view b).

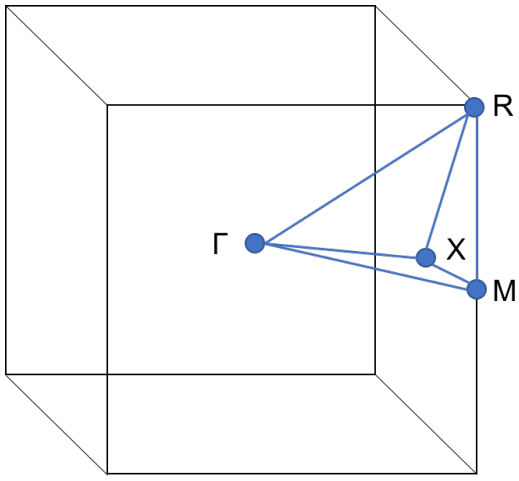

Figure 1.7 Schematic of 1st cubic Brillouin zone showing positions of Γ (polar, zone centre), M, R (described in the text) and X (centre of face) points in the reciprocal lattice. The T-line runs between R and M, and is discussed further in Chapter 4. The X point often relates to cation displacements.

Upon undergoing a symmetry-lowering structural change or distortion, certain symmetry elements present in the parent structure are necessarily lost whilst others persist. Those that persist form the basis of the space group symmetry of the lower symmetry phase and result in the systematic relationship between the distorted phase and the parent phase. Thus, the distorted phase is referred to as an "isotropy" subgroup of the parent phase. Within a given isotropy subgroup, several unique distortions can occur related to the new degrees of structural freedom introduced by the lower symmetry space group. The available distortion modes are therefore dependent upon the symmetry restrictions imposed by the space group of the distorted phase. Stokes and Hatch[48] conducted a systematic evaluation detailing all isotropy subgroups of the 230 crystallographic space groups induced at special ***k***-points originating from a singular *irrep* of the parent. The ISOTROPY and ISODISTORT[49] online tools permit exploration of subgroups associated with non-special ***k***-points and coupled *irreps.*, made possible by computation techniques to assist the group theory analysis. This ability to explore group sub-group relationships and identify the numerous individual distortion modes possible in the lower symmetry phase is particularly valuable when characterising the phase diagram of perovskite systems with the use of diffraction techniques.

A further use of symmetry mode representations is as a means of characterising a phase transition in terms of primary and secondary order parameters. Analysis of the individual mode amplitudes of the symmetry adapted modes can identify the structural "driving force" *i.e.* the distortion mode responsible for the phase transition. An order parameter is considered to be "primary" if its condensation lowers the overall energy of the system, resulting in the stabilisation of the lower symmetry phase. Additional order parameters which couple to or co-operate with the primary mode are referred to as "secondary". Using the ISODISTORT online software suite[49] (see Chapter 3 Section 3.10) the primary and secondary order

parameters associated with a phase transition can be identified by examination of the evolution of the symmetry-adapted modes as a function of temperature or composition, paying close attention to their behaviour in the vicinity of the phase transition. Symmetry analysis such as that just described is exploited extensively in this work.

1.8 Magnetism and the Superexchange Interactions

An important property that the perovskite structure can exploit is that of long range magnetic ordering. With selective choosing of the B-site cation various perovskites that exhibit magnetic ordering can be synthetically obtained. Magnetic materials are characterised as those that have unpaired electrons, typically with transition metal (TM) cations in which the unpaired electrons occupy d or f orbitals. The magnetic moment or dipole is created due to the orbital spin and charge associated with the electron. The orientation of the unpaired electrons, and by extension the magnetic dipoles, in a material determine what type, if any, of magnetic ordering is present. The intriguing phenomenon of colossal magnetoresistance (CMR) has been observed in manganese oxide perovskites[50, 51], whilst coupling of electric and magnetic ordering can result in often desirable multiferroic properties (see Chapter 1, section 1.14).

The word paramagnetic is used to describe a system in which the unpaired electrons are orientated randomly relative to those on different atoms. Magnetic ordering is introduced when all the unpaired electrons are aligned parallel (ferromagnetism) or antiparallel (antiferromagnetism). Ferrimagnetism describes a system in which electron spins are aligned antiparallel but in unequal amounts, resulting in a small net magnetic moment.

Antiferromagnetic ordering can be present as one of three simple types. So-called "A-type" antiferromagnetic ordering describes a system in which the intra-plane coupling is ferromagnetic with antiferromagnetic inter-plane coupling. C-type antiferromagnetism involves intra-planar antiferromagnetic coupling with inter-planar ferromagnetic coupling. Finally, G-type antiferromagnetism describes a system in which both the inter-and intra-planar coupling are antiferromagnetic. Basic representations of the various types of magnetic ordering are shown in Figure 1.8.

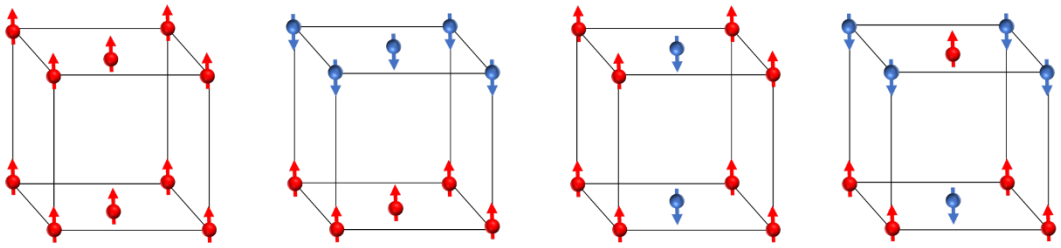

Figure 1.8 Schematics of the various types of magnetic ordering, from left to right, showing ferromagnetic (F-type), and A-type, C-type and G-type antiferromagnetic ordering of the magnetic moments.

Magnetic ordering is a low temperature phenomenon. The critical temperature of the magnetic ordering, which varies between materials, is known as the Curie temperature, T_C, for ferromagnetic ordering, and the Néel temperature, T_N, for antiferromagnetic ordering. Above this critical temperature, the material is paramagnetic[52]. The onset of magnetic ordering in antiferromagnetic perovskites is typically facilitated *via* a "superexchange" mechanism in which the spins on the nearest neighbour transition metal cations are aligned antiferromagnetically. This is mediated through the non-magnetic oxygen anion. For magnetic spin ordering to occur in this manner, the orbital overlap between the transition metal 3d orbitals and O 2p orbitals in the TM-O-TM linkages must be maximised (see Figure 1.9). Therefore, the optimal angle for the superexchange interaction is 180 °.

Smaller cations at the perovskite A-site lower the value of T_N as the tilting of octahedra to maximise A-O bonding interactions[53] incurs a reduction in the TM-O-TM bond angle, decreasing orbital overlap.

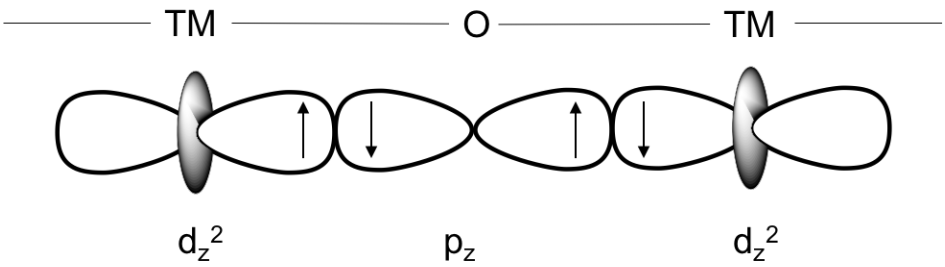

Figure 1.9 Schematic highlighting the mechanism of antiferromagnetic superexchange facilitated through orbital overlap in the TM-O-TM linkages.

1.9 Shubnikov Symmetry

As traditional space group classifications give no indication of the magnetic structure, Shubnikov symmetry offers a way to describe the magnetic ordering by assigning "colours" to the symmetry operations. Spin directions are often described as axial vectors; in magnetic materials, the electron spins are treated as an axial current loop perpendicular to the polar axis. The colour description with regards to specific symmetry elements is applied if that symmetry element brings about a change in direction of the spin orbit (flips the magnetic spin). Using this notation, a symmetry element that causes a change in the spin orbit direction is indicated with a prime symbol, '; for example, m becomes m' if the mirror plane acts on the current loop in an appropriate orientation. Symmetry elements such as inversion centres do not change the direction of the spin orbit and are therefore not primed. Donnay *et al.*[54], in their work on the symmetry restrictions implicated by space group symmetry, demonstrate that the presence of a mirror plane

parallel to the electron alignment (and therefore perpendicular to the magnetic moment), changes the direction of the current loop. For mirror planes that are parallel to the magnetic moment the current loop is flipped and the symmetry element is primed (Figure 1.10).

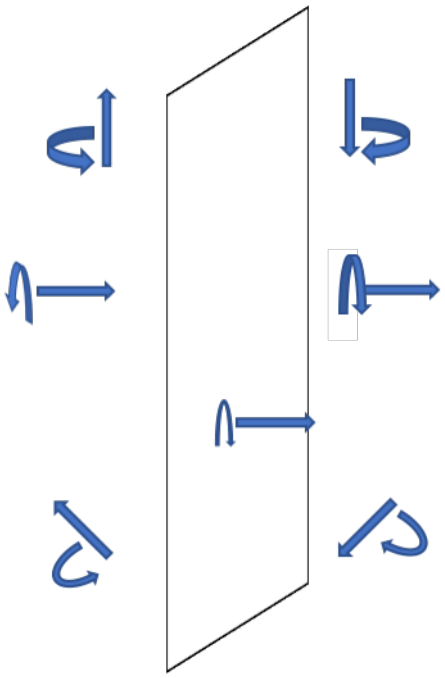

Figure 1.10 Schematic demonstrating the effect of the mirror plane symmetry operation on the direction of the magnetic spin orbit.

The rare earth orthoferrite perovskites are examples of G-type antiferromagnets. $LaFeO_3$, investigated in chapter 6 of this thesis, crystallises in the *Pnma* space group. However, the full description of the structure of $LaFeO_3$, taking into account both the magnetic and nuclear structures is *Pn'ma'*. The description below, with the use of Figure 1.11, illustrates how the magnetic structure is described using Shubnikov notation.

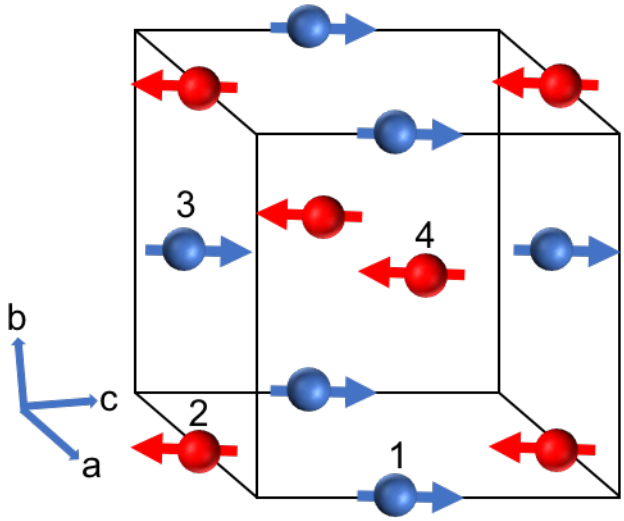

Figure 1.11 *Pn'ma'* G_z-type magnetic cell showing the direction of the magnetic moment, highlighting symmetry operations on selected spins. For simplicity only the B-sites are shown as only they contribute to the magnetic superstructure.

Atomic positions

1. 0, 0, ½
2. ½, 0, 0
3. ½, ½, 0
4. 0, ½, ½

In *Pnma* symmetry, it is only the a-glide symmetry element that is perpendicular to the moment, therefore:

An *a*-glide at z = ¼ from 1 to 2 maintains the spin orbit direction, and is therefore primed.

n-glide at x = ¼ from 1 to 3 changes the spin orbit direction, and is therefore primed.

mirror plane at y = ¼ from 1 to 4 changes the spin orbit direction, and therefore is not primed.

In the GSAS software package[55] primed spin operators (often referred to as "time reversal" operators) correspond to "red" spin operators, with "black" spin operators representing symmetry elements that conserve the direction of the spin orbit. The *Pn*'*ma*' structure is therefore input as red, black, red[56].

In contrast to the Shubnikov symmetry approach, irreducible representations of the actual space group (in a similar manner to the symmetry mode approach described in section 1.7 of this chapter) can be exploited to describe the transformation properties of the magnetic structure. The individual basis vectors of the irreducible representations comprise of linear combinations of the spins and hence describe the magnetic structure. Assigning the irreducible representations along each of the Cartesian axes allows for the formation of a full basis set and a description of the magnetic ordering in three dimensions[57]. This approach is arguably superior as three dimensional representations can be described associated with any value of **k**, as opposed to Shubnikov symmetry which only describes real one dimensional representations of the 230 space groups.

1.10 Dielectric Ceramics

As discussed in Section 1.1 of this chapter, the discovery of new polar and ferroelectric materials is the subject of much research in the materials science community worldwide, as they can often be exploited for their dielectric properties in the use of various electronic devices[58]. Polarity can arise in the perovskite structure *via* co-operative A- or B-site cation shifts; this differentiates them from polar dielectrics which involve distortion of the electron cloud. A dielectric material is an insulator (does not possess free electrons for electronic

conduction) which is polarised in an electric field. There are several types of polar dielectric; these are piezoelectric (polarisation induced upon application of a mechanical strain[59]), pyroelectric (temperature induced polarisation[60]) and ferroelectric materials. The work in this thesis concerns the last of these, the ferroelectric class of dielectrics. Ferroelectric materials are inherently pyroelectric and piezoelectric as the classes are related by increasing symmetry and energetic considerations. The relationship of the various polar dielectric properties is shown in Figure 1.12.

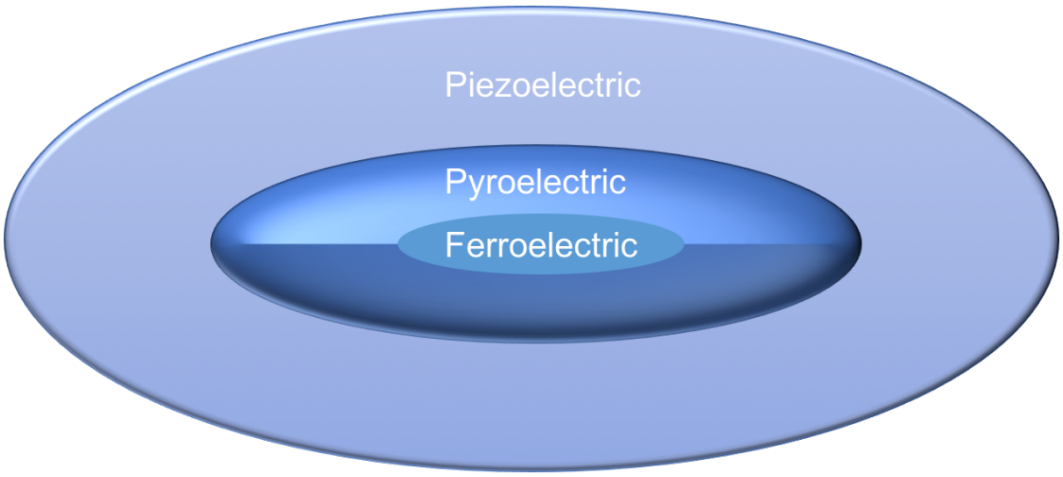

Figure 1.12 Venn diagram showing the relationship between the various classes of polar dielectrics.

Ferroelectricity is defined as a spontaneous polarisation that is reversible upon switching of an applied electric field. Ferroelectrics differ from normal dielectrics as some residual polarisation within the structure remains upon removal of the applied electric field. In addition to the residual or remnant polarisation, ferroelectric materials typically exhibit extremely large dielectric constants or permittivity values[61]. For linear dielectrics, as the name suggests, increasing the applied electric field (E) results in a proportional increase in the polarisation of the system (P), satisfying the equation,

$$P = \varepsilon_0 \chi_e E \qquad \text{Equation 1.2}$$

where ε_0 permittivity of a vacuum and χ_e is the susceptibility of the material.

In ferroelectrics, however, this linear relationship between applied electric field (*E*) and polarisation (*P*) no longer applies. Instead hysteresis is observed, with different behaviour displayed by the polarisation upon application and removal of the potential difference. When applying a potential difference, once a strong enough field is achieved, the polarisation reaches a maximum. This is referred to as the saturation polarisation, P_s. The residual or remnant polarisation retained upon reduction of the potential difference to zero is referred to as P_r. The process of reducing and reversing the polarisation requires a reverse field, known as the coercive field, E_c. An example of a typical hysteresis loop generated by a ferroelectric material is included in Figure 1.13.

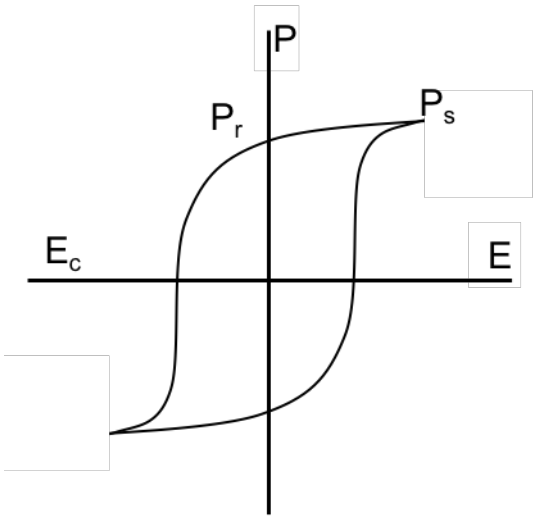

Figure 1.13 Schematic showing a typical P-E hysteresis loop resulting from ferroelectricity showing the remnant polarisation, P_r and polarisation saturation, P_s.

Ferroelectric materials such as $BaTiO_3$ are characterised by one cation that can displace significantly relative to its anionic neighbours, thus generating electrical dipoles with high dielectric constants. Similarly to magnetism, in perovskites these electrical dipoles can be aligned in-parallel due to cooperative cation shifts (in ferroelectric materials), creating a net polarisation, or anti-parallel (in antiferroelectric materials). Anti-parallel alignment results in no net polarisation due to the cancelling out of equal and opposite dipoles. The A-site cation displacements in the *Pnma* space group are an example of an antiferroelectric distortion.

1.11 Chemical Origin of Ferroelectricty

In traditional ABO_3 perovskite ferroelectrics, the ferroelectric behaviour can originate at either the A or B cationic sites *via* a second order Jahn-Teller (SOJT) mechanism. For activity to occur at the A-site typically a cation with a stereochemically active (polarisable) lone pair is necessary *e.g*. $BiFeO_3$[62].

For B-site ferroelectric activity, typically a transition metal cation with a completely empty set of d-orbitals is necessary *e.g*. the Ti^{4+} d^0 cation in $BaTiO_3$[63]. From a geometric approach, this occurs when a B-site cation is too small for its site. B-site displacements toward oxygen sites occur to enhance B-O bonding interactions. The direction in which the B-site cation is displaced within the BO_6 octahedra determines the crystal symmetry of the resulting ferroelectric structure.

In terms of electronics and a molecular orbital approach, a hybridisation or charge transfer mechanism occurs between the full 2p orbitals on oxygen and the empty

3d orbitals of the B-site cation. This p-d hybridisation can occur as the energy of the LUMO of the highly charged B-site cation is low enough to facilitate orbital mixing with the HOMO (2p orbital) of the oxygen. This hybridisation lowers the overall energy of the system and stabilises the underbonded B-site. The interactions between the A-site and O 2p orbitals can be covalent as in $PbTiO_3$, or completely ionic as in $BaTiO_3$[64].

Ferroelectricity, like magnetism, is a phenomenon favoured by lower temperatures as the increased thermal motion induced by increased temperatures results in the loss of the polar displacements. The temperature at which the ferroelectric ordering is lost is known as the Curie temperature, T_C. Above T_C the material is paraelectric. The ferroelectric – paraelectric transition may be a displacive or an order-disorder phase transition.[52]

1.12 The Shortage of Perovskite Ferroelectric Materials

Whilst many of the most well-known ferroelectrics are perovskites, only a very small proportion of the unique perovskite phases discovered to date adopt ferroelectric or even polar structures. This problem was traditionally thought to be due to an uncooperative relationship between octahedral tilting and ferroelectric distortions (*i.e.* the octahedral tilting supressed ferroelectric distortions). Octahedral tilting occurs to maximise A-O bonding interactions, whereas most ferroelectric distortions occur to compensate for underbonding of the B-site cation, suggesting that one is not compatible with the other. Ferroelectric $BaTiO_3$ and $PbTiO_3$ both adopt structures with no octahedral tilting for example, whereas structures with octahedral tilts are typically

centrosymmetric. The ability to induce ferroelectric distortions in tilted structures could have a large impact on the discovery of new ferroelectric materials.

A breakthrough in this area was made in the work of Benedek and Fennie[65], who crucially discovered that structures with low tolerance factor values and increased octahedral tilting in fact showed a greater instability to ferroelectric distortions. Using Density Functional Theory (DFT) calculations they discovered that it is the energy benefits associated with the anti-polar A-site displacements in the most commonly adopted room temperature perovskite phase, *Pnma*[66], that suppress ferroelectricity and stabilise this centrosymmetric structure. This suggests that tilt patterns which involve large octahedral rotations but do not allow for anti-polar A-site displacements should be targeted in intelligent design approaches for new ferroelectric materials. With 80 - 90 % of perovskite structures adopting room temperature structures that involve octahedral tilts[67], a link in which the octahedral tilts induce ferroelectric distortions could lead to a wealth of new perovskite ferroelectrics.

1.13 Layered Perovskite-like Phases as "Hybrid Improper" Ferroelectrics

The layered perovskite-like phases offer a solution to the problem of antiferroelectric A-site distortions. In these layered phases the inversion symmetry through the B-site is now lost, due to the inequivalent intra-layer and inter-layer A-sites. This can result in a net polarisation caused by octahedral tilting and cooperative A-site displacements. Whilst certain Aurivillius phases were shown to be ferroelectric as early as the 1960s[68, 69] the novel mechanism through which this ferroelectricity is attained was first elucidated by Bousquet in 2008[70].

This new mechanism for ferroelectricity is rationalised as the combination of two non-polar lattice modes that couple to yield a polar or ferroelectric lattice distortion. This is commonly referred to as a "tri-linear coupling" mechanism or "hybrid improper" ferroelectricity. The importance of the octahedral rotations is described in several independent studies on the Aurivillius ($Bi_2O_2[A_{n-1}B_nO_{3n+1}]$)[71, 72], Dion-Jacobson ($A'[A_{n-1}B_nO_{3n+1}]$)[73, 74] and double-perovskite ($A'AB_2O_6$)[67, 75, 76] structures. Examples of the Aurivillius, Ruddlesden-Popper and Dion-Jacobson structures are shown in Figure 1.14.

This class of hybrid improper ferroelectrics are characterised by large temperature-dependent dielectric constants, but differ from traditional ferroelectrics in which the dielectric constant evolves considerably in the vicinity of T_C. They also differ from previous improper ferroelectrics that exhibit temperature dependent but small dielectric constants.

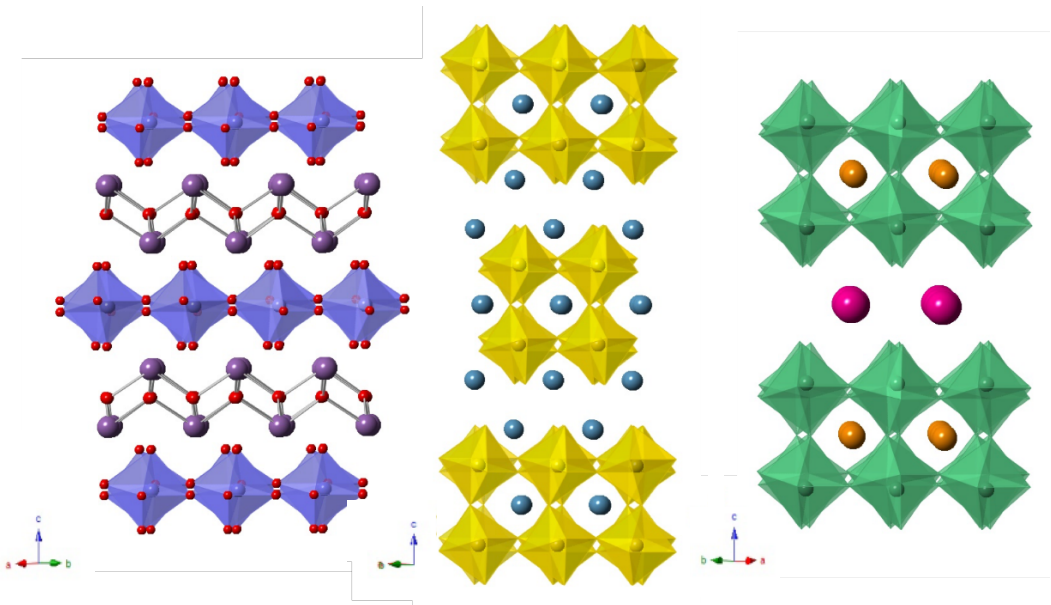

Figure 1.14 The layered perovskite-like phases including, from left to right, the Aurivillius phase Bi_2WO_6, a known ferroelectric[71], the polar Ruddlesden-Popper phase, $Ca_3Ru_2O_7$[77], and ferroelectric Dion-Jacobson phase, $CsNdNb_2O_7$[73].

1.13.1 Trilinear coupling mechanism

In the trilinear coupling mechanism through which hybrid-improper ferroelectricity arises, a free energy term ($\mathcal{F}$) describes the coupling between the polarisation (*P*) and two zone-boundary non-polar order parameters (R_1 and R_2). Mathematically they display a linear dependency (Equation 1.3), hence the origin of the term trilinear coupling.

$$\mathcal{F} \propto \gamma P \mathrm{R}_1 \mathrm{R}_2 \qquad \text{Equation 1.3}$$

where γ is a linear coefficient[78].

The structural driving force behind the transition to the polar or ferroelectric phase can be any of these three terms, *P*, R_1 *or* R_2. Commonly in hybrid improper ferroelectrics, the two non-polar lattice modes combine, and generate the polarisation. However, in practice any two of these modes can combine to generate the third. In cases where the trilinear coupling is very strong, two of the independent structural distortion modes can condense simultaneously to induce the third. This is what is known as an "avalanche" transition and is observed in the Aurivillius phase $SrBi_2Nb_2O_9$[79], to give one example. In reference to Chapter 7 of this thesis, much of the structural characterisation and symmetry mode analysis is devoted to investigating the nature of the trilinear coupling mechanism involved in the paraelectric-ferroelectric phase transition of the layered Dion-Jacobson phase $CsBi_{0.6}La_{0.4}Nb_2O_7$.

In addition to the discovery of new ferroelectric materials, the trilinear coupling mechanism could have important implications in the field of multiferroics and magnetoelectric coupling for new design-led materials. Few multiferroic materials exist due to the difficulty in achieving a coupling of the ferroelectric and magnetic

properties. As octahedral rotations have been proven to couple strongly to magnetic properties[80], ferroelectricity that is controlled or induced by octahedral tilts (such as that of hybrid improper ferroelectrics) could help solve the coupling problem between polarisation and magnetism[33, 81]. This has already been observed for Aurivillius phases with magnetically active cations at the B-site[82, 83].

1.14 Multiferroics and Magnetoelectric Coupling

Multiferroic materials are defined as those that exhibit more than one ferroic order simultaneously[84] and thus have interesting potential for use in novel multifunctional devices. The three main ferroic orders that can contribute to multiferrocity are ferroelectricity, ferromagnetism and ferroelasticity. Magnetoelectric multiferroics which simultaneously exhibit coupled ferroelectricity and ferromagnetism in which the polarisation can be controlled magnetically and *vice versa* are rarely observed, however perovskites offer some of the most promising candidates[62, 84, 85]. Of the few single-phase multiferroics already known, their use in applications is hindered as their magnetoelectric responses are either too weak or only occur at impractically low temperatures[86].

The paucity of multiferroic materials which exhibit magnetoelectric coupling effects is highlighted in work by Spaldin[87] (neé Hill). In general, this is due to the incompatible requirements at the B-site imposed by ferroelectricity and ferromagnetism. As previously discussed, for ferroelectric activity at the B-site, d^0 transition metals are usually necessary to facilitate a SOJT mechanism. However, for magnetic ordering to occur, there must be at least one unpaired electron in the 3d orbitals of the transition metal. A way to circumvent this, is to design materials that can accommodate A-site ferroelectricity (*i.e.* a cation with a

polarisable lone pair) and B-site ferromagnetism, however even these structures are rare (although there is perhaps new potential in the layered phases described above). An example of this, and the most famous and widely studied of the multiferroics is $BiFeO_3$[62, 88, 89].

Despite the difficulty in obtaining suitable multiferroic materials a large research effort is devoted to the field as coupling of magnetic and ferroelectric properties is highly desirable for use in multifunctional devices that are constantly evolving to achieve faster speeds and be more compact[90]. The effects of magnetoelectric coupling can often result in novel effects not associated with ferromagnetism or ferroelectricity alone[91]. One final advantage, is the ability of multiferroics to exploit the advantages of each of the coupled ferroic orders whilst avoiding the drawbacks. An example of this is in data storage applications where information can be written electronically (negating the need for the large magnetic fields associated with writing magnetically) and read magnetically, avoiding the problems encountered when reading ferroelectric random access memory (FeRAM)[84].

1.15 References

1. Mackenzie, A. P.; Julian, S. R.; Diver, A. J.; McMullan, G. J.; Ray, M. P.; Lonzarich, G. G.; Maeno, Y.; Nishizaki, S.; Fujita, T., Quantum oscillations in the layered perovskite superconductor Sr_2RuO_4. *Physical Review Letters* **1996,** *76*, 3786-3789.
2. Stahn, J.; Chakhalian, J.; Niedermayer, C.; Hoppler, J.; Gutberlet, T.; Voigt, J.; Treubel, F.; Habermeier, H. U.; Cristiani, G.; Keimer, B.; Bernhard, C., Magnetic proximity effect in perovskite superconductor/ferromagnet multilayers. *Physical Review B* **2005,** *71*, 140509.
3. Bokov, A. A.; Ye, Z. G., Recent progress in relaxor ferroelectrics with perovskite structure. *Journal of Materials Science* **2006,** *41*, 31-52.
4. Dawber, M.; Scott, J. F., A model for fatigue in ferroelectric perovskite thin films. *Applied Physics Letters* **2000,** *76*, 1060-1062.
5. Haertling, G. H., Ferroelectric ceramics: History and technology. *Journal of the American Ceramic Society* **1999,** *82*, 797-818.
6. Scott, J. F., Room-temperature multiferroic magnetoelectrics. *Npg Asia Materials* **2013,** *5*, 1-11.
7. Abdalla, A. M.; Hossain, S.; Petra, P. M. I.; Savaniu, C. D.; Irvine, J. T. S.; Azad, A. K., Novel layered perovskite $SmBaMn_2O_{5+\delta}$ for SOFCs anode material. *Materials Letters* **2017,** *204*, 129-132.
8. Snaith, H. J., Perovskites: The Emergence of a New Era for Low-Cost, High-Efficiency Solar Cells. *Journal of Physical Chemistry Letters* **2013,** *4*, 3623-3630.
9. Shin, H.; Hong, S.; Moon, J.; Jeon, J. U., Read/write mechanisms and data storage system using atomic force microscopy and MEMS technology. *Ultramicroscopy* **2002,** *91*, 103-110.
10. Sun, J. Z.; Gupta, A.; Xiao, G.; Trouilloud, P. L.; Lecoeur, P. P., Magnetic devices and sensors based on perovskite manganese oxide materials. Google Patents: 1998.
11. Fergus, J. W., Perovskite oxides for semiconductor-based gas sensors. *Sensors and Actuators B: Chemical* **2007,** *123*, 1169-1179.
12. Raveau, B., The perovskite history: More than 60 years of research from the discovery of ferroelectricity to colossal magnetoresistance via high T_C superconductivity. *Progress in Solid State Chemistry* **2007,** *35*, 171-173.
13. Megaw, H. D., Crystal Structure of Barium Titanium Oxide at Different Temperatures. *Experientia* **1946,** *2*, 183-184.
14. Wainer, E.; Soloman, S. Titanium Alloy Manufacturing Co., 1942.
15. Zahn, M., The Contributions of Arthur von Hippel to Electrical Insulation Research. *IEEE Transactions on Electrical Insulation* **1988,** *23*, 790 - 800.
16. Von Hippel, A. R., *Molecular Science and Molecular Engineering*. Published jointly by the Technology Press of M.I.T. and J. Wiley: 1959.

17. Ginsburg, V. L., On the dielectric properties of ferroelectric (seignetteelectric) crystals and barium titanate. *Journal of Experimental Theoretical Physics* **1946,** *15*.
18. Megaw, H. D., Origin of Ferroelectricity in Barium Titanate and Other Perovskite-Type Crystals. *Acta Crystallographica* **1952,** *5*, 739-749.
19. Blattner, H.; Matthias, B.; Merz, W., Single crystals of Barium-Titanium Compounds. *Helvetica Physica Acta* **1947,** *20*.
20. Izyumskaya, N.; Alivov, Y.; Morkoc, H., Oxides, Oxides, and More Oxides: High- Oxides, Ferroelectrics, Ferromagnetics, and Multiferroics. *Critical Reviews in Solid State and Materials Sciences* **2009,** *34*, 89-179.
21. Bednorz, J. G.; Muller, K. A., Possible High-T_C Superconductivity in the Ba-La-Cu-O System. *Zeitschrift Fur Physik B: Condensed Matter* **1986,** *64*, 189-193.
22. Saito, Y.; Takao, H.; Tani, T.; Nonoyama, T.; Takatori, K.; Homma, T.; Nagaya, T.; Nakamura, M., Lead-free piezoceramics. *Nature* **2004,** *432*, 84-87.
23. Shrout, T. R.; Zhang, S. J., Lead-free piezoelectric ceramics: Alternatives for PZT? *Journal of Electroceramics* **2007,** *19*, 113-126.
24. Panda, P. K.; Sahoo, B., PZT to Lead Free Piezo Ceramics: A Review. *Ferroelectrics* **2015,** *474*, 128-143.
25. Cross, E., Materials science - Lead-free at last. *Nature* **2004,** *432*, 24-25.
26. Noheda, B.; Gonzalo, J. A.; Cross, L. E.; Guo, R.; Park, S. E.; Cox, D. E.; Shirane, G., Tetragonal-to-monoclinic phase transition in a ferroelectric perovskite: The structure of $PbZr_{0.52}Ti_{0.48}O_3$. *Physical Review B* **2000,** *61*, 8687-8695.
27. 2002/95/EC, E.-D., Restriction of the Use of Certain Hazardous Substances in Electrical and Electronic Equipment (RoHS). *Official Journal of the European Union* **2003,** *46 [L37]*, 19-23.
28. 2002/95/EC, E.-D., Waste Electrical and Electronic Equipment (WEEE). *Official Journal of the European Union* **2003,** *46 [L37]*, 24-39.
29. Rodel, J.; Jo, W.; Seifert, K. T. P.; Anton, E. M.; Granzow, T.; Damjanovic, D., Perspective on the Development of Lead-free Piezoceramics. *Journal of the American Ceramic Society* **2009,** *92*, 1153-1177.
30. Yuzyuk, Y. I.; Gagarina, E.; Simon, P.; Reznitchenko, L. A.; Hennet, L.; Thiaudiere, D., Synchrotron X-ray diffraction and Raman scattering investigations of $(Li_xNa_{1-x})NbO_3$ solid solutions: Evidence of the rhombohedral phase. *Physical Review B* **2004,** *69*, 144105.
31. Zhang, S. J.; Xia, R.; Shrout, T. R., Modified $(K_{0.5}Na_{0.5})NbO_3$ based lead-free piezoelectrics with broad temperature usage range. *Applied Physics Letters* **2007,** *91*.
32. Wang, K.; Li, J. F.; Liu, N., Piezoelectric properties of low-temperature sintered Li-modified (Na, K)NbO_3 lead-free ceramics. *Applied Physics Letters* **2008,** *93*.
33. Mulder, A. T.; Benedek, N. A.; Rondinelli, J. M.; Fennie, C. J., Turning ABO_3 Antiferroelectrics into Ferroelectrics: Design Rules for Practical Rotation-Driven

Ferroelectricity in Double Perovskites and $A_3B_2O_7$ Ruddlesden-Popper Compounds. *Advanced Functional Materials* **2013,** *23*, 4810-4820.
34. Megaw, H. D., The seven phases of sodium niobate. *Ferroelectrics* **1974,** *7*, 87-89.
35. Oka, K.; Azuma, M.; Chen, W.; Yusa, H.; Belik, A. A.; Takayama-Muromachi, E.; Mizumaki, M.; Ishimatsu, N.; Hiraoka, N.; Tsujimoto, M.; Tucker, M. G.; Attfield, J. P.; Shimakawa, Y., Pressure-Induced Spin-State Transition in $BiCoO_3$. *Journal of the American Chemical Society* **2010,** *132*, 9438-9443.
36. Goldschmidt, V. M., Die Gesetze der Krystallochemie. *Naturwissenschaften* **1926,** *14*, 477-485.
37. Randall, C. A.; Bhalla, A. S.; Shrout, T. R.; Cross, L. E., Classification and Consequences of Complex Lead Perovskite Ferroelectrics with Regard to B-site Cation Order. *Journal of Materials Research* **1990,** *5*, 829-834.
38. Glazer, A. M., The classification of tilted octahedra in perovskites. *Acta Crystallographica Section B* **1972,** *B 28*, 3384-3392.
39. Glazer, A. M., Simple ways of determining perovskite structures. *Acta Crystallographica Section A* **1975,** *31*, 756-762.
40. Megaw, H. D., *Crystal structures: a working approach*. Saunders: 1973.
41. Reaney, I. M.; Colla, E. L.; Setter, N., Dielectric and Structural Characteristics of Ba-Based and Sr-Based Complex Perovskites as a Function of Tolerance Factor. *Japanese Journal of Applied Physics* **1994,** *33*, 3984-3990.
42. Woodward, P. M., Octahedral tilting in perovskites .II. Structure stabilizing forces. *Acta Crystallographica Section B* **1997,** *53*, 44-66.
43. Hume-Rothery Rules. - *Van Nostrand's Scientific Encyclopedia* **2005**.
44. Howard, C. J.; Stokes, H. T., Group-theoretical analysis of octahedral tilting in perovskites. *Acta Crystallographica Section B* **1998,** *54*, 782-789.
45. Glazer, A., The classification of tilted octahedra in perovskites. *Acta Crystallographica Section B* **1972,** *28*, 3384-3392.
46. Stokes, H. T.; Hatch, D. M.; Wells, J. D., Group-theoretical methods for obtaining distortions in crystals - Applications to vibrational-modes and phase-transitions. *Physical Review B* **1991,** *43*, 11010-11018.
47. Miller, S. C.; Love, W. F., *Tables of Irreducible Representations of Space Groups and Co-representations of Magnetic Space Groups*. Pruett: Boulder: 1967.
48. Stokes, H. T.; Hatch, D. M., *Isotropy Subgroups of the 230 Crystallographic Space Groups*. 1989.
49. Campbell, B. J.; Stokes, H. T.; Tanner, D. E.; Hatch, D. M., ISODISPLACE: a web-based tool for exploring structural distortions. *Journal of Applied Crystallography* **2006,** *39*, 607-614.
50. Ramirez, A. P., Colossal magnetoresistance. *Journal of Physics: Condensed Matter* **1997,** *9*, 8171.
51. Rodriguez-Martinez, L. M.; Attfield, J. P., Cation disorder and size effects in magnetoresistive manganese oxide perovskites. *Physical Review B* **1996,** *54*, R15622-R15625.

52. West, A. R., *Basic solid state chemistry*. John Wiley & Sons: 1999.
53. Kundu, A. K., *Magnetic Perovskites: Synthesis, Structure and Physical Properties*. Springer India: 2016.
54. Corliss, L. M.; Donnay, J. D. H.; Elliott, N.; Hastings, J. M., Symmetry of Magnetic Structures - Magnetic Structure of Chalcopyrite. *Physical Review* **1958,** *112*, 1917-1923.
55. Larson, A. C.; Von Dreele, R. B., Los Alamos Natl. Lab: 1994.
56. Cui, J.; Huang, Q.; Toby, B. H., Magnetic structure refinement with neutron powder diffraction data using GSAS: A tutorial. *Powder Diffraction* **2006,** *21*, 71-79.
57. Bertaut, E., Representation analysis of magnetic structures. *Acta Crystallographica Section A* **1968,** *24*, 217-231.
58. Gupta, K. M.; Gupta, N., Dielectric Materials: Types and Applications. In *Advanced Electrical and Electronics Materials*, John Wiley & Sons, Inc.: 2015; pp 343-378.
59. Ok, K. M.; Chi, E. O.; Halasyamani, P. S., Bulk characterization methods for non-centrosymmetric materials: second-harmonic generation, piezoelectricity, pyroelectricity, and ferroelectricity. *Chemical Society Reviews* **2006,** *35*, 710-717.
60. Jaffe, B.; Cook, W. R.; Jaffe, H. L., *Piezoelectric ceramics*. Academic Press: 1971.
61. Bhalla, A. S.; Guo, R. Y.; Roy, R., The perovskite structure - a review of its role in ceramic science and technology. *Materials Research Innovations* **2000,** *4*, 3-26.
62. Catalan, G.; Scott, J. F., Physics and Applications of Bismuth Ferrite. *Advanced Materials* **2009,** *21*, 2463-2485.
63. Zhong, W.; Vanderbilt, D.; Rabe, K. M., Phase Transitions in $BaTiO_3$ from First Principles. *Physical Review Letters* **1994,** *73*, 1861-1864.
64. Cohen, R. E., Origin of ferroelectricity in perovskite oxides. *Nature* **1992,** *358*, 136-138.
65. Benedek, N. A.; Fennie, C. J., Why Are There So Few Perovskite Ferroelectrics? *Journal of Physical Chemistry C* **2013,** *117*, 13339-13349.
66. Zhou, J. S.; Goodenough, J. B., Universal Octahedral-Site Distortion in Orthorhombic Perovskite Oxides. *Physical Review Letters* **2005,** *94*, 065501.
67. King, G.; Woodward, P. M., Cation ordering in perovskites. *Journal of Materials Chemistry* **2010,** *20*, 5785-5796.
68. Smolenski, G. A.; Isupov, V. A.; Agranovskaya, A.I.; Krainik, N. N., New ferroelectrics of complex composition. *Soviet Physics - Solid State* **1961,** *2*, 196.
69. Subbarao, E. C., Ferroelectricity in $Bi_4Ti_3O_{12}$ and Its Solid Solutions. *Physical Review* **1961,** *122*, 804-808.
70. Bousquet, E.; Dawber, M.; Stucki, N.; Lichtensteiger, C.; Hermet, P.; Gariglio, S.; Triscone, J. M.; Ghosez, P., Improper ferroelectricity in perovskite oxide artificial superlattices. *Nature* **2008,** *452*, 732-736.

71. Withers, R. L.; Thompson, J. G.; Rae, A. D., The Crystal chemistry underlying ferroelectricity in $Bi_4Ti_3O_{12}$, Bi_3TiNbO_9, and Bi_2WO_6. *Journal of Solid State Chemistry* **1991,** *94*, 404-417.
72. Hervoches, C. H.; Snedden, A.; Riggs, R.; Kilcoyne, S. H.; Manuel, P.; Lightfoot, P., Structural behavior of the four-layer aurivillius-phase ferroelectrics $SrBi_4Ti_4O_{15}$ and $Bi_5Ti_3FeO_{15}$. *Journal of Solid State Chemistry* **2002,** *164*, 280-291.
73. Snedden, A.; Knight, K. S.; Lightfoot, P., Structural distortions in the layered perovskites $CsANb_2O_7$ (A = Nd, Bi). *Journal of Solid State Chemistry* **2003,** *173*, 309-313.
74. Goff, R. J.; Keeble, D.; Thomas, P. A.; Ritter, C.; Morrison, F. D.; Lightfoot, P., Leakage and Proton Conductivity in the Predicted Ferroelectric $CsBiNb_2O_7$. *Chemistry of Materials* **2009,** *21*, 1296-1302.
75. Knapp, M. C.; Woodward, P. M., A-site cation ordering in $AA'BB'O_6$ perovskites. *Journal of Solid State Chemistry* **2006,** *179*, 1076-1085.
76. King, G.; Thimmaiah, S.; Dwivedi, A.; Woodward, P. M., Synthesis and characterization of new $AA'BWO_6$ perovskites exhibiting simultaneous ordering of A-site and B-site cations. *Chemistry of Materials* **2007,** *19*, 6451-6458.
77. Yoshida, Y.; Ikeda, S. I.; Matsuhata, H.; Shirakawa, N.; Lee, C. H.; Katano, S., Crystal and magnetic structure of $Ca_3Ru_2O_7$. *Physical Review B* **2005,** *72*, 054412.
78. Benedek, N. A., Origin of Ferroelectricity in a Family of Polar Oxides: The Dion-Jacobson Phases. *Inorganic Chemistry* **2014,** *53*, 3769-3777.
79. Snedden, A.; Hervoches, C. H.; Lightfoot, P., Ferroelectric phase transitions in $SrBi_2Nb_2O_9$ and $Bi_5Ti_3FeO_{15}$: A powder neutron diffraction study. *Physical Review B* **2003,** *67*, 092102.
80. Goto, T.; Kimura, T.; Lawes, G.; Ramirez, A. P.; Tokura, Y., Ferroelectricity and giant magnetocapacitance in perovskite rare-earth manganites. *Physical Review Letters* **2004,** *92*, 257201.
81. Lei, Z. W.; Chen, T.; Li, W. G.; Liu, M.; Ge, W.; Lu, Y. L., Cobalt-Substituted Seven-Layer Aurivillius $Bi_8Fe_4Ti_3O_{24}$ Ceramics: Enhanced Ferromagnetism and Ferroelectricity. *Crystals* **2017,** *7*, 76.
82. Keeney, L.; Maity, T.; Schmidt, M.; Amann, A.; Deepak, N.; Petkov, N.; Roy, S.; Pemble, M. E.; Whatmore, R. W., Magnetic Field-Induced Ferroelectric Switching in Multiferroic Aurivillius Phase Thin Films at Room Temperature. *Journal of the American Ceramic Society* **2013,** *96*, 2339-2357.
83. Keeney, L.; Kulkarni, S.; Deepak, N.; Schmidt, M.; Petkov, N.; Zhang, P. F.; Cavill, S.; Roy, S.; Pemble, M. E.; Whatmore, R. W., Room temperature ferroelectric and magnetic investigations and detailed phase analysis of Aurivillius phase $Bi_5Ti_3Fe_{0.7}Co_{0.3}O_{15}$ thin films. *Journal of Applied Physics* **2012,** *112*.
84. Eerenstein, W.; Mathur, N. D.; Scott, J. F., Multiferroic and magnetoelectric materials. *Nature* **2006,** *442*, 759-765.
85. Kimura, T.; Goto, T.; Shintani, H.; Ishizaka, K.; Arima, T.; Tokura, Y., Magnetic control of ferroelectric polarization. *Nature* **2003,** *426*, 55-58.

86. Nan, C. W.; Bichurin, M. I.; Dong, S. X.; Viehland, D.; Srinivasan, G., Multiferroic magnetoelectric composites: Historical perspective, status, and future directions. *Journal of Applied Physics* **2008,** *103*.
87. Hill, N. A., Why are there so few magnetic ferroelectrics? *Journal of Physical Chemistry B* **2000,** *104*, 6694-6709.
88. Wang, J.; Neaton, J. B.; Zheng, H.; Nagarajan, V.; Ogale, S. B.; Liu, B.; Viehland, D.; Vaithyanathan, V.; Schlom, D. G.; Waghmare, U. V.; Spaldin, N. A.; Rabe, K. M.; Wuttig, M.; Ramesh, R., Epitaxial $BiFeO_3$ multiferroic thin film heterostructures. *Science* **2003,** *299*, 1719-1722.
89. Ramesh, R.; Spaldin, N. A., Multiferroics: progress and prospects in thin films. *Nature Materials* **2007,** *6*, 21-29.
90. Gururangan, K., Applications of Magnetoelectric Materials for Solid-State Devices. *Berkeley Scientific Journal* **2014,** *18*.
91. Spaldin, N. A.; Fiebig, M., The renaissance of magnetoelectric multiferroics. *Science* **2005,** *309*, 391-392.

2 Aims and Objectives

The primary aim of this thesis is to establish the temperature-dependent phase diagrams of various functional perovskites, with a focus on polar or ferroelectric materials. Of the systems investigated the aim is to provide detailed structural characterisation of new and emergent phases with scrutiny of the structural behaviour close to the phase boundary. This is primarily achieved with the use of high resolution neutron powder diffraction techniques and often aided with symmetry mode analysis and relative permittivity measurements.

The first system reported (in Chapters 4 and 5) is the $Li_xNa_{1-x}NbO_3$ solid solution, with four compositions which lie in key regions of the room temperature phase diagram selected for variable temperature neutron diffraction experiments. As the alkali niobates have been highlighted for their potential as lead-free dielectric materials[1], fundamental understanding of their structural behaviour is important in order to rationalise their physical properties. From a crystallographic point of view compounds analogous to $NaNbO_3$ are of great structural interest, as pure $NaNbO_3$ exhibits instabilities to several different lattice distortions, both zone boundary and zone-centre (ferroelectric), and as such has arguably one of the most complex phase diagrams of any of the ABO_3 perovskites[2]. The instability to the T_4 complex octahedral tilt mode (phases P, R and S in $NaNbO_3$[3]) opens up a wealth of possibly unique structures with novel tilt systems that are not typically considered (symmetry descent relationships are normally only considered in terms of M_3^+ and R_4^+ modes[4, 5]).

In addition to dielectric materials, the crystal structure of the magnetic rare earth orthoferrite, $LaFeO_3$ is studied, in depth, in Chapter 6. The rare earth orthoferrites are prototypical examples of G-type antiferromagnets, adopting the *Pnma* crystal

structure across the series. The reported anomalous evolution in the lattice metrics for $LaFeO_3$, specifically the *c>a* crossover[6] as a function of temperature, provided the motivation behind the variable temperature neutron diffraction experiments. The sensitivity of neutron diffraction techniques to oxygen atoms enables a detailed structural analysis of the various lattice strains and distortions exhibited by the structure. By careful examination of individual bond lengths and bond angles, the structural driving force behind this *c>a* crossover is isolated. In addition to the evolution of the lattice metrics, $LaFeO_3$ was chosen for comparison to the related multiferroic compound $Bi_{0.5}La_{0.5}FeO_3$ (BLFO50)[7], which exhibits some peculiar structural behaviour most likely due to magnetoelectric coupling effects. As both BLFO50 and $LaFeO_3$ adopt a G-type antiferromagnetic structure at room temperature, differences due to magnetostriction are minimised allowing $LaFeO_3$ to offer a structural comparison which exhibits typical perovskite behaviour without the complicating factor of the lone pair on Bi^{3+}.

The final system detailed in chapter 7 of this work, focuses on a relatively new class of ferroelectrics that exhibit so-called hybrid improper ferroelectricity. Inspired by the recent work by Reece which details the first experimental evidence of ferroelectric properties in the Dion-Jacobson compound, $CsBiNb_2O_7$[8], the ferroelectric – paraelectric phase transition in the analogous compound $CsBi_{0.6}La_{0.4}Nb_2O_7$ is investigated with the use of PND techniques, permittivity measurements and symmetry mode analysis. The trilinear coupling mechanism that drives the paraelectric – ferroelectric transition is of interest as it can occur numerous ways *via* different couplings of the three symmetry modes with similar or different temperature dependencies. Both direct “avalanche” transitions and discontinuous transitions have been demonstrated in various hybrid improper ferroelectrics, with no clear trends in the selectivity for the type of transition shown, making experimental investigation necessary. Elucidating the subtleties of

the mechanism involved in this paraelectric-ferroelectric transition could potentially have implications in the design of new ferroelectric materials.

2.1 References

1. Wang, X.; Wu, J.; Xiao, D.; Zhu, J.; Cheng, X.; Zheng, T.; Zhang, B.; Lou, X.; Wang, X., Giant Piezoelectricity in Potassium–Sodium Niobate Lead-Free Ceramics. *Journal of the American Chemical Society* **2014,** *136*, 2905-2910.
2. Megaw, H. D., The seven phases of sodium niobate. *Ferroelectrics* **1974,** *7*, 87-89.
3. Peel, M. D.; Thompson, S. P.; Daoud-Aladine, A.; Ashbrook, S. E.; Lightfoot, P., New Twists on the Perovskite Theme: Crystal Structures of the Elusive Phases R and S of $NaNbO_3$. *Inorganic Chemistry* **2012,** *51*, 6876-6889.
4. Glazer, A., The classification of tilted octahedra in perovskites. *Acta Crystallographica Section B* **1972,** *28*, 3384-3392.
5. Howard, C. J.; Stokes, H. T., Group-theoretical analysis of octahedral tilting in perovskites. *Acta Crystallographica Section B* **1998,** *54*, 782-789.
6. Selbach, S. M.; Tolchard, J. R.; Fossdal, A.; Grande, T., Non-linear thermal evolution of the crystal structure and phase transitions of $LaFeO_3$ investigated by high temperature X-ray diffraction. *Journal of Solid State Chemistry* **2012,** *196*, 249-254.
7. Kavanagh, C. M.; Goff, R. J.; Daoud-Aladine, A.; Lightfoot, P.; Morrison, F. D., Magnetically Driven Dielectric and Structural Behavior in $Bi_{0.5}La_{0.5}FeO_3$. *Chemistry of Materials* **2012,** *24*, 4563-4571.
8. Chen, C.; Ning, H. P.; Lepadatu, S.; Cain, M.; Yan, H. X.; Reece, M. J., Ferroelectricity in Dion-Jacobson $ABiNb_2O_7$ (A = Rb, Cs) compounds. *Journal of Materials Chemistry C* **2015,** *3*, 19-22.

3 Experimental Techniques

3.1 Solid State Synthesis Techniques

Solid state, otherwise known as ceramic methods, are employed in the synthesis of all perovskite compounds detailed in this work. Reactions are not conducted at temperatures higher than the melting point of the individual reactants, hence the name solid state. Ceramic methods are essentially a diffusion process that can be described by Fick's first law (Equation 3.1). Fick's law states that a species will move from a region of high concentration to a region of low concentration with a magnitude proportional to the concentration gradient.

$$J = -D\left(\frac{dc}{dx}\right) \qquad \text{Equation 3.1}$$

where J is the diffusion flux, D is the diffusion coefficient, c is the concentration and x is the position.

Small particle sizes that have been thoroughly mixed facilitate the diffusion process by maximising the contact area between the reagents. According to Tamman's rule[1], a temperature of approximately two thirds the melting point of the lowest melting reagent is necessary to ensure the reaction is completed within an acceptable time frame. Therefore, high temperatures in the region of $500 \leq T \leq 2000$ °C are required. This allows for the large energy barrier associated with the diffusion of cations between different sites to be overcome. Reactions can proceed very slowly, but generally, increasing the temperature increases the rate of diffusion and speeds up the reaction.

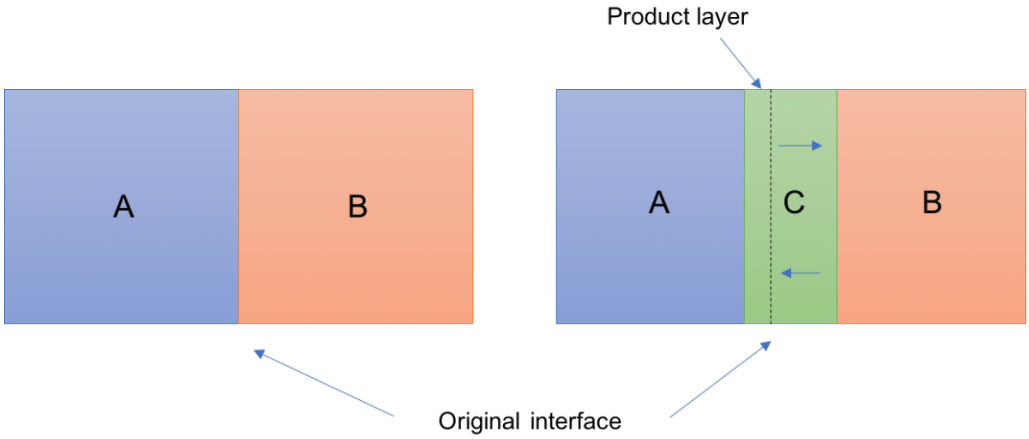

Figure 3.1 Schematic showing the contact area in solid state reactions through which the diffusion process can occur. Reactants A and B are shown, with the product formed upon diffusion identified as C.

Preparing samples for solid state synthesis requires thorough grinding (samples were ground with a pestle and mortar for a period of up to 30 minutes) to ensure a homogenous mixture. To maximise the contact area of the crystallites, the powdered reactants were pressed with a hydraulic pellet press using 1 tonne of pressure. The reaction times for each of the samples detailed in this work did not exceed 24 hours, however, it is often the case that reactions in the solid state can take several days with intermittent grinding. The furnaces used in the heating process are capable of very high temperatures ($T \leq 1400$ °C) and use resistance heating with a SiC or $MoSi_2$ heating element. The samples are held in alumina crucibles during the heating process. This is due to its inert nature, which allows it to withstand the high temperatures required (T up to 1800 °C for the alumina crucibles used in the various syntheses detailed)[2]. A schematic of the diffusion process between reactants, (A and B) to make the product, (C) is shown in Figure 3.1.

3.2 X-ray Diffraction Methods

X-ray diffraction is an invaluable, non-destructive analytical tool for the characterisation of crystalline solids. The diffraction patterns generated from a crystal lattice offer information on the symmetry of the system, such as bond lengths, bond angles and unit cell dimensions. Diffraction experiments can also be used to confirm phase purity before further analysis on the physical properties of a material are carried out.

To generate a coherent diffraction pattern from which quantitative information can be extracted, the material for analysis must be crystalline (*i.e.* exhibit long-range periodic order). As previously discussed in Chapter 1, Section 1.2.1, the smallest repeating arrangement of atoms is referred to as the unit cell. These repeating units demonstrate the translational periodicity of the crystal structure and are depicted by an array of lattice points. The planes of a crystal lattice are separated by a distance, *d*, referred to as the d-spacing. This d-spacing can be determined from the resulting diffraction pattern.

Diffraction occurs when a wave (*i.e.* light, X-ray *etc*.) encounters an obstacle or an aperture. In the case of X-ray diffraction in crystalline materials, this diffraction occurs when the X-ray interacts with the electron cloud of an atom in the periodic structure. The interaction that occurs between the electromagnetic radiation and the electron cloud of the atom alters the path of the X-ray, causing it to diffract. These diffracted waves are recorded by a detector (this can be a fixed detector with the sample rotating, or setup as a rotating angle detector with fixed sample position). The X-rays that arrive at the diffractometer “in-phase” (where their respective path lengths differ by an integer number of wavelengths) lead to constructive interference and give rise to a diffraction pattern. Nobel prize winning work by William Lawrence Bragg and Henry William Bragg established the

relationship between the diffraction angle and the d-spacing known as Bragg's law[3]. X-rays diffracted at certain angles known as Bragg angles satisfy the requirements of this equation, which is demonstrated in Figure 3.2.

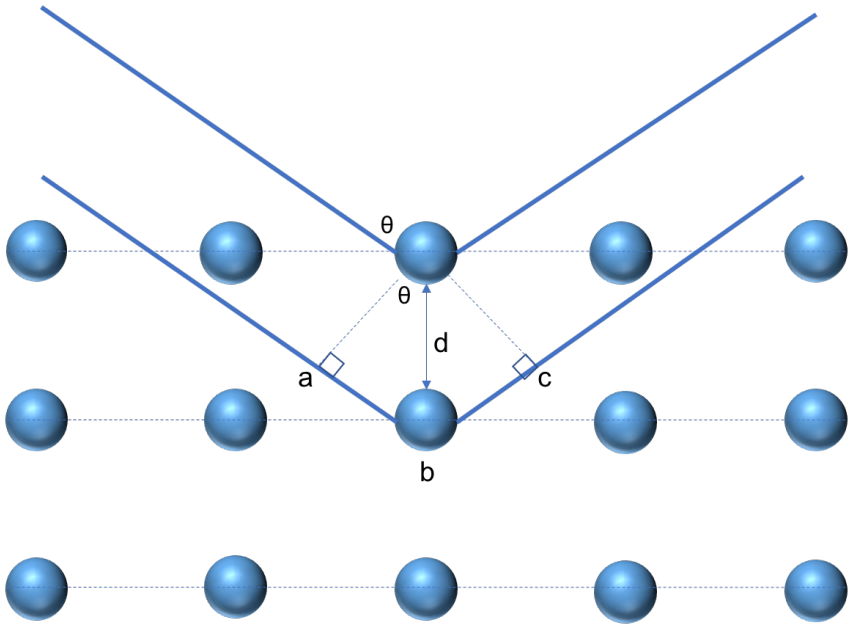

Figure 3.2 Schematic demonstrating how Bragg's law relates the path difference travelled by separate waves and the incident angle of the X-ray radiation to the d-spacing in the crystal lattice.

For two waves diffracting off adjacent planes in the crystal lattice, the path difference (abc) must be an integer number of wavelengths ($n\lambda$) for constructive interference to occur.

$$abc = n\lambda \qquad \text{Equation 3.2}$$

Equation 3.2 describes the path difference, (abc), travelled by two separate waves in Figure 3.2.

Using simple trigonometry, the length of ab and ac, which when combined give the total path difference, can be determined. This is demonstrated in equations 3.3 and 3.4.

$$ab = ac = d\sin\theta \qquad \text{Equation 3.3}$$

$$abc = 2d\sin\theta \qquad \text{Equation 3.4}$$

Equations 3.2 and 3.4 combine to create Bragg's Law (Equation 3.5),

$$n\lambda = 2d\sin\theta \qquad \text{Equation 3.5}$$

3.3 Ewald's Representation and the Reciprocal Lattice

An alternate and useful description of diffraction phenomena is given in Ewald's representation. In this approach, the crystal lattice is described in reciprocal space. Ewald's representation is useful as it describes a lattice plane in real space as a single point in reciprocal space. This point in reciprocal space relates to a spot produced by diffraction of a single crystal.

The real and reciprocal lattices are related *via* a transformation between real and reciprocal space. Following the right hand rule, the cross product of two vectors gives a third vector perpendicular to the plane of the original two. Both the real and reciprocal lattices possess the same origin. The lattice parameters in reciprocal space upon the transformation, a^*, b^*,c^* and V^* are equivalent to

those of real space *a*, *b*, *c* and *V*. The following conditions are satisfied upon transformation from the real to the reciprocal lattice[4]:

$$\boldsymbol{a}^* \cdot \boldsymbol{b} = \boldsymbol{a}^* \cdot \boldsymbol{c} = \boldsymbol{b}^* \cdot \boldsymbol{c} = \boldsymbol{a} \cdot \boldsymbol{b}^* = \boldsymbol{a} \cdot \boldsymbol{c}^* = \boldsymbol{b} \cdot \boldsymbol{c}^* = 0 \qquad \text{Equation 3.6}$$

$$\boldsymbol{a}^* \cdot \boldsymbol{a} = \boldsymbol{b}^* \cdot \boldsymbol{b} = \boldsymbol{c}^* \cdot \boldsymbol{c} = 1 \qquad \text{Equation 3.7}$$

As the scalar product of $\boldsymbol{a}^* \cdot \boldsymbol{b}$ and $\boldsymbol{a}^* \cdot \boldsymbol{c}$ are both equal to zero, $\boldsymbol{a}^*$ must be located perpendicular to both *b* and *c* and the plane defined by them. Equation 3.7 establishes the reciprocal relationship between the unit cell dimensions in real and reciprocal space.

The volume of the unit cell is given as the triple scalar product of the 3 unit cell edges (Equation 3.8).

$$V = \boldsymbol{a} \cdot \boldsymbol{b} \times \boldsymbol{c} \qquad \text{Equation 3.8}$$

Any of the six unit cell parameters can be expressed in terms of the reciprocal lattice and vice versa by consideration of the relationships in Equations 3.7 and 3.8. For example,

$$\boldsymbol{a}^* = \frac{\boldsymbol{b} \times \boldsymbol{c}}{V} \qquad \text{Equation 3.9}$$

and therefore,

$$a^* = \frac{bc \sin \alpha}{V}$$ Equation 3.10

The real space parameter *a* is similarly related. Permutation of *a*,*b*,*c* and α,β,γ can yield the corresponding reciprocal lattice parameters and *vice versa*. Exploiting these relationships enables information on the position of atoms in real space to be obtained from the location of the diffraction spots in reciprocal space.

In Ewald's representation, the incident beam is described by the vector, $\mathbf{k_0}$, and a wavelength that remains constant upon elastic interactions with a single crystal. The diffracted wave has a separate vector, $\mathbf{k_1}$. The shared origin joins the two vectors $\mathbf{k_0}$ and $\mathbf{k_1}$, and from this Ewald's sphere can be visualised. The absolute magnitudes of these vectors are equal to the reciprocal of the wavelength so that,

$$|\boldsymbol{k}_0| = |\boldsymbol{k}_1| = \frac{1}{\lambda}$$ Equation 3.11

As such, the radius of the sphere is equal to the reciprocal of the wavelength $1/\lambda$. The third vector, connecting points on $\mathbf{k_0}$ and $\mathbf{k_1}$ (which are located on the surface of the sphere) is equal to $\mathbf{d^*}_{hkl}$. This is the point in reciprocal space that corresponds to the d-spacing between planes in the crystal lattice in real space, d_{hkl}. The reciprocal relationship between the two quantities is shown in Equation 3.12.

$$\boldsymbol{d}^*_{\boldsymbol{hkl}} = \frac{1}{d_{hkl}}$$ Equation 3.12

The angle between vectors $\mathbf{k_0}$ and $\mathbf{k_1}$ is equal to 2θ. Points in the diffraction pattern only appear when a reciprocal lattice point (other than the origin) lies on the

surface of Ewald's sphere[5]. A schematic representing Ewald's sphere is shown in Figure 3.3.

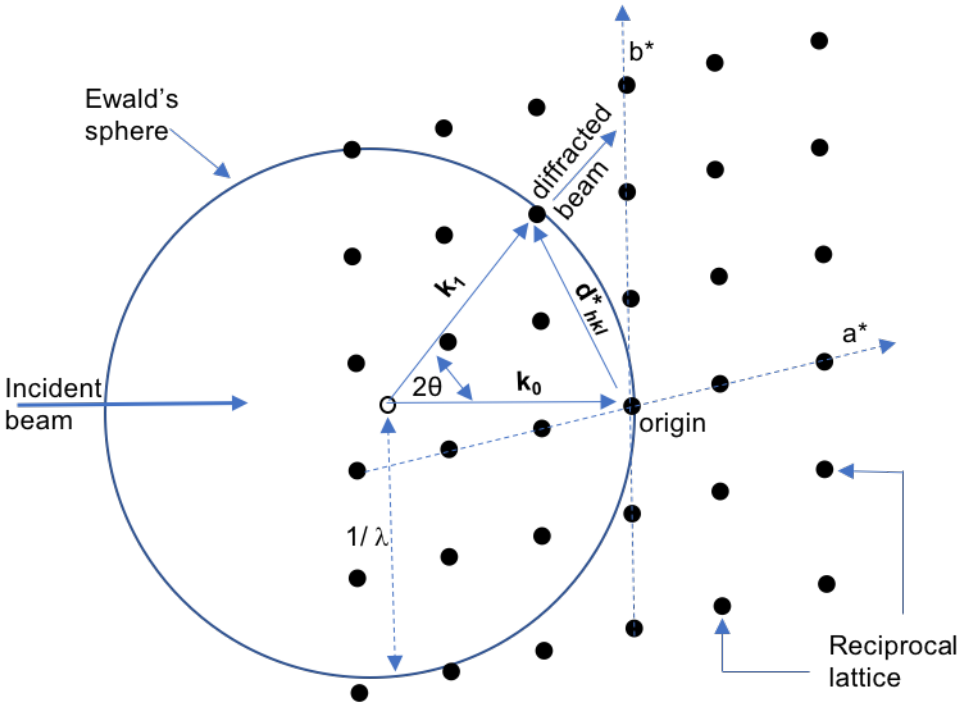

Figure 3.3 Schematic of Ewald's sphere and the two-dimensional reciprocal lattice with lattice parameters *a** and *b**. The radius of the sphere is equal to 1/λ of the incident beam.

3.4 Generation of X-rays

The X-rays used in diffraction experiments are generated by bombardment of a metal target (typically Cu or Mo) with high energy electrons. Electrons are accelerated through a high potential difference (~ 30 kV) and gain energies sufficient to ionise the copper, creating a vacancy or "hole" in the 1s subshell. An electron from a higher energy subshell (2p or 3p), then drops down to occupy the

vacancy. This transition is accompanied by an energy emission with an associated wavelength that lies in the X-ray region of the electromagnetic spectrum. The transition energies have finite values and therefore a characteristic X-ray spectrum results. The 2p -> 1s emission, known as Kα, has a wavelength of 1.5418 Å. The 3p -> 1s transition has a different wavelength of 1.3922 Å and is known as Kβ radiation. The 2p -> 1s transition is much more frequent and makes up the majority of the X-ray spectrum. This transition occurs as a doublet, with the two components $K\alpha_1$ and $K\alpha_2$ possessing wavelengths of 1.5405 Å and 1.5443 Å for Cu source radiation respectively. Filtering of the X-ray beam with a monochromator yields a coherent, monochromatic beam of X-rays, removing unwanted wavelengths associated with inelastic collisions. This is desirable for analytical purposes as a beam comprising different wavelengths will lead to several diffraction profiles, particularly at higher scattering angles. X-ray radiation is utilised in the diffraction of crystalline materials as it has a wavelength roughly equal to the diameter of an atom (~ 1 Å)[6, 7]. A typical X-ray spectrum showing the variation in wavelength and intensity of the three major emissions is depicted in Figure 3.4.

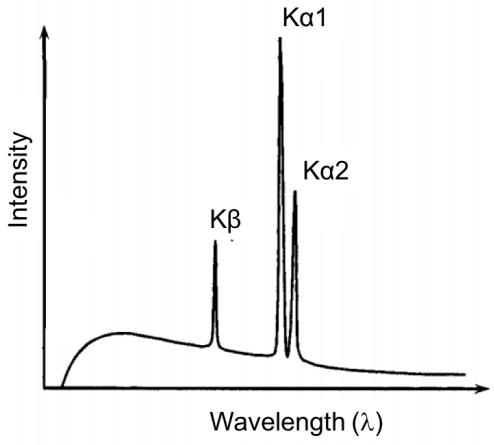

Figure 3.4 Schematic of a characteristic X-ray emission spectrum. Only the three wavelengths with the greatest intensity, $K\alpha_1$, $K\alpha_2$ and Kβ shown for simplicity[6].

3.5 Powder X-ray Diffraction

Powder X-ray diffraction (PXRD) is widely used in the structural characterisation of perovskites, as it does not require large single crystals which can often prove too difficult to synthesise. The sample is prepared for analysis by thorough grinding with a pestle and mortar. In this manner crystallites are orientated in all possible directions with a relatively even distribution of orientations, thus ensuring that a proportion of crystallites in each plane will be orientated at the Bragg angle, θ.

In experiments that utilise mobile detectors, the diffracted beams arrive at the detector in a cone-like formation (Figure 3.5), with the angle between the diffracted and undiffracted beams equal to twice that of the Bragg angle, θ. The detector moves in a circular path, ensuring all cones of diffracted beams from every set of planes within the crystal lattice are recorded. The measurements recorded are the intensity of the beam as a function of angle.

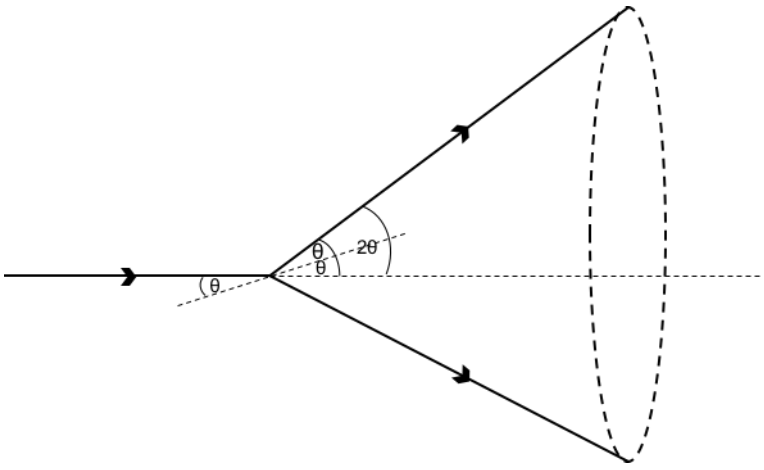

Figure 3.5 Schematic of the cone of diffracted radiation that is formed in powder diffraction methods.

Each unique crystalline material generates a characteristic diffraction pattern, akin to a fingerprint in its uniqueness, through which the symmetry of the material can be determined. The intensity of the peaks is related to the nature and positions of the atoms present in the unit cell, with atoms that possess a larger electron density interacting more strongly with the X-ray beam, resulting in higher intensity peaks. Using Bragg's law, the 2θ values of the diffracted beams can be used to calculate the d-spacing of the adjacent planes. Full indexing of the powder pattern provides the parameters of the unit cell[6, 8].

Samples were measured using either a PANalytical Empyrean powder X-ray diffractometer, with Cu $K\alpha_1$ radiation source or a Rigaku MINIFLEX 600 with a dichromatic Cu $K\alpha_1$ and $K\alpha_2$ radiation source. Patterns were recorded over a 2θ range of $3 < 2\theta < 70$ ° for a period of one hour, and 2θ range $5 < 2\theta < 70$ ° for a period of 16 minutes on the PANalytical and Rigaku instruments respectively. Patterns were recorded in reflection mode and loaded into metal discs containing wells. The sample was packed tightly and flush to the edges of the well.

3.6 Neutron Diffraction Techniques

Powder neutron diffraction (PND) experiments were carried out at the ISIS neutron spallation source at the STFC Harwell campus, Oxford. Generation of the neutron beam involves an injector which produces hydride ions (H^-) with the use of an electric discharge. These hydride ions are separated into bunches by a Radio Frequency Quadrupole accelerator. A linear accelerator is used to accelerate the H^- ions to 37 % the speed of light. The hydride ions then enter the synchrotron (a ring of magnets that bend the beam into a circle which is 163 m in circumference), where an alumina foil strips the H^- ions of their electrons resulting in a beam of protons. These protons are then accelerated to speeds of 84 % the speed of light.

Fast kicker magnets extract the beams which are subsequently used, in pulses, to bombard a tungsten metal target. This releases neutrons *via* a spallation process and generates a high-energy neutron pulse. Hydrogenous moderators are used to slow the neutrons to speeds useful for studying condensed matter. The neutron beam is then directed to various instruments specialised to investigate specific properties of materials.

Inside each of the various instruments samples are suspended in the path of the neutron beam. Neutrons penetrate the material, diffracting off the nuclei of atoms present in the crystal structure and are detected by an array of detectors. At this point the same basic principles of diffraction apply as in the X-ray case, with the angles of the diffracted neutron beams giving information of the arrangement of atoms in the periodic crystal lattice[9].

3.7 Neutron *versus* X-ray – How Do They Differ?

The largest difference between neutron and X-ray diffraction lies in the interaction between the radiation beam and the atoms. Whilst X-rays interact with the electron cloud, as discussed in Section 3.2, neutrons interact directly with the nucleus through the nuclear force (an additional interaction between the magnetic moments of a neutron and any unpaired electrons present in the crystalline structure is discussed below). This carries with it some important advantages such as a greater sensitivity to lighter atoms, for example oxygen, in the presence of heavier ones (*i.e.* perovskite A-site cations), as the scattering factor of an atom is now no longer dependent on its electron density. This is particularly useful in the study of perovskites where the distorted and lower symmetry structures are predominantly characterised by tilting of the BO_6 octahedra. In a similar manner, atoms with very similar atomic numbers can be

easily distinguished as their neutron scattering lengths are likely to be quite different. This independent relationship between electron density and neutron scattering length allows isotopes of the same element to possess different scattering lengths. The tendency for peaks to drop off in intensity as a function of scattering angle as in X-ray diffraction is not observed with neutrons, therefore well-defined and intense peaks are visible at high scattering angles (or low d-spacings). One further advantage of neutron scattering is the ability to determine the magnetic structure for magnetic materials. This is possible as neutrons carry a spin and can therefore interact with magnetic moments (*i.e.* unpaired electrons with spin + or – ½). Magnetic scattering by neutrons is seen to fall off at higher scattering angles as the neutron spin interacts with the electronic spin and not the nucleus.

Interactions of a neutron with a nucleus are relatively weak, thus giving neutrons high penetrating depths and allowing probing of the interior of materials, as opposed to X-rays which only interact with the surface environment. The highly penetrating nature of neutrons allows for measurements to be carried out in complex sample environments such as pressure cells, furnaces and cryostats[6, 8].

3.8 The HRPD Instrument

The high resolution powder diffractometer (HRPD) instrument consists of three detector banks at fixed 2θ angles for time-of-flight (TOF) diffraction measurements. These include a “backscattering” bank (2θ = 168 °), a 90 ° bank and a low angle bank (30 °). In TOF diffraction the wavelength, and consequently the d-spacing, are obtained from the time it takes for the neutron to reach the detector after travelling a flight path of known length. The wavelength of the

neutron can be obtained by exploitation of the de Broglie relationship and the kinetic energy of a particle, detailed in Equation 3.13 below,

$$\lambda = \sqrt{h^2/2mE} \qquad \text{Equation 3.13}$$

where *h* is Planck's constant, *m* is the mass of a neutron at rest and *E* is the kinetic energy.

As ISIS is a spallation neutron source, the neutrons that make up the beam possess a range of different energies, and by extension velocities, that travel the flight path, L, over a range of times, t. This is an example of variable wavelength (energy-dispersive) diffraction as opposed to angle-dispersive.

Incorporation of Equation 3.13 above, with Bragg's law (Equation 3.5) describes the relationship between TOF and d-spacing.

$$\sqrt{\frac{h^2}{2mE}} = 2d_{hkl}\sin\theta = ht/mL \qquad \text{Equation 3.14}$$

The resolution of a diffractometer, $\Delta d/d$, is a measure of the spread of the Bragg reflection for a specific *d*-spacing. For a pulsed neutron source, such as that at ISIS, the diffractometer resolution (Equation 3.15) has three major components: a timing uncertainty ΔT, an angular uncertainty, $\Delta\theta$, and flight path uncertainties, ΔL.

$$R(d) = \frac{\Delta d}{d} = \left[\Delta\theta^2\cot^2\theta + \left(\frac{\Delta T}{T}\right)^2 + \left(\frac{\Delta L}{L}\right)^2\right]^{1/2} \qquad \text{Equation 3.15}$$

The long flight path (L) travelled by neutrons between the pulse source and the HRPD instrument (~ 100 m) clearly minimises $\Delta L/L$ term, but additionally minimises the $\Delta T/T$ term, due to the longer flight time the neutrons travel. Maximum resolution is obtained for the backscattering bank with $\theta = 90°$ as $\cot\theta \sim 0$. The HRPD instrument is designed to achieve very high resolutions, R(d) greater than 10^{-3}.

The detector array includes three detectors each of which offers various advantages. The backscattering bank, (bank 1) has the highest resolution and is based on a ZnS scintillator. Data collection for bank 1 is possible over the d-spacing range $0.6 \leq d \leq 4.6$ Å. The 90 ° detector bank, (bank 2) has a lower resolution but higher signal to noise ratio owing to the higher count rate (allowing better quality data to be collected over a shorter timescale). Bank 2 is also based on a ZnS scintillator and collects data over the d-spacing range $0.9 \leq d \leq 6.6$ Å. Finally, the low-angle detector bank, (bank 3) collects data over a much larger d-spacing range of $2.2 \leq d \leq 16.5$ Å. This wide d-spacing range allows investigation of structures with extremely large periodic order, however this bank has the lowest resolution of the three. The data collected in banks 1 and 2 only are employed in the structural determination detailed in the following chapters as combined they offer high resolution data over a sufficient d-spacing range. The arrangement of the detector banks within the HRPD instrument is shown in Figure 3.6.

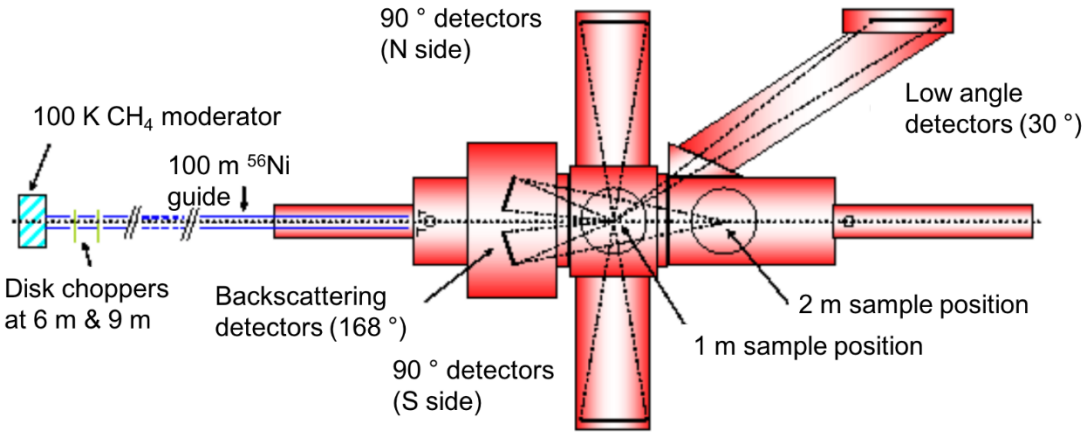

Figure 3.6 Schematic of HRPD instrument showing the configuration of the detector array[10].

3.9 The Rietveld Method

Rietveld refinement is a powerful tool in the characterisation of crystalline solids, allowing for attainment of quantitative information from the characteristic diffraction patterns obtained through powder methods. The method was first proposed by Hugo Rietveld in 1966[11], and first published in 1969[12] with as many as 172 structures refined using the method before 1977[13]. Initially, the method was used to refine structures against patterns obtained *via* fixed wavelength neutron powder diffraction; however, the method soon became accepted for X-ray data, for both fixed wavelength and fixed angle diffraction. The method involves refinement of a crystal structure against an experimentally obtained diffraction pattern.

Traditionally, powder diffraction methods have been considered inferior, due to the loss of information when a 3D pattern is represented in 2D (resulting in the overlap of several Bragg peaks). A diffraction pattern is, in essence, an assortment of individual reflection profiles. Each of which has an individual peak height, breadth, position and integrated area which is proportional to the Bragg intensity, I_K (*K* in this case stands for the Miller indices, *h*, *k*, *l*). I_K is proportional to the square of the absolute structure factor, $|F_K|^2$. For the vast majority of powder patterns, and certainly those that describe complex structures, a number of these profiles overlap with each other due to the random orientations of crystallites, resulting in multiple diffraction spots generated by a single reflection. This makes structural resolution of complex powder patterns impossible without the use of the Rietveld method. As no attempt is made to assign specific Bragg reflections or to resolve overlapping reflections in the Rietveld method, a good starting model is necessary. Therefore, this method is considered more as structural refinement than structural solution (*i.e.* it does not solve the "phase problem").

The intensities associated with each reflection in the diffraction pattern, I_{hkl}, are dependent upon the coordinates and scattering power of the atom, the occupancy level, and the distribution in the thermal motion. These parameters are described by the atomic scattering factor, f_i. The cumulative intensity from all atoms in the unit cell for a given Miller plane is described by the structure factor F_{hkl}.

$$I_{hkl} = |F_{hkl}|^2 \qquad \text{Equation 3.15}$$

the structure factor for X-rays is expressed mathematically as,

$$F_{hkl} = \sum_j f_j \exp\left[2\pi i\left(hx_j + ky_j + lz_j\right)\right]\exp T' \qquad \text{Equation 3.16}$$

where f_j is the atomic scattering factor of atom i, x_j, y_j and z_j are the atomic coordinates, T' is the temperature factor for isotropic refinements and is given by,

$$T' = -\left[8\pi^2 U_{iso} sin^2 \frac{\theta}{\lambda^2} \frac{\sin^2\theta}{\lambda^2}\right] \quad \text{Equation 3.17}$$

where U_{iso} is the refinable temperature factor, θ is the Bragg angle and λ is the wavelength.

An additional magnetic component (F^2_{mag}) is incorporated into the structure factor for PND data on magnetic materials.

$$F^2 = F^2_{nuc} + F^2_{mag} + F^2_{nuc} + \sum_i q_i p_i exp[2\pi i h x_i] \quad \text{Equation 3.18}$$

where p_i is the magnetic cross section and q_i is the magnetic interaction vector.

A broadening of the reflection observed in the diffraction pattern can be caused by instrumental factors such as beam divergence or sample considerations such as crystallite size or strain defects. Gaussian and Lorentzian functions are used to model peak broadening and the overall peak shape. Convolution of these functions is necessary as any sample broadening is affected by instrumental broadening.

The Rietveld method involves least-squares refinements until the best fit between the observed pattern and the simulated pattern (based on the simultaneously refined crystal structure) is obtained. Instrumental factors, background, peak shape, lattice metrics and atomic coordinates are some of the common parameters that undergo least squares refinement in order to achieve a reliable and accurate fit. The high-resolution powder diffraction instruments available

today enable crystal structures of modest size to be determined with high accuracy using the Rietveld method. The optimised term in the refinement process is known as the Residual, S_y. The value of this will reach a minimum when the best fit between the experimental and simulated patterns has been obtained. The definition of the Residual is given in equation 3.19 below.

$$S_y = \sum_i w_i \, (y_i - y_{ci})^2 \qquad \text{Equation 3.19}$$

Calculation of the Residual, S_y; $w_i = 1/y_i$, y_i = observed intensity at the *i* th step, y_{ci} = calculated intensity at the *i* th step.

Insight into the accuracy of the fit is obtained from the R-factors. The two most often quoted are those of the R-profile (R_p) and the R-weighted profile (R_{wp}). The R_{wp} value is arguably the most useful as it gives fits to all peaks equally with no preference towards more intense peaks (its numerator is the Residual minimised). R-factors are only referred to once the value of S_y has reached a minimum. R_p and R_{wp} are defined as follows:

$$R_p = \frac{\sum |y_i(obs) - y_i(calc)|}{\sum y_i(obs)} \qquad \text{Equation 3.20}$$

$$R_{wp} = \left\{ \frac{\sum w_i \, (y_i(obs) - y_i(calc))^2}{\sum w_i \, (y_i(obs))^2} \right\}^{1/2} \qquad \text{Equation 3.21}$$

An additional statistic that is given upon minimisation of the S_y value is the "goodness of fit" or χ^2 value. This is the most commonly used indicator of the quality of the fit and is often used in conjunction with the R-weighted profile factor, R_{wp}. The χ^2 is in fact the ratio of R_{wp}/R_e (the expression for R_e is given in

equation 3.22). A "goodness of fit" equal to 1 indicates a perfect fit of the refined structural model to the observed pattern. A χ^2 value of less than 1 indicates a model with more parameters than can be justified by the quality of the data and is therefore unrealistic. A deceptively low value of χ^2 can also be obtained if the value of R_e is high due to insufficient counting time. Similarly, if R_{wp} is low due to a large background signal that minimises the amount of refinable data points[11]a misleadingly low χ^2 value will result.

$$R_e = \left\{ \frac{(n-p)}{\sum_{i=1}^{n} w_i y_i^2} \right\}^{1/2} \qquad \text{Equation 3.22}$$

where n is the number of points and p is the number of parameters.

Analysis of diffraction data *via* Rietveld refinement methods was carried out using the general structural analysis system (GSAS)[14] with the graphical interface program (EXPGUI)[15].

3.10 ISODISTORT Symmetry Mode Analysis

The ISODISTORT software suite[16] is a valuable tool for any materials chemist interested in the crystal chemistry of distorted structures and phase transitions as it allows examination of the various individual symmetry operations that act upon a distorted crystal structure in a completely decorrelated manner. Using group theory approaches and starting from the highest symmetry (aristotype) space group, a distorted structure can be generated or examined in terms of symmetry modes of the irreducible representations of the parent space group symmetry. The irreducible representations of the parent structure that condense to form the unit cell of the isotropic subgroup are acted upon by various symmetry modes.

These symmetry modes can then be used to describe the distorted structure relative to the parent. Physical order parameters such as atomic displacements, lattice strains and magnetic moments are all comprised of sets of symmetry adapted modes.

The number of symmetry adapted modes is equal to the number of independent degrees of structural freedom for any given system. Each structural order parameter can be defined as a linear combination of symmetry mode amplitudes, therefore the relationship between both is that of an invertible square matrix. The ISODISTORT tool uses group representation theory to automatically calculate the transformation matrix necessary for going from the parent space group symmetry to that of the distorted structure. Octahedral tilting modes such as in-phase and out-of-phase tilts, of particular interest in perovskite research, can be described by individual symmetry adapted modes (M_3^+ and R_4^+ as described in Chapter 1, Section 1.7) which are completely decorrelated from one another. Giving useful quantitative information on their variation as a function of temperature or composition, for example.

The ISODISTORT tool has an incredibly broad functionality. With this tool, it is possible to search for all isotropy subgroups deriving from a parent crystal structure. This is particularly useful when determining the phase evolution in structures such as perovskites. Similarly, it can be used to identify the primary order parameter involved in a specific phase transition or identify those phase transitions that are required by Landau theory to be discontinuous. Simulated diffraction patterns based on distorted structures can be visualised, allowing for the identification of specific superlattice peaks and the contributing symmetry modes. Additionally, it is possible to conduct a search for all possible space group symmetries that can result from specific distortion modes acting upon an aristotype structure, typically $Pm\bar{3}m$. The numerous features offered within this

software suite make it incredibly useful in the identification of new phases and in the investigation of phase transitions. In subsequent chapters the use of symmetry mode arguments aided by the ISODISTORT tool will be used extensively when rationalising the structural behaviour associated with the various phase transitions described.

The mode decomposition method for evaluating the amplitude of active modes in the distorted structure gives two standardised values for each mode, A_s and A_p. A_s is the standard supercell-normalised mode amplitude, the magnitude of which is the square root of the sum of the squares of the mode-induced changes within the primitive supercell volume. This makes it less useful when comparing mode amplitudes across a range of distorted structures of the parent with differing supercell volumes. In contrast, A_p is the parent cell-normalised amplitude, and this is the value that is used in the symmetry mode analysis detailed in the following chapters. A_p is defined as,

$$A_p = A_s \times \sqrt{\frac{V_p}{V_s}} \qquad \text{Equation 3.23}$$

where V_p is the primitive cell volume and V_s is the supercell volume.

The sign of A_s and A_p indicates the direction of the distortion relative to the mode vector but is not particularly meaningful when comparing mode amplitudes. For this, it is only necessary to consider the magnitude.

In addition to individual amplitudes, the total amplitude for each *irrep.* and an overall amplitude for the entire distortion (the root-summed squared amplitude

over all *irreps.*) is also given. This is useful when wanting to track the overall magnitude of the polar or ferroelectric distortion modes for example[17].

3.11 Alternating current – Immitance Spectroscopy

Alternating current immitance spectroscopy (ac-IS) is a useful tool for investigating a wide range of properties and trends in the electrical behaviour of a crystalline system. Most relevant to the work described in the following chapters are the relative permittivity values, which allow changes in the crystal structure to be identified as a function of temperature. This not only provides accurate critical temperatures, T_c's, for the phase transition but can also indicate a phase transition has occurred that is not apparent from observation of the diffraction data alone. In addition to the identification of phase transitions, quantitative information regarding the dielectric properties of ferroelectric and ferroelastic structures can be probed. The ac-IS technique applies a small oscillating potential difference through the sample yielding the time or temperature dependent current response. Data are collected over a wide frequency range of typically 10^{-2} – 10^{6} Hz. In terms of the development of new high performance materials, immitance spectroscopy has proven to be a vital tool as it permits scrutiny of the electric properties of a material in a decorrelated manner, allowing for optimisation of individual features[18].

Electrical properties of crystalline materials are sensitive to microstructure and inhomogeneity. In a single phase material, several unique electrical regions can exist. These relate to different regions within the sample and are referred to as grain boundaries. These distinct regions have differing capacitive (C) and resistive (R) behaviour, associated with the polarisation and charge transfer processes

respectively. The resistive and capacitive components are typically placed in a parallel series, shown in Figure 3.7.

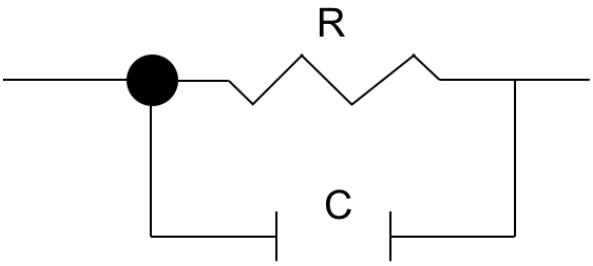

Figure 3.7 An RC element (resistor and capacitor in parallel series) representing an electroactive region.

Ac-immitance, in contrast to direct current (DC) techniques allows for the separation of the resistive and capacitive components. This separation occurs due to the difference in the relaxation times and their interaction with the external ac-field. The relaxation time is expressed as,

$$\tau = RC = \frac{1}{2\pi f_{max}} \qquad \text{Equation 3.24}$$

where τ is the relaxation time, *R* is the resistance and *C* is the capacitance.

3.11.1 Impedance notation

Complex impedance (Z*) is an adaptation of Ohm's law which relates the impedance of a resistor with an applied alternating electric field. This results in the phase angle (ω), shown in Equation 3.25.

$$Z^* = \frac{U_{\max \sin(\omega t + \phi_U)}}{I_{\max \sin(\omega t + \phi_I)}} = Z' - jZ''$$ Equation 3.25

The impedance of a sample is related to three other terms, admittance (Y*), modulus (M*) and permittivity (ε*). These four formalisms form the basis of immitance spectroscopy. The mathematical relationships linking each of these are shown in equation 3.26 – 3.28.

$$Y^* = Y' + jY'' = \frac{1}{Z^*}$$ Equation 3.26

$$M^* = M' + jM'' = j\omega C_0 z^* = \frac{1}{\varepsilon^*}$$ Equation 3.27

$$\varepsilon^* = \varepsilon' - j\varepsilon'' = \frac{1}{j\omega C_0 z^*}$$ Equation 3.28

where *Y'* is the conductance, *Y''* is the susceptance, ε' is the dielectric constant and ε'' is the dielectric loss of the sample[18]. $C_0 = \varepsilon_0 \times$ A/d, where A is the pellet area and d is the pellet thickness, $\omega = 2\pi f$ and $j = \sqrt{-1}$.

The property analysed in the dielectric data presented in this thesis is the relative permittivity, ε. This is measured at various frequencies as a function of temperature. The relative permittivity of a material is expressed as its absolute permittivity relative to the permittivity of a vacuum (Equation 3.29) and is the factor by which the electric field between two point charges is decreased relative to a vacuum. Large changes in the permittivity values indicate a structural phase change has taken place, corresponding to a change in the electronic configuration of the material.

$$\varepsilon_r = \frac{\varepsilon^*}{\varepsilon_0}$$ Equation 3.29

where ε_r is the relative permittivity, ε^* is the complex permittivity and ε_0 is the permittivity of free space.

3.11.2 Sample preparation for permittivity measurements

Sample preparation for dielectric measurements involved ball-milling for a period of one hour at a rate of 600 rev min^{-1} of a phase pure powdered sample to ensure homogeneity. The ball-milled sample was then pressed into thin pellets before annealing at temperatures between 900 – 1100 °C depending on the desired product. Prior to application of electrodes the surfaces of the pellet are sanded down to ensure a smooth surface. Samples were electroded with either Ag paste or sputtered Pd or Au. Electrodes are applied parallel to each other on each surface of the pellet as shown in Figure 3.8. The geometric factor (g.f.), which must be known when calculating the permittivity of the sample over the temperature range studied, can be evaluated from the surface area of the electrode (*a*) and the thickness (*d*) *via* the following relationship;

$$g.f. = \frac{d}{a}$$ Equation 3.30

Once electrodes were applied, the pellet was dried before mounting in the furnace, which is attached to a Wayne-Kerr 6500B impedance analyser. Loss and capacitance data were recorded in the frequency range 100 Hz – 10 MHz over the temperature range studied in each case (typically $40 \leq T \leq 600$ °C). Measurements were recorded over heating and cooling cycles of 2 °Cmin^{-1}.

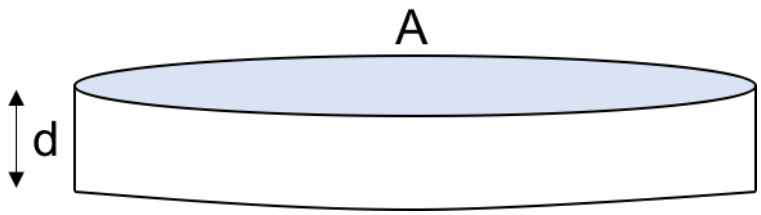

Figure 3.8 Schematic of electroded pellet for permittivity measurements, highlighting the dimensions used to calculate the geometric factor. Both faces of the pellet parallel to each other are coated in the conductive material to form an electrode.

3.12 Second Harmonic Generation (SHG)

The discovery of SHG by Franken *et al*. (1961)[19] is widely regarded as the birth of non-linear optics. It is a hugely important diagnostic tool for determining the optical properties of materials. SHG techniques are often used to change the output frequency of lasers and additionally, have applications in non-linear microscopy. "Non-linear" optical phenomena are deemed non-linear as the response of the system to an applied optical field (such as a high intensity laser beam) exhibits a non-linear dependence on the strength of the optical field, $\tilde{E}$(t). In linear optics, the relationship between the polarisation $\tilde{P}$(t) and field strength, $\tilde{E}$(t) is as follows;

$$\tilde{P}(t) = \varepsilon_0 \chi^{(1)} \tilde{E}(t) \qquad \text{Equation 3.31}$$

where $\chi^{(1)}$ is the linear susceptibility and ε_0 is the permittivity of free space.

Second harmonic generation occurs when the polarisation scales quadratically to the strength of the applied optical field, (described in Equation 3.32). This occurs

when the second-order nonlinear coefficient, χ_{ijk}, is not equal to zero. This is only the case for non-centrosymmetric materials. The relationship is,

$$\tilde{P}(t) = \chi_{ij}E_j + \chi_{ijk}E_jE_k + \chi_{ijkl}E_jE_kE_l \qquad \text{Equation 3.32}$$

where the indices *i,j* and *k* correspond to the three Cartesian axes x,y and z.

As structures that crystallise in non-centrosymmetric space groups are non-linear optics they will generate a SHG signal. For this reason, SHG is widely used to indicate the absence of a centre of inversion in crystalline materials. This is particularly helpful in instances in which the diffraction data does not unambiguously discriminate between polar and centrosymmetric space groups.

An SHG response is generated when a laser beam with frequency, ω, is incident upon and passes through a non-linear optic material, creating a beam with double the frequency, 2ω. This occurs when two photons from the incident beam effectively combine resulting in the output of one phonon with double the frequency. This phenomenon is illustrated in Figure 3.9.

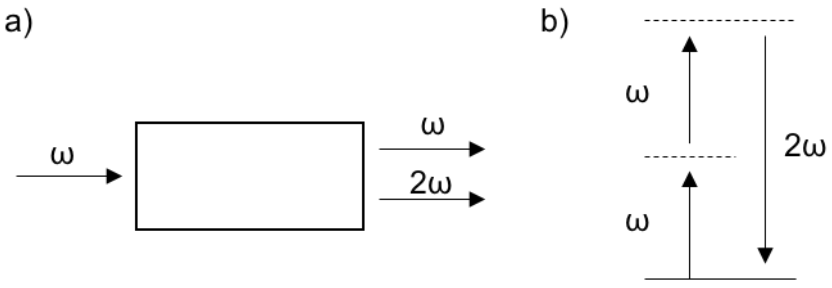

Figure 3.9 (a) Schematic showing how a SHG process occurs when passing through a non-linear optical material, (b) shows the quantum process whereby two photons are destroyed resulting in the emission of one photon with double the frequency[20].

Measurements were carried out using a Q-switched Nd:YAG laser (λ = 1064 nm). The second harmonic signal, if any was present, was measured using a photomultiplier (PMT) and displayed on an oscilloscope as signal *versus* time. The SHG response is then normalised by dividing by the maximum of the fundamental squared[21].

3.13 Bond Valence Sums (BVS)

Bond valence sums exploit the inherent relationship between bond valencies and bond lengths. They are a useful tool in the characterisation of perovskites in which octahedral tilts and cation displacements are driven by bonding-site preferences and thus can be used to rationalise and track the distortive behaviour. In addition to this BVSs are often used to assess the reliability of a predicted structure or to predict bond lengths from a known bond valence.

The valence v_{ij} of a bond between two atoms, *i* and *j*, is defined so that that the sum of these individual valencies sum to give the overall valency of the atom as follows;

$$\sum_j v_{ij} = V_i \qquad \text{Equation 3.33}$$

The variation in the bond valence as a function of bond lengths (d_{ij}) is expressed as,

$$v_{ij} = \exp\left[\frac{R_{ij} - d_{ij}}{b}\right]$$ Equation 3.34

where R_{ij} is the relevant bond-valence parameter and b is a universal constant equal to 0.37 Å[22].

The values of BVSs are dimensionless as the units of R_{ij}, d_{ij} and b are in Angstroms and therefore cancel out.

3.14 References

1. Merkle, R.; Maier, J., On the Tamman Rule. *Journal of inorganic and General Chemistry* **2005,** *631*, 1163-1165.
2. Segal, D., *Chemical Synthesis of Advanced Ceramic Materials*. Cambridge University Press: 1991.
3. Bragg, W. H.; Bragg, W. L., The reflection of X-rays by crystals. *Proceedings of the Royal Society of London Series A, Mathematical, Physical and Engineering sciences* **1913,** *88*, 428-428.
4. Woolfson, M. M., *An Introduction to X-ray Crystallography (second edition)*. Cambridge University Press: 1997.
5. Ewald, P. P., Introduction to dynamical theory of X-ray diffraction. *Acta Crystallographica Section A* **1969,** *A 25*, 103-108.
6. West, A. R., *Basic solid state chemistry*. John Wiley & Sons: 1999.
7. Pecharsky, V.; Zavalij, P., *Fundamentals of Powder Diffraction and Structural Characterization of Materials*. Springer US: 2003.
8. Dinnebier, R. E.; Billinge, S. J. L., *Powder Diffraction: Theory and Practice*. Royal Society of Chemistry: 2008.
9. How ISIS works - in depth. www.isis.stfc.ac.uk/about/how-isis-works---in-depth4371.html (accessed 02/07/17).
10. HRPD User Manual www.isis.stfc.ac.uk/instruments/hrpd/documents/hrpd-manual6735.pdf (accessed 15/07/17).
11. Young, R. A., *The Rietveld Method*. Oxford University Press: 1995.
12. Rietveld, H. M., A profile refinement method for nuclear and magnetic structures. *Journal of Applied Crystallography* **1969,** *2*, 65-71.
13. Cheetham, A. K.; Taylor, J. C., Profile analysis of powder neutron diffraction data: Its scope, limitations, and applications in solid state chemistry. *Journal of Solid State Chemistry* **1977,** *21*, 253-275.
14. Larson, A. C.; Von Dreele, R. B., Los Alamos Natl. Lab: 1994.
15. Toby, B. H., EXPGUI, a graphical user interface for GSAS. *Journal of Applied Crystallography* **2001,** *34*, 210-213.
16. Campbell, B. J.; Stokes, H. T.; Tanner, D. E.; Hatch, D. M., ISODISPLACE: a web-based tool for exploring structural distortions. *Journal of Applied Crystallography* **2006,** *39*, 607-614.
17. ISODISTORT Help. http://stokes.byu.edu/iso/isodistorthelp.php (accessed 28/07/2017).
18. Irvine, J. T. S., Sinclair, D. C., West, A. R., Electroceramics: Characterisation by Impedance Spectroscopy. Advanced Materials, **1990**, *2*, 132-138.
19. Franken, P. A.; Weinreich, G.; Peters, C. W.; Hill, A. E., Generation of Optical Harmonics. *Physical Review Letters* **1961,** *7*, 118-120.
20. Boyd, R. W., *Nonlinear Optics*. Academic Press: 2003.

21. Kurtz, S. K.; Perry, T. T., A Powder Technique for the Evaluation Of Nonlinear Optical Materials. *Journal of Applied Physics* **1968,** *39*, 3798-3813.
22. Brese, N. E.; O'Keeffe, M., Bond-valence parameters for solids. *Acta Crystallographica Section B* **1991,** *47*, 192-197.

4 Novel Tilt Systems Exhibited in Key Members of the $Li_xNa_{1-x}NbO_3$ System

4.1 Introduction

As discussed in the introduction to this thesis, one of the largest tasks faced by materials chemists today is the pursuit of lead-free high performance piezoelectric materials to replace the industry standard PZT ($PbZr_xTi_{1-x}O_3$)[1, 2]. PZT is both piezoelectric and ferroelectric, demonstrating large intrinsic polarisations and high Curie temperatures, (T_C typically ~ 200 °C[3]). Due to the desirable properties of PZT, it is utilised in a vast number of devices such as ultrasound transducers[4], infrared detectors[5] and memory storage devices[6]. Thus far the search for a suitable replacement has proven challenging. Some of the most promising candidates to have emerged are the family of alkali niobates, with much research carried out on the potassium doped sodium niobate solid solution, $K_xNa_{1-x}NbO_3$[7-9], which displays heightened dielectric responses at the morphotrophic phase boundary (MPB) in compositions of ~ x = 0.5.

The parent compound $NaNbO_3$, has arguably one of the most complex phase diagrams of any of the simple ABO_3 perovskites. Work carried out by Megaw[10] in 1974 characterised a total of seven distinct phases adopted by $NaNbO_3$ in the temperature region -100 ≤ T ≤ 640 °C. Although antiferroelectric at room temperature (*Pbcm* space group symmetry, phase P), $NaNbO_3$ adopts a ferroelectric structure (phase N, *R*3*c* symmetry) at temperatures below -100 °C[10]. Phase Q ($P2_1ma$), a ferroelectric polymorph, can be induced at room temperature *via* chemical doping with as little as 2 % Li or K[11, 12]. The $Li_xNa_{1-x}NbO_3$ (referred hereafter as LNN-*X*) solid solution is interesting as the end member $LiNbO_3$ adopts

a ferroelectric structure with rhombohedral *R*3*c* symmetry at room temperature[13], isostructural with phase N but different to the ferroelectric structure at low doping levels, phase Q. Previous work on the room temperature phase diagram for the LNN-*X* solid solution found a region of phase co-existence between these two distinct ferroelectric structures for *x* values of $0.04 < x < 0.20$[11]. The LNN-12 composition exhibits heightened dielectric properties at room temperature likened to the effect of the MPB in PZT and other systems and derivatives[9, 14, 15]. This is due to the presence of two energy equivalent states with differently orientated ferroelectric domains, thus increasing the dielectric response on poling due to their collective reorientation[16].

Whilst the room temperature LNN-*X* phase diagram has previously been characterised in full, little to no attention has been afforded to the behaviour of these materials as a function of temperature. This is perhaps surprising, given the wealth of structure types exhibited by $NaNbO_3$ and the sensitivity it shows to both doping and temperature effects. Therefore, in this work the thermal evolution of several of the lithium doped structures at varying compositions within key regions of the LNN-*X* phase diagram is investigated with the use of high resolution powder neutron diffraction (PND) techniques. The room temperature phase diagram can be split into five key regions and is included in Figure 4.1 below. The ferroelectric phase, Q, is stable for values of $0.01 < x < 0.05$ and exists as a single phase within this composition range. The following region at values of $0.05 < x < 0.2$ as mentioned above, introduces a second co-existent ferroelectric phase (Na-*R*3*c*). This phase is isostructural with the low temperature ferroelectric phase of $NaNbO_3$ (at $T < -100$ °C) Work by Peel *et al*.[11] demonstrated the dependency of the relative phase fractions of these two phases as a function of composition with increasing Na-R3*c* phase occurring as a result of increased Li concentration. This work was of further importance as it removed the ambiguity that had previously existed over which phase, N or Q, preferentially forms as the major phase in this composition

region. Confusingly, publications by Chaker[17] and Yuzyuk[9] had formerly reported contradictory results on this matter. In the publication by Chaker the orthorhombic phase Q is formed exclusively up to compositions of x = 0.15, whereas Yuzyuk reports that both the orthorhombic (Q) and rhombohedral (N) phases form in the region 0.04 < x <0.15, excluding a narrow region at x = 0.12 where the rhombohedral phase, bizarrely, formed exclusively. Peel *et al*. carried out an extensive systematic survey of these compounds by varying synthesis conditions such as annealing temperature and cooling rates in order relieve any uncertainty. From this they concluded that the rhombohedral phase was favoured under conditions of higher annealing temperatures (1100 °C) and fast cooling (quenching). Conversely, the orthorhombic phase was favoured under synthesis conditions using lower annealing temperatures (950 °C) and slow-cooling. It was also serendipitously discovered that phase Q converts to phase N over time, if simply left in an air-tight container[11].

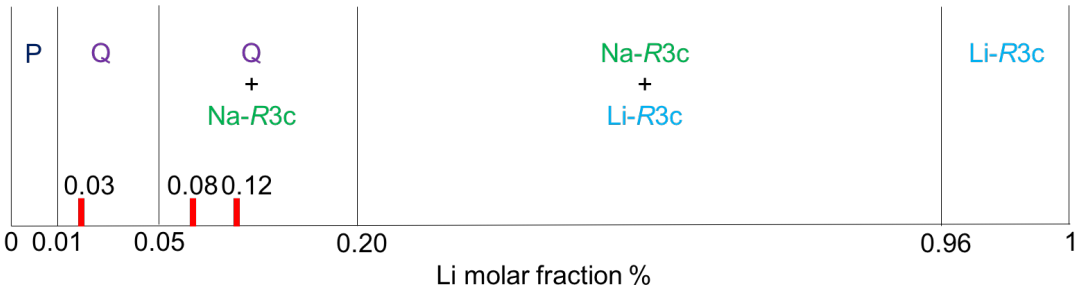

Figure 4.1 Room temperature phase diagram established by the work of Peel *et al*[11]. Highlighted in red are the three compositions of LNN-*X* discussed in this chapter. Diagram not drawn to scale.

The next phase region in the LNN-*X* solid solution consists of a phase co-existence of sodium-rich (Na-*R*3*c*) and lithium-rich rhombohedral phases (Li-*R*3*c*). For the purposes of this chapter, as only compositions of x which crystallise in the Na-*R*3*c*

space group are investigated, it shall generally hereafter be referred to as phase N. Compositions with values of *x* above 0.96 yield the Li-R3*c* structure exclusively.

Four compositions lying in key regions of the room temperature phase diagram were chosen for closer inspection, $x = 0.03$ (LNN-3), $x = 0.08$ (LNN-8), $x = 0.12$ (LNN-12) and $x = 0.20$ (LNN-20). This chapter details the LNN-3, LNN-8 and LNN-12 systems. LNN-20 is discussed in detail in Chapter 5.

4.1.1 Synthesis

Pure samples (~ 5g) of $Li_{0.03}Na_{0.97}NbO_3$, $Li_{0.08}Na_{0.92}NbO_3$ and $Li_{0.12}Na_{0.88}NbO_3$ were synthesised using traditional ceramic methods. Stoichiometric amounts of Li_2CO_3 (99.9 % Sigma-Aldrich), Na_2CO_3 (99.9 % Sigma-Aldrich) and Nb_2O_5 (99.9% Alfa Aesar) were ground thoroughly using a pestle and mortar for a period of up to 30 minutes. The ground reagents were then pressed into pellets of approximately 10 mm thickness and 20 mm diameter under 5 tonnes of pressure. Pellets were then annealed at 1100 °C for LNN-12 and 950 °C for both LNN-3 and LNN-8 samples for a period of 24 hours, with a heating and cooling rate of 10 °C min^{-1}. Purity of samples was confirmed with use of powder X-ray diffraction (PXRD) analysis using a PANalytical Empyrean diffractometer (Cu $K\alpha_1$ radiation source).

4.1.2 Powder neutron diffraction (PND)

Variable temperature PND experiments within the temperature regime $20 \leq T \leq 900$ °C were carried out using the High Resolution Powder Diffractometer (HRPD) instrument at the ISIS facility, Harwell laboratory. Detector banks 1 (168.3 °) and 2 (89.6 °) were used for data analysis on these samples. This covered a d-spacing

range of 0.7 < *d* < 2.6 Å and 0.9 < *d* < 4.0 Å respectively. The samples were held in an 8 mm cyclindrical vanadium can. Data collection was performed over a period of ~ 1 hour per data set with a diffraction pattern measured at 20 °C, followed by collection in 50 ° intervals in the temperature range 50 < *T* < 900 °C. Measurements were carried out with the assistance of Dr. Aziz Daoud-Aladine.

Analysis of the PND data was completed *via* Rietveld refinement techniques utilising the GSAS software package[18] and the EXPGUI interface[19]. A consistent refinement strategy was employed for each data set, unless otherwise stated. This involved 18 background terms, 3 diffractometer constants, 6 profile coefficients, with additional refinement of lattice parameters, atomic coordinates and atomic displacement parameters (ADPs). Na and Li sites were constrained to be equal in the refinement of atomic coordinates and ADPs. For each composition, site occupancies of Na and Li sites were refined at RT to ensure the desired stoichiometry was attained. Upon confirmation of this, Na and Li site occupancies were fixed, according to composition, for all subsequent structural refinements within the temperature regime recorded. Decomposition of the symmetry modes acting upon the derivative structures was carried out with use of the ISODISTORT suite[20].

4.1.3 Sample preparation for dielectric measurements

Dielectric measurements were carried out on a phase pure sample of LNN-12. The phase pure samples (~ 7g each) were suspended in ethanol and ball-milled for one hour at a rate of 600 rev min^{-1}. Ethanol was evaporated off and the remaining white powder was pressed into thin pellets and sintered at 1000 °C for 12 hours. The resulting hard, thin pellets were coated in Au electrodes before permittivity measurements were performed using a Wayne-Kerr 6500B impedance analyser

with the sample mounted in a tube furnace. Loss and capacitance data were recorded in the frequency range 100 Hz – 10 MHz on both heating and cooling cycles at a rate of 2 K min^{-1} over the temperature range $50 \leq T \leq 550$ °C. Dielectric measurements were carried out with the assistance of Dr. Finlay Morrison and Mr. Jason McNulty.

4.2 Results

4.2.1 $Li_{0.12}Na_{0.88}NbO_3$ (LNN-12)

4.2.1.1 PND analysis

4.2.1.1.1 $50 \leq T \leq 300$ °C

The PND study on LNN-12 commences at 50 °C. Inspection of the raw data indicates the rhombohedral phase (Na-*R*3*c*) is present as the majority phase at this temperature. This is as expected as the synthesis strategy employed for the sample of LNN-12 was strategically chosen to yield a majority phase with rhombohedral symmetry at room temperature. This Na-*R*3*c* phase is isostructural with the low temperature ferroelectric phase (phase N) of pure $NaNbO_3$, but can also be considered as a variant of the stable phase of $LiNbO_3$. Observations of the raw PND data at 50 °C indicate the presence of additional peaks which cannot be indexed in the Na-*R*3*c* unit cell. These are found to be due to the minority orthorhombic phase, Q. As previously mentioned in the introduction to this chapter, a phase co-existence of orthorhombic (Q) and rhombohedral (N) phases occurs for values of *x* where $0.05 < x < 0.20$. A two-phase refinement of the diffraction data recorded at 50 °C (Figure 4.2), finds the orthorhombic phase present at a level of 9 % with respect to the bulk. Crystallographic information

regarding the majority rhombohedral phase, N, at 50 °C is included in Table 4.1. The orthorhombic phase, Q, increases at the expense of the rhombohedral phase with increasing temperature (phase fraction of Q:N is 47:53 % at 100 °C) until only phase Q is present at a temperature of 150 °C. The phase transition is first order, as indicated by the region of phase co-existence, with a Glazer tilt system change of $a^-a^-a^-$ to $a^+b^-b^-$. Both the $a^-a^-a^-$ and $a^+b^-b^-$ are common tilt systems found in various perovskite systems, however in both phase N and Q the tilt systems are accompanied by an additional polar distortion. In the rhombohedral phase, this manifests as a polarisation along *c* in the form of co-operative niobium shifts. The orthorhombic phase Q ($P2_1ma$) involves a similar cation shift but directed along the *a*-axis.

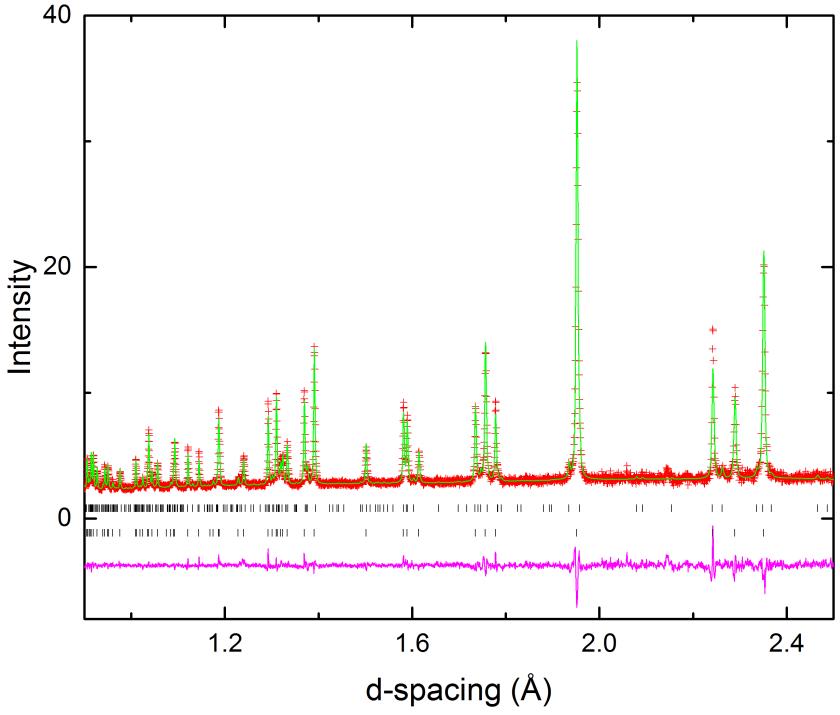

Figure 4.2 Rietveld refinement of PND data (bank 1) for LNN-12 at 50 °C with a phase co-existence model of N and Q phases; $\chi^2 = 2.11$, $R_{wp} = 0.0383$. The top set of Bragg peaks are attributed to phase Q, with the bottom set of Bragg peaks indicating phase N.

Table 4.1 Crystallographic data for LNN-12 at 50 °C modelled in the *R*3*c* (N) space group; a = 5.47746(10) Å, c = 13.7331(3) Å.

Atom	Wyckoff position	x	y	z	100 * U_{iso} (Å^2)
Na*	6a	0	0	0.2533(3)	0.81(7)
Nb	6a	0	0	0	-0.24(3)
O	18b	0.10298(17)	0.3387(3)	0.06776(11)	0.63(3)

*position Na has fixed occupancy $Na_{0.88}Li_{0.12}$.

The N -> Q transition is associated with a change in sense of the original $a^-a^-a^-$ tilt system upon the introduction of an in-phase tilt about one axis. Such phase transitions are considered unusual in perovskite chemistry. However, they are observed relatively often in the $NaNbO_3$ series, with the P -> Q transition in $NaNbO_3$ and additional phase transitions in LNN-20 (see Chapter 5) all involving direct reversals of tilt sense. As the $P2_1ma$ phase (Q) involves condensation of the M_3^+ in-phase tilt mode, this generates superlattice peaks at specific d-spacings in the diffraction pattern (see Chapter 1 Section 1.6 & 1.7). The location of these peaks corresponds to the point in reciprocal space in the cubic parent Brillouin zone in which the symmetry-adapted mode condenses. Condensation of the M_3^+ tilt mode at (***k*** = ½, ½, 0), results in characteristic peaks at d-spacings of ~ 2.1 and 2.5 Å. The out-of-phase tilt that acts about the *b*-axis, corresponds to condensation of the R_4^+ tilt mode at (***k*** = ½, ½, ½), generating a peak at a d-spacing of ~ 2.3 Å. The in-phase and out-of-phase tilts act around the (100) and (010) directions respectively, with all peaks possessing Miller indices consisting of odd-odd-odd integers arising from the out-of-phase tilt, and peaks with Miller indices of odd-odd-even integers attributable to the in-phase tilt. (Chapter 1, Section 1.6)

The polar nature of the phase at 150 °C is assumed based on previous knowledge of the LNN-*X* solid solution, however to confirm the validity of this assumption a comparative refinement was made in the centrosymmetric setting of the $a^+b^-b^-$ tilt system, *Pnma*. This results in a considerably poorer fit to the data ($P2_1ma$ χ^2 = 2.18 for 56 variables; *Pnma* χ^2 = 4.50 for 43 variables), confirming that the polar model is indeed the correct one. The fit to $P2_1ma$ at 150 °C can be seen in Figure 4.3.

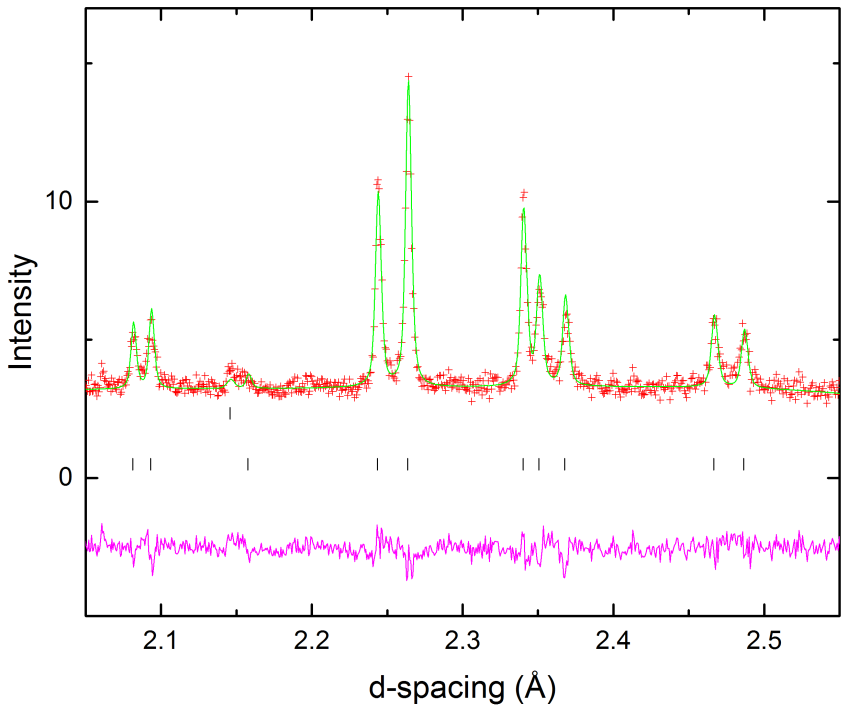

Figure 4.3 Portion of Rietveld refinement of phase Q in LNN-12 at 150 °C showing peaks attributable to both the in-phase M_3^+ and out-of-phase R_4^+ tilt modes. The peak at ~ 2.19 Å originates from the vanadium canister in which the sample was loaded. χ^2 = 2.18, R_{wp} = 0.0391.

Phase Q is fitted as the sole phase throughout the temperature regime 150 ≤ *T* ≤ 250 °C. Structural information obtained upon Rietveld refinement in phase Q at

200 °C is included in Table 4.2. The fit at 300 °C proves to be statistically poorer, however, (χ^2 = 2.14 at 300 °C compared with χ^2 = 1.92 at 250 °C) with some low intensity peaks that cannot be accounted for in the $P2_1ma$ model. These peaks are seen to grow in rapidly between 300 °C and 350 °C before the emergent phase becomes fully established as the sole phase at 400 °C. Figure 4.4 shows the fits to the data at 250 °C and 300 °C using a model with $P2_1ma$ symmetry, highlighting the 1st order nature of the phase transition. Refinements using a phase co-existence model were attempted at both 300 °C and 350 °C. However, the phase fraction of the emergent phase was too small to allow for accurate refinement at 300 °C, whilst, conversely, phase Q was present in too small a quantity to allow for a good two phase model refinement of the data at 350 °C. Thus this emergent phase is treated as the sole phase from a temperature above and including 350 °C.

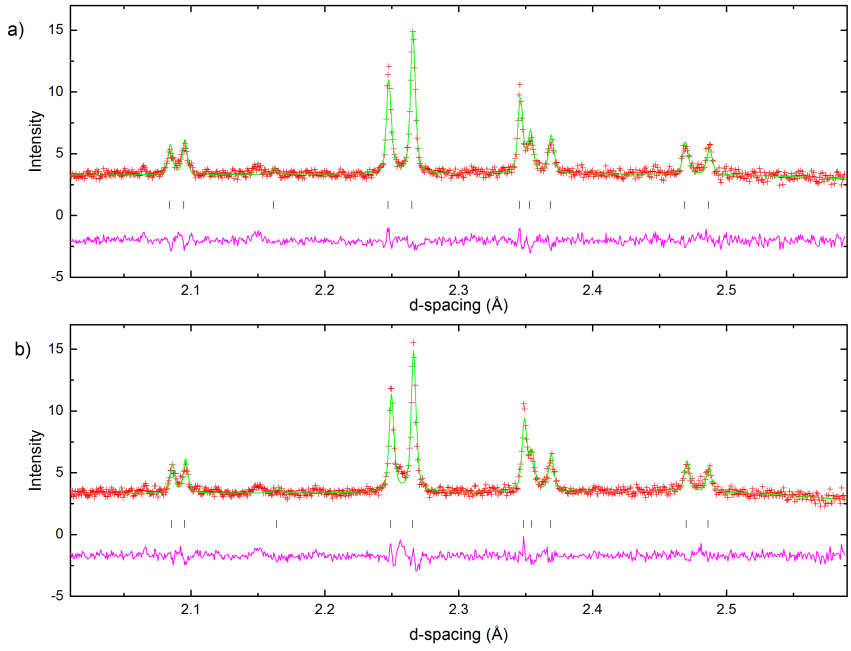

Figure 4.4 Rietveld refinements of phase Q at a) 250 °C (χ^2 = 1.92, R_{wp} = 0.0366) and b) 300°C (χ^2 = 2.22, R_{wp} = 0.0392), (bank 1 data). Changes in the diffraction pattern (*i.e.* at ~ 2.25 Å and 2.35 Å) are indicative of a 1st order phase transition from Q -> S'.

Table 4.2 Crystallographic data for LNN-12 at 200 °C modelled in the $P2_1ma$ (Q) space group; a = 5.57467(12) Å, b = 7.76623(15) c = 5.50400(11) Å.

Atom	Wyckoff position	x	y	z	100 * U_{iso} (Å^2)
Na1*	2a	0.2569(15)	0	0.7425(13)	1.5(3)
Na2	2b	0.25	0.5	0.7385(13)	1.5(3)
Nb	4c	0.2672(5)	0.2507(6)	0.2469(5)	0.09(2)
O1	2a	0.2401(7)	0	0.3187(11)	0.77(19)
O2	2b	0.2227(7)	0.5	0.1968(11)	0.71(18)
O3	4c	0.0194(3)	0.2794(7)	0.5298(5)	1.20(10)
O4	4c	-0.0476	0.2188(6)	0.0415(6)	0.90(9)

*positions Na1 and Na2 have fixed occupancy $Na_{0.88}Li_{0.12}$.

4.2.1.1.2 $350 \leq T \leq 600$ °C

To establish the identity of this emergent phase, it is important to assign the symmetry modes responsible for the newly introduced peaks that appear at d-spacings of ~ 2.23 and 2.44 Å (see Figure 4.5). The peaks attributed to the new phase appear characteristic of those arising from instabilities along the T-line (***k*** = ½, ½, γ) which contribute to the long-range tilt system in phases R and S in $NaNbO_3$. The M- and R-point peaks are still present in this phase. In previous work on $NaNbO_3$, Peel *et al*.[21] carried out an exhaustive analysis of the possible space group symmetries that could result in these characteristic T-line peaks. In that work they show that the resultant diffraction peaks are largely induced by octahedral tilting, allowing, by extension, modes associated with other types of distortion to be ruled out in the present case. This assumption proves invaluable as ISODISTORT

identifies an impossibly large number of supercells that can arise due to M, R and T modes, if all distortion modes are considered. To identify the space group symmetry of this new phase, it is important to understand the significance of the positions of the superlattice peaks in the d-spacing region 2.0 < *d* < 2.6 Å. The peaks at *d* ~ 2.09, 2.36 and 2.47 Å (resulting from the in-phase and out-of-phase octahedral tilts along *a* and *b*, also shown in Figure 4.5) can only be indexed by applying either a $\sqrt{2}a_p \times \sqrt{2}a_p$ or a $2a_p \times 2a_p$ expansion along the *a*- and *b*-axes of the unit cell. The T-line peaks at d-spacings of ~ 2.24 and 2.44 Å can only be indexed by applying a $4a_p$ multiplicity along the *c*-axis, making the minimum unit cell metric for this phase $\sqrt{2}a_p \times \sqrt{2}a_p \times 4a_p$ (reminiscent of phases P and S in $NaNbO_3$[21]). Using the ISODISTORT software suite it is possible to search for all unit cells deriving from the parent cubic aristotype structure that possess the M_3^+, R_4^+ and T_4 *irreps.* simultaneously. It is therefore necessary to trial any suitable candidates based on their unit cell metrics. The issue of pseudosymmetry can become a challenge at this point, as determining the symmetry modes is only a part in being able to determine the precise symmetry of the unit cell. Whilst the nature of the modes is unambiguously known, the direction in which they are orientated within the crystal lattice, and indeed whether they are each associated with an individual axis or superimposed along the same axis, can become a subtlety difficult to determine. In cases where there is a high degree of similarity between the unit cell axial lengths (which can be purely coincidental and not symmetry related), the ability to unambiguously assign directions of the various octahedral tilts can become almost impossible within the limits of powder diffraction techniques. However, based on careful consideration of all possible models, it is possible using the high-resolution neutron diffraction currently available to determine the best answer among several similar models.

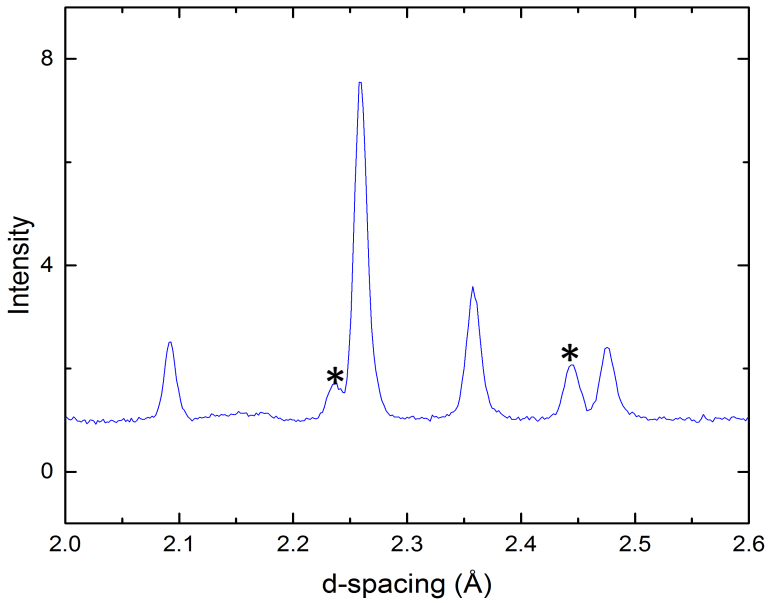

Figure 4.5 Raw data at 350 °C recorded on bank 2 on HRPD. The two peaks arising from the T_4 mode condensation are highlighted with an *.

It should be noted at this stage that there are two possible configurations of T_4 tilt mode describing the four layers of NbO_6 octahedra along *c*. These two configurations are described with a new notation, AACC (previously observed in Phase P of $NaNbO_3$[22]) and A0C0, as Glazer notation is only applicable to $2a_p \times 2a_p \times 2a_p$ unit cells (note that within this new notation A and C are symmetry constrained to be of equal magnitude). In this description A represents an anticlockwise tilt, C a clockwise tilt and 0 corresponds to zero tilting. Schematics of the two configurations possible for the T_4 mode are given in Figure 4.6. An ISODISTORT search for supercells comprising the M_3^+, R_4^+ and T_4 tilt modes results in 96 possibilities, however most can be ruled out as being of too low symmetry to have evolved from a structure with an $a^+b^-b^-$ tilt system. Interestingly, a number of non-centrosymmetric and even polar space groups are present in the list, highlighting that the addition of the T_4 mode can lead to a digression from the

strictly centrosymmetric space groups that arise from a combination of M_3^+ and R_4^+ tilt modes. This could be of potential interest in the search for new ferroelectric materials, using intelligent design principles in a similar way to cation ordering for example. For the purpose of restricting the number of potential models to a more reasonable number, it is assumed that the phase at 350 °C is firstly centrosymmetric and secondly of index value i = 96. This index is used to 'rate' the subgroup based on how diluted its symmetry operations are compared to the parent. In mathematical form this can be described as $i = M_p/M_s \times V_s/V_p$, where M_s and M_p give the multiplicity of a general site in the unit cells of the subgroup and parent, with V_s and V_p representing the corresponding unit cell volumes. Using this criterion, the list diminishes from 96 possibilities to just 9. Of these, six are trialled as fits to the data at 400 °C (chosen due to the small amount of residual phase Q present at 350 °C). These 6 options (listed in in Table 4.3) are chosen as they encompass all simple variations on how the tilt systems can be configured. For example, model LNN-S1 has all three *irreps.* condense along the same axis, whereas LNN-S3 and LNN-S8 have each tilt oriented along a different axis but include different configurations of the T_4 mode (*i.e.* one with AACC and the other with A0C0).

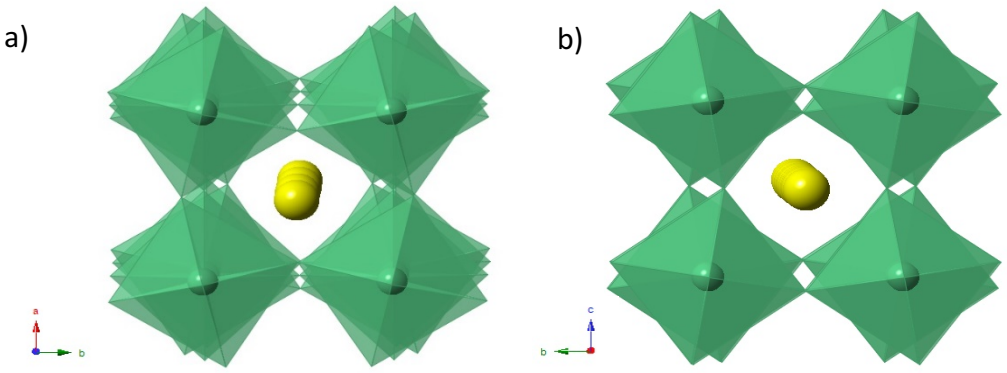

Figure 4.6 Representations of the two configurations of the T_4 octahedral tilting mode as a) A0C0 and b) AACC.

Initially this emergent phase is considered as a phase isostructural with phase S of $NaNbO_3$ (present over the temperature range 480 < T < 520 °C[10, 21]). Phase S consists of a $2a_p \times 2a_p \times 4a_p$ unit cell with *Pmmn* space group symmetry ($a^+a^+c^*$ in Glazer notation, * denotes a compound tilt system '0CAC' where A and C are no longer constrained by symmetry to be equal). The refinement in phase S (LNN-S5 in Table 4.3) can be made with cautious application of damping factors. Refinement of lattice parameters, profile parameters, fractional coordinates and thermal parameters (grouped according to element type) is possible using this model, however upon close inspection the fit of the T_4 mode is unsatisfactory in this setting (see Figure 4.7 (a)) and therefore other options must necessarily be considered. Decomposition of the symmetry modes of the LNN-S5 model using ISODISTORT enables estimation of the individual amplitudes for the R_4^+, M_3^+ and T_4 modes. These amplitudes provide good starting points for refinement in the subsequent five models. Mode amplitudes were therefore set at a value of 1.4 Å for R_4^+ and M_3^+ modes and 1.2 Å for the T_4^+ mode. Each model is treated similarly in terms of refinement strategy to LNN-S5. Details on the outcome of these refinements are given in Table 4.3. Of the 5 remaining, two stand out as markedly superior (statistically, and graphically), those of LNN-S3 and LNN-S8. As previously discussed, both these models have each of the three *irreps*. acting around a unique axis, differing only in the configuration of the T_4 mode. LNN-S3 has the T_4 mode in the AACC configuration, whilst the T_4 mode in LNN-S8 is in the A0C0 configuration. Given the number of variables versus quality of fit for both models, it is not valid at this time to suggest one is a more correct answer than the other. Both models do however confirm that this new phase is unique in its overall tilt system. Figure 4.7 shows the results of refinement in (a) the phase S model (b) the LNN-S3 model with *Pnma* symmetry and a $2a_p \times 2a_p \times 4a_p$ unit cell at 400 °C, highlighting the superior fit obtained in the LNN-S3 model. The phase at 350 °C is hereafter referred to as phase S'. Taking into account both symmetry considerations from Landau theory and the region of phase co-existence evidenced in the PND data it

can be concluded that the phase transition Q -> S' is of 1st order in nature. Phase S' was refined for the data in the temperature range 350 ≤ *T* ≤ 600 °C. The crystallographic model for S' (fit to LNN-S3) is included in Table 4.4. It should be noted there is no evidence in the PND data for a second phase reminiscent of phase R in $NaNbO_3$ arising from condensation of the T_4 mode at (***k*** = $\frac{1}{2}, \frac{1}{2}, \frac{1}{3}$).

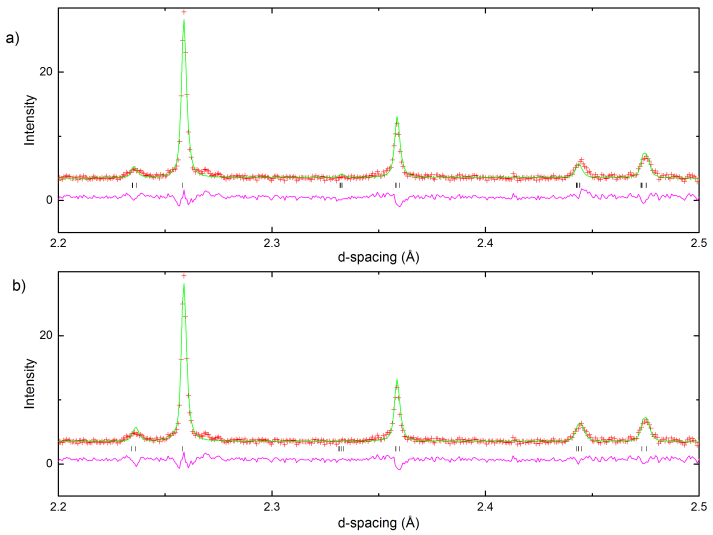

Figure 4.7 Results of Rietveld refinement on PND data obtained at 400 °C modelled in a) Phase S and b) Phase S'. Note the poor modelling of the T-point peak near *d* = 2.44 Å in the Phase S model.

Table 4.3 Trial models for LNN-12 at 400 °C ("Phase S"-like) derived from superposition of M_3^+, R_4^+ and T_4 tilts (see text). The two most suitable models LNN-S3 and LNN-S8 are highlighted in bold.

Model	Space group	N_{xyz}	Metrics	Origin	R_4^+ M_3^+ T_4	T_4	χ^2
LNN-S1	*P4/mbm*	9	$\sqrt{2}$ $\sqrt{2}$ 4	(0,0,0)	*c c c*	A0C0	11.2
LNN-S2	*Pbcm*	29	2 4 2	(0,0,0)	*a a b*	A0C0	4.74
LNN-S3	***Pnma***	**31**	**2 2 4**	**(0,0,0)**	***a b c***	**A0C0**	**2.61**
LNN-S4	*C2/m*	30	2 2 4	(1/2,1/2,0)	*(a,c) c c*	A0C0	~4
LNN-S5	*Pmmn*	33	2 2 4	(0,0,0)	*c (a,b,c) c*	A0C0	3.04
LNN-S6	*Pmma*		4 2 2	(-1/2,1/2,0)	*c c a*	AACC	
LNN-S7	*Pmma*		2 2 4	(-1/2,0,1/2)	*c a c*	AACC	
LNN-S8	***Pmmn***	**35**	**4 2 2**	**(1/2,0,1/2)**	***c b a***	**AACC**	**2.45**
LNN-S9	$P2_1/c$		4 $\sqrt{2}$ $\sqrt{2}$	(0,0,0)	*(bc, a) c c*	A0C0	

* N_{xyz} is the number of allowed variable atomic coordinates; additionally, for each case, three ADPs, relevant lattice parameters and the same set of 29 profile parameters were refined. 'Metrics' illustrate the multiplicity of the supercell relative to the cubic parent. 'Origin' defines the origin choice relative to the cubic parent (space group $Pm\bar{3}m$: Nb at (0,0,0,); Na at (½, ½, ½); O at (½,0,0)). The sixth column denotes the supercell axes upon which each of the tilt modes act; the seventh column states which of the two possible T_4 *irreps* are active. The refinement for the LNN-S4 model did not converge.

Table 4.4 Crystallographic data for Phase S' in LNN-12 at 400 °C; *a* = 7.82835(15) Å, *b* = 7.8196(2) *c* = 15.6409(4) Å.

Atom	Wyckoff position	*x*	*y*	*z*	100 * U_{iso} (Å^2)
Na1*	4c	0.236(5)	0.25	0.873(3)	2.30(12)
Na2	4c	0.242(16)	0.25	0.122(2)	2.30(12)
Na3	4c	0.249(7)	0.25	0.376(3)	2.30(12)
Na4	4c	0.250(6)	0.25	0.376(3)	2.30(12)
Nb1	4a	0	0	0	0.70(3)
Nb2	8d	0.00010(8)	0.0005(7)	0.2506(8)	0.70(3)
O1	8d	0.0252(11)	0.0334(14)	0.8752(9)	1.57(3)
O2	8d	0.0235(12)	0.0182(11)	0.3749(9)	1.57(3)
O3	8d	0.2500(17)	-0.0359(10)	-0.0161(6)	1.57(3)
O4	8d	0.2483(12)	0.0151(9)	0.2690(7)	1.57(3)
O5	4c	0.039(2)	0.25	0.0144(10)	1.57(3)
O6	4c	-0.0076(16)	0.25	0.2345(12)	1.57(3)
O7	4c	-0.033(2)	0.25	0.5214(9)	1.57(3)
O8	4c	0.0290(19)	0.25	0.7260(8)	1.57(3)

*positions Na1-Na4 have fixed occupancy $Na_{0.88}Li_{0.12}$.

4.2.1.1.3 $650 \leq T \leq 900$ °C

At a temperature of 650 °C the peaks arising from condensation of the T_4 mode are no longer present. Both peaks attributable to the M_3^+ and R_4^+ tilt modes remain, therefore centrosymmetric space groups deriving from Glazer tilt systems comprising of both in-phase and out-of-phase tilts are considered as potential fits to the data at 650 °C. In the case of pure $NaNbO_3$, phase S evolves to phase T1 (space group *Cmcm*, Glazer tilt system $a^0b^+c^-$). As this meets the criteria set out by the PND data in terms of tilt modes, a model with *Cmcm* symmetry is initially trialled as a fit. The fit to this model is satisfactory both statistically and graphically, but for completeness the two other centrosymmetric tilt systems arising from combinations of R and M modes, orthorhombic *Pnma* ($a^+b^-b^-$) and tetragonal $P4_2/nmc$ ($a^+a^+c^-$) were trialled as potential models to the data at 650 °C (details on the various fits are included in Table 4.5, with graphical representations shown in Figure 4.8). From the results of the Rietveld refinement, it is found that neither model provides an improvement over *Cmcm,* therefore the phase at 650 °C is assigned as T1. Crystallographic information regarding the T1 phase at 650 °C is included in Table 4.6.

Table 4.5 Details of the outcomes of the Rietveld refinement for the various models used to fit the PND data of LNN-12 at 650 °C.

Space group	χ^2	N_{ref}	N_{xyz}	N_{Uiso}
Cmcm	2.838	45	7	6
$P4_2/nmc$	3.092	44	7	7
Pnma	3.570	43	7	4

Table 4.6 Crystallographic data for LNN-12 at 650 °C modelled in the *Cmcm* (T1) space group; a = 7.86345(17) Å, b = 7.85644(17) Å, c = 7.786992(17) Å. U_{iso} values for all A-site cations (Na,Li) are constrained together.

Atom	Wyckoff position	x	y	z	100 * U_{iso} (Å^2)
Na1*	4c	0	0.005(3)	0.25	4.71(17)
Na2	4c	0	0.493(3)	0.25	3.7(5)
Nb	8d	0.25	0.25	0	1.16(3)
O1	8e	0.2832(6)	0	0	3.50(14)
O2	8f	0	0.2312(6)	0.0129(8)	2.25(15)
O3	8g	0.2653(8)	0.2635(10)	0.25	4.44(17)

*positions Na1 and Na2 have fixed occupancy $Na_{0.88}Li_{0.12}$.

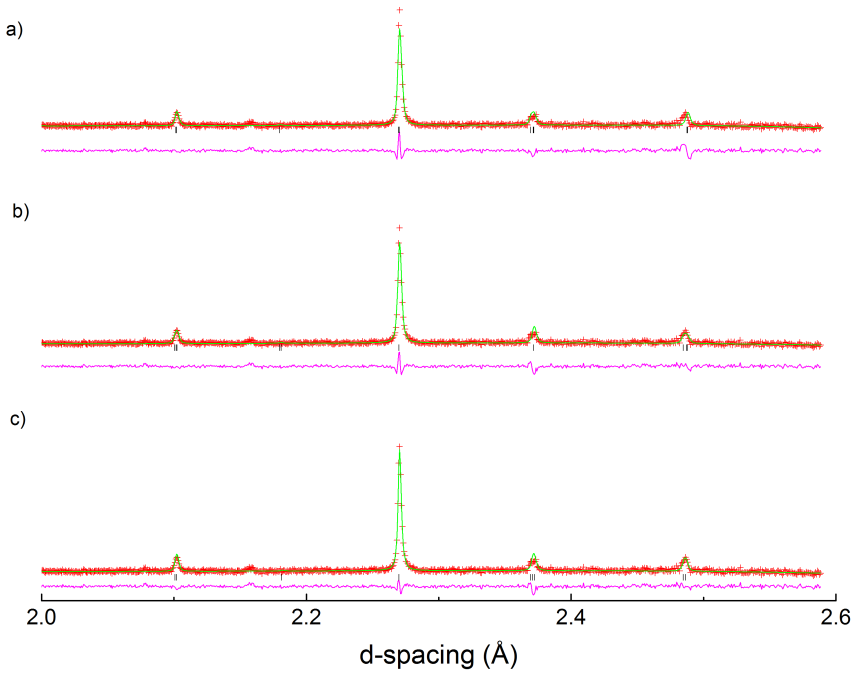

Figure 4.8 Comparison of the various Rietveld fits to PND data of LNN-12 collected at 650 °C, using a *Pnma* model (a), $P4_2/nmc$ model (b), and *Cmcm* model (c).

Upon elevating the temperature to 700 °C, evidence of a 2nd order continuous phase transition is observable with the complete disappearance of the R-point peaks. With reference to the work by Howard and Stokes[23], the only phase transition that is permitted to be continuous is *Cmcm* -> *P*4/*mbm* (T1 -> T2 in $NaNbO_3$). This corresponds to a Glazer tilt system change of $a^0b^+c^-$ to $a^0a^0c^+$. Therefore, it appears that LNN-12 proceeds *via* the same structural evolution at high temperatures as that of $NaNbO_3$[10]. The *P*4/*mbm* (T2) model provides a good fit to the data (χ^2 = 1.44), whilst also allowing for anisotropic refinement of the thermal parameters. Crystallographic information regarding the T2 phase at 700 °C is given in Table 4.7. The fit to T2 at 700 °C is shown in Figure 4.9.

Table 4.7 Crystallographic data for LNN-12 at 700 °C modelled in the *P*4/*mbm* space group; *a* = 5.56482(8) Å, *c* = 3.94063(6) Å. U_{iso} values for all A-site cations (Na,Li) are constrained together.

Atom	Wyckoff position	*x*	*y*	*z*	100 * $U_{11/22}$ (Å^2)	100*U_{33} (Å^2)
Na*	2a	0	0.5	0.5	4.71(17)	3.1(3)
Nb	2c	0	0	0	1.23(6)	1.25(12)
O1	2b	0	0	0.5	7.0(2)	0.86(14)
O2	4g	0.27136(18)	0.22865(18)	0	2.34(8)	6.36(14)

*position Na has fixed occupancy $Na_{0.88}Li_{0.12}$.

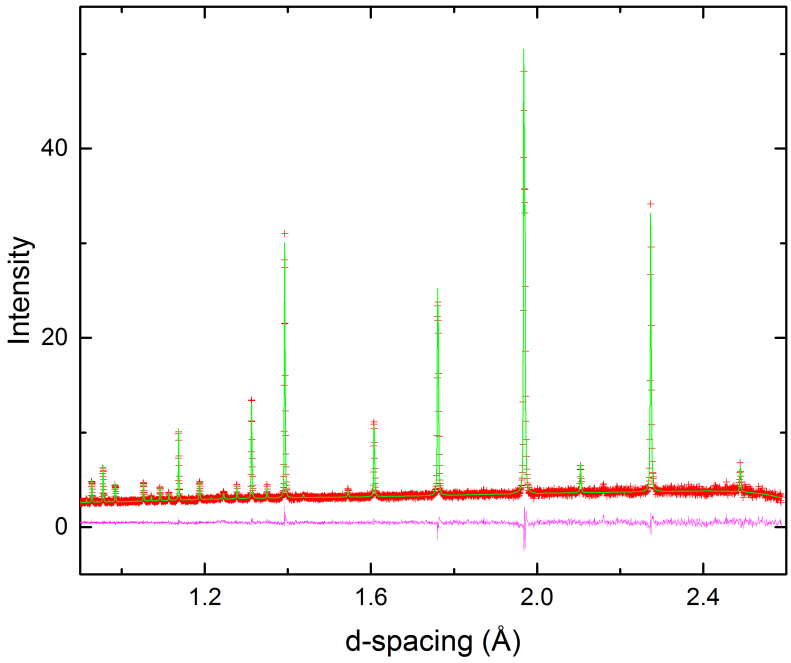

Figure 4.9 Fit to PND data at 700 °C on LNN-12 for the tetragonal phase, T2, with *P*4/*mbm* symmetry; χ^2 = 1.44, R_{wp} = 0.0316.

Within the next temperature interval of 50 °C, the disappearance of the M-point peaks indicates complete loss of the distorted supercell and adoption of parent cubic symmetry, $Pm\bar{3}m$ (U). Again, this phase transition goes *via* a 2nd order continuous mechanism as dictated by Landau theory (corresponding to a Glazer tilt system change $a^0a^0c^+$ to $a^0a^0a^0$). The fit to $Pm\bar{3}m$ at 750 °C is statistically excellent (χ^2 = 1.50). Despite the absence of superlattice peaks in the PND data, anisotropic refinement of the atomic displacement parameters (ADPs) suggests some degree of octahedral tilting remains even at 900 °C (U_{11} = 0.081(4), U_{22}/U_{33} = 0.0642(3) Å^2). This phenomenon is also observed in the cubic region of the archetype, $NaNbO_3$[10]. Structural information on phase U at 900 °C is included in Table 4.8. A fit to phase U at 900 °C is shown in Figure 4.10.

Table 4.8 Crystallographic data for LNN-12 at 900 °C modelled in the $Pm\bar{3}m$ (U) space group; a = 3.95246(3) Å. U_{aniso} values for all A-site cations (Na,Li) are constrained together.

Atom	Wyckoff position	x	y	z	100 * U_{11} (Å^2)	100*$U_{22/33}$ (Å^2)
Na*	2a	0	0	0	6.07(5)	6.07(5)
Nb	2c	0.5	0.5	0.5	1.299(18)	1.299(18)
O	2b	0	0.5	0.5	0.95(3)	6.49(3)

*position Na has fixed occupancy $Na_{0.88}Li_{0.12}$.

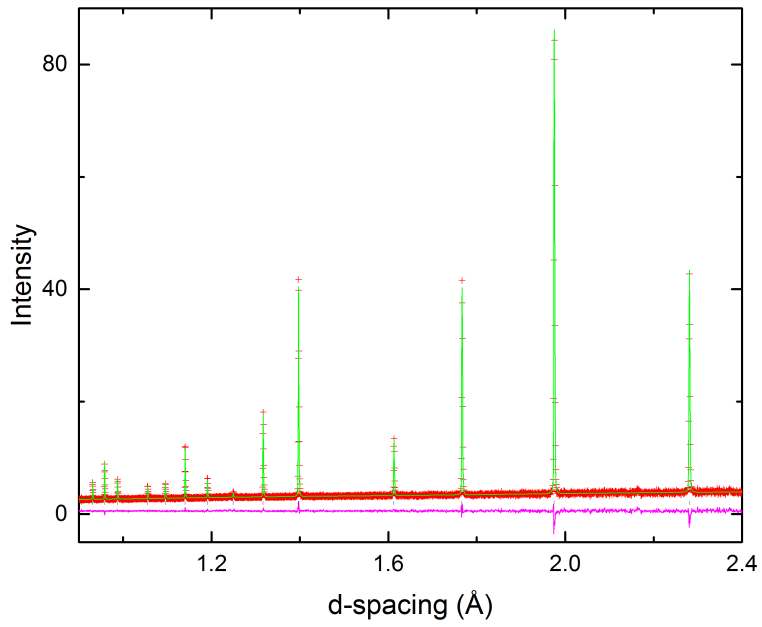

Figure 4.10 Fit to PND data at 900 °C on LNN-12 for the cubic phase, U, $Pm\bar{3}m$ symmetry; χ^2 = 1.30, R_{wp} = 0.0301.

4.2.1.2 Relative permittivity data

Relative Permittivity data obtained on a sample of LNN-12 over the temperature range $50 \leq T \leq 600$ °C is shown in Figure 4.11. A slight hysteresis effect is observable between the heating and cooling cycles. A clear peak in the permittivity measurement can be seen at $T \sim 310$ °C. This is in accordance with PND data that shows phase S' begins to form in a small amount at 300 °C before becoming the majority phase at 350 °C. The transition from phase S' to T1, which PND data indicate is in the temperature region $600 < T < 650$ °C does not lie within the temperature limitations of this data measurement. However, in the 100 Hz data in particular, the relative permittivity values appear to be increasing rapidly suggestive of a second dielectric event and phase transition just beyond 600 °C. The N –> Q transition between 100 and 150 °C is not evidenced in the relative permittivity data. However, this is most likely as phase Q is present at the beginning of the measurement process (50 °C) and therefore no structural rearrangement is introduced as such. The small values in the permittivity, which typically, could be expected to be at least two orders of magnitude larger are likely due to decreased conductivity as a consequence of water uptake. This, however, does not diminish the validity of the qualitative information presented in the permittivity measurements regarding the temperature of the observed phase transitions. LNN-12 exhibits classic ferroelectric-type behaviour with the permittivity maximum independent of the frequency at which the sample is measured.

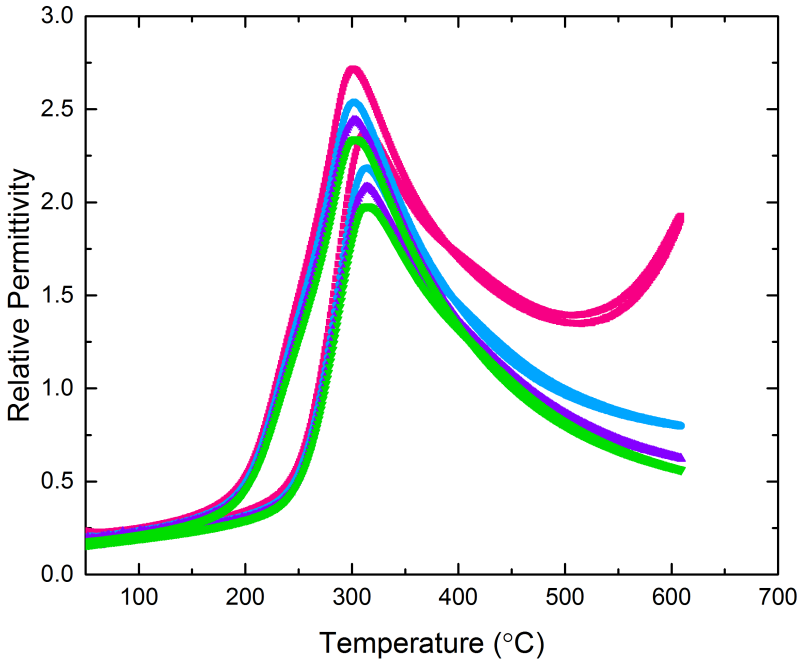

Figure 4.11 Relative permittivity data obtained on a sample of LNN-12 showing both heating and cooling cycles at selected frequencies. 100 Hz data is shown in pink, 1 kHz in blue, 10 kHz in purple and 1 MHz in green. Data on cooling is characterised by the higher permittivity value and maxima located at lower T due to a slight thermal hysteresis effect.

4.2.1.3 Symmetry mode analysis

Symmetry mode analysis on LNN-12 in the temperature region $350 \leq T \leq 600$ °C was performed using the ISODISTORT online resource[20]. The mode amplitude output from ISODISTORT for the T_4 mode *versus* temperature (Figure 4.12) shows a declining magnitude as the S' -> T1 transition is approached, however, still retains a significant amplitude at 600 °C. To evaluate the critical temperature (T_c) associated with the T_4 order parameter, the mode amplitude is fitted to a weighted power law expression of the form; mode amplitude = $A(T_c\text{-}T)^{\beta}$. The critical exponent, β, was calculated to be 0.152, with fit constant A = 0.123 and T_c = 623 °C. Whilst not enough data points are available to give a completely reliable

fit, this result from the fit is encouraging as it is in good agreement with direct interpretation of the crystallographic data that gives T_c to be in the region 600 < T_c < 650 °C. The low value of β is suggestive of a 1st order discontinuous mechanism. The power law expression used to fit the mode amplitudes is adapted from the following; mode amplitude = B (1 – /*T*/ T_c)$^{\beta}$. As such, the value for A carries the units, Å $K^{-\beta}$, for the expression used in the analysis; mode amplitude = A(T_c-*T*)$^{\beta}$.

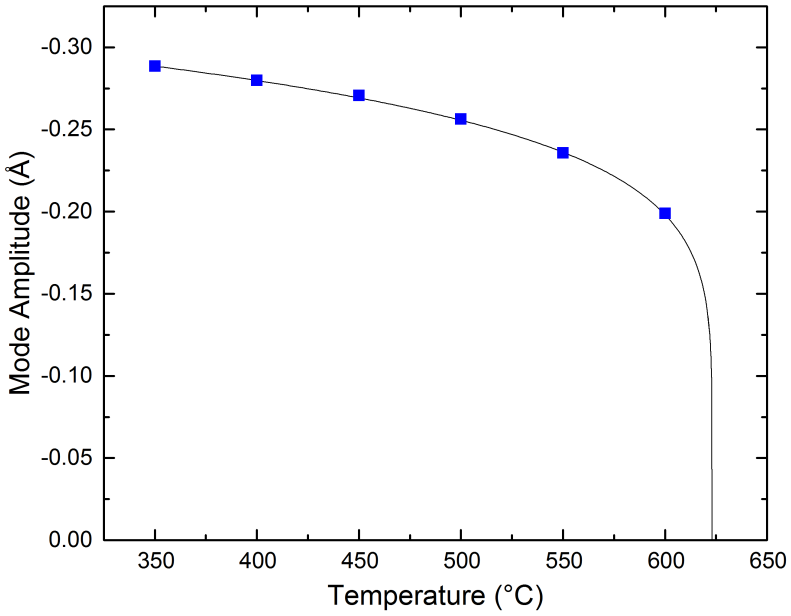

Figure 4.12 Thermal evolution of the T_4 mode along *c* in the temperature range 350 ≤ *T* ≤ 600 °C. The T_4 mode has been fit to the expression; mode amplitude = A(T_c-*T*)$^{\beta}$. The fit is shown as a black line.

The evolution of the R_4^+ and M_3^+ modes over the temperature ranges each is respectively present for is shown in Figure 4.13. As might be expected, both tilt modes follow the general trend showing a tendency to decrease with increasing temperature. Discontinuities in the evolution of the R_4^+ mode can be seen for the N -> Q and Q -> S' transitions, providing further evidence of their 1st order

nature. The S' -> T1 transition is required by Landau theory to be discontinuous, which can be clearly seen in the evolution of the M_3^+ mode amplitude.

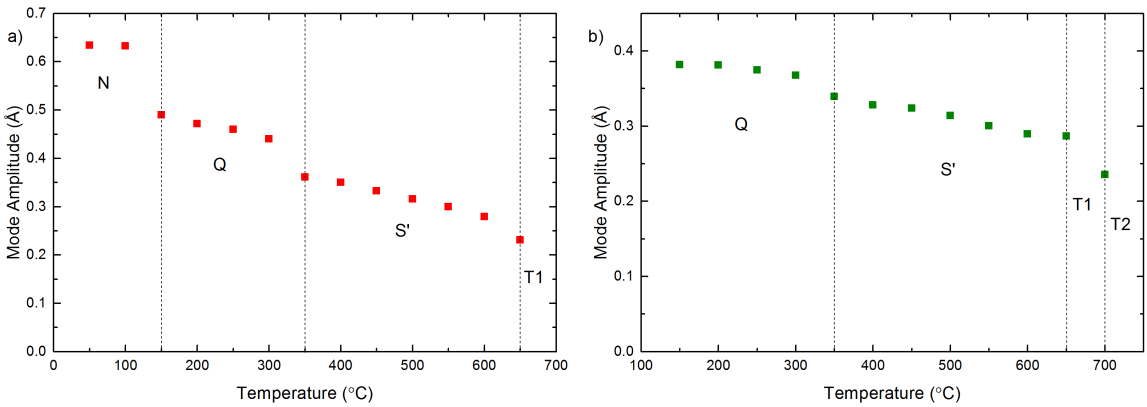

Figure 4.13 Thermal evolution of R_4^+ out-of-phase tilt mode (a) and M_3^+ in-phase tilt mode (b) for sample of LNN-12.

4.2.2 Discussion

4.2.2.1 Evolution of lattice parameters in LNN-12

The evolution of the normalised lattice parameters and cell volume as a function of temperature for LNN-12 (Figure 4.14 (a) and (b)) show evidence for a discontinuous phase transition upon transformation from *R*3*c* (N, $a^-a^-a^-$) to $P2_1ma$ (Q, $a^+b^-b^-$) symmetry, in agreement with symmetry mode analysis and PND data. Similarly, the jump in lattice parameters on going from Phase Q to Phase S' confirms the 1st order nature of this phase transition. Whilst the S' -> T1 phase transition appears to be continuous from observation of the trends in both the lattice parameters and unit cell volume, symmetry mode analysis has already shown that this transition is 1st order, in accordance with Landau theory. Due to the rapid succession of T1 -> T2 -> U phases (occurring over a 150 °C interval), no meaningful trend can be deduced from the lattice parameters with only one data

set available for each phase, however no discontinuity in the lattice parameters or unit cell volume is evidenced upon adoption of each subsequent phase. This is in keeping with both symmetry arguments based on Landau theory and observations of the PND data.

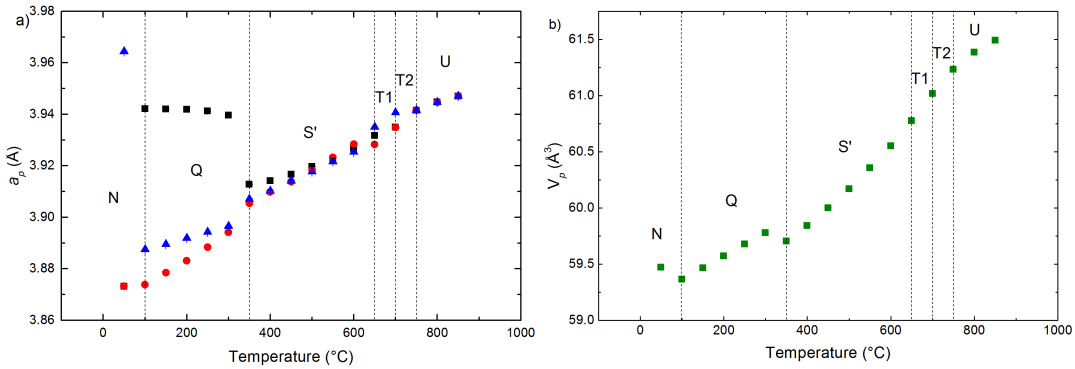

Figure 4.14 Thermal evolution of normalised lattice parameters (a) and normalised unit cell volume (b) for a sample of LNN-12. The *a* lattice parameter is represented by black squares, *b* by red circles and *c* by blue triangles. For regions in which a phase co-existence is present only the majority phase is depicted.

4.2.2.2 Phase S'

A schematic of the structure of phase S' (obtained from refinement in the LNN-S3 model) at 400 °C is shown in Figure 4.15. In this model, each of the *irreps.* act about an individual axis, with the R_4^+ out-of-phase tilt around *a*, the in phase M_3^+ tilt around *b* and the T_4 tilt in the A0C0 configuration acting around *c*. In contrast, the related $NaNbO_3$ phase, S, has a compound tilt system along *c* with contributions from all three tilt modes (although predominantly from the R_4^+ and T_4 modes) in CCCC (M_3^+), ACAC (R_4^+) and A0C0 (T_4) configurations. In the new notation, this compound tilt is described as '0CAC' (with A and C no longer constrained to be equal). No evidence for a complex compound tilt system such

as that in phase S of $NaNbO_3$ is witnessed in LNN-12, as both the potential models for this phase, LNN-S3 and LNN-S8, possess each of the three tilts along an individual crystallographic axis. As discussed previously, the only difference between these two models is found in the configuration of the T_4 mode, with the A0C0 configuration in LNN-S3 and the AACC configuration in the model named as LNN-S8. At this level of detail, issues related to pseudosymmetry become a significant problem, making it impossible to distinguish which configuration the T_4 mode adopts in Phase S' even with the high resolution achieved using the HRPD instrument. Despite this slight ambiguity, both models show that whilst closely related to Phase S in $NaNbO_3$, Phase S' in LNN-12 adopts a novel and distinct tilt system. The long-range tilt system in LNN-12 also shows greater thermal stability ($350 < T < 600$ °C) than that of phase S in $NaNbO_3$ ($480 < T < 520$ °C)[21]. Interestingly, the PND data on LNN-12 shows no evidence for a second phase reminiscent of phase R in $NaNbO_3$ ($360 < T < 480$ °C)[21]. However, whilst only one long-range tilt system is stabilised in LNN-12, the temperature range in which both $NaNbO_3$ and LNN-12 show a susceptibility to softening of the T_4 mode is comparable.

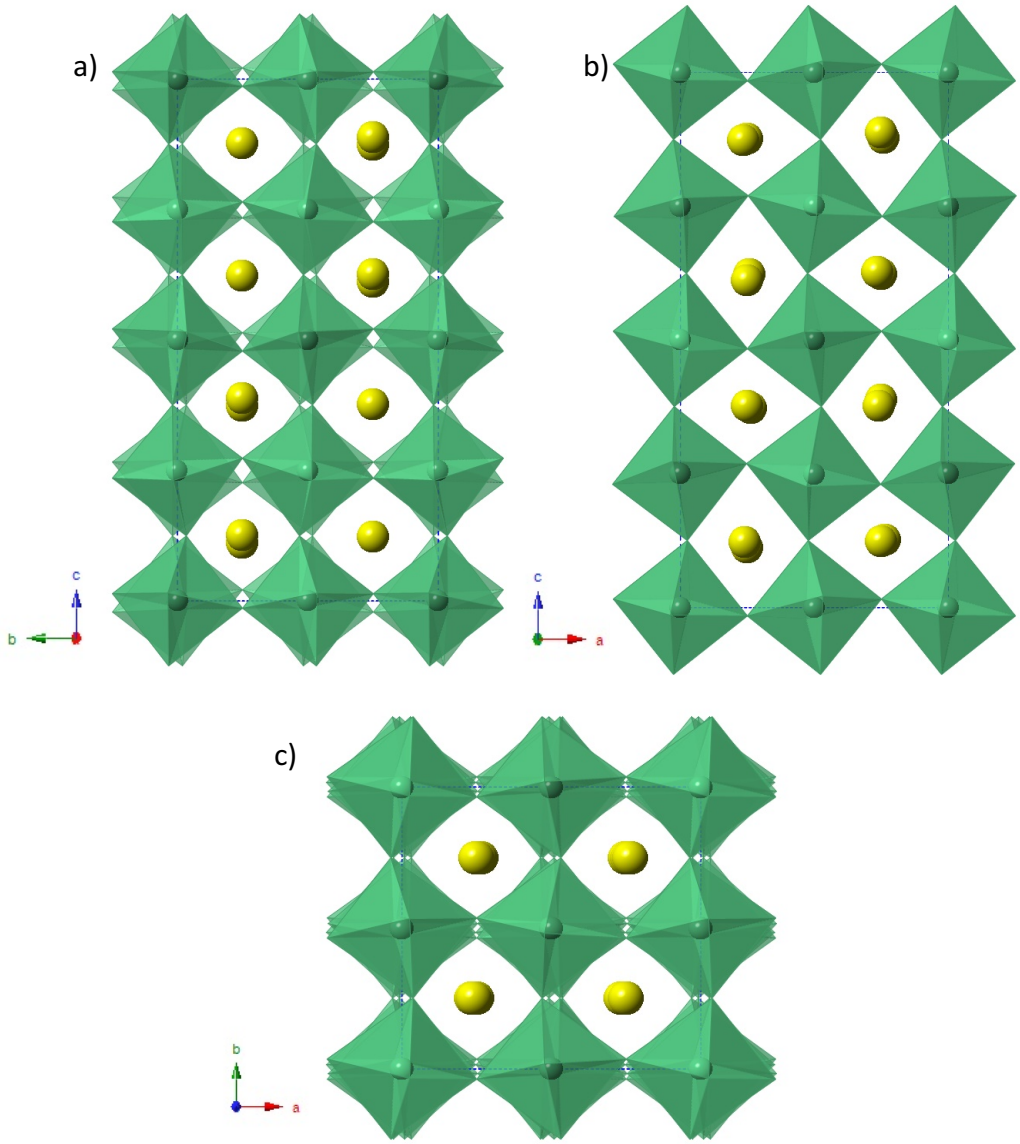

Figure 4.15 Structure of Phase S' from refinement of model LNN-S3 at 400 °C showing view of a) the out-of-phase tilt (R_4^+) around *a*, b) the in-phase tilt (M_3^+) around *b* and c) the T_4 mode in the A0C0 configuration along *c*.

4.2.2.3 Comparison to Mishra study

The structural evolution as a function of temperature of the system $Li_{0.12}Na_{0.88}NbO_3$ has previously been reported by Mishra[24]. In that study, the

temperature dependent phase diagram of LNN-12 is analysed using a combination of PXRD and PND techniques for the temperature regime $27 \leq T \leq 827$ °C. It should be emphasised that the data quality for both PXRD and PND in the study by Mishra was in general poorer than that available from HRPD. Mishra reports the phase progression, N/*Q* -> Q –> Q/T1 –> T1 –>T2-> U (with / indicating phase coexistence). For the most part this in agreement with the present study which determines the phase progression to be N/Q – >Q –> S' –> T1 –> T2 -> U.

At the lower end of the temperature regime (*i.e*. RT < *T* < 150 °C), both studies are in agreement, describing a region of phase co-existence between N and Q phases. The relative phase fractions differ, with phase Q found to be the majority phase in the study by Mishra. However, this is probably due to the synthesis conditions employed (samples were heated at 1100 °C, as opposed to the sample used in this study, which was heated at a lower temperature of 950 °C). In both studies the presence of the rhombohedral phase is diminished upon reaching a temperature of 150 °C. The presence of phase Q up to and including a temperature of 250 °C, reported by Mishra, is in agreement with the present work.

It is in the intermediate temperature region that discrepancies between this study and that of Mishra become apparent. Mishra reports the introduction of a phase with orthorhombic *Cmcm* symmetry (T1) at a much lower temperature of 300 °C, modelling the diffraction data in the temperature region 250 < *T* < 380 °C as a phase coexistence of orthorhombic Q and T1 phases. The T1 phase is subsequently fitted as the sole phase in the temperature region 380 < *T* < 650 °C. Whilst the temperatures of the various phase transitions concur with those identified in this PND study, the nature of the phase introduced at 300 °C and present to a temperature of 650 °C differs significantly.

The T1 phase proposed by Mishra is based on a $2a_p \times 2a_p \times 2a_p$ repeating unit with a Glazer tilt system of $a^0b^+c^-$. It is clear from their data that peaks arising from condensation of the M_3^+ and R_4^+ octahedral tilt modes are present at 600 °C (peaks centred around a 2θ value of 31.4 ° corresponding to a d-spacing of 2.39 Å with a neutron source of λ = 1.244 Å). Crucially, the peaks corresponding to condensation of the T_4 mode are not visible, allowing for a good fit to be obtained in the C*mcm* setting. Therefore, it must be acknowledged that the assignment of T1 is merely due to limitations in the resolution of the instrument with which the sample was measured, as opposed to any more serious misinterpretation of the data. A fit to the PND data using the T1 structural model at 550 °C (Figure 4.16) proposed by Mishra clearly demonstrates a complete lack of modelling of the peaks at $d \sim 2.25$ Å and 2.45 Å, which this study has attributed to the T_4 mode in phase S'.

At higher temperatures, the Mishra study is generally in agreement with the findings presented here with a T1- T2 - U phase progression reported. However, the phase at 650 °C is assigned as T2, whereas in the PND data presented here a phase with T1 symmetry is assigned at this temperature. It appears that the incorrect assignment of T1 over the temperature range $370 < T < 650$ °C, leads to a 'knock-on' effect and misinterpretation of the subsequent phase transitions. The phase diagram reported by Mishra and that which is presented here are included in Figure 4.17 for comparison.

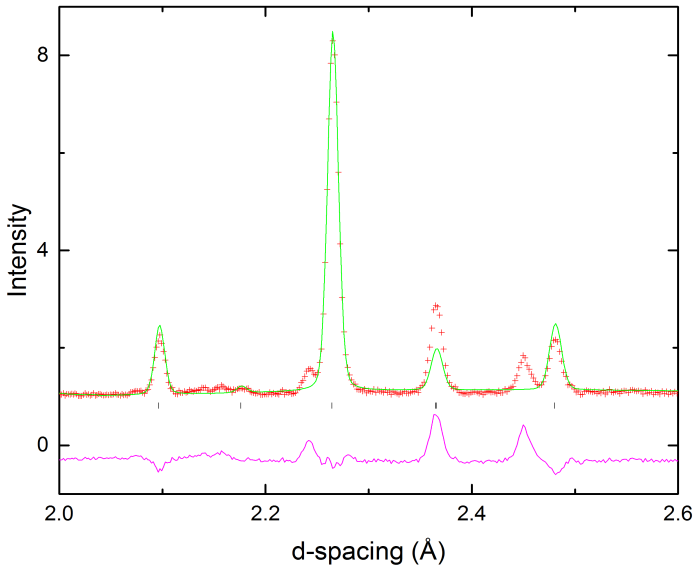

Figure 4.16 Rietveld fit using the T1 model put forward by Mishra[24] in *Cmcm* space group setting on PND data obtained at 550 °C. Note the absence of any modelling of the T-point peaks.

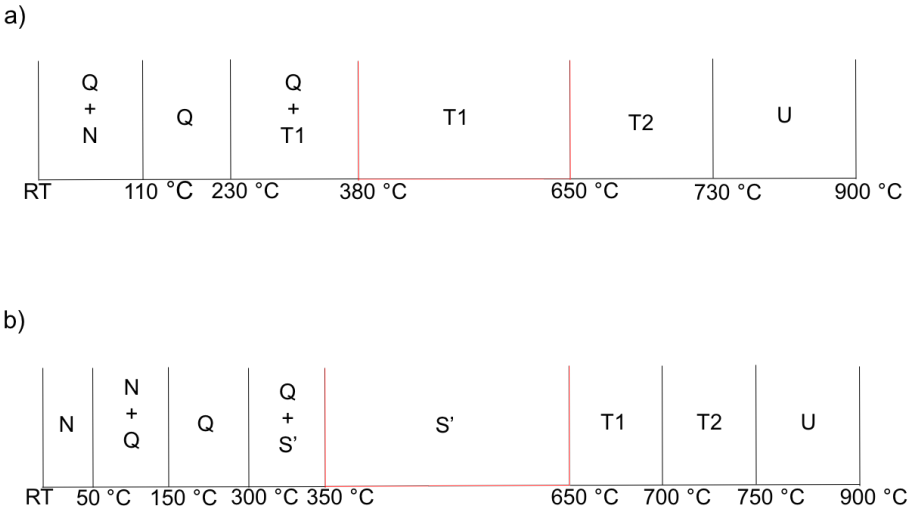

Figure 4.17 Phase diagrams for LNN-12 constructed from results reported by Mishra[24] (a) and the findings presented in this study (b). Note the absence of phase S' or any long-range tilt system involving condensation of the T_4 mode in the phase diagram proposed by Mishra. Diagrams not drawn to scale.

4.2.2.4 Previous dielectric studies

A number of studies have been carried out on the dielectric behaviour of various members of the LNN-*X* series[25-27]. Noble and Lanfredi previously reported the dielectric behaviour of LNN-12[28]. Samples of LNN-12 were synthesised by chemical evaporation methods, however the nature of the crystalline phase or phases at room temperature is not discussed. The dielectric data presented by Noble and Lanfredi shows three clear transitions centred at $T \sim 250$ °C, 448 °C and 574 °C. Unfortunately, none of these transitions match the phase evolution observed in the PND data. A separate dielectric study by Mitra[29] shows anomalies in the relative permittivity at temperatures of ~ 250 °C and ~ 320 °C. Characterisation by laboratory XRD analysis of the LNN-12 sample utilised in the study by Mitra indicates that only phase Q was present, contra to the majority rhombohedral phase described here, therefore the discrepancies in the dielectric data obtained at lower temperatures may be due to differences in the synthetic approach. The peak at 320 °C is within 10 °C of that observed in the present study, whilst also lying within the parameters proposed for the Q -> S' transition from the crystallographic data ($250 < T_c < 350$ °C). It is difficult to draw many definitive conclusions from these studies as all three permittivity experiments report different results for the same system. Encouragingly, the dielectric data obtained in this study provides corroboration of the PND data, lending validity to the phase diagram proposed here. This emphasises the need for the complementary use of precise analysis of crystallographic data on the *same samples* used for physical property characterisation in very complex systems such as this.

4.2.3 $Li_{0.08}Na_{0.92}NbO_3$ (LNN-8)

4.2.3.1 PND analysis

4.2.3.1.1 $20 \leq T \leq 300$ °C

The room temperature (20 °C) diffraction pattern of LNN-8 can be indexed as a phase mixture of orthorhombic (Q) and rhombohedral (N) phases. Synthesis conditions were chosen to ensure that Phase Q was present as the majority phase, in contrast to the sample of LNN-12 discussed above. It should be noted that refinement for the PND data collected on the sample of LNN-8 was carried out for bank 1 only. This was due to an unfortunate "twinning" of the data in bank 2 that was most likely caused by an error in processing, although the exact nature of this error is unknown. Rietveld refinement of the PND data at 20 °C using a phase co-existence model gives the relative phase fractions for phase Q and N as 93%: 3 %. Figure 4.18 shows refinement using this phase co-existence model at 50 °C. Upon elevation of the temperature to 150 °C, the peak associated with the rhombohedral phase at a d-spacing of ~ 2.2 Å is lost and complete conversion to the orthorhombic phase, Q, is confirmed by Rietveld refinement (crystallographic data for this phase is detailed in Table 4.9). A refinement model of phase Q is satisfactory up to and including a temperature of 300 °C. The fit to phase Q at 300 °C is shown in Figure 4.19.

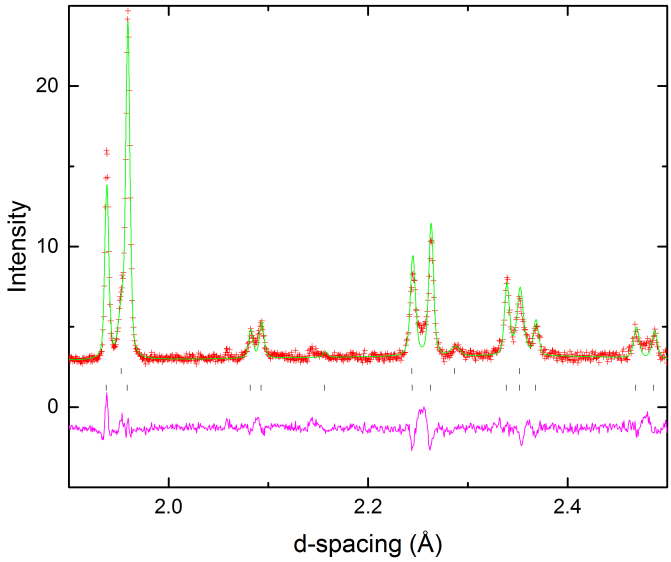

Figure 4.18 Rietveld refinement of PND data for LNN-8 obtained at 50 °C using phase co-existence model of rhombohedral phase (N, top set of Bragg peaks) and orthorhombic phase (Q, bottom set of Bragg peaks); χ^2 = 1.79, R_{wp} = 0.0404.

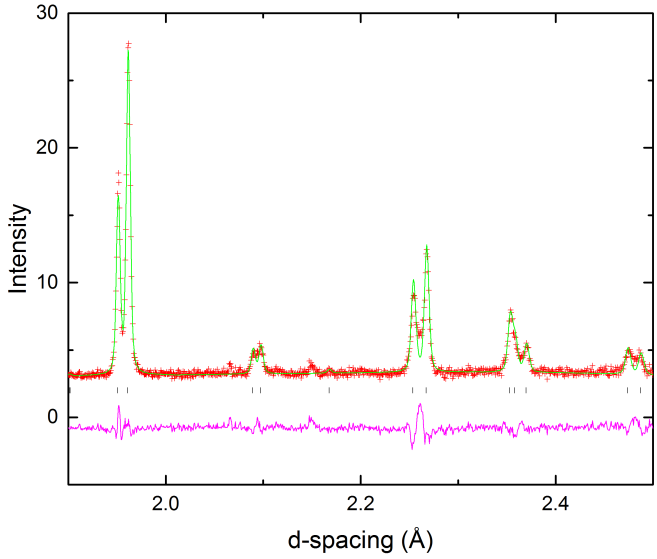

Figure 4.19 Rietveld refinement on PND data obtained at 300 °C showing the pure orthorhombic phase, Q; χ^2 = 1.79, R_{wp} = 0.0402.

Table 4.9 Crystallographic data for LNN-8 at 150 °C modelled in the $P2_1ma$ (Q) space group; a = 5.57530(14) Å, b = 7.76647(18) Å c = 5.51157(14) Å.

Atom	Wyckoff position	x	y	z	100 * U_{iso} (Å^2)
Na1*	2a	0.25	0	0.749(2)	2.5(3)
Na2	2b	0.275(4)	0.5	0.740(2)	2.7(3)
Nb	4c	0.255(3)	0.2490(9)	0.2447(9)	1.14(4)
O1	2a	0.226(3)	0	0.3210(14)	1.6(2)
O2	2b	0.209(3)	0.5	0.2024(14)	1.8(2)
O3	4c	0.007(3)	0.2764(8)	0.5366(10)	1.89(12)
O4	4c	-0.060(3)	0.2173(8)	0.0323(10)	1.97(13)

*positions Na1 and Na2 have fixed occupancy $Na_{0.92}Li_{0.08}$

4.2.3.1.2 $350 \leq T \leq 550$ °C

Inspection of the raw data in the temperature region $350 \leq T \leq 550$ °C reveals the appearance of an additional superlattice peak at a d-spacing of ~ 2.45 Å. This emergent phase is co-existent with phase Q at 350 °C, and present as the sole phase upon elevation of the temperature to 400 °C. Upon first instinct, the peak at d ~2.45 Å appears to be a T-point peak condensing at (***k*** = ½, ½, ¼) along the T-line, reminiscent of phases S in $NaNbO_3$ and S' in LNN-12. As previously discussed, phase S has a compound tilt system with R_4^+ and T_4 tilts acting simultaneously along c (although there is an additional, smaller contribution from the M_3^+ mode), whereas each tilt in phase S' acts about an individual axis. Whilst the cell metrics of these two models obviously differ, the subcell metrics (a_p) are in fact very similar (3.915, 3.916 and 3.920 Å) making the assignment of tilts along particular

axes challenging using powder diffraction methods. Both models are fitted to the PND data at 400 °C, however the resulting Rietveld fits prove unsatisfactory, specifically with regard to fitting of the T-line peak. Refinement using the Phase S model gives a χ^2 value of 2.44 (for 31 variables). Fractional atomic coordinates could not be refined for the oxygen sites in a phase with this symmetry, suggesting that the complex compound octahedral tilt system present along *c* in Phase S is not adopted in LNN-8. Refinement with a Phase S' model gives a χ^2 of 2.12 (for 21 variables). Similarly, modelling of the M-point peak at *d* ~2.5 Å is poor in this model, providing further evidence that the conformation of octahedral tilts in this phase is different to those of phase S. Arguably, the T-point peak is modelled slightly better in the Phase S' setting, however the fit is still unsatisfactory and the model too unstable to allow for refinement of the atomic coordinates. Graphical representations of the fits to both Phase S and S' models for LNN-8 at 400 °C are shown in Figure 4.20. To test the validity of the assumption that the T_4 point in LNN-8 condenses at (***k*** = ½, ½, ¼), fits to the data were attempted using a phase S' model with permutation of the subcell axes along each direction. It was found that no permutation of the 'long', 'short' and 'medium' subcell axes offers adequate modelling of the T_4 mode at *d* ~ 2.45 Å. Thus confirming that none of the subcell axes corresponds to a $4a_p$ multiplicity. Therefore, other points along the T-line must therefore be considered in order to determine the nature of this emergent phase.

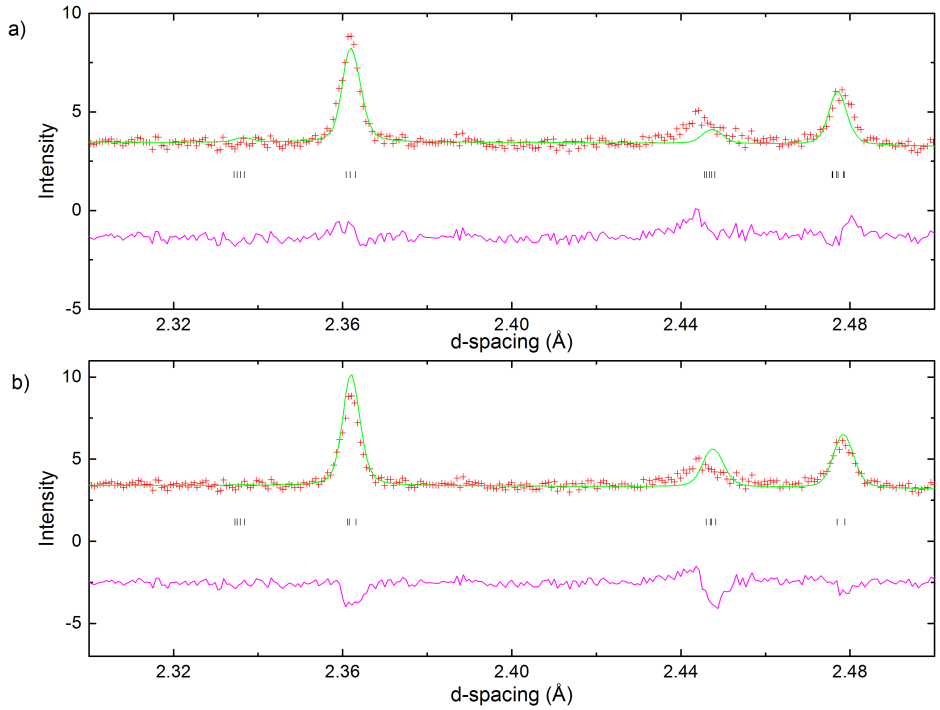

Figure 4.20 Rietveld refinement of LNN-8 at 400 °C modelled in Phase S (a), and Phase S' (b) highlighting poor modelling of the T-point peak at $d \sim 2.44$ Å.

A systematic analysis of all possible superlattices deriving from condensation of the T_4 mode at various positions along the T-line was carried out with the help of the ISODISTORT tool. The T_4 peak lies on the T-line in the parent cubic Brillouin zone between R- and M-point peaks (see Chapter 1, Section 1.7), therefore values of γ for $0 < \gamma < ½$ in reciprocal space are valid. This range can be further narrowed in light of the fit to the T_4 mode at $\gamma = ¼$. From the fit to a T_4 mode with $\gamma = ¼$ the calculated intensity of the T_4 peak is located close to but at a slightly higher d-spacing than the observed peak in the PND data. Therefore, when considering the multiplicity of the unit cell for the new phase at 400 °C, T_4 modes that occur in the range $¼ < \gamma < ½$ along the T-line are henceforth considered. Further clues can be gleaned from the PND data, as it is clear that the location of the T_4 mode is going to be closer to (***k*** = ½, ½, ¼) than (***k*** = ½, ½, ½). Using the ISODISTORT software

suite, models with a $\sqrt{2}a_p \times \sqrt{2}a_p \times n\ a_p$ unit cell containing as a minimum requirement a T_4 mode were derived. For T-points that occur between $1/10 \leq \gamma \leq 1/3$, the simplest models that can be derived all possess tetragonal symmetry, belonging to the *P*4/*mbm* space group. The origin choice for each of these models is the same as that of the cubic aristotype (*i.e.* Nb at (0,0,0)). A trial fit to a T_4 mode at ($\boldsymbol{k} = \frac{1}{2}, \frac{1}{2}, \frac{2}{7}$) along the generic T-line generates a T-point peak with too low a d-spacing value to match the peak in the observed pattern, therefore points at fractions less than 2/7 and greater than 1/4 must be considered. Through a process of trial and error, a model with the T_4 mode located at ($\boldsymbol{k} = \frac{1}{2}, \frac{1}{2}, \frac{4}{15}$) is found to yield the most satisfactory fit. Figure 4.21 shows the relative fits of the T_4 modes with γ = 1/4, 4/15 and 2/7. This would indicate that the smallest unit cell metric is $\sqrt{2}a_p \times \sqrt{2}a_p \times 15a_p$. However, the R_4^+ mode is only present for unit cells with an even multiplicity, therefore the simplest cell that can accommodate all three tilts simultaneously is one with a $\sqrt{2}a_p \times \sqrt{2}a_p \times 30a_p$ repeating unit and *P*4/*mbm* symmetry.

Unfortunately, due to the size of the unit cell in this case, an ISODISTORT search for all possible cell symmetries based on a $2a_p \times 2a_p \times 30a_p$ unit cell possessing M_3^+, R_4^+ and T_4 octahedral tilt modes simultaneously requires more computing power than is available. Even in the event that each viable model was identified the process would likely prove too exhaustive to perform manually. For the purposes of further reference this phase is named Phase S''.

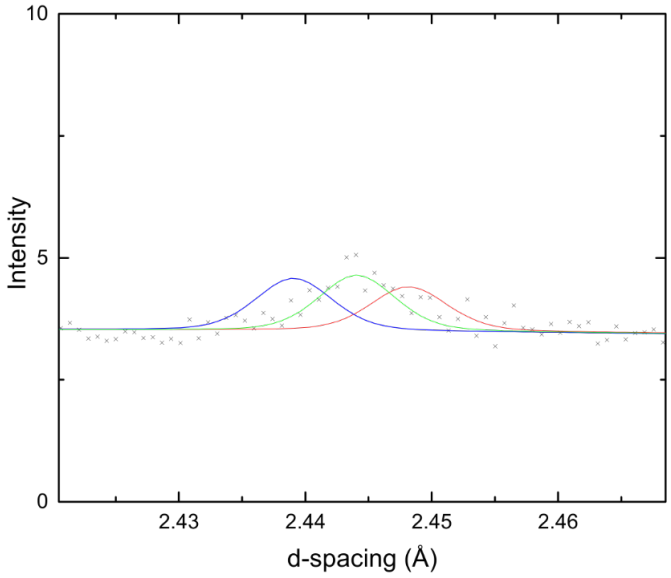

Figure 4.21 Dummy histograms generated using a *P*4/*mbm* model with T_4 modes occurring at k = ½, ½, γ, where γ = 2⁄7 (blue), 4⁄15 (green), 1⁄4 (red). Comparison to the observed peak (represented by black crosses) indicates that the T_4 mode with a γ = 4/15 provides the closest match in terms of d-spacing.

4.2.3.1.3 $600 \leq T \leq 900$ °C

At 600 °C the peak originating from condensation of the T_4 mode is completely diminished, therefore centrosymmetric space groups deriving from tilt systems with simultaneous in-phase and out-of-phase tilts are considered as viable candidates. There are three such tilt systems according to Howard and Stokes, *Cmcm* ($a^0b^+c^-$), *Pnma* ($a^+b^-b^-$) and $P4_2/nmc$ ($a^+a^+c^-$). With consideration to the structural behaviour in both the LNN-12 and $NaNbO_3$ systems, a phase with *Cmcm* symmetry can be considered most likely at this temperature, however all alternative viable space groups are trialled for completeness. Refinement using a model in the *Pnma* setting results in a poor fit ($\chi^2 = 8.82$) and fails to model the

M-point peak at $d \sim 2.5$ Å adequately, with the calculated peak offset to a slightly higher d-spacing than the observed peak in the diffraction pattern. This suggests that the configuration of the tilts relative to each other is not correct in the *Pnma* setting. In addition to this, the *Pnma* model shows peak splitting for the (200) cubic subcell peak. This splitting is not observed in the raw data and therefore results in a lower quality fit both graphically and statistically. This difference in the splitting pattern of the observed data and the *Pnma* model lead the refinement to diverge when profile parameters are "switched on". Modelling the data in the $P4_2/nmc$ space group (χ^2 = 2.09) also results in an offset on the same M-point peak, confirming unambiguously that the phase at 600 °C adopts a structure with orthorhombic *Cmcm* symmetry (T1). Graphical representations of the various fits to the data at 650 °C are shown in Figure 4.22. Crystallographic data obtained upon Rietveld refinement using a phase with *Cmcm* symmetry is detailed in Table 4.10.

Table 4.10 Crystallographic data for LNN-8 at 600 °C modelled in the *Cmcm* (T1) space group; a = 7.8647(2) Å, b = 7.8593(2) Å, c = 7.87390(17) Å. U_{iso} values for all A-site cations (Na,Li) are constrained together.

Atom	Wyckoff position	x	y	z	100 * U_{iso} (Å^2)
Na1*	4c	0	0.013(3)	0.25	4.5(8)
Na2	4c	0	0.492(3)	0.25	4.7(8)
Nb	8d	0.25	0.25	0	2.02(5)
O1	8e	0.2849(11)	0	0	4.0(2)
O2	8f	0	0.2310(12)	0.0110(12)	3.7(3)
O3	8g	0.2779(8)	0.2635(10)	0.25	3.83(15)

*positions Na1 and Na2 have fixed occupancy $Na_{0.92}Li_{0.08}$.

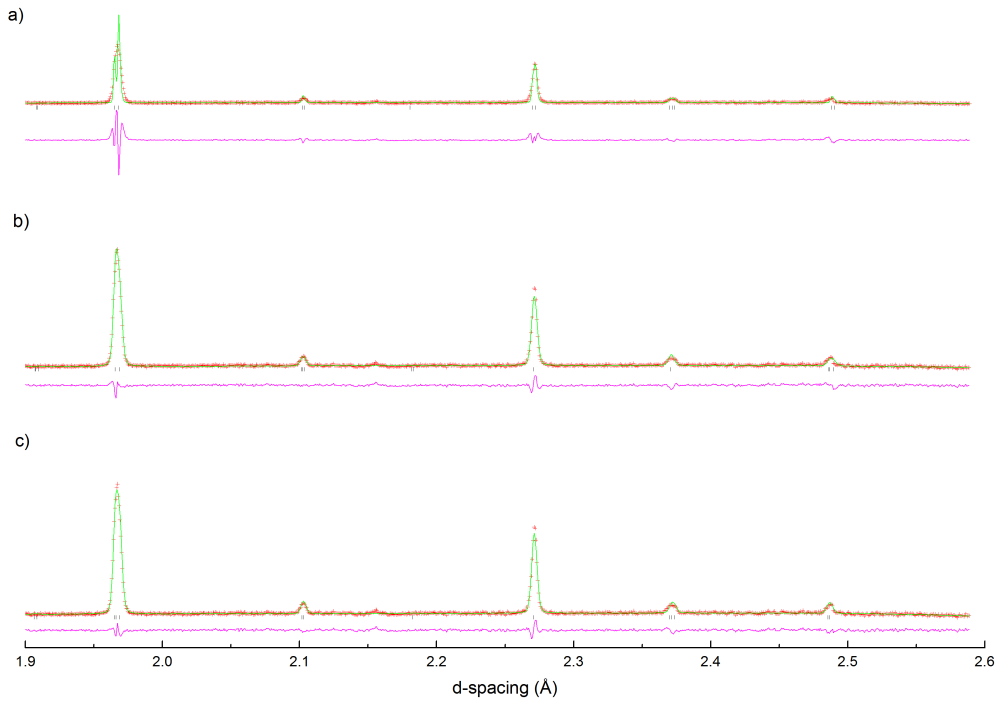

Figure 4.22 Comparison of Rietveld refinements carried out at 600 °C in a) *Pnma*, b) $P4_2/nmc$ and c) *Cmcm* models. Note the extra splitting required in the *Pnma* model at $d \sim 1.96$ Å, and the poor fitting of the M-point peak at $d \sim 2.45$ Å in both the *Pnma* and $P4_2/nmc$ models.

Elevation of the temperature to 650 °C reveals almost complete loss of the R-point peaks associated with the out-of-phase tilt mode, however, the M-point peaks attributed to the in-phase tilt mode are still present with a significant intensity at this temperature. Increasing the temperature by 50 °C reveals complete loss of both the R- and M-point peaks, indicating that cubic symmetry is adopted at this temperature. The PND data is suggestive of a two-step continuous transition from T1 – U *via* T2, however due to the lack of further data sets in the region $700 < T < 750$ °C it is not possible to state this categorically at present. A phase with $Pm\bar{3}m$ symmetry is used to model the PND data at 700 °C. Anisotropic refinement of the atomic displacement parameters suggest that this phase does still retain some localised octahedral tilting, as observed for both LNN-12 and $NaNbO_3$. The results

of anisotropic refinement for the ADPs associated with O1 site in the cubic phase are given in Table 4.11. The results highlight a tendency for the degree of anisotropy to decrease with increasing temperature as would be expected, however differences in the U11 and U22 values are still present even at the highest temperature recorded, 900 °C. A crystallographic model of the cubic phase of LNN-8 at 900 °C is included in Table 4.12. The graphical fit at 900 °C is shown in Figure 4.23.

Table 4.11 Anisotropic atomic displacement parameters (ADPs) for cubic $Pm\bar{3}m$ phase in sample of LNN-8.

Temperature (°C)	100* U_{11} (Å^2)	100* U_{22}/U_{33} (Å^2)
700	1.76(6)	7.29(5)
750	1.91(5)	7.27(5)
800	1.91(5)	7.11(4)
850	1.98(5)	7.18(5)
900	2.10(5)	7.18(4)

Table 4.12 Crystallographic data for LNN-8 at 900 °C modelled in the $Pm\bar{3}m$ (U) space group; a = 3.95246(3) Å. U_{aniso} values for all A-site cations (Na,Li) are constrained together.

Atom	Wyckoff position	*x*	*y*	*z*	100*U_{11} (Å^2)	100*$U_{22/33}$ (Å^2)
Na*	2a	0	0	0	6.57(8)	6.57(8)
Nb	2c	0.5	0.5	0.5	2.62(3)	2.62(3)
O1	2b	0	0.5	0.5	2.10(5)	7.18(4)

*position Na has fixed occupancy $Na_{0.92}Li_{0.08}$.

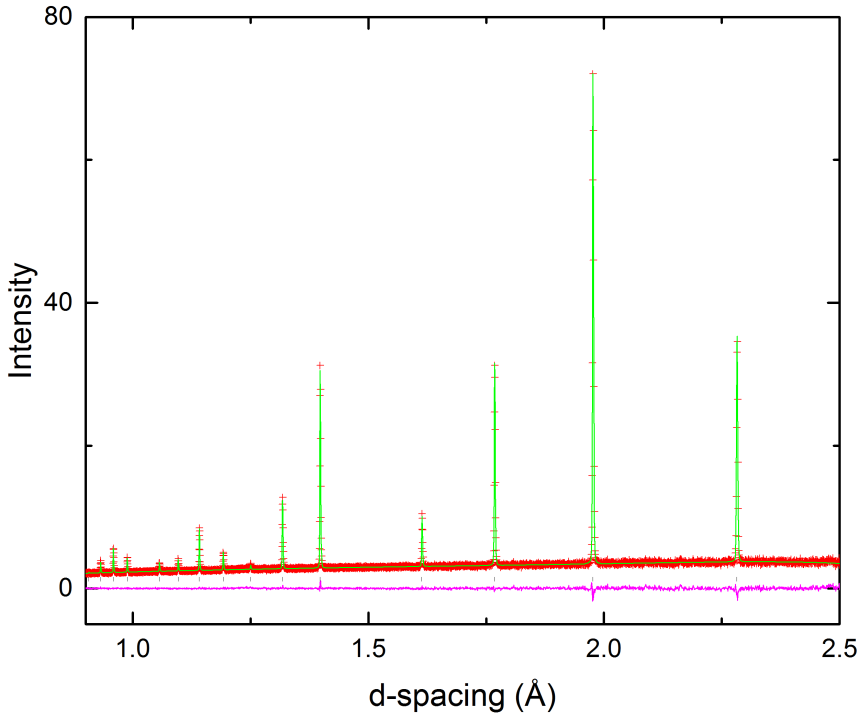

Figure 4.23 Rietveld refinement to PND data of cubic phase, $Pm\bar{3}m$ (U), in LNN-8 at 900 °C; $\chi^2 = 1.17$, $R_{wp} = 0.0328$.

4.2.4 $Li_xNa_{1-x}NbO_3$ (LNN-3)

4.2.4.1 PND analysis

4.2.4.1.1 $20 \leq T \leq 300$ °C

The room temperature PND data indicate that LNN-3 adopts orthorhombic $P2_1ma$ symmetry (Q) exclusively, as determined in previous work on the $Li_xNa_{1-x}NbO_3$ solid solution[9, 11]. The fit to the data measured at 20 °C in phase Q is shown in Figure 4.24. Diffraction data throughout the temperature regime $20 \leq T \leq 300$ °C are fitted to a phase Q model. Whilst the fit is both statistically and graphically

very good, again, as in LNN-8 and -12, the centrosymmetric variant of the $a^+b^-b^-$ tilt system, *Pnma*, is trialled as a fit to the data at both 20 °C and 300 °C. A self-consistent refinement model, as described in the experimental section (4.1.2), is used for both space group symmetries to ensure a fair comparison. At both temperatures, the *Pnma* model results in a poorer fit overall to the data than the model with $P2_1ma$ symmetry (at 20°C $P2_1ma$: χ^2 = 2.44 for 56 variables; *Pnma* χ^2 = 5.86 for 43 variables, and at 300 °C $P2_1ma$: χ^2 = 2.28; *Pnma* χ^2 = 3.49). The decrease in the polar nature of phase Q as the ferroelectric - paraelectric phase transition is approached is witnessed in the increased similarity in the goodness of fit for the centrosymmetric and polar models at 300 °C.

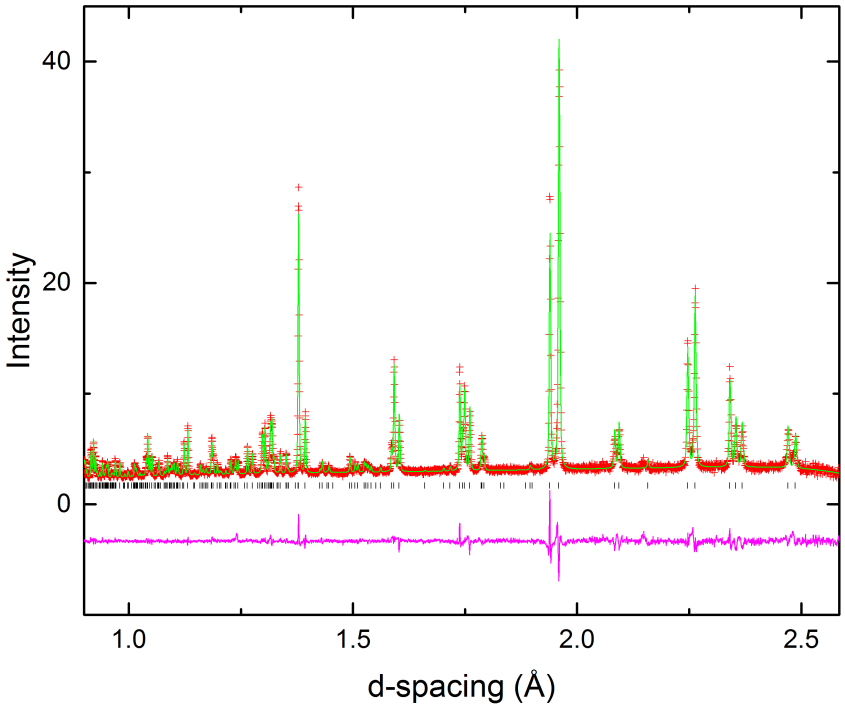

Figure 4.24 Rietveld refinement of PND data obtained for LNN-3 at 20 °C using a model with $P2_1ma$ space group symmetry (phase Q); χ^2 = 2.44, R_{wp}= 0.0342.

4.2.4.1.2 $350 \leq T \leq 500$ °C

Elevation of the temperature from 300 °C to 350 °C reveals a dramatic change in the PND data. The difference in the diffraction profile at $d \sim 1.95$ Å, shown in Figure 4.25(a), indicates a 1st order phase transition with a region of phase co-existence at 350 °C, confirmed by the small amount of residual phase Q observable at a d-spacing of ~ 2.27 Å (Figure 4-25(b)). The relative intensities of the peaks attributed to phase Q and the emergent phase at 350 °C suggest that phase Q is present as the minority phase at this temperature. Increasing the temperature by a further 50 °C reveals the isolation of this new phase with the disappearance of peaks relating to phase Q. Observation of the PND data from bank 1 at 350 °C indicates that both superlattice peaks corresponding to the M_3^+ and R_4^+ modes are present, however no additional peaks associated with a more complex superlattice are visible. In contrast, upon inspection of the raw data measured using the Bank 2 detector, extended development of the superlattice is observed with the presence of low intensity peaks in the d-spacing region $2.25 < d < 2.50$ Å. The higher signal to noise ratio for Bank 2 allows for these low intensity peaks, unresolved in the Bank 1 data, to be seen with some clarity. These unidentified superlattice peaks are present throughout the temperature regime $350 \leq T \leq 500$ °C. The two emergent peaks are diffuse in appearance with very low intensities as previously stated. Thus, assigning the distortion mode or modes responsible for these emergent peaks is somewhat more challenging in the first instance.

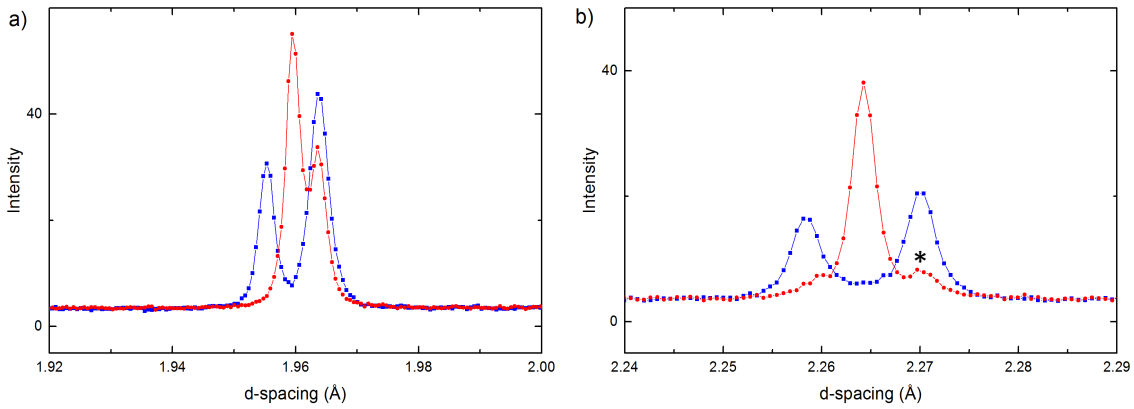

Figure 4.25 Raw PND data taken from bank 1 on LNN-3 at 300 °C (blue) and 350 °C (red) highlighting the 1st order nature of the transition mechanism, as evidenced by the change in the peak profile in (a), and the small residual amount of phase Q * (b).

With consideration to the structural behaviour of both LNN-12 and LNN-8 compositions over a similar temperature region, and additionally, the positioning of these peaks relative to those of the R and M modes, it can once again be assumed that these emergent peaks occur as a consequence of condensation of the T_4 octahedral tilt mode at a specific point along the generic T-line. Fits to both the R and S phases of $NaNbO_3$ prove that neither offer adequate modelling of the T_4 mode. Once again, a systematic search using the ISODISTORT software suite for various $2a_p \times 2a_p \times na_p$ cells with a minimum requirement of a T_4 mode is used to aid the assignment of the T_4 peaks at 400 °C. As the Phase S model simulates a peak at a higher d-spacing than that observed in the PND data (Figure 4.26), T_4 modes condensing at values larger than $\gamma = 1/4$ along the T-line are kept as viable models.

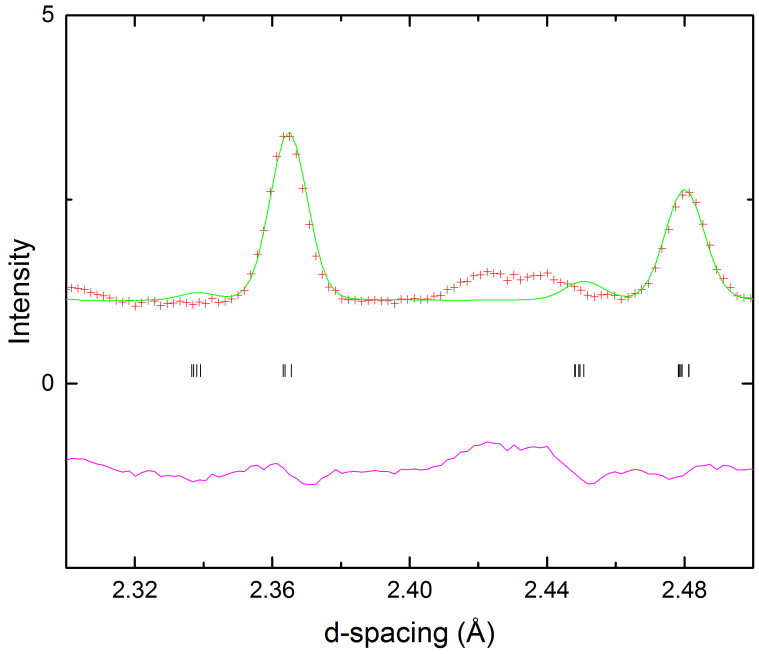

Figure 4.26 Rietveld refinement on PND of LNN-3 at 400 °C (bank 2) using the Phase-S model of $NaNbO_3$. Whilst R- and M-point peaks are reasonably modelled, there is a large offset in the location of the T_4 peak at $d \sim 2.44$ Å.

A methodical appraisal of various T_4 modes occurring at different integer values of $x/10$ along the T-line is described. Simulated models are compared to the observed data with no further refinement processes performed. Using the ISODISTORT software suite a model of *P*4/*mbm* symmetry with a $2a_p \times 2a_p \times 10a_p$ unit cell and a T_4 mode specified at ($\boldsymbol{k} = \frac{1}{2}, \frac{1}{2}, \frac{3}{10}$) is compared to the observed T_4 peaks arising from the extended superlattice. This approach proves fruitful as the simulated T_4 mode with $\gamma = 3/10$ appears at a d-spacing comparable to that of the observed pattern at 400 °C (~2.44 Å). Due to the proximity of the second T_4 peak centred at $d \sim 2.42$ Å the model trialled against the data involves a T_4 mode with $\gamma = 4/10$ (Figure 4.27). In this case the peak attributable to the T_4 mode is present at too low a d-spacing to provide an accurate fit to the PND data, therefore it is

necessary to look at positions at γ values in the region $3/10 < \gamma < 4/10$. As an aside it can also be noted that the two peaks which arise when a T_4 mode is "switched on" move closer together as the value of the fraction is increased, *i.e.* as the multiplicity of the cell increases the two peaks generated from the T_4 mode move toward one another in reciprocal space.

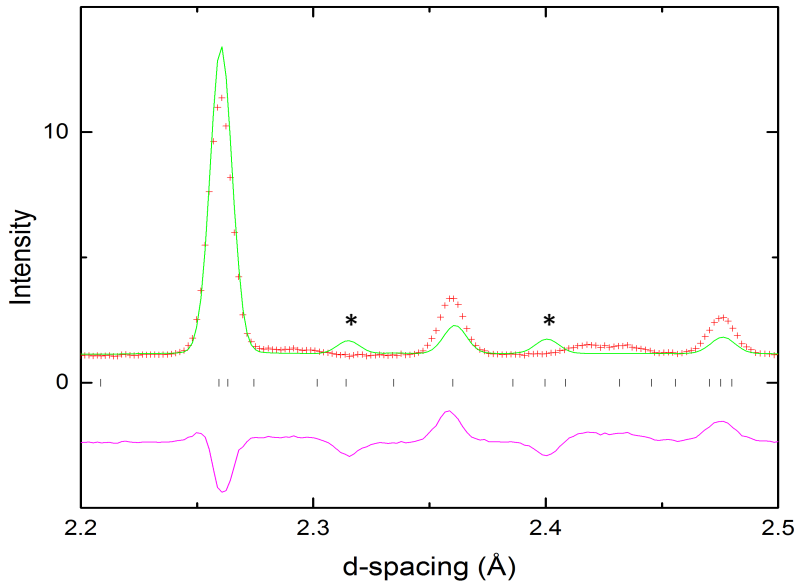

Figure 4.27 Rietveld refinement on PND data at 400 °C of LNN-3 with T_4 mode at γ = 4/10. Note the increased proximity of the peaks arising from the T_4 modes (*) as the fraction of γ is increased.

Due to the proximity of the major peaks arising from the T_4 modes (at $d \sim 2.42$ Å and ~ 2.44 Å) a *P*4/*mbm* model with a $2a_p \times 2a_p \times 20a_p$ unit cell is now trialled instead. This doubling of the unit cell along *c* enables peaks to be generated in smaller increments along the T-line with the aim of finding a more accurate fit. A model with a T_4 mode present at ($\boldsymbol{k}$ = $\frac{1}{2}$, $\frac{1}{2}$, $\frac{7}{20}$) offers a good match to the second peak at lower d-spacing, therefore, the best solution that can be obtained from

the data is a model with T_4 modes present at γ = 6/20 (equivalent to 3/10) and γ = 7/20 along the T-line in a $\sqrt{2}a_p \times \sqrt{2}a_p \times 20a_p$ unit cell. The fit to the data at 400 °C using this model is shown in Figure 4.28. Whilst the fits to the peaks arising from both the T_4 modes and the M_3^+ mode are satisfactory, the fit to the peak generated by the R_4^+ mode at $d \sim 2.35$ Å is less well modelled. This could suggest that a simple model in which the T_4, M_3^+ and R_4^+ modes act about a unique axis is an unsatisfactory description, and a more complex compound tilt system reminiscent of that seen in phase S of $NaNbO_3$ is adopted for a composition of x = 0.03 at 350 °C. Unfortunately, similarly to LNN-8, the simplest unit cell is still too large, making any meaningful attempt to assign the exact space group symmetry futile. It should be noted that assignment of these modes is ambiguous *in lieu* of the observable T-line peaks in the high-resolution data from Bank 1, and therefore no definitive conclusion with regards to the exact multiplicity of the unit cell can be gleaned in the present study. Despite this, it does appear that LNN-3 adopts a novel tilt system related to, but distinct from, the various long range tilt systems adopted in $NaNbO_3$ and its analogous compounds. The distinct nature of the long-range tilt systems present at each composition highlights the extreme sensitivity of $NaNbO_3$ to the effects of doping.

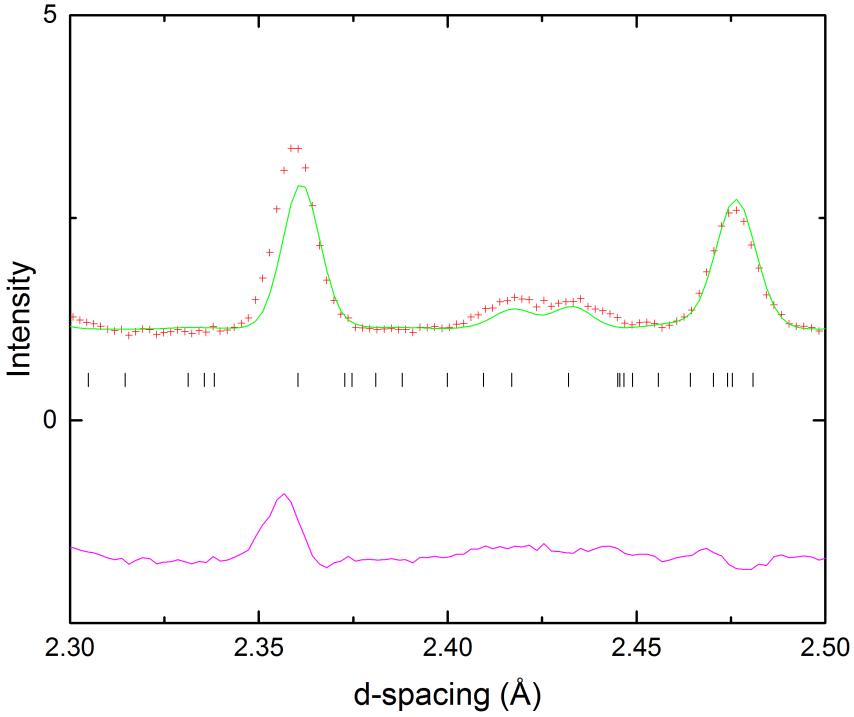

Figure 4.28 Modelling of the T_4 peaks in LNN-3 at 400 °C with T_4 modes with γ= 6/20 and 7/20.

4.2.4.1.3 $550 \leq T \leq 900$ °C

Evidence for the long-range tilt system arising from condensation of the T_4 mode is present in the PND data up to and including a temperature of 500 °C. Increasing the temperature by 50°C indicates a phase transition has occurred with the associated loss of the diffuse superlattice peaks attributed to the two potential T_4 modes. Both the R- and M-point peaks remain upon the transition, therefore a phase with *Cmcm* symmetry is fitted to the data at 550 °C (χ^2 = 3.72 for 45 variables), given the behaviour of the previous compositions. As before, the data at 550 °C are also fitted to models with *Pnma* and $P4_2/nmc$ symmetry. A

comparative fit to *Cmcm* can be made in the $P4_2/nmc$ setting (χ^2 = 4.55 for 45 variables), however, statistically the fit is poorer in the tetragonal space group. Fitting the data at 550 °C to a *Pnma* model reveals the refinement is highly unstable. The splitting of the (200) subcell peak imposed by *Pnma* symmetry is not observed in the diffraction data, whilst the modelling of the M-point peak is inadequate in this setting. Given the evidence and precedent, it is appropriate to conclude that LNN-3 adopts a phase with *Cmcm* symmetry at 550 °C. At 600 °C a further phase transition is indicated with the loss of the R-point peak corresponding to an out-of-phase octahedral tilt (R_4^+ mode). A model with *P*4/*mbm* symmetry (T2) provided an excellent fit to the data at 600 °C (χ^2 = 1.60) and allowed for anisotropic refinement of the ADPs. A crystallographic model of T2 at 600 °C is given in Table 4.13**.** The next data set, measured at 700 °C indicates cubic symmetry is adopted with complete loss of all peaks attributed to the distorted superlattice. Subsequently, the data in the region $700 \leq T \leq 900$ °C is modelled using $Pm\bar{3}m$ symmetry (χ^2 at 700 °C = 1.63). Anisotropic refinement of the ADPs indicates a small amount of localised octahedral tilting is still present at 900 °C, continuing the trend observed for LNN-8, -12 and pure $NaNbO_3$ itself. Structural information for the cubic phase at 900 °C is detailed in Table 4.14. Graphical representations of the fits to T1, T2 and U phases are shown in Figure 4.29.

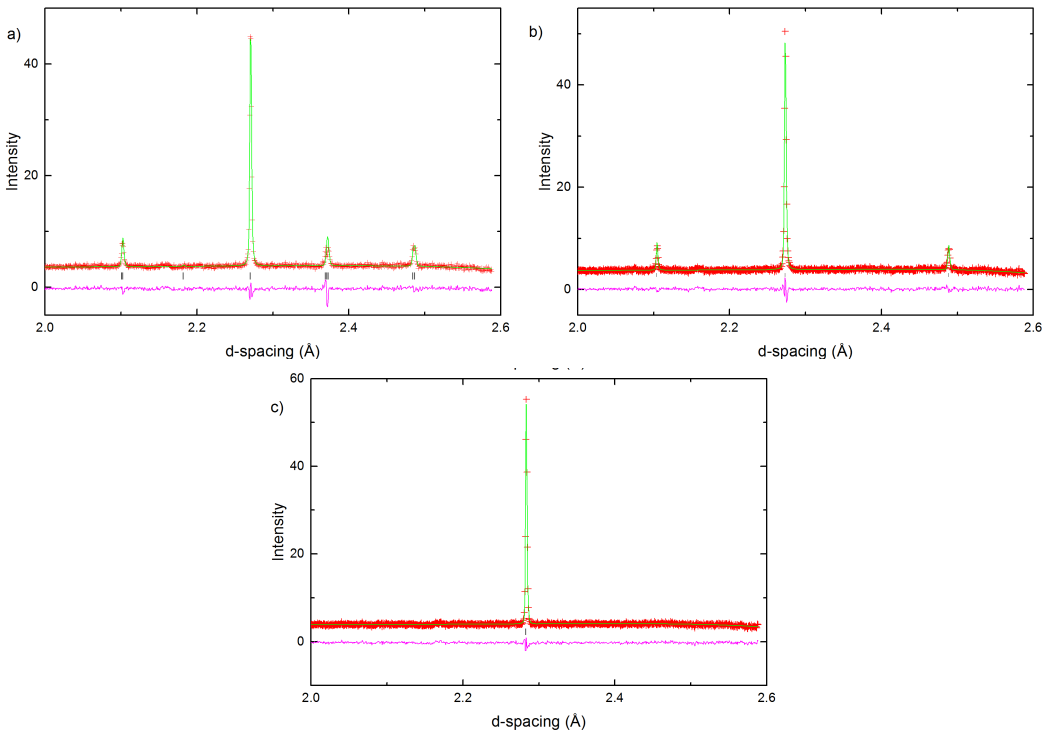

Figure 4.29 Fits to PND data of LNN-3; (a) *Cmcm* at 550 °C (χ^2 = 3.79, R_{wp}= 0.0428) (b) *P*4/*mbm* at 600 °C (χ^2 = 1.64, R_{wp}= 0.0274). and (c) $Pm\bar{3}m$ at 900 °C (χ^2 = 1.47, R_{wp}= 0.0262).

Table 4.13 Crystallographic data for LNN-3 at 600 °C modelled in the *P*4/*mbm* space group; *a* = 5.56367(5) Å, *c* = 3.94190(4) Å. U_{aniso} values for all A-site cations (Na,Li) are constrained together.

Atom	Wyckoff position	*x*	*y*	*z*	100 * $U_{11/22}$ (Å^2)	100*U_{33} (Å^2)
Na*	2a	0	0.5	0.5	4.68(9)	4.57(18)
Nb	2c	0	0	0	1.23(3)	1.49(7)
O1	2b	0	0	0.5	5.91(10)	1.09(8)
O2	4g	0.27420(11)	0.22579(11)	0	2.18(4)	5.98(8)

*position Na has fixed occupancy $Na_{0.97}Li_{0.03}$.

Table 4.14 Crystallographic data for LNN-3 at 900 °C modelled in the $Pm\bar{3}m$ space group; a = 3.95410(2) Å. U_{aniso} values for all A-site cations (Na,Li) are constrained together.

Atom	Wyckoff position	*x*	*y*	*z*	100 * U_{11} (Å^2)	100*$U_{22/33}$ (Å^2)
Na*	2a	0	0	0	6.05(4)	6.05(4)
Nb	2c	0.5	0.5	0.5	1.648(15)	1.648(15)
O1	2b	0	0.5	0.5	1.17(3)	6.08(2)

*position Na has fixed occupancy $Na_{0.97}Li_{0.03}$.

4.2.5 Unit cell metrics for *x* = 0.03 and *x* = 0.08 compositions

The thermal evolution of the lattice parameters in both LNN-8 and LNN-3 (Figure 4.30) show a discontinuity in the normalised *a* unit cell metric upon the transition from the Q to S'' phase. This discontinuity is echoed in a plot of the normalised unit cell volume *versus* temperature, providing further evidence that the Q -> S' transition proceeds *via* a 1st order mechanism. For the purpose of observing general trends, data in the region $400 \leq T \leq 550$ °C is fitted to phase S of $NaNbO_3$ for LNN-8 and phase R for LNN-3, from which normalised lattice parameters are obtained. Phases S and R were chosen for refinement against the data for LNN-8 and -3 as they offer the best modelling of each respectively amongst the well-defined long-range tilt systems. The precision of the lattice parameters obtained is insufficient to draw clear conclusions, with trends in the unit cell volume indicating the S'' and S''' -> T1 transitions may both be 2nd order. This however is not possible according to symmetry restrictions from Landau theory, and echoes the continuous trend in the cell volume for the S' -> T1 transition in LNN-12, which was contradicted by the discontinuous evolution of the symmetry modes.

Therefore, it must be assumed that these transitions similarly proceed *via* a 1st order mechanism. All subsequent phase transitions *i.e.* T1 – T2 – U appear to be continuous in LNN-8 and -3 from observation of trends in both the normalised lattice parameters and unit cell volume.

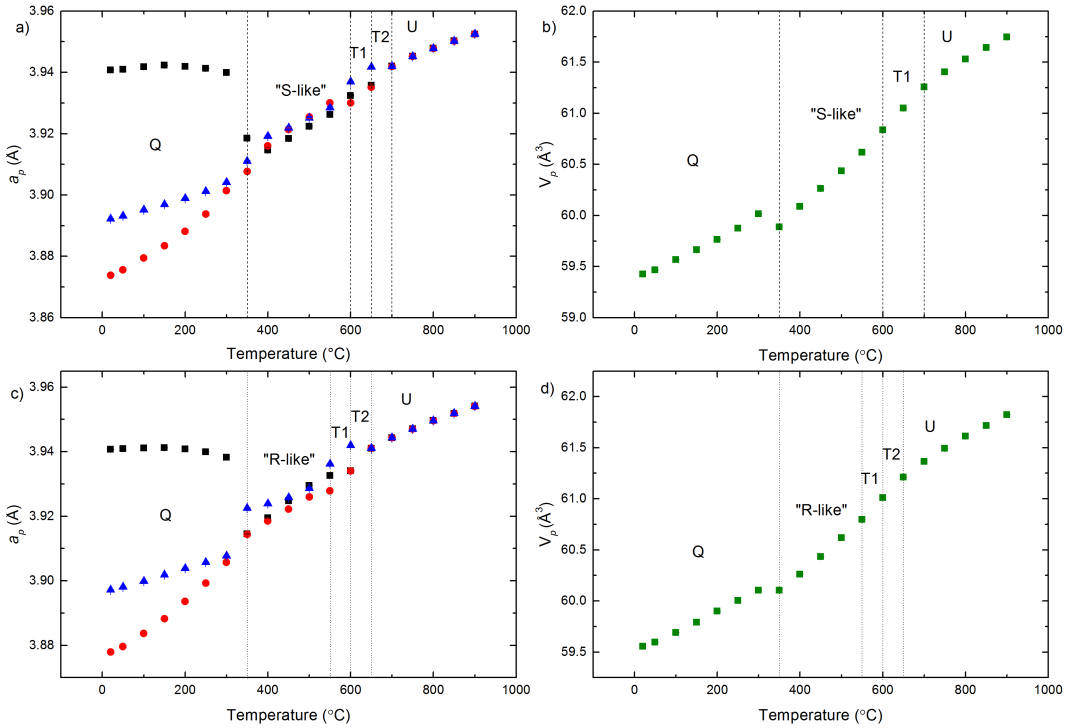

Figure 4.30 Thermal evolution of normalised lattice parameters and normalised unit cell volume obtained from PND data on a sample of LNN-8, (a and b) and LNN-3, (c and d). The *a* lattice parameter is represented by black squares, red circles denote *b* and blue triangles denote *c*. Lattice parameters from the majority phase only in regions of phase co-existence are shown.

4.2.6 Discussion

The long-range superlattices which evolve from phase Q observed in both the LNN-3 and LNN-8 systems, whilst perhaps surprisingly large, highlight the interesting behaviour of this system as a function of lithium content. It appears that the S and R phases in $NaNbO_3$ with well-defined $4a_p$ and $6a_p$ superlattices give way to the more diffuse longer-range tilt systems in LNN-3 and LNN-8 before returning to a well-defined $\sqrt{2}a_p \times \sqrt{2}a_p \times 4a_p$ repeating unit in LNN-12 (albeit with a different tilt arrangement to that exhibited in phase S of $NaNbO_3$). The difficulty associated with assigning the exact space group symmetry of the longer-range superlattices adopted in LNN-3 and LNN-8 is regrettable as they both appear to be unique with regard to the range of structures adopted by $NaNbO_3$ and its analogous compounds. The progression in these extended superlattices as a function of *x* could, perhaps in part, be rationalised as the system progressing between phases reminiscent of phase R (at lower values of *x*) and phases increasingly closely related to phase S as the value of *x* increases condensing at different points along the T-line between $\gamma = 1/3$, and $\gamma = 1/4$. Whilst condensation of the T_4 mode does without doubt occur in both LNN-3 and LNN-8, it is not currently possible to suggest definitive tilt systems adopted in either of these compositions, as the orientation of the relevant modes relative to each other, and indeed, the possibility of a complex compound tilt system involving more than one *irrep*. along a single axis, cannot be determined. However, the results of Rietveld refinement do suggest a trend in the orientation of the tilt modes for the three compositions studied. It is established that LNN-12 adopts a novel tilt system with each of the three *irreps.* or modes acting about an individual axis. Whilst not fully elucidated, it appears similarly that no compound tilt system like that adopted in phase S is realised in LNN-8 (with the fit to Phase S providing poor modelling of the M-point peak and proving unstable to refinement of the oxygen fractional coordinates). LNN-3, however, when refined in a simple model in which each *irrep*.

acts about an individual axis, results in poor modelling of the R-point peak. This perhaps suggests a compound tilt system in which the R_4^+ acts about the same axis as an additional tilt mode (as in phase S) is adopted in LNN-3. Collectively, this may indicate that as more distortion is introduced into the structure (*i.e.* with increased Li concentration) the tilt modes show a decreasing tendency towards adopting compound tilt conformations.

Examples of structures which show instability toward a T-point distortion mode are not included in the theoretical work by Glazer[30] and later by Howard and Stokes[23]. Both these approaches list derivative structures related to the cubic aristotype *via* M_3^+ and R_4^+ tilt modes only, therefore classifying unit cells based on repeats of a 2×2×2 array of octahedra. In practice, this has proven to be mostly valid, however in theory, octahedral tilt modes can occur at any value of γ between 0 and 1/2 (*i.e.* along the T-line), thus providing a much more extensive range of derivative structures than those traditionally considered. The susceptibility of perovskites to the 'softening' of these alternative octahedral tilting modes has been shown in previous systems, such as the $Ca_xSr_{1-x}TiO_3$ series[31]. Analysis using both neutron and electron diffraction techniques show that for the composition range $0.59 \leq x \leq 0.65$ the $Ca_xSr_{1-x}TiO_3$ system, shows instability to the T_4 mode at ($\boldsymbol{k} = \frac{1}{2}, \frac{1}{2}, \frac{1}{4}$) resulting in a *Pbcm* structure with a $\sqrt{2}a_p \times \sqrt{2}a_p \times 4a_p$ periodicity, isostructural with Phase P in $NaNbO_3$.

In addition to the $Ca_xSr_{1-x}TiO_3$ solid solution, such long-range structures in perovskites have been witnessed in $KLaMnWO_6$, with a $10a_p \times 10a_p \times 2a_p$ repeat unit[32]. In this structure, it was found that the out-of-phase tilt acting around both the *a*- and *b*-axes is interrupted periodically by an in-phase tilt every five octahedra. This is described as octahedral tilt twinning, with the in-phase tilt denoting the twinning boundary. The driving force for this twinning in $KLaMnWO_6$ is proposed to be cation ordering of the K^+ and La^{3+} ions, therefore due to size

considerations no such effect is anticipated to be the cause of any of the long-range tilt systems observed in the LNN-*X* series. The Phase P-like AACC tilt system has also been observed in $Na_2MoO_2F_4$[33]; the only example of characterisation of a non-Glazer tilt by single crystal X-ray diffraction methods.

Previous work has shown that the R and S phases in $NaNbO_3$ adopt largely commensurate structures that are characterised by condensation of the T_4 mode[34, 35], therefore, with a T_4 mode condensing at ($\boldsymbol{k} = \frac{1}{2}, \frac{1}{2}, \frac{1}{4}$) in Phase S' (in LNN-12), there is no reason to assume incommensurate modulations are present here. However, due to the large multiplicities proposed for the LNN-8 and -3 systems, it is possible that incommensurate modulations which involve T_4 mode condensation at fractions that are as such unrelated to the supercell of the bulk crystalline phase are present and it are these modulations that manifest as T-peaks in the PND data. The diffuse nature of the superlattice peaks arising from the T_4 mode in LNN-3 and their presence at two distinct locations along the T-line perhaps hint strongly at their incommensurate nature. Further refinement of the structure to include incommensurate modulations, or an experiment using high resolution transmission electron microscopy (HRTEM) techniques to visualise any stacking faults present would therefore be beneficial. Additionally, visualisation of the peaks in the high resolution back scattering (bank 1), observed over the temperature range $350 \leq T \leq 500$ °C, is necessary in order to accurately identify the γ value along the T-line at which the T_4 mode becomes unstable. To achieve this, additional data collection for longer periods of time would be required to improve the signal to noise ratio in bank 1. A careful study using electron diffraction techniques at elevated temperatures would also be very helpful in this regard.

Whilst all three compositions appear to adopt quite different long-range tilt systems, the general phase progression as observed for LNN-3, -8 and -12 compositions is the same, being Q -> 'S-like' -> T1 -> T2 -> U. Figure 4.31 highlights the group-subgroup relationship between these phases as determined by Howard and Stokes[23]. The continuous mechanisms associated with the T1 –> T2 –> U transitions corroborate the findings from the present crystallographic analysis.

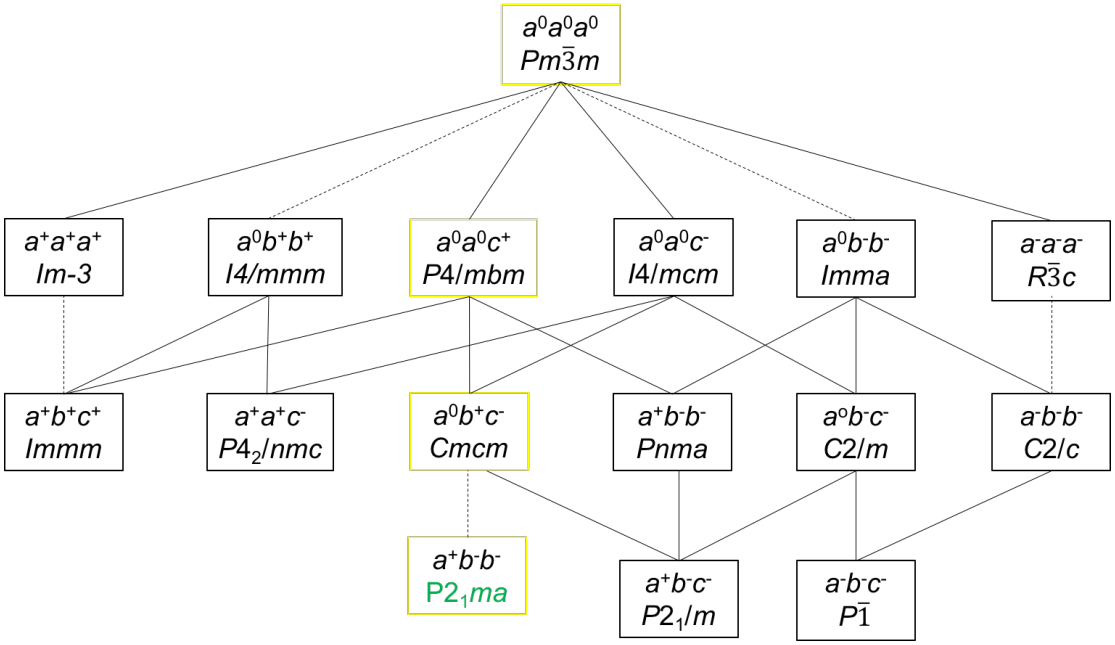

Figure 4.31 Schematic showing group-subgroup relations as reported by Howard and Stokes[23]. The ferroelectric $P2_1ma$ phase has been included as the original paper relates centrosymmetric groups arising from R_4^+ and M_3^+ tilts only. Dashed lines represent transitions that are forbidden by Landau theory to be continuous. Solid lines represent pathways that can proceed via one continuous mechanism. The general pathway observed for each of the compositions of LNN described in this chapter is highlighted in yellow. As discussed the transition from $P2_1ma$ to $Cmcm$ proceeds via the S-like phases.

4.3 Conclusions and Further Work

The temperature dependent phase diagrams are elucidated for compositions of $Li_xNa_{1-x}NbO_3$ where x = 0.03, 0.08 and 0.12 with the use of neutron powder diffraction, symmetry mode analysis and dielectric measurements. Interestingly, both Phase S and R of $NaNbO_3$ are absent at a doping level of as little as 3 % Li. LNN-12 has been shown to adopt an 'S-like' phase at 350 °C, (phase S'). This is in contrast to previous reports that suggested a phase with *Cmcm* phase was adopted at this temperature[24]. Whilst similar in nature to phase S of $NaNbO_3$, the distinction is found in the relative orientations of the various tilt modes, with M_3^+, R_4^+ and T_4 each acting around an independent axis in phase S'. The subtle nature of assigning specific tilts to a specific axis or axes highlights the power, but also the limitations, of neutron powder diffraction techniques when definitive structure determination is required. Whilst previous dielectric studies on the LNN-12 system presented conflicting results, the dielectric data described within this study corroborated the results obtained from the crystallographic analysis. PND data analysis on LNN-3, whilst inconclusive, suggests a long-range tilt system (phase S''') arising from instability of the T_4 mode at $T \sim 350$ °C. Similarly, in LNN-8, phase S'' is identified for the temperature region $350 \leq T \leq 600$ °C. The extended superlattices of phase S'' and S''' are of interest as they too appear to adopt unique tilt systems relative to phases S and R of $NaNbO_3$. Therefore, further work to clarify the exact symmetries of these phases is merited. Observations of the raw PND data and subsequent analysis with the use of ISODISTORT, indicate that the T_4 mode condenses along the T-line from ($\boldsymbol{k} = \frac{1}{2}, \frac{1}{2}, \frac{1}{3}$) to ($\boldsymbol{k} = \frac{1}{2}, \frac{1}{2}, \frac{1}{4}$) as a function of x in the range $0 \leq x \leq 0.12$. Rietveld refinement methods also suggest that the three tilt modes show an increasing selectivity toward acting about individual axes (as opposed to adopting compound tilts) as a function of x. From the crystallographic data it can be concluded that the relative stability of the long-range tilt systems increases as a function of Li content, with phase S''' in LNN-3 stable over the

temperature range 350 ≤ T ≤ 500 °C, Phase S'' in LNN-8 stable across 350 ≤ T ≤ 550 °C and finally, phase S' in LNN-12 stable for 350 ≤ T ≤ 600 °C. Given the results presented in this study, it can be concluded that compositions at the lower end of the $Li_xNa_{1-x}NbO_3$ solid solution prove highly susceptible to softening of octahedral tilting modes along the T-line.

Given the marked differences between the three compositions investigated, it is highly possible that more novel long-range tilt systems are as yet undiscovered within the composition range 0.02 ≤ x ≤ 0.19. The higher temperature behaviour for each system was consistent, mimicking that of pure $NaNbO_3$, proceeding from the 'S-like' phases through the sequence T1-T2-U.

4.4 References

1. Panda, P. K.; Sahoo, B., PZT to Lead Free Piezo Ceramics: A Review. *Ferroelectrics* **2015,** *474*, 128-143.
2. Panda, P. K., Review: environmental friendly lead-free piezoelectric materials. *Journal of Materials Science* **2009,** *44*, 5049-5062.
3. Jaffe, B.; Cook, W. R.; Jaffe, H. L., *Piezoelectric ceramics*. Academic Press: 1971.
4. Berlincourt, D., Piezoelectric Crystals and Ceramics. In *Ultrasonic Transducer Materials*, Mattiat, O. E., Ed. Springer US: Boston, MA, 1971; pp 63-124.
5. Muralt, P., Ferroelectric thin films for micro-sensors and actuators: a review. *Journal of Micromechanics and Microengineering* **2000,** *10*, 136-146.
6. Randall, C. A.; Kim, N.; Kucera, J. P.; Cao, W. W.; Shrout, T. R., Intrinsic and extrinsic size effects in fine-grained morphotropic-phase-boundary lead zirconate titanate ceramics. *Journal of the American Ceramic Society* **1998,** *81*, 677-688.
7. Saito, Y.; Takao, H.; Tani, T.; Nonoyama, T.; Takatori, K.; Homma, T.; Nagaya, T.; Nakamura, M., Lead-free piezoceramics. *Nature* **2004,** *432*, 84-87.
8. Cross, E., Materials science - Lead-free at last. *Nature* **2004,** *432*, 24-25.
9. Yuzyuk, Y. I.; Gagarina, E.; Simon, P.; Reznitchenko, L. A.; Hennet, L.; Thiaudiere, D., Synchrotron x-ray diffraction and Raman scattering investigations of $(Li_xNa_{1-x})NbO_3$ solid solutions: Evidence of the rhombohedral phase. *Physical Review B* **2004,** *69*, 144105.
10. Megaw, H. D., The seven phases of sodium niobate. *Ferroelectrics* **1974,** *7*, 87-89.
11. Peel, M. D.; Ashbrook, S. E.; Lightfoot, P., Unusual Phase Behavior in the Piezoelectric Perovskite System, $Li_xNa_{1-x}NbO_3$. *Inorganic Chemistry* **2013,** *52*, 8872-8880.
12. Baker, D. W.; Thomas, P. A.; Zhang, N.; Glazer, A. M., A comprehensive study of the phase diagram of $K_xNa_{1-x}NbO_3$. *Applied Physics Letters* **2009,** *95*.
13. Hsu, R.; Maslen, E. N.; du Boulay, D.; Ishizawa, N., Synchrotron X-ray studies of $LiNbO_3$ and $LiTaO_3$. *Acta Crystallographica Section B* **1997,** *53*, 420-428.
14. Henson, R. M.; Zeyfang, R. R.; Kiehl, K. V., Dielectric and Electromechanical Properties of (Li, Na)NbO_3 Ceramics. *Journal of the American Ceramic Society* **1977,** *60*, 15-17.
15. Eitel, R. E.; Randall, C. A.; Shrout, T. R.; Rehrig, P. W.; Hackenberger, W.; Park, S. E., New high temperature morphotropic phase boundary piezoelectrics based on $Bi(Me)O_3$-$PbTiO_3$ ceramics. *Japanese Journal of Applied Physics* **2001,** *40*, 5999-6002.
16. Shrout, T. R.; Zhang, S. J., Lead-free piezoelectric ceramics: Alternatives for PZT? *Journal of Electroceramics* **2007,** *19*, 113-126.
17. Chaker, C.; El Gharbi, W.; Abdelmoula, N.; Simon, A.; Khemakhem, H.; Maglione, M., $Na_{1-x}Li_xNbO_3$ ceramics studied by X-ray diffraction, dielectric,

pyroelectric, piezoelectric and Raman spectroscopy. *Journal of Physics and Chemistry of Solids* **2011,** *72*, 1140-1146.
18. Larson, A. C.; Von Dreele, R. B., Los Alamos Natl. Lab: 1994.
19. Toby, B. H., EXPGUI, a graphical user interface for GSAS. *Journal of Applied Crystallography* **2001,** *34*, 210-213.
20. Campbell, B. J.; Stokes, H. T.; Tanner, D. E.; Hatch, D. M., ISODISPLACE: a web-based tool for exploring structural distortions. *Journal of Applied Crystallography* **2006,** *39*, 607-614.
21. Peel, M. D.; Thompson, S. P.; Daoud-Aladine, A.; Ashbrook, S. E.; Lightfoot, P., New Twists on the Perovskite Theme: Crystal Structures of the Elusive Phases R and S of $NaNbO_3$. *Inorganic Chemistry* **2012,** *51*, 6876-6889.
22. Sakowski-Cowley, A. C.; Lukaszewicz, K.; Megaw, H. D., Structure of Sodium Niobate at Room Temperature and Problem of Reliability in Pseudosymmetric Structures. *Acta Crystallographica Section B* **1969,** *B 25*, 851-865.
23. Howard, C. J.; Stokes, H. T., Group-theoretical analysis of octahedral tilting in perovskites. *Acta Crystallographica Section B* **1998,** *54*, 782-789.
24. Mishra, S. K.; Krishna, P. S. R.; Shinde, A. B.; Jayakrishnan, V. B.; Mittal, R.; Sastry, P. U.; Chaplot, S. L., High temperature phase stability in $Li_{0.12}Na_{0.88}NbO_3$: A combined powder X-ray and neutron diffraction study. *Journal of Applied Physics* **2015,** *118*, 7.
25. Pardo, L.; Durán-Martin, P.; Mercurio, J. P.; Nibou, L.; Jiminez, B., Temperature behaviour of structural, dielectric and piezoelectric properties of sol-gel processed ceramics of the system $LiNbO_3$-$NaNbO_3$. *Journal of Physics and Chemistry of Solids* **1997,** *58*, 1335-1339.
26. Smiga, W.; Garbarz-Glos, B.; Kus, C.; Suchanicz, J.; Burzynska, M., Electrical properties of $Na_{0.98}Li_{0.02}NbO_3$ under axial pressure in phase transition region. *Ferroelectrics* **2003,** *292*, 145-150.
27. Wang, C. L.; Zhang, P. L.; Zhong, W. L.; Zhao, H. S., Dielectric and Pyroelectric Properties of Lithium Sodium Niobate Ceramics at Low-Temperature. *Journal of Applied Physics* **1991,** *69*, 2522-2524.
28. Lanfredi, S.; Lente, M. H.; Eiras, J. A., Phase transition at low temperature in $NaNbO_3$ ceramic. *Applied Physics Letters* **2002,** *80*, 2731-2733.
29. Mitra, S.; Kulkarni, A. R.; Prakash, O., Diffuse phase transition and electrical properties of lead-free piezoelectric $(Li_xNa_{1-x})NbO_3$ ($0.04 \leq x \leq 0.20$) ceramics near morphotropic phase boundary. *Journal of Applied Physics* **2013,** *114*.
30. Glazer, A., The classification of tilted octahedra in perovskites. *Acta Crystallographica Section B* **1972,** *28*, 3384-3392.
31. Howard, C. J.; Withers, R. L.; Knight, K. S.; Zhang, Z., $(Ca_{0.37}Sr_{0.63})TiO_3$ perovskite - an example of an unusual class of tilted perovskites. *Journal of Physics-Condensed Matter* **2008,** *20,* 135202.
32. Garcia-Martin, S.; King, G.; Urones-Garrote, E.; Nenert, G.; Woodward, P. M., Spontaneous Superlattice Formation in the Doubly Ordered Perovskite KLaMnWO6. *Chemistry of Materials* **2011,** *23*, 163-170.

33. Ishikawa, H.; Munao, I.; Bode, B. E.; Hiroi, Z.; Lightfoot, P., $Na_2MoO_{2-\delta}F_{4+\delta}$ - a perovskite with a unique combination of atomic orderings and octahedral tilts. *Chemical Communications* **2015,** *51*, 15469-15471.
34. Mishra, S. K.; Mittal, R.; Pomjakushin, V. Y.; Chaplot, S. L., Phase stability and structural temperature dependence in sodium niobate: A high-resolution powder neutron diffraction study. *Physical Review B* **2011,** *83*, 134105.
35. Chen, J.; Feng, D., TEM Study of Phases and Domains in $NaNbO_3$ at Room-Temperature. *Physica Status Solidi. A, Applications and Materials Science* **1988,** *109*, 171-185.

5 Unprecedented Phase Progression in $Li_{0.20}Na_{0.80}NbO_3$

5.1 Introduction

In addition to the x = 0.03, 0.08 and 0.12 compositions detailed in Chapter 4, the thermal evolution of one further member in the $Li_xNa_{1-x}NbO_3$ series at a value of x = 0.20 (LNN-20) is investigated for the temperature regime $20 \leq T \leq 900$ °C *via* PND techniques, relative permittivity measurements and symmetry mode analysis. Previous work regarding the crystalline phase of LNN-20 at room temperature has been the source of some confusion, with contradictory reports in the literature. Separate publications by both Chaker[1] and Tse[2] report a co-existence of two distinct phases at room temperature for compositions of $x \geq 0.20$. No explanation is offered regarding the nature of these phases in the publication by Tse, however, Chaker assigns the two phases with orthorhombic and rhombohedral symmetry upon analysis of the room temperature XRD pattern. A subsequent PND study by Peel *et al*.[3] confirmed that this is in fact a phase co-existence of two isostructural phases with rhombohedral symmetry, one Na-rich (Na-*R*3*c*) and one Li-rich (Li-*R*3*c*). These two ferroelectric rhombohedral phases are present over the wide composition range of $0.20 \leq x \leq 0.96$. Relative phase fractions have a linear dependency as a function of Li content, with the relative quantity of Li in both structures constant (22 % Li in Na-*R*3*c* and 96 % Li in Li-*R*3*c*). As the reported T_C of pure $LiNbO_3$ is ~ 1195 °C[4, 5], the Li-*R*3*c* phase is stable within the temperature remit of this study. Structural characterisation therefore focuses on the evolution of the Na-*R*3*c* phase. Given the susceptibility of the x = 0.03, 0.08 and 0.12 compositions to softening of the T_4 mode it is of interest to ascertain if such instabilities are still energetically favoured at a composition of x = 0.20, or if indeed the higher doping

level gives way to new distortion types and lattice instabilities. Whilst both the Na-*R*3*c* and Li-*R*3*c* phases are ferroelectric, this does not result in a heightened dielectric response similar to that observed in LNN-12 as the thermal stability of the Li-*R*3*c* phase is much greater than that of Na-*R*3*c* (i.e no MPB is present).

5.2 Experimental

5.2.1 Synthesis

A phase pure sample weighing ~ 5 g of LNN-20 was synthesised *via* traditional ceramic methods. Stoichiometric amounts of Li_2CO_3 (99.9 % Sigma-Aldrich), Na_2CO_3 (99.9 % Sigma-Aldrich) and Nb_2O_5 (99.9 % Alfa Aesar) were ground for a period of up to 30 minutes using a pestle and mortar. The loose powder was then pressed under 5 tonnes of pressure using a pellet press, before being transferred to an alumina crucible and sintered at 1000 °C for a period of 24 hours with a heating and cooling rate of approximately 10 ° min^{-1}. The pellets formed were approximately 10 mm in diameter and 5 mm thick. The annealed pellets were reground after the sintering process was complete so that phase analysis could be carried out. Phase purity was determined using PXRD analysis. Measurements were carried out on a RIGAKU miniflex using a dichromatic copper X-ray source ($CuK\alpha_{1,2}$). Measurements were obtained over a 2θ range of $5 \leq 2\theta \leq 70$ °.

5.2.2 Powder neutron diffraction (PND)

Variable temperature PND experiments within the temperature regime $20 \leq T \leq 900$ °C were carried out using the High Resolution Powder Diffractometer (HRPD)

instrument at the ISIS facility, Harwell laboratory. Data from Banks 1 (2θ = 168.3 °) and 2 (89.6 °) were used in the analysis on this sample, covering a d-spacing range of 0.7 < *d* < 2.6 Å and 0.9 < *d* < 4.0 Å respectively. The sample was held in a cylindrical vanadium can with a diameter of 13 mm. Data collection was carried out over a period of approximately 1 hour per data set with diffraction patterns recorded at 20 °C and then in 50 ° intervals in the temperature range $50 \leq T \leq 900$ °C. Measurements were carried out with the assistance of Dr. Aziz Daoud-Aladine.

Analysis of the PND data was completed using Rietveld refinement techniques in the GSAS software package[6] and EXPGUI interface[7]. Symmetry mode analysis of the refined structures was carried out using the ISODISTORT suite[8]. A self-consistent refinement strategy was employed throughout; this involved refinement of 18 background coefficients, 3 instrument parameters, 2 scale factors (for single-phase refinements, 3 for two phase refinements), and 6 profile parameters. In addition to this, lattice parameters, atomic coordinates (with Na and Li atoms constrained to the same site) and atomic displacement parameters (ADPs) were refined for each data set (again with equivalent Na and Li atoms constrained to be equal, and some additional constraints in specific cases, detailed in the text). Site occupancies of Na and Li were refined at RT to ensure an approximate 0.8:0.2 ratio was accurate. The site occupancies were then fixed at this ratio over the temperature range investigated.

5.2.3 Dielectric measurements

Ag paste was used to coat the pellet and form an electrode. A Wayne Kerr 6500B impedance analyser was used to perform the dielectric measurements with the sample mounted in a tube furnace. Capacitance and loss data were recorded in the frequency range 100 Hz - 10 MHz using a heating and cooling at a rate of 2 K

min^{-1}. Measurements were recorded over the temperature range $40 \leq T \leq 600$ °C. Measurements and interpretation of results were assisted by Jason M^{c} Nulty and Dr. Finlay Morrison.

5.2.4 Second harmonic generation (SHG) experiments

A polycrystalline powder sample of LNN-20 was held within glass cells sufficiently durable to withstand a high temperature study. Calibration of the furnace was performed, followed by null checks. After calibration, the sample was placed in a small furnace with an aperture normal to the orientation of the sample. Through this aperture, an intense beam (100 mJ, 100 ms pulse) from a Q-switched Nd:YAG laser (λ = 1064 nm) following the setup of Kurtz & Perry (1968) was exposed to the sample. The second harmonic signal (if any was present) was measured using a photomultiplier (PMT) and subsequently displayed on an oscilloscope as signal *versus* time. Filtration of the scattered radiation was carried out to remove traces of the fundamental beam with the use of a green filter. A beam splitter and photodiode were used to monitor the fundamental beam. This allowed for the necessary corrections to variations in the laser output. Finally, the intensity of the second harmonic was normalised *via* division by the square of the intensity of the incident beam (Kurtz & Perry, 1968)[9]. Repeat measurements were carried out to remove any residual strain present from the sample preparation and ensure the result was reproducible. Measurements were kindly carried out by Dr. Steven Huband and Professor Pamela A. Thomas at the University of Warwick.

5.3 Results and Discussion

5.3.1 PND data

5.3.1.1 $20 \leq T \leq 100$ °C

The RT (20 °C) PND data can be successfully modelled to the Na-rich rhombohedral phase (Na-R3c) with *R*3*c* symmetry (Glazer tilt system $a^-a^-a^{-10}$), in agreement with previous work on the $Li_xNa_{1-x}NbO_3$ solid solution[3]. This rhombohedral phase is isostructural with the low temperature ferroelectric phase of pure $NaNbO_3$[11] or alternatively, can be considered as a variant of the stable ambient phase of $LiNbO_3$[12]. Analysis of the room temperature data with Rietveld refinement allowed for an excellent structural model of this phase to be obtained (detailed in Table 5.1), however the presence of additional peaks in the data that cannot be indexed in the Na-*R*3*c* model indicate a small secondary phase is formed at the synthesis stage. This is due to a second rhombohedral phase closer to $LiNbO_3$ in composition (Li-R3c). A two-phase refinement of the room temperature data is not detailed here as the isostructural nature of the two rhombohedral phases results in severe overlapping of several peaks making quantifiable information with regard to phase fractions unreliable. A graphical representation of the fit to a phase with Na-*R*3*c* symmetry at 20 °C is shown in Figure 5.1.

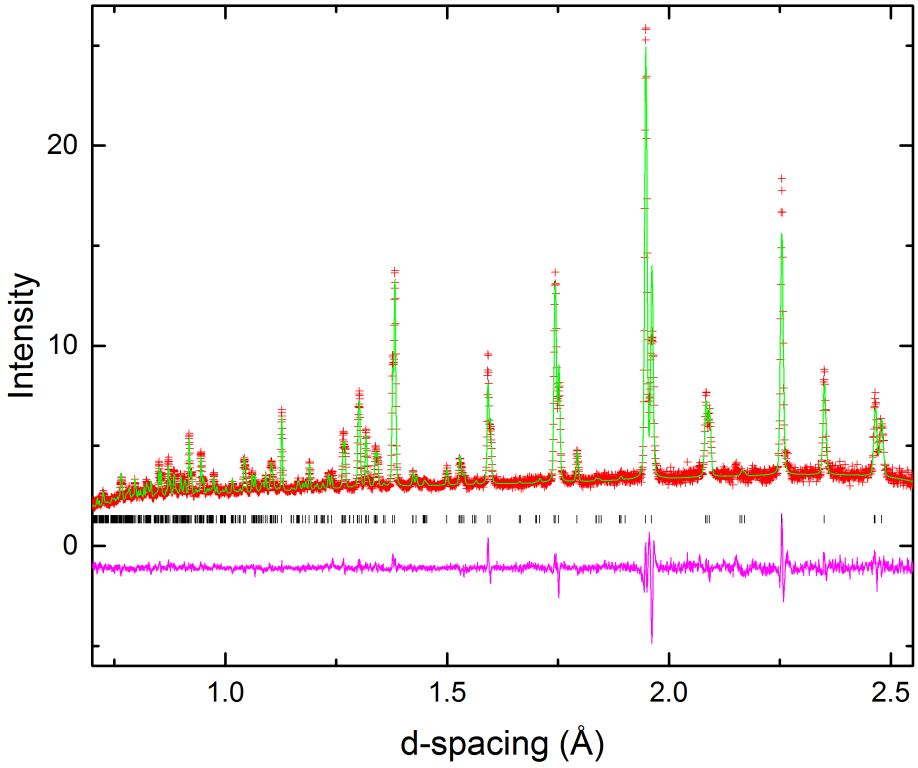

Figure 5.1 Portion of Rietveld refinement on PND data obtained from a sample of LNN-20 modelled in the Na-*R*3*c* phase at 20 °C; χ^2 = 3.88, R_{wp} = 0.0428.

Table 5.1 Crystallographic data for LNN-20 at 20 °C modelled in the Na-*R*3*c* space group; *a* = 5.45751(13) Å, *c* = 13.7442(4) Å.

Atom	Wyckoff position	*x*	*y*	*z*	100 * U_{iso} (Å^2)
Na*	6a	0	0	0.2646(3)	0.165(5)
Nb	6a	0	0	0.010337	-0.23(2)
O	18b	0.09889(15)	0.3391(3)	0.07740(9)	0.56(19)

*position Na has fixed occupancy $Na_{0.8}Li_{0.2}$.

5.3.1.2 150 °C ≤ *T* ≤ 600 °C

The Na-*R*3*c* phase persists to a temperature of 150 °C, at which point additional peaks begin to emerge in the raw data. Initially quite small, these emergent peaks can be seen to "grow in" significantly between 150 °C and 200 °C. This new phase is fully established at 300 °C suggesting a 1st order discontinuous phase transition has taken place (phase fractions ~ 74/26 %, 20/80% and 7/93%, for the rhombohedral and the emergent phase respectively). The diffraction peaks attributable to this new phase are present at d-spacings of ~ 2.07 and 2.09 Å, along with two at a slightly higher d-spacing of ~ 2.46 and 2.48 Å (see Figure 5.2). The positioning of these peaks in relation to the reciprocal cubic lattice indicates they are coincidental with condensation of the M_3^+ tilt mode. It can therefore be concluded that this new phase must possess an in-phase tilt along at least one of the three unique crystallographic axes. The out-of-phase tilt present in the Na-*R*3*c* phase is preserved, therefore Glazer tilt systems with simultaneous in-phase and out-of-phase tilts must necessarily be considered as potential fits to the data. The work by Howard and Stokes which establishes the group-subgroup relationships between the 15 distinct tilt systems deriving from the cubic parent, P$m\bar{3}m$, through combinations of M_3^+ and R_4^+ octahedral tilting modes[13], is used as a guide when attempting to assign the space group symmetry of this emergent phase. Of the 15 unique tilt systems only four possess both an in-phase and out-of-phase tilt thus meeting the criteria required; $a^+b^-c^-$ (*P*2$_1$/*m*), $a^+a^+c^-$ (*P*4$_2$/*nmc*), $a^0b^+c^-$ (*Cmcm*) and $a^+b^-b^-$ (*Pnma*). The first of these ($a^+b^-c^-$) is discarded from the outset as it is of unnecessarily low symmetry. The three remaining models are trialled as fits to the data at 300 °C. Refinement of the data in the P*nma* ($a^+b^-b^-$) spacegroup reveals it is unable to model the peak splittings adequately. The C*mcm* model gives a better fit to the data (χ^2 = 6.70), however, interestingly, the tetragonal model (*P*4$_2$/*nmc*), corresponding to the rarely seen $a^+a^+c^-$ Glazer tilt system, provides the most satisfactory fit both statistically and graphically (χ^2 = 4.55). Both the *Cmcm* and

$P4_2/nmc$ models have the same number of refinable atomic parameters (atomic coordinates plus isotropic thermal displacement parameters) allowing for a fair comparison to be made. Further confirmation of the suitability of the $P4_2$/nmc model over C*mcm* can be found in the U_{iso} values obtained for the oxygen sites in both, 0.0152(7), 0.0136(7), 0.0179(4) $Å^2$ for $P4_2$/nmc and 0.0137(6), -0.0028(6), 0.0348(10) for *Cmcm*. Fits to the data at 100 °C and 300 °C in the Na-*R*3*c* phase and $P4_2/nmc$ models respectively are shown in Figure 5.2. The centrosymmetric tetragonal phase was originally carried forward in the temperature region 300 ≤ *T* < 600 °C, however a distinct and sudden merging of several peaks in the diffraction data between 450 °C and 500 °C in addition to a spike in the permittivity data in the corresponding temperature region (see section 5.3.2) suggest a further structural transition takes place.

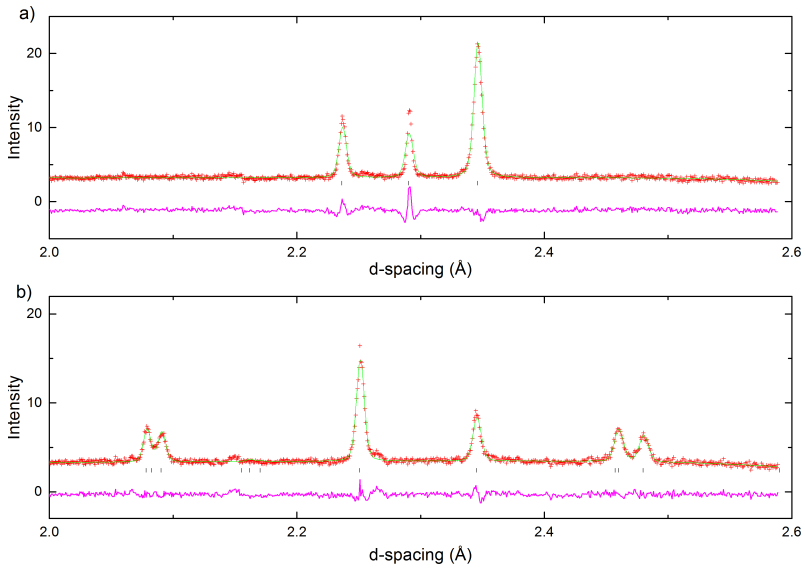

Figure 5.2 Portions of Rietveld refinement carried out on PND data at a) 100 °C in the Na-*R*3*c* setting (χ^2 = 3.866, R_{wp} = 0.0427) and b) 300 °C in the $P4_2/nmc$ setting (χ^2 = 3.513, R_{wp} = 0.0414). In (a) the peaks in the region 2.2 – 2.3 Å arise from the subcell; the peak near 2.35 Å in both (a) and (b) is due to the R_4^+ tilt mode. The additional peaks near *d* = 2.09 and 2.48 Å) in (b) are due to M_3^+ tilt mode. The small peak at a d-spacing of ~ 2.14 Å is from the vanadium sample holder and the "shoulder" near *d* = 2.27 Å is due to the minority Li-*R*3*c* phase.

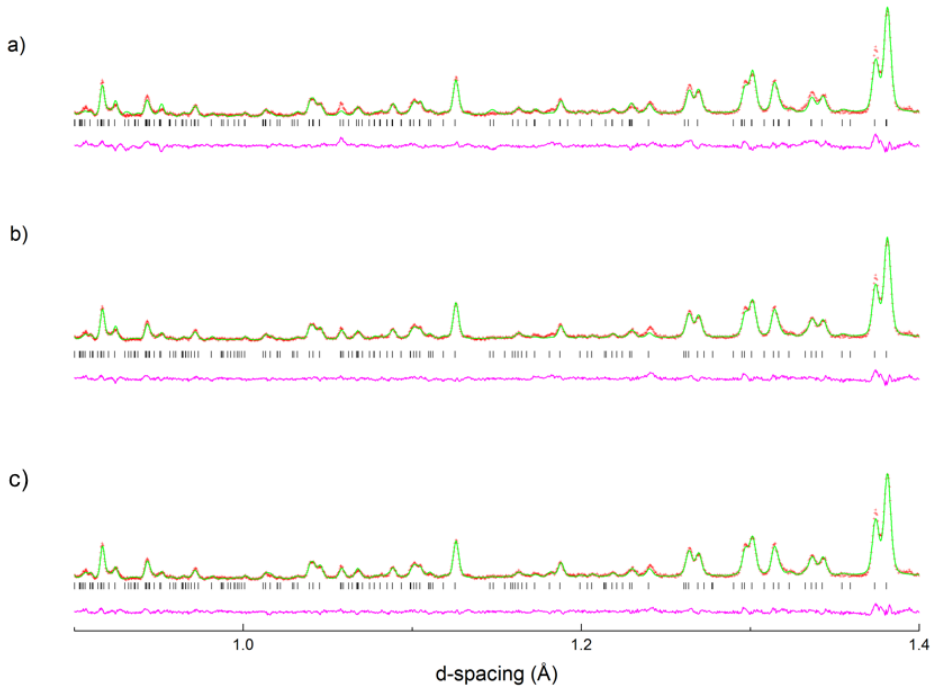

Figure 5.3 Portion of Rietveld refinement on LNN-20 system at 300 °C modelled in a) *Cmcm* b) $P4_2/nmc$ and c) $P4_2mc$ space groups.

In light of the evidence of a further structural change in the temperature region $450 < T < 500$ °C, both the *Pnma* and *Cmcm* models are trialled again as fits to the diffraction data at 500 °C, however neither offer an improvement to the fit when compared to the original $P4_2/nmc$ model (χ^2 value for $P4_2/nmc$ = 3.18, *Pnma* = 4.05 and *Cmcm* = 4.44) and are therefore discarded. As the $P4_2/nmc$ model still offers the best fit to the data at 500 °C (however it should be noted that thermal parameters for sodium and lithium sites had to be constrained as equal to allow a stable refinement), the lower symmetry phase at $300 \leq T \leq 450$ °C is most likely an isomorphic subgroup of the parent $P4_2/nmc$ phase. Such a direct relationship also accounts for the 2nd order nature of the phase transition as indicated by the PND data. Four possible models with differing space group symmetries derive from the parent $P4_2/nmc$ phase therefore these were trialled as fits to the data at 300 °C. Of these potential models the $P4_2mc$ space group gave the most

satisfactory fit to the data. *P4$_2$mc* is the only polar subgroup, the three others being non-centrosymmetric but also non-polar. The outcomes of the various fits trialled to the data at 300 °C is included in Table 5.2. The graphical outputs of the fits to *Cmcm*, *P*4$_2$/*nmc* and *P*4$_2$*mc* are shown in Figure 5.3. Note the biggest improvement that can be seen graphically between the centrosymmetric and polar models is fitting of the (206) subcell peak at a d-spacing of ~ 1.24 Å.

Table 5.2 Comparison of the respective Rietveld refinements for the two viable centrosymmetric models according to PND data at 300 °C, in addition to non-centrosymmetric subgroups of *P*4$_2$/*nmc.* N_{ref} denotes the total number of variable parameters refined, N_{xyz} describes the number of fractional atomic coordinates refined in each setting and N_{Uiso} indicates the number of isotropic ADPs refined. Fixed occupancies at the A-site are set at 80:20 Na:Li, with ADPs constrained to be equal for the Na and Li sites. For the non-centrosymmetric models, O atom ADPs were constrained in pairs according to the splitting patterns from the parent phase where appropriate.

Space group	χ^2	N_{ref}	N_{xyz}	N_{Uiso}
*P*4$_2$*mc*	3.513	55	17	7
P$\bar{4}$*m*2	4.263	55	17	7
*P*4$_2$2$_1$2	4.428	50	12	7
P$\bar{4}$2$_1$*c*	4.582	51	13	7
*P*4$_2$/*nmc*	4.553	44	7	7
Cmcm	6.692	44	7	7

The refinement strategy for the *P*4$_2$*mc* phase over the temperature region 250 < *T* < 500 °C includes refinement of 18 background coefficients, 1 scale factor, 3

instrument parameters, 3 unit cell dimensions, 6 profile parameters, 17 atomic coordinates and 7 thermal parameters. Atomic coordinates are constrained so that equivalent sodium and lithium sites are equal, with thermal parameters for Na and Li constrained similarly. Transformation to the polar subgroup from centrosymmetric $P4_2/nmc$ involves splitting of two of the oxygen atom sites and one sodium site, thus in the $P4_2mc$ setting thermal parameters for oxygen atoms 1,4 and 2,3 are constrained to be equal in addition to those of the Na/Li1 and Na/Li2 sites, in order to achieve both a reliable and stable refinement. A structural model obtained for LNN-20 at 300 °C, refined in the $P4_2mc$ space group is given in Table 5.3. The finalised refinements of the PND data collected over $150 \leq T \leq 500$ °C determine a phase co-existence of R3*c* and $P4_2mc$ over the temperature regime $150 \leq T \leq 250$ °C, single-phase $P4_2mc$ in the temperature region $300 \leq T \leq 450$ °C and centrosymmetric $P4_2/nmc$ at 500 °C. It should be noted that a fit to a $P4_2mc$ model at 500 °C offers a slight improvement statistically (χ^2 = 3.02 in $P4_2mc$ as opposed to 3.18 in $P4_2/nmc$), however, this is most likely a consequence of the increased degree of freedom allowed for in a lower symmetry space group as opposed to any meaningful result. The fit to the centrosymmetric variant of the $a^+a^+c^-$ tilt system at 500 °C is shown in Figure 5.4. A structural model for this phase is given in Table 5.4.

Table 5.3 Crystallographic data for LNN-20 at 300 °C modelled in the $P4_2mc$ space group; a = 7.7706(2), c = 7.8498(3) Å.

Atom	Wyckoff position	x	y	z	100 * U_{iso} (Å^2)
Na1*	2c	0	0.5	0.726(3)	4.1(3)
Na2	2c	0	0.5	0.258(6)	4.1(3)
Na3	2b	0.5	0.5	0.253(3)	0.2(4)
Na4	2a	0	0	0.236(2)	-0.7(3)
Nb	8f	0.2489(5)	0.7493(5)	0	0.48(2)
O1	4e	0.2281(8)	0.5	0.4843(7)	1.39(9)
O2	4e	0.2781(8)	0.5	0.0552(7)	0.75(7)
O3	4d	0.2864(8)	0	0.5538(8)	0.75(7)
O4	4d	0.2115(8)	0	0.0026(6)	1.39(9)
O5	8f	0.2858(10)	0.7874(11)	0.2655(4)	1.52(4)

*positions Na1 – Na4 have fixed occupancy $Na_{0.8}Li_{0.2}$; The U_{iso} values obtained for the A-site cations, particularly the small negative value attributed to Na4 could indicate the possibility of Na:Li ordering.

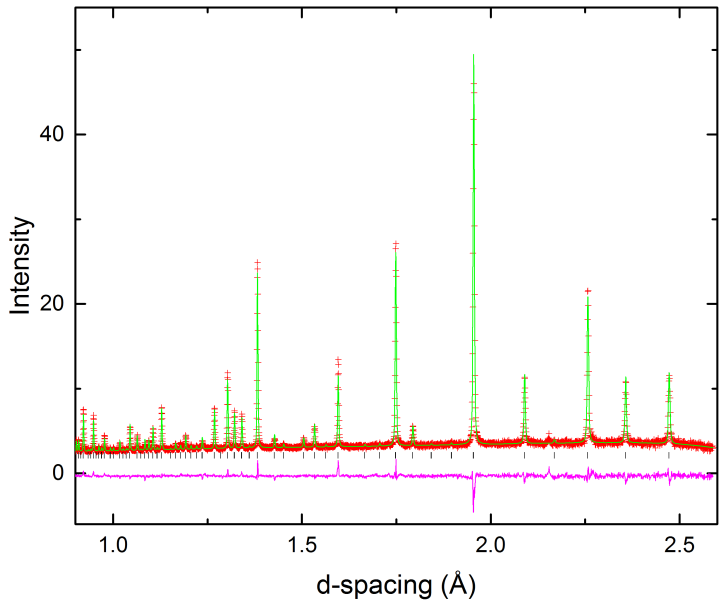

Figure 5.4 Portion of Rietveld refinement on PND data of LNN-20 at 500 °C to $P4_2/nmc$ space group; $\chi^2 = 3.18$, $R_{wp} = 0.0394$.

Table 5.4 Crystallographic data for LNN-20 at 500 °C modelled in the $P4_2/nmc$ space group; $a = 7.8163(16)$, $c = 7.8182(2)$ Å

Atom	Wyckoff position	*x*	*y*	*z*	100 * U_{iso} (Å^2)
Na1*	4d	0.25	0.25	0.7404(13)	2.68(5)
Na2	2b	0.75	0.25	0.25	2.68(5)
Na3	2a	0.75	0.25	0.75	2.68(5)
Nb	8e	0	0	0	0.703(18)
O1	8g	0.25	-0.0332(5)	0.0328(3)	1.87(8)
O2	8g	0.25	0.0308(5)	0.4777(4)	1.72(7)
O3	8f	-0.0329(3)	0.0329(3)	0.25	1.90(5)

*positions Na1 – Na3 have fixed occupancy $Na_{0.8}Li_{0.2}$

5.3.1.3 650 °C ≤ *T* ≤ 900 °C

The centrosymmetric aristotype of the $a^+a^+c^-$ tilt system, $P4_2/nmc$, is successfully fitted as the sole phase to the PND data in the temperature range 500 ≤ *T* ≤ 600 °C. Structural changes begin to manifest in the data upon elevation of the temperature to 650 °C, with an increased asymmetry developing in several peaks. These shoulders are seen to "grow in" over the temperature range 650 ≤ *T* ≤ 750 °C, at which point the peak corresponding to the R_4^+ out-of-phase tilt mode is lost completely, indicative of a 1st order discontinuous phase transition. With reference to the group-subgroup relationships established by Howard and Stokes[13], there are two space groups comprising solely of an in-phase tilt that could occur *via* a discontinuous phase transition, cubic $Im\bar{3}$ ($a^+a^+a^+$) and tetragonal $P4/mbm$ ($a^0a^0c^+$). The third option, tetragonal $I4/mmm$ ($a^0b^+b^+$) should, according to Landau theory, proceed as a continuous transition. Therefore, $I4/mmm$ symmetry is considered the least likely of the three viable models given the changes observed in the PND data. For completeness, a model with $I4/mmm$ symmetry is fitted to the data at 800 °C, however the fit is statistically poor with unreliable values for the reported ADPs (χ^2 = 12.71, negative U_{iso} values for sodium and lithium sites, and isotropic ADPs unable to be refined freely for the A-site cations). With consideration to the two models that are permitted to evolve *via* a discontinuous mechanism from $P4_2/nmc$, the model with $Im\bar{3}$ symmetry proves to be an unsatisfactory model for the data at 800 °C (χ^2 = 8.04) and furthermore, is unstable to anisotropic refinement of the thermal parameters. The final model (space group $P4/mbm$; Glazer tilt system $a^0a^0c^+$) gives the most satisfactory fit to the data at 800 °C (χ^2 = 3.29, Figure 5.6) and allows for anisotropic refinement of the thermal parameters, providing convincing evidence for a 1st order phase transition from $P4_2/nmc$ ($a^+a^+c^-$) to $P4/mbm$ ($a^0a^0c^+$). A phase with $P4/mbm$ symmetry is successfully modelled as part of a two-phase refinement with $P4_2/nmc$ over the temperature range 650 ≤ *T* ≤ 750 °C (relative phase fractions for

$P4_2/nmc$: $P4/mbm$ are 89:11 %, 77:33 % and 55:45% respectively). The fit to the two phase model at 750 °C is included in Figure 5.5.

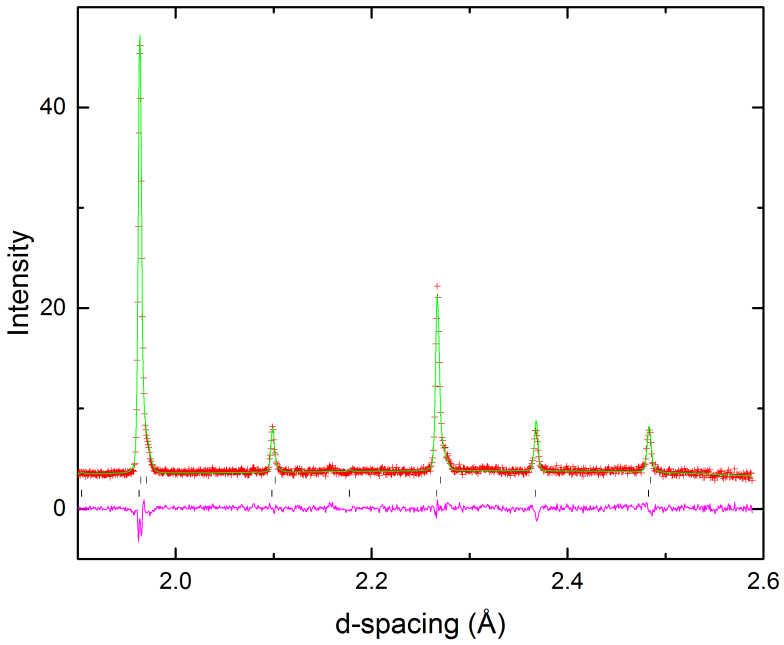

Figure 5.5 Portion of Rietveld fit to PND data measured at 750 °C modelled as a phase coexistence of $P4_2/nmc$ and $P4/mbm$ tetragonal phases; χ^2 = 4.64, R_{wp} = 0.0476. The top set of Bragg peaks represent the $P4/mbm$ phase, whilst the bottom set of Bragg peaks are associated with the phase with $P4_2/nmc$ symmetry.

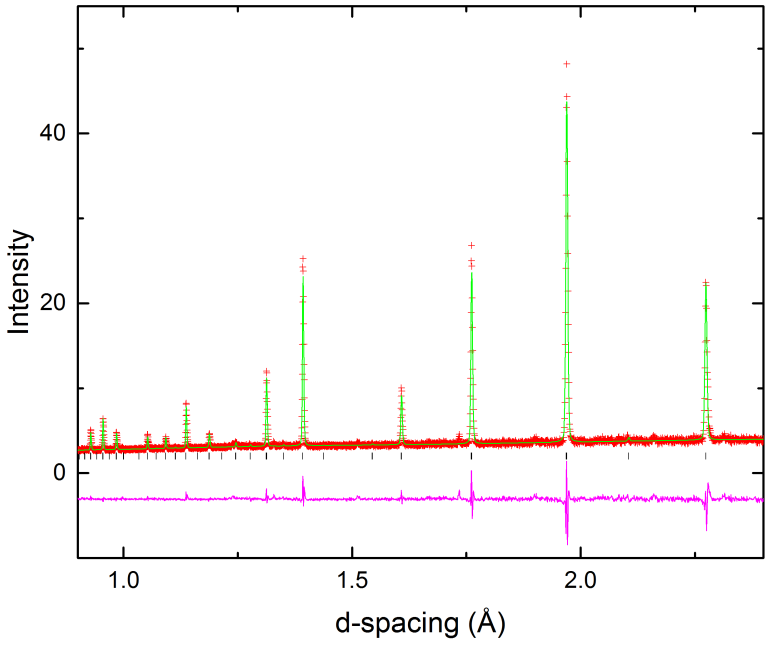

Figure 5.6 Portion of Rietveld fit to PND data at 800 °C modelled in the tetragonal *P*4/*mbm* space group; χ^2 = 3.30, R_{wp} = 0.0402.

At a temperature of 850 °C, the M-point peaks arising from the tetragonal cell are no longer visible in the raw PND data, signalling a structure with cubic, $Pm\bar{3}m$ symmetry is adopted at this temperature. Refinement of the data in the cubic model at 900 °C gives a χ^2 value of 2.90. Additional peaks, attributable to the Li-*R*3*c* phase formed at the synthesis stage are clearly visible in the data at 900 °C. The loss of complicating factors, such as the high degree of peak overlap experienced at RT, enables refinement using a phase co-existence model of $Pm\bar{3}m$ and Li-*R*3*c* phases at this temperature. This phase co-existence model (Figure 5.7) offers a significant improvement to the χ^2 value (χ^2 = 1.52), quantifying the percentage of the Li-*R*3*c* present with respect to the bulk as ~ 3%. It can be assumed this is constant throughout the temperature range studied. Lattice

parameters obtained upon Rietveld refinement for the Li-*R*3*c* phase at 900 °C are a = 5.2536(2), c = 13.8746(11) Å.

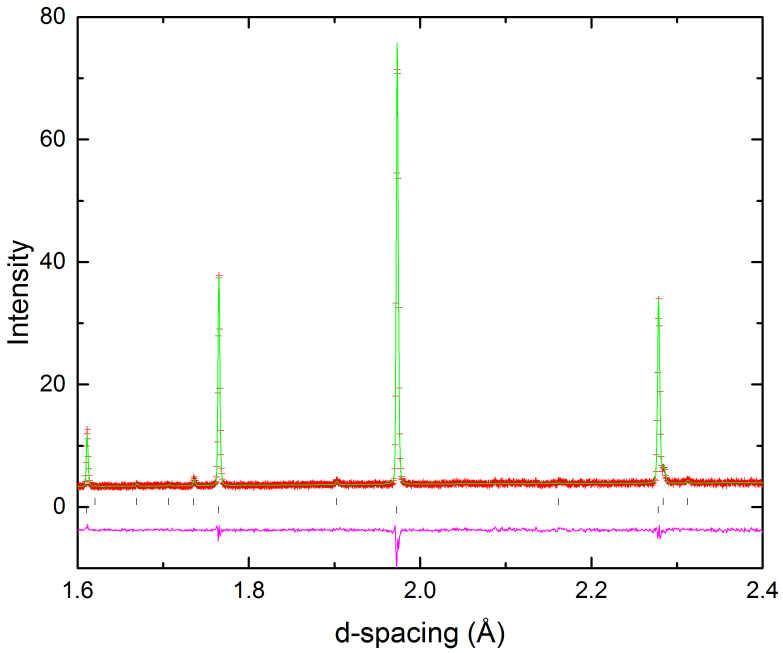

Figure 5.7 Portion of Rietveld fit to PND data at 900 °C for LNN-20; χ^2 = 1.52, R_{wp} = 0.0269. The two-phase refinement gives phase fractions of 97%:3% for the cubic and Li-*R*3*c* phases respectively. The first set of Bragg peaks indicate peaks attributable to the Li-*R*3*c* phase, with the second set of Bragg peaks indicating the main cubic phase, $Pm\bar{3}m$.

5.3.2 Relative permittivity measurements

Relative permittivity measurements obtained on a sample of LNN-20 were collected over the temperature range $40 \leq T \leq 550$ °C (shown in Figure 5.8). From the data, two dielectric events are clearly present. The first centred at $T \sim 315$ °C

can be attributed to the Na-*R*3*c* - $P4_2mc$ transition. This is slightly higher than the interpretation of the crystallographic data which identifies the transition in the range 250 < *T* < 300 °C. However, a two-phase refinement at 300 °C suggests that the rhombohedral phase does remain (albeit as only 1 % with respect to the bulk), therefore for simplicity $P4_2mc$ is treated as the sole phase at 300 °C. The second notable dielectric event is visible just above 450 °C and is pursuant to the $P4_2mc$ – $P4_2/nmc$ phase transition, in agreement with the deductions obtained from the PND data. Dielectric permittivity measurements on a sample of LNN-20 have been reported previously in a publication by Mitra[14]. In agreement with those presented in this study, Mitra observes a clear dielectric event at *T* ~ 450 °C. In addition to this, a very broad peak can be observed just above 200 °C, which whilst not in agreement with the permittivity measurements shown in Figure 5.8, coincides with the temperature at which $P4_2mc$ becomes the majority phase according to the PND data presented here.

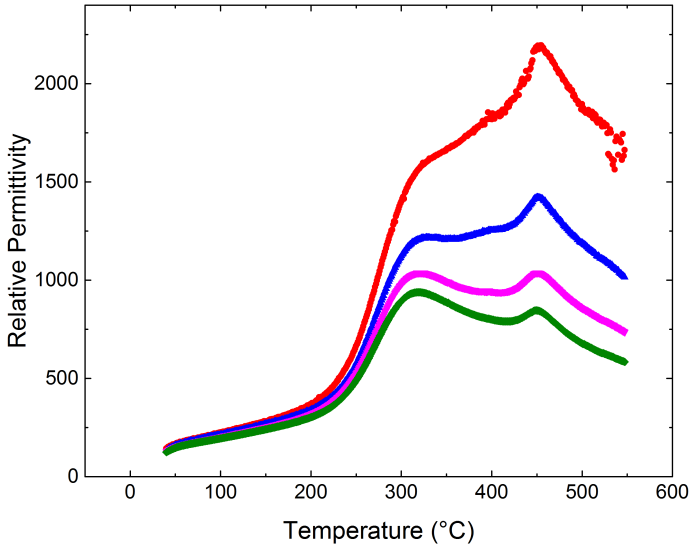

Figure 5.8 Relative permittivity data for LNN-20 at selected frequencies, obtained on cooling. Data collected at a frequency of 1 kHz is shown in red, 10 kHz data (blue), 100 kHz data (pink) and lastly 1 MHz data (green).

5.3.3 Second harmonic generation (SHG)

A non-zero SHG response can be seen in the temperature range $20 \leq T \leq 450$ °C signifying the presence of a polar (or at least non-centrosymmetric) phase in this temperature region. The presence of this SHG signal adds further evidence, in addition to the PND data, on the nature of the phase adopted in the temperature range $300 \leq T \leq 450$ °C. The SHG data also corroborates the transition temperature associated with the $P4_2mc$ – $P4_2/nmc$ transition taken from both PND data and dielectric measurements. Due to the small amount of Li-*R*3*c* phase that exists throughout the temperature regime measured, a non-zero SHG response would be expected at all temperatures owing to the ferroelectric nature of this phase. However, the Li-*R3c* phase is only present in a very small amount (~ 3 %), therefore whilst the small residual signal seen beyond 450 °C can be attributed to this phase, the majority of the signal seen at lower temperatures results from the main perovskite phases Na-*R*3*c* and subsequently $P4_2mc$.

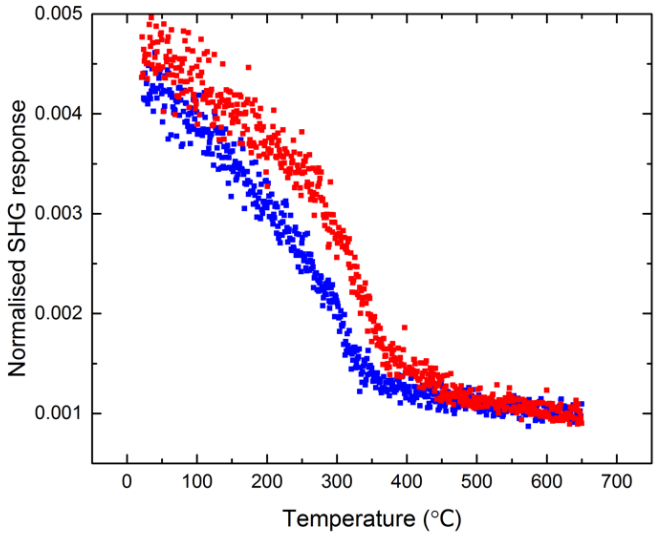

Figure 5.9 SHG data generated from sample of LNN-20 for the temperature regime $20 \leq T \leq 650$ °C. A clear SHG response is observed to at least 450 °C on heating. Data obtained on heating is shown in red, with cooling data shown in blue.

5.3.4 Symmetry mode analysis

5.3.4.1 Na-*R*3*c* phase

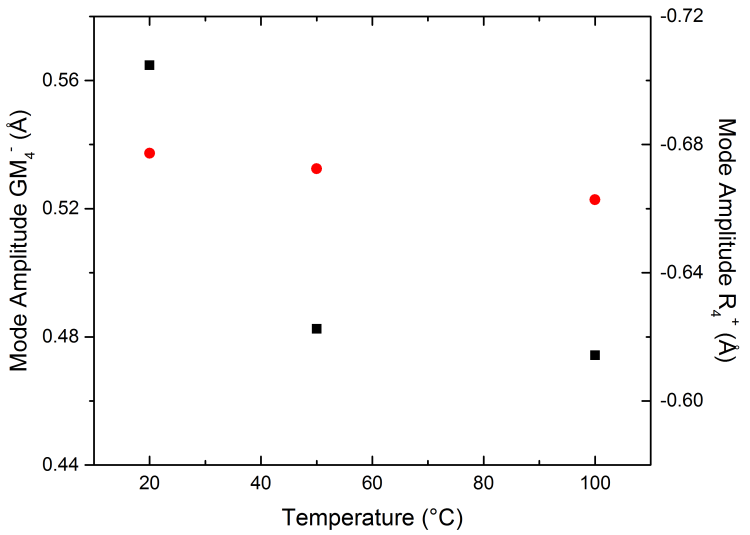

Figure 5.10 Symmetry mode analysis obtained on the Na-*R*3c phase present over the temperature range 20 ≤ *T* ≤ 100 °C. Black squares represent the Γ_4^- mode, red circles depict the R_4^+ tilt mode.

Symmetry mode analysis on the Na-*R*3*c* phase over the temperature range 20 ≤ *T* ≤ 100 °C gives quantitative information on the changing amplitudes of the two most significant structural distortion modes for this phase; the ferroelectric geometric strain (Γ_4^-) and out-of-phase tilt mode (R_4^+) (Figure 5.10). The Γ_4^- mode amplitude corresponds to the ferroelectric distortion and as such directly relates to the polarisation along *c*. The polarisation, whilst decreasing with increasing temperature as is the expected trend, retains a significant amplitude at a temperature of 100 °C. The R_4^+ tilt mode corresponding to the out-of-phase tilt (which acts upon all three crystallographic axes simultaneously in the *R*3*c* setting $a^-a^-a^-$) shows a close to linear decrease over the temperature range for the rhombohedral phase but still retains a significant amplitude at a temperature of

100 °C. This is to be expected as it acts about the [001] direction (*i.e.* around the *c*-axis) in the subsequent $P4_2mc$ phase, prior to which, it is still present in the Na-*R*3*c* phase for the region of phase co-existence at 100 < *T* < 300 °C.

5.3.4.2 $P4_2mc$ phase

Trends in the mode amplitudes for the two principle *irreps.* acting upon the $P4_2mc$ and $P4_2/nmc$ structures are depicted in Figure 5.11. The isomorphic relationship between the polar and centrosymmetric phases makes a continuous appraisal of the mode amplitudes for both valid in this case. Both the R_4^+ and M_3^+ tilt modes show a tendency to increase with decreasing temperature, as is the typical trend exhibited by the perovskite structure type. The evolution of the R_4^+ tilt mode over both tetragonal phases shows a noticeable kink upon transition from the polar to centrosymmetric phase whereas the evolution of the M_3^+ mode is continuous. The R_4^+ tilt is relatively small compared to the M_3^+ mode and adopts a steady decline in the $P4_2/nmc$ structure as the phase transition is approached. As the M_3^+ persists in the higher temperature *P*4/*mbm* phase observed at 800 °C, it is not surprising that this is the dominant mode throughout this temperature region and retains a significant amplitude at 600 °C.

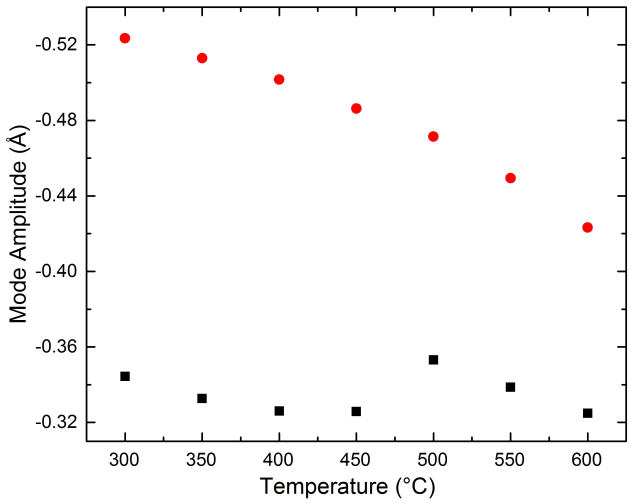

Figure 5.11 Thermal evolution of the two most significant tilt modes (M_3^+ shown as red circles and R_4^+ shown as black squares) throughout the *P*4$_2$*mc* - *P*4$_2$/*nmc* phase region. Note the discontinuous evolution of the R_4^+ mode upon adoption of the centrosymmetric phase.

The ferroelectric distortion mode (Γ_4^-) that persists in the *P*4$_2$*mc* phase is shown in Figure 5.12 over the temperature region 300 ≤ *T* ≤ 450 °C. The mode amplitude undergoes a rapid decline as the transition to the centrosymmetric setting of the $a^+a^+c^-$ tilt system is approached. The initial increase in the Γ_4^- mode, could be an artefact due to the small amount (~ 1 %) of Na-*R*3*c* present at 300 °C, with the polar *P*4$_2$*mc* structure not yet fully established. Alternatively, it was considered whether the errors associated with the mode amplitude could negate this initial increase. The Γ_4^- mode relates to the total displacive motion of all atoms along the polar *c*-axis. By considering the average error on the z parameters obtained from Rietveld refinement, a dummy CIF file in which the atomic positions are displaced along z by the greatest amount of error was uploaded to ISODISTORT in order to compare the resulting mode amplitudes for the Γ_4^- mode. This gave an error

margin of ~ 0.7 % in the mode amplitude at 300 °C, which is not sufficient to compensate for the increase in the Γ_4^- mode observed between 300 and 350 °C.

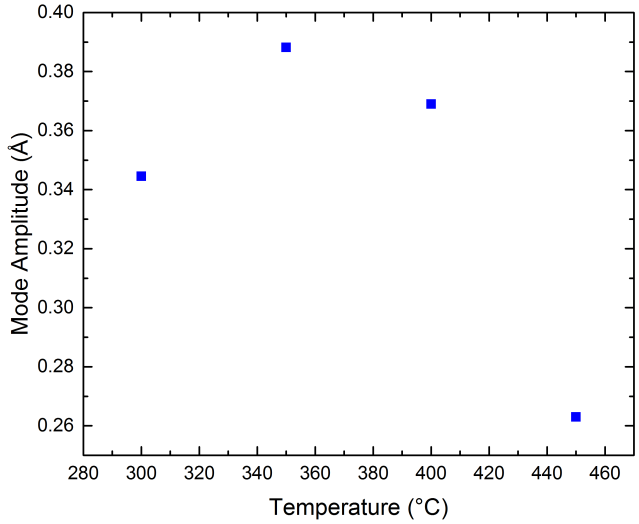

Figure 5.12 Thermal evolution of the overall Γ_4^- mode across the temperature range 300 < *T* < 450 °C in which the polar *P*4$_2$*mc* phase exists exclusively.

5.3.5 Evolution of lattice parameters

Trends in the lattice parameters obtained from Rietveld refinement of the PND data in the temperature range 20 ≤ *T* ≤ 900 °C are illustrated in Figure 5.13. A discontinuous evolution of both the *a* and *c* lattice parameters is observed upon the transition from Na-*R*3*c* – *P*4$_2$*mc* in agreement with a 1st order discontinuous mechanism established from analysis of the crystallographic data. Conversely the gradual merging observed for the *a* and *c* parameters as the polar – centrosymmetric transition is approached indicate this transition is 2nd order, when lattice parameters alone are considered. Whilst there is no evidence of a 1st order transition mechanism from the PND data, it is possible that the 50 °C

temperature increments preclude observation of any phase co-existence. The kink observed in the R_4^+ tilt mode upon adoption of the centrosymmetric phase at 500 °C, indicates that this transition proceeds *via* a discontinuous mechanism. This is highly plausible as Landau theory only dictates that a specific phase transition is permitted to proceed continuously, not that it necessarily does. The enhanced tetragonality of the $P4_2mc$ phase as a result of the polar displacements along *c* is clearly demonstrated by the large discrepancy in *a* and *c* lattice parameters at 200 °C. This is in contrast to the pseudocubic unit cell metrics observed in the centrosymmetric tetragonal $P4_2/nmc$ phase. The 1st order phase transition from $P4_2/nmc$ – $P4/mbm$ is evidenced by the jump in the *c* lattice parameter at 750 °C prior to coalescence of *a* and *c* at 850 °C, at which point the structure is metrically cubic.

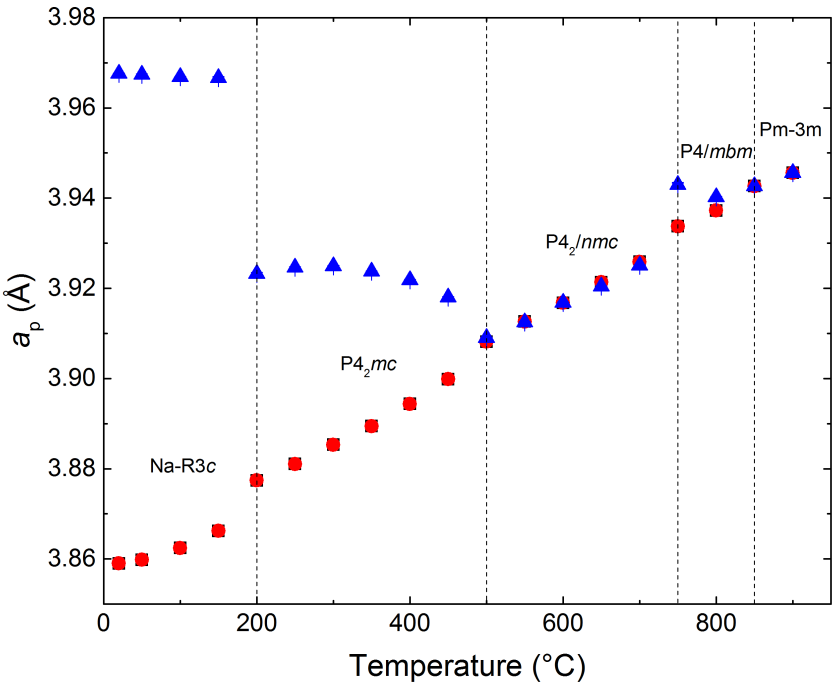

Figure 5.13 Normalised lattice parameters versus *T* obtained from Rietveld refinement of PND data. The *a* lattice parameter is represented by red circles and *c* by blue triangles. In regions where phase co-existence occurs, only the majority phase present at each temperature is shown.

5.4 Discussion

The general trend for in-phase tilt systems at high temperatures and out-of-phase tilt systems at lower temperatures as observed in pure $NaNbO_3$, LNN-3, -8 and-12 compositions, is continued in LNN-20[15, 16] (phase progression of Na-*R*3*c* – *P*4_2*mc* – *P*4_2/*nmc* – *P*4/*mbm* - *Pm*$\bar{3}$*m*). However, LNN-20 is different to the lower doped regions of the LNN-*X* phase diagram as it does not adopt any of the long-range tilt systems reminiscent of phases R and S that occur upon condensation of the T_4 symmetry-adapted mode. Instead, in this system two of the rarest space group symmetries exhibited in perovskites are observed in a phase progression that is not only unprecedented but also highly unusual. The Na-*R*3*c* – *P*4_2*mc* transition, is particularly peculiar. To facilitate this transition the out-of-phase tilt about the [111] axis of the parent cubic cell in the Na-*R*3*c* phase must change direction to act about [001] in *P*4_2*mc*. This, in itself, is not unusual. However, in order to meet the symmetry requirements imposed by the *P*4_2*mc* phase, a one-tilt system necessarily becomes two, with the addition of an in-phase tilt simultaneously about [110] (corresponding to a Glazer tilt system change of $a^-a^-a^-$ -> $a^+a^+c^-$). It can be assumed that the RT structure is adopted due to energy stabilising benefits associated with the $a^-a^-a^-$ tilt system. Whilst such changes in tilt system are generally rare among perovskites as a function of temperature, as highlighted in Chapter 4, similar instances of this type of structural behaviour are seen in the R –> P and P – >Q transitions in pure $NaNbO_3$[15]. These unusual tilt transitions only prove to further demonstrate the interesting structural chemistry of $NaNbO_3$ and its related compounds.

5.4.1 RT structure

As previously discussed the rhombohedral phase stabilised at room temperature (Figure 5.14) can be considered either as isostructural with the low temperature ferroelectric phase of $NaNbO_3$ or as a heavily doped variant of the room temperature phase of $LiNbO_3$ with reduced unit cell dimensions (a = 5.148(3)Å, c = 13.863(3) Å in $LiNbO_3$[12]). The Na-$R3c$ phase is defined by a $\sqrt{2}_{ap} \times \sqrt{2}_{ap} \times 2\sqrt{3}_{ap}$ unit cell in the hexagonal setting (supercell with three irreducible rhombohedral units). Co-operative niobium shifts result in a polarisation along the c-axis with out-of-phase octahedral tilting acting simultaneously about each of the three crystallographic axes. See Table 5.1 in the previous section for details on the crystallographic model of the Na-$R3c$ phase at 20 °C.

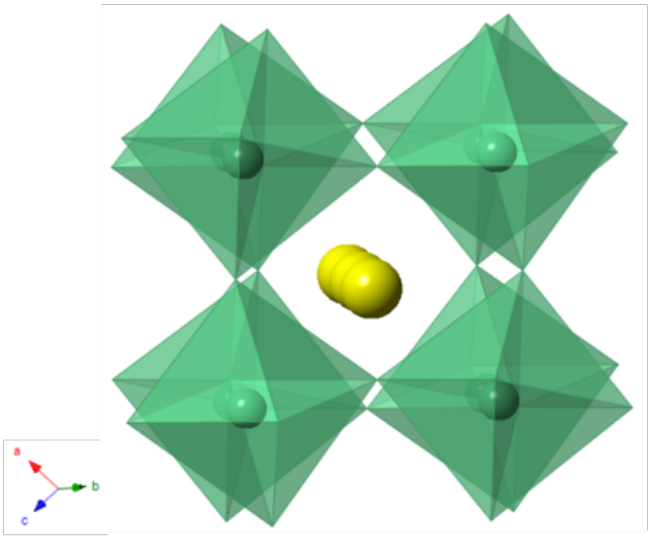

Figure 5.14 Crystal structure of the Na-rich rhombohedral phase (space group $R3c$) at 20 °C.

5.4.2 Rare $a^+a^+c^-$ tilt system

The $P4_2mc$ and $P4_2/nmc$ phases observed at intermediate temperatures are examples of the very rare $a^+a^+c^-$ tilt pattern. The presence of not only one but two variants of the $a^+a^+c^-$ tilt in a single system is unprecedented in perovskite chemistry. The $a^+a^+c^-$ tilt system is one of the few in which the octahedral tilts remove the crystallographic degeneracy of the A-site cations[17], and as such it has only been previously observed in perovskites that exhibit columnar A-site ordering.

The $a^+a^+c^-$ tilt pattern is indeed so rare that it has been observed as little as twice in the aristotype form ($P4_2/nmc$), in the double perovskites $CaFeTi_2O_6$[18] and $LnMn(Ga_{0.5}Ti_{0.5})_2O_6$ (Ln = Sm, Gd)[19] and only once in the polar form ($P4_2mc$) in $CaMnTi_2O_6$[20]. It occurs naturally in the mineral gillespite, $FeGe(OH)_6$, where additional ordering of the Fe and Ge sites removes both the mirror plane and c-glide symmetry resulting in $P2_1/n$ spacegroup symmetry[21]. Synthetically the $P2_1/n$ variant has also recently been observed in the A- and B-site ordered $MnRMnSbO_6$ (R = La, Pr, Nd, Sm) system[22]. Each of the previous synthetic examples of the polar and aristotype form are double perovskites which incorporate unusually small cations at the A-site (Fe^{2+} or Mn^{2+} typically occupy the perovskite B-site), synthesised under very high pressure conditions (12-15 GPa for $CaFeTi_2O_6$ for example). In this context, LNN-20 is unique as it is the first example of this tilt system exhibited in a more conventional ABO_3 perovskite with alkali metal cations at the A-site, crystallising under standard conditions of atmospheric pressure.

5.4.3 Unusual A-site co-ordination in the $a^+a^+c^-$ tilt system

Three crystallographically unique A-sites are present in the centrosymmetric setting (see Figure 5.22); one A-site in a ten coordinate configuration (note there are two ten coordinate sites in the polar phase for four unique A-sites, with 10-coordinate geometries adopted at half of the A-sites in both spacegroups) and two smaller sites with four shortened A-O bonds adopting square planar and tetrahedral geometries (together these account for half of all A-site geometries). The smaller square planar and tetrahedral sites are formally 4 coordinate, however they can be described using higher coordination numbers, occuring in three distinct shells. In the first shell the A-site is tetrahedrally coordinated to its four nearest neighbouring oxygen anions. Upon rotation through 90 ° it forms a larger, more distorted tetrahedron with its second four nearest neighbours and finally a square planar geometry with its four third nearest neighbours. The opposite is true for the second 4 coordinate site, with four nearest neighbours in a square planar arrangement, four second nearest neighbours forming a tetrahedron and third nearest neighbours in a larger, distorted tetrahedron.

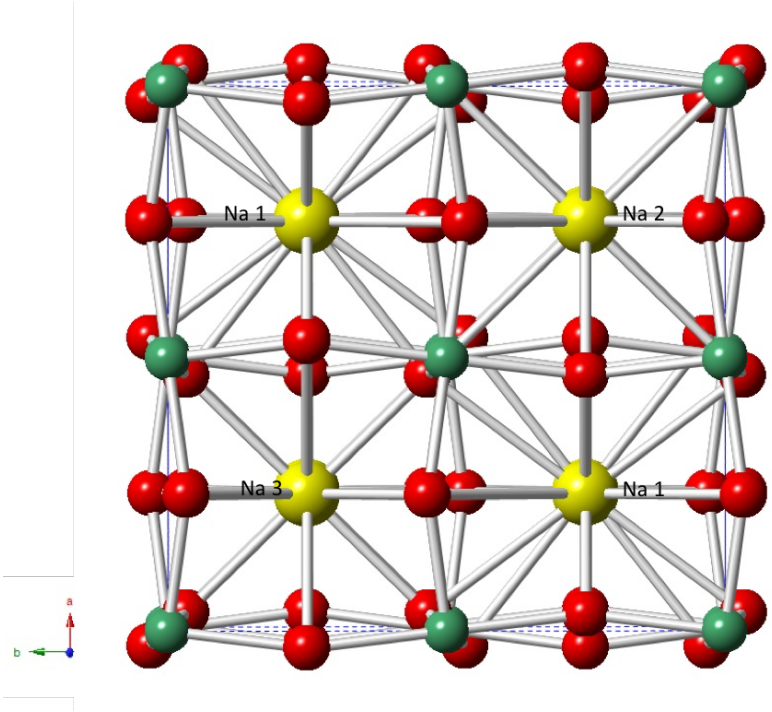

Figure 5.15 Ball and stick representation of $P4_2/nmc$ structure of LNN-20 at 500 °C. The 10 coordinate A-sites alternate with either tetrahedral or square planar sites in both the *a* and *b* directions. Tetrahedral and square planar sites alternate along *c* creating columns of ten coordinate and four coordinate sites. Oxygen is shown in red and niobium in green.

In both $CaFeTi_2O_6$ and $CaMnTi_2O_6$ the presence of the unusually small Fe^{2+} and Mn^{2+} cations promotes A-site ordering (with Fe and Mn occupying the smaller tetrahedral and square planar sites). This results in columns of 10 coordinate Ca and alternating tetrahedral and square planar Fe or Mn along the *c*-axis. No evidence of similar ordering of Na and Li sites in LNN-20 can be found from the available data, which would make it the first example of this tilt system in a structure in which A-site ordering is absent. A ball and stick representation of the centrosymmetric phase highlighting the columnar ordering of the three A-site geometries is shown in Figure 5.15. The polar phase exhibits the same A-site coordinations differing only in the presence of two crystallographically unique 10

coordinate sites which alternate along *c*. For simplicity all A-sites will be referred to as Na1, Na2 *etc*. throughout.

5.4.4 $P4_2mc$ phase at 300 °C

Intriguingly, the only previous example of a perovskite structure with $P4_2mc$ symmetry, $CaMnTi_2O_6$ [20], exhibits polarisation-field hysteresis at room temperature with a reported Curie temperature (T_C) of 357 °C. Unfortunately, attempts to observe hysteresis in LNN-20 with the use of pyroelectric measurements proved unsuccessful. The origin of ferroelectricity in $CaMnTi_2O_6$ is rationalised as a coupled effect involving both a second-order Jahn-Teller (SOJT) type distortion (off-centring of Ti^{4+} cations at the B-site) and A-site displacements in the form of ordered shifts of Mn^{2+} cations in the square planar geometry. This was found to be a novel mechanism for ferroelectricity and as such can inspire design-led research. With regard to LNN-20, the off-centre displacement of the Ti^{4+} cation at room temperature in $CaMnTi_2O_6$ (~ 0.1 Å)[20] is similar to and in fact slightly smaller than the displacement of Nb in LNN-20 at 300 °C (~ 0.12(3) Å), however their co-ordination geometries differ at the A-site, with the four coordinate geometry strongly exhibited in $CaMnTi_2O_6$ less regimented in LNN-20. The crystal structure for the $P4_2mc$ phase obtained from Rietveld refinement of the PND data at 300 °C is shown in Figure 5.16. The A-site geometries for the polar phase are shown in Figure 5.17.

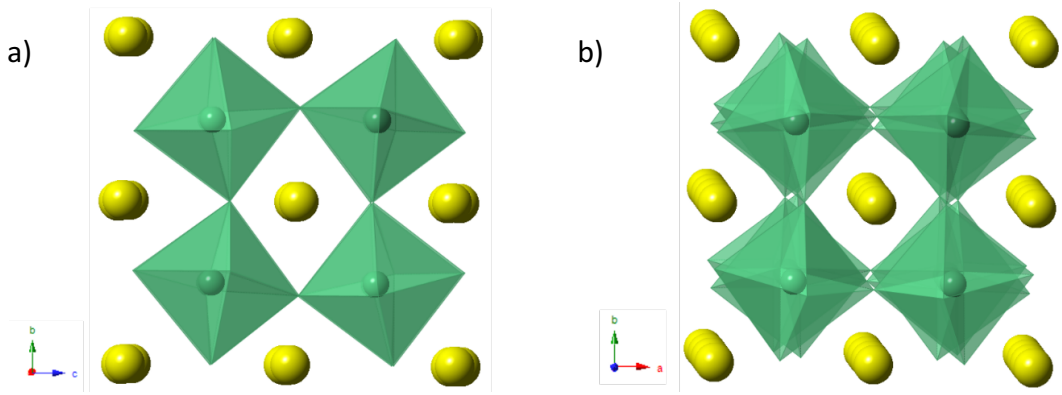

Figure 5.16 Crystal structure of $P4_2mc$ phase at 300 °C showing a) view down the *a*-axis highlighting in-phase tilting in this direction, and off-centring of Nb atoms along the polar *c*–axis and b) the out-of-phase tilt along the *c*-axis.

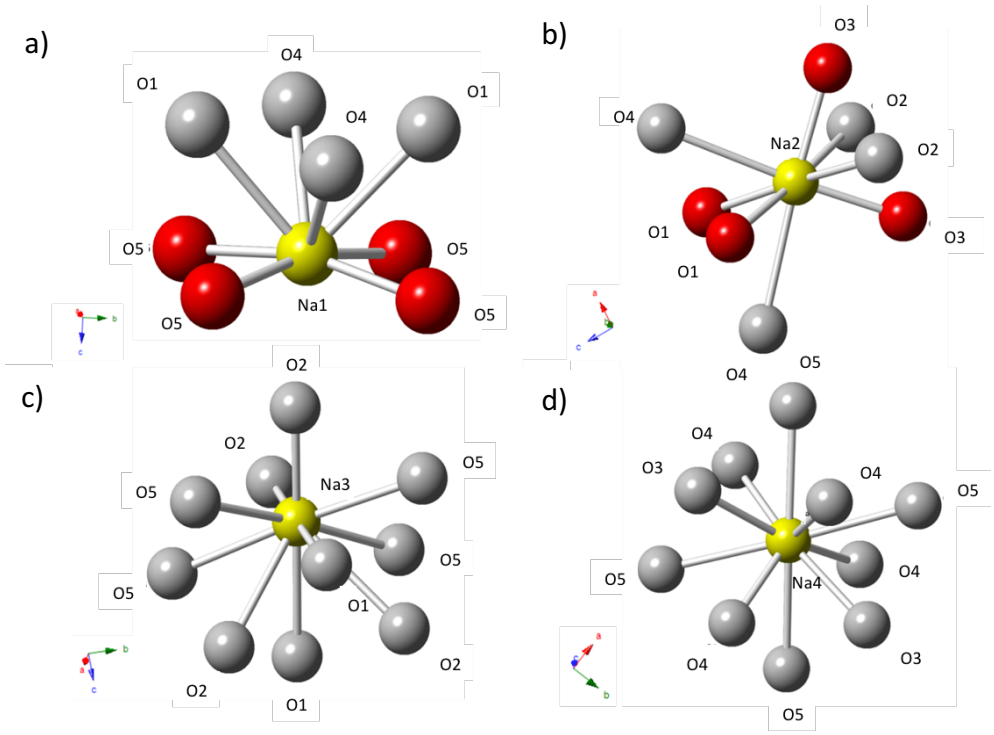

Figure 5.17 Na – O co-ordination in the $P4_2mc$ phase (at 300 °C) showing co-ordination of Na to O at the four unique Na crystallographic sites. Oxygen atoms of the shortest Na-O bonds shown in red. The approximate square planar geometry (a) and tetrahedral geometry (b) of Na1 and Na2 sites mirrors that of the Mn co-ordination in $CaMnTi_2O_6$[20].

5.4.4.1 A-site displacements in the P42mc phase

As shown in Figure 5.18 the square planar geometry lies along the Na1-O5 plane, in line with the *b*-axis of the unit cell. O5-Na1-O5 bond angles show that this is a distorted square planar geometry with bond angles of 89.4(6) °, 88.6(6) ° and 165.0(11) °, associated with Na cation shifts directed along the *c*-axis. In $CaMnTiO_6$, a square planar geometry with a greater degree of distortion for the Mn1 co-ordination environment is described, with corresponding bond angles of ~ 87.57 °, 87.73 ° and 156.63 °[20]. Selected bond lengths and bond angles for the polar phase at 300 °C are given in Table 5.6. The geometry of the tetrahedral Na2 site is shown in Figure 5.19.

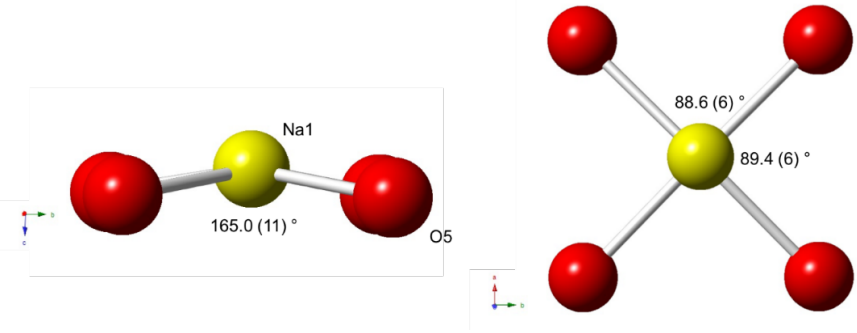

Figure 5.18 Ball and stick representation showing square planar geometry at the Na1 A-site in the $P4_2mc$ phase at 300 °C, with the Na1 cation shifted out of plane along the *c*-axis.

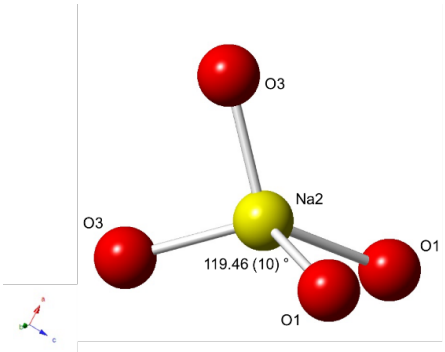

Figure 5.19 Schematic showing tetrahedral geometry adopted at the Na2 site in $P4_2mc$ phase at 300 °C.

Calculation of the bond valence sums[23] for the square planar and tetrahedral sites, expectedly show that the Na^+ cations are underbonded. The degree of underbonding is less severe than that of the Mn^{2+} cations in $CaMnTi_2O_6$, which is most likely due to the larger alkali cation at the A-site in LNN-20 (Ionic radii (IR) of 4 coordinate Mn^{2+} = 0.66 Å, compared with 0.99 Å for Na[24]). The degree of underbonding for the square planar site in $CaMnTi_2O_6$ is more severe than that in LNN-20, but the bonding at the tetrahedral sites is comparable. Whilst the tetrahedral site in $CaMnTi_2O_6$ has a significantly higher BVS value than the square planar site, the two 4 coordinate sites in LNN-20 have more comparable values, with the tetrahedral site in this case slightly more underbonded. A comparison of both the tetrahedral and square planar sites in LNN-20 and $CaMnTi_2O_6$ is included in Table 5.5.

Table 5.5 BVS calculations for the A-site cations of the $P4_2mc$ phase at 300 °C in LNN-20 compared to those reported for $CaMnTi_2O_6$. Both sets of calculations were carried out assuming a 4 coordinate A-site environment.

A-site	BVS in LNN-20	BVS in $CaMnTi_2O_6$
Na/Li_{Sq}	0.87	1.38
Na/Li_{Tet}	0.80	1.60

Table 5.6 Bond lengths and selected bond angles of $P4_2mc$ phase at 300 °C, Na-O bond lengths over 2.7 Å are not reported.

Na-O	Bond length (Å)	Nb-O	Bond length (Å)	Nb-O-Nb	Bond angle (°)
Na1-O1 × 2	2.597(17)	Nb-O1	1.963(4)	Nb-O1-Nb	167.8(4)
Na1-O5 × 4	2.365(3)	Nb-O2	1.999(4)	Nb-O2-Nb	150.8(4)
Na2-O1 × 2	2.51(3)	Nb-O3	1.999(4)	Nb-O3-Nb	151.1(4)
Na2-O2 × 2	2.69(3)	Nb-O4	1.969(4)	Nb-O4-Nb	163.3(4)
Na2-O3 × 2	2.31(3)	Nb-O5	2.125(3)	Nb-O5-Nb	156.77(10)
Na3-O2 × 2	2.322(17)	Nb-O5’	1.882(3)		
Na4-O3 × 2	2.644(12)				
Na4-O4 × 2	2.460(15)				
Na4-O4 × 2	2.664(15)				

5.4.4.2 B-site displacement in $P4_2mc$

The second polar distortion acting upon the $P4_2mc$ structure is a SOJT distortion with off-centring of the Nb^{5+} cations along the *c*-axis (illustrated in Figure 5.21). At 300 °C, with the polar phase fully established, the displacement is at its most significant with Nb displaced 0.120(3) Å along *c*, toward the O5’ oxygen atom. As the temperature increases, the Nb-O5’ bond lengthens at the expense of Nb-O5, reducing the polarity in the O5-Nb-O5’ bond as the polar - centrosymmetric phase transition at 500 °C is approached. The trend in Nb-O bond lengths as a function of temperature can be seen in Figure 5.20.

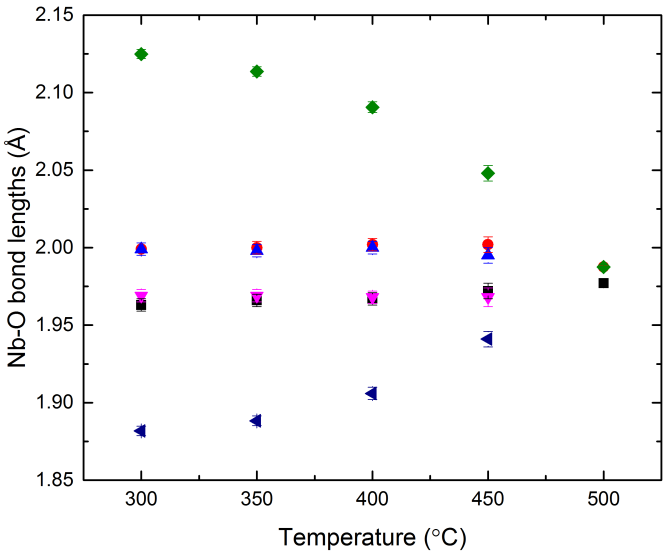

Figure 5.20 Thermal evolution of Nb-O bond lengths over the temperature region 300 ≤ T ≤ 500 °C, demonstrating the decrease in the off-centre displacement of the Nb atom within the NbO_6 octahedron as the $P4_2mc$ – $P4_2/nmc$ phase transition is approached. The bonds are represented as follows; Nb-O1 (black squares), Nb-O2 (red circles), Nb-O3 (blue triangles), Nb-O4 (pink triangles), Nb-O5 (green squares) and Nb-O5' (purple triangles). Related bond lengths in the centrosymmetric phase are given as Nb-O1 (red circle), Nb-O2 (black square) and Nb-O3 (green square).

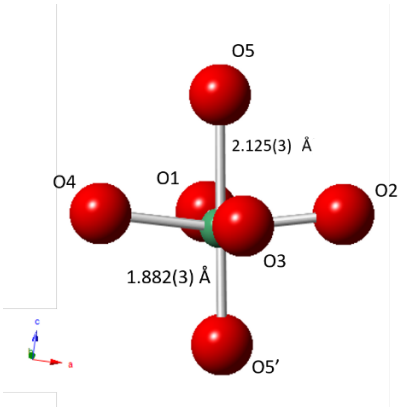

Figure 5.21 Schematic of NbO_6 octahedron in the $P4_2mc$ phase at 300 °C highlighting the polar Nb displacement (difference between Nb-O5 and Nb-O5' bond lengths ~ 0.243 Å). The symmetry operators acting upon the Nb-O5 and Nb-O5' bonds are x, y, z and 1-y, 1-x, -1/2 + z, respectively.

5.4.5 $P4_2/nmc$ phase at 500 °C

Transformation to the centrosymmetric parent space group at 500 °C necessarily involves the loss of both the A-site cation displacements and the SOJT B-site displacements. This is highlighted in Figures 5.23 and 5.24(a) which show the more regular NbO_6 octahedra and A-site square planar geometries, respectively. The Na-O bond distances in the *P*4_2/*nmc* phase at 500 °C are slightly longer than those observed for $CaFeTi_2O_6$ (Fe-O_{Tet} = 2.084(2) Fe-$O_{sq.}$ = 2.097(2) in $CaFeTi_2O_6$[18]). This can be expected due to the presence of the unusually small Fe^{2+} cation at the A-site (IR of 4 coordinate Fe^{2+} = 0.63). The four shortened Na-O bonds in both $CaFeTi_2O_6$ and LNN-20 exhibit very similar bond lengths across the two sites despite the differing geometries, with the Na-O bonds forming the square planar and tetrahedral geometries in LNN-20 identical within the margin of error (Na-O_{Sq} = 2.400(3) Å and Na-O_{Tet} = 2.399(3) Å). Selected bond distances and bond angles are included in Table 5.7.

Table 5.7 Bond lengths and selected bond angles for the *P*4_2/*nmc* phase at 500 °C; Na-O bond lengths over 2.7 Å are not reported.

Na-O	Bond length (Å)	Nb-O	Bond length (Å)	Nb-O-Nb	Bond angle (°)
Na1-O2 × 2	2.525(8)	Nb-O1 × 2	1.9880(6)	Nb-O1-Nb	158.84(19)
Na1-O2 × 2	2.675(9)	Nb-O2 × 2	1.9765(6)	Nb-O2-Nb	162.7(2)
Na2-O3 × 4	2.400(3)	Nb-O3 × 2	1.9881(6)	Nb-O3-Nb	158.93(18)
Na3-O1 × 4	2.399(3)				

Consequently, the BVSs for both 4 coordinate sites in LNN-20 (Table 5.8) are identical when rounded to two significant figures. The trend exhibited in the polar

phase in LNN-20, whereby the tetrahedral site is less underbonded, is echoed in the BVS values reported for $CaFeTi_2O_6$. The greater similarity in the BVSs for the tetrahedral and square planar sites in the centrosymmetric space group is most likely due to the absence of the polar shifts in the square planar geometry. Schematics highlighting the ten coordinate, square planar and tetrahedral geometries adopted at the Na1, Na2 and Na3 sites respectively are included in Figure 5.22. The inability to refine the isotropic ADPs of the A-sites freely may suggest there is some disorder present in this structure that cannot be modelled in the $P4_2/nmc$ setting. Parise *et al*. report an elongation of the thermal ellipsoid for the Fe site in square planar geometry perpendicular to the plane, *i.e.* along *c*. Therefore, it is possible there is some degree of inherent disorder in the phase adopted by LNN-20 at 500 °C. A schematic of the tetrahedral geometry of the Na3 site is shown in Figure 5.24(b).

Table 5.8 BVS calculations for the A-site cations of the $P4_2/nmc$ phase at 500 °C in LNN-20 compared to those reported for $CaFeTi_2O_6$. Both sets of calculations were carried out assuming a 4 coordinate A-site environment.

A-site	BVS in LNN-20	BVS in $CaFeTi_2O_6$
Na/Li_{Sq}	0.79	1.47
Na/Li_{Tet}	0.79	1.55

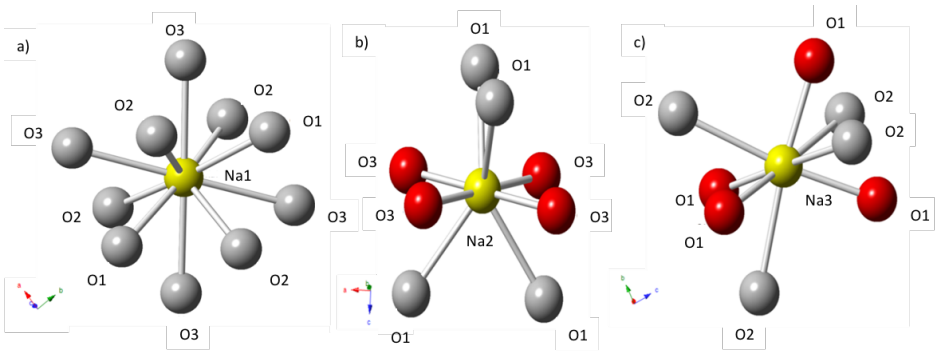

Figure 5.22 Schematic showing Na-O co-ordination in $P4_2/nmc$ phase for the three crystallographically unique Na sites. Red oxygen atoms again highlight the square planar geometry (b) and tetrahedral geometry (c) as seen in $CaFeTi_2O_6$[18].

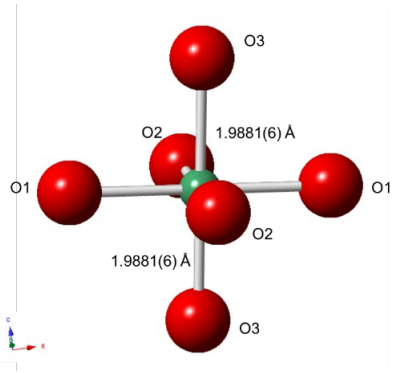

Figure 5.23 Schematic of NbO_6 octahedron in the $P4_2/nmc$ phase at 500 °C showing three sets of symmetry equivalent bonds Nb-O bonds. The now symmetry equivalent axial Nb-O3 bonds along *c* are highlighted.

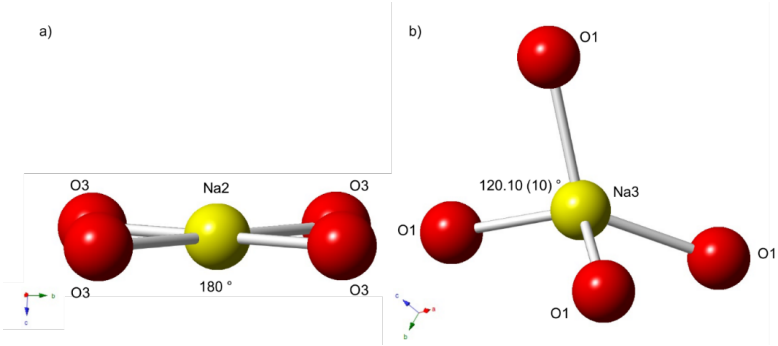

Figure 5.24 Schematic showing regular square planar and tetrahedral geometries adopted at the Na2 and Na3 sites in the $P4_2/nmc$ phase at 500 °C.

5.4.6 High temperature tetragonal and cubic phases

The high temperature tetragonal polymorph, *P*4/*mbm* ($a^0a^0c^+$, Figure 5.25), is a common phase observed in many perovskites including pure $NaNbO_3$ over the temperature range 570 < *T* < 575 °C[15]. It adopts a $\sqrt{2}a_p \times \sqrt{2}a_p \times a_p$ unit cell. The out-of-phase tilt in the previous $a^+a^+c^-$ phase is now lost, but the in-phase tilt is carried forward into this new phase, with a change in direction from about [110] to about [001] (Glazer tilt system change $a^+a^+c^-$ to $a^0a^0c^+$). As previously discussed, this transition is required by Landau theory to be 1st order, with evidence for a region of phase co-existence between the $a^+a^+c^-$ and $a^0a^0c^+$ structures observed in the temperature region 650 ≤ *T* ≤ 750 °C. Refinement of anisotropic ADPs is allowed for in this model. A full structural model for the *P*4/*mbm* phase at 800 °C given in Table 5.9. Despite the vastly different behaviour exhibited by LNN-20 at intermediate temperatures, the evolution of the structure at high temperatures mimics the pattern observed for the LNN-3, LNN-8 and LNN-12 compositions in the previous chapter.

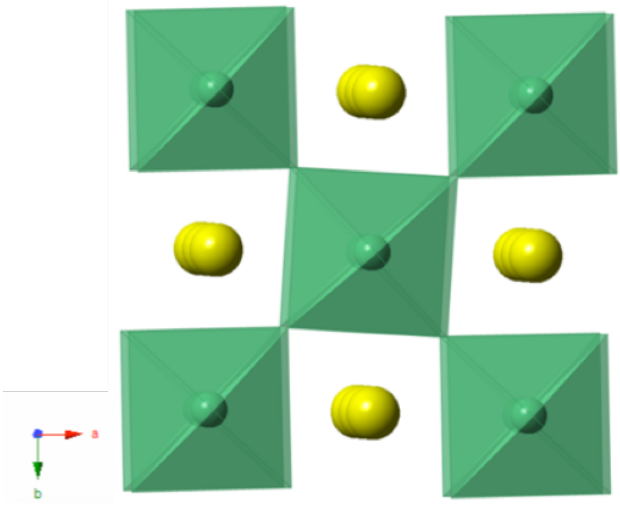

Figure 5.25 Crystal structure of the *P*4/*mbm* phase at 800 °C, viewed along the *c*-axis, highlighting the in-phase tilt.

Table 5.9 Crystallographic data for LNN-20 at 800 °C modelled in the *P*4/*mbm* space group; a = 5.5682(14), c = 3.9407(17) Å. U_{iso} values for all A-site cations (Na,Li) are constrained together.

Atom	Wyckoff position	*x*	*y*	*z*	100*$U_{11/22}$ (Å^2)	100*U_{33} (Å^2)
Na*	2a	0	0.5	0.5	1.1(1)	2.6(3)
Nb	2c	0	0	0	4.2(4)	3.1(8)
O1	2b	0	0	0.5	8.7(4)	2.4(4)
O2	4g	0.2602(3)	0.2398(3)	0	2.98(18)	6.4(3)

*position Na has fixed occupancy $Na_{0.8}Li_{0.2}$

The cubic structure adopted at 850 °C occurs upon loss of the remaining in-phase tilt. However, the anisotropic ADPs obtained from Rietveld refinement suggest retention of at least some degree of octahedral tilting even at this temperature (oblate ellipsoid indicated for O1 as $U_{33} - U_{22} < U_{22} - U_{11}$). The degree of anisotropy observed for the ADPs of the oxygen site is similar to the analogous compounds investigated in the previous chapter (*e.g*. in LNN-12 $100*U_{11}$ = 0.59(3), $100*U_{22}/U_{33}$ = 6.49(3)). A structural model for the cubic phase at 900 °C obtained from Rietveld refinement of the PND data is given in Table 5.10.

Table 5.10 Crystallographic data for LNN-20 at 900 °C modelled in the $Pm\bar{3}m$ space group; a = 3.94560(3) Å. U_{aniso} values for all A-site cations (Na,Li) are constrained together.

Atom	Wyckoff position	x	y	z	100*U_{11} (Å^2)	100*$U_{22/33}$ (Å^2)
Na*	2a	0	0	0	4.06(4)	4.06(4)
Nb	2c	0.5	0.5	0.5	1.353(16)	1.353(16)
O	2b	0	0.5	0.5	0.93(3)	6.73(3)

*position Na has fixed occupancy $Na_{0.8}Li_{0.2}$

5.5 Conclusions and Further Work

The unprecedented thermally-induced phase progression $R3c$ – $P4_2mc$ – $P4_2/nmc$ – $P4mbm$ - $Pm\bar{3}m$ is observed for the system $Li_{0.2}Na_{0.8}NbO_3$, determined through a combination of PND, SHG, and relative permittivity measurements. The $a^+a^+c^-$ Glazer tilt system is adopted twice, both in its polar and centrosymmetric forms, and is the first example of either in a simple ABO_3 perovskite synthesised under ambient pressure. The polar nature of the phase present for the temperature range $300 \leq T \leq 450$ °C is confirmed *via* SHG experiments, however attempts to demonstrate ferroelectricity for the $P4_2mc$ phase proved unsuccessful. Relative permittivity measurements provide corroboration of the temperature regions identified for the observed phase transitions in the PND data. With consideration to the diverse range of structures adopted involving T_4 tilt modes described in the previous chapter, the similarly unique but vastly different structural behaviour exhibited by LNN-20 further demonstrates the crystallographic intrigue of the $NaNbO_3$ family. Whilst the reasons behind the unusual phase progression adopted

by LNN-20 are unclear, the exotic structural behaviour of the lithium sodium niobate system should be of great interest to those in the field of ferroelectrics and perovskites.

5.6 References

1. Chaker, C.; El Gharbi, W.; Abdelmoula, N.; Simon, A.; Khemakhem, H.; Maglione, M., $Na_{1-x}Li_xNbO_3$ ceramics studied by X-ray diffraction, dielectric, pyroelectric, piezoelectric and Raman spectroscopy. *Journal of Physics and Chemistry of Solids* **2011,** *72*, 1140-1146.
2. Juang, Y. D.; Dai, S. B.; Wang, Y. C.; Chou, W. Y.; Hwang, J. S.; Hu, M. L.; Tse, W. S., Phase transition of $Li_xNa_{1-x}NbO_3$ studied by Raman scattering method. *Solid State Communications* **1999,** *111*, 723-728.
3. Peel, M. D.; Ashbrook, S. E.; Lightfoot, P., Unusual Phase Behavior in the Piezoelectric Perovskite System, $Li_xNa_{1-x}NbO_3$. *Inorganic Chemistry* **2013,** *52*, 8872-8880.
4. Lehnert, H.; Boysen, H.; Frey, F.; Hewat, A.; Radaelli, P., A neutron powder investigation of the high-temperature structure and phase transition in stoichiometric $LiNbO_3$. *Zeitschrift Fur Kristallographie* **1997,** *212*, 712-719.
5. Miller, R. C.; Savage, A., Temperature Dependence of the Optical Properties of Ferroelectric $LiNbO_3$ AND $LiTaO_3$. *Applied Physics Letters* **1966,** *9*, 169-171.
6. Larson, A. C.; Von Dreele, R. B., Los Alamos Natl. Lab: 1994.
7. Toby, B. H., EXPGUI, a graphical user interface for GSAS. *Journal of Applied Crystallography* **2001,** *34*, 210-213.
8. Campbell, B. J.; Stokes, H. T.; Tanner, D. E.; Hatch, D. M., ISODISPLACE: a web-based tool for exploring structural distortions. *Journal of Applied Crystallography* **2006,** *39*, 607-614.
9. Kurtz, S. K.; Perry, T. T., A Powder Technique for the Evaluation Of Nonlinear Optical Materials. *Journal of Applied Physics* **1968,** *39*, 3798-3813.
10. Glazer, A., The classification of tilted octahedra in perovskites. *Acta Crystallographica Section B* **1972,** *28*, 3384-3392.
11. Lanfredi, S.; Lente, M. H.; Eiras, J. A., Phase transition at low temperature in $NaNbO_3$ ceramic. *Applied Physics Letters* **2002,** *80*, 2731-2733.
12. Hsu, R.; Maslen, E. N.; du Boulay, D.; Ishizawa, N., Synchrotron X-ray studies of $LiNbO_3$ and $LiTaO_3$. *Acta Crystallographica Section B* **1997,** *53*, 420-428.
13. Howard, C. J.; Stokes, H. T., Group-theoretical analysis of octahedral tilting in perovskites. *Acta Crystallographica Section B* **1998,** *54*, 782-789.
14. Mitra, S.; Kulkarni, A. R.; Prakash, O., Diffuse phase transition and electrical properties of lead-free piezoelectric $(Li_xNa_{1-x})NbO_3$ ($0.04 \leq x \leq 0.20$) ceramics near morphotropic phase boundary. *Journal of Applied Physics* **2013,** *114*.
15. Megaw, H. D., The seven phases of sodium niobate. *Ferroelectrics* **1974,** *7*, 87-89.
16. Peel, M. D.; Thompson, S. P.; Daoud-Aladine, A.; Ashbrook, S. E.; Lightfoot, P., New Twists on the Perovskite Theme: Crystal Structures of the Elusive Phases R and S of $NaNbO_3$. *Inorganic Chemistry* **2012,** *51*, 6876-6889.

17. King, G.; Woodward, P. M., Cation ordering in perovskites. *Journal of Materials Chemistry* **2010,** *20*, 5785-5796.
18. Leinenweber, K.; Parise, J., High-Pressure Synthesis and Crystal-Structure of $CaFeTi_2O_6$, a New Perovskite Structure Type. *Journal of Solid State Chemistry* **1995,** *114*, 277-281.
19. Shimura, G.; Niwa, K.; Shirako, Y.; Hasegawa, M., High-Pressure Synthesis and Magnetic Behavior of A-Site Columnar-Ordered Double Perovskites, $LnMn(Ga_{0.5}Ti_{0.5})_2O_6$ (Ln = Sm, Gd). *European Journal of Inorganic Chemistry* **2017,** 835-839.
20. Aimi, A.; Mori, D.; Hiraki, K.; Takahashi, T.; Shan, Y. J.; Shirako, Y.; Zhou, J. S.; Inaguma, Y., High-Pressure Synthesis of A-Site Ordered Double Perovskite $CaMnTi_2O_6$ and Ferroelectricity Driven by Coupling of A-Site Ordering and the Second-Order Jahn-Teller Effect. *Chemistry of Materials* **2014,** *26*, 2601-2608.
21. Hazen, R.M.; BurnhamC.W., The crystal structures of gillespite I and II: A structure determination at high pressure. *American Mineralogist* **1974,** *59*, 1166 - 1176.
22. Solana-Madruga, E.; Arevalo-Lopez, A. M.; Dos Santos-Garcia, A. J.; Urones-Garrote, E.; Avila-Brande, D.; Saez-Puche, R.; Attfield, J. P., Double Double Cation Order in the High-Pressure Perovskites $MnRMnSbO_6$. *Angewandte Chemie-International Edition* **2016,** *55*, 9340-9344.
23. Brese, N. E.; O'Keeffe, M., Bond-valence parameters for solids. *Acta Crystallographica Section B* **1991,** *47*, 192-197.
24. Shannon, R. D., Revised Effective Ionic-Radii and Systematic Studies of Interatomic Distances in Halides and Chalcogenides. *Acta Crystallographica Section A* **1976,** *32*, 751-767.

6 Thermal Evolution of $LaFeO_3$ – Origin of the $c > a$ Crossover

6.1 Introduction

In addition to materials with ferroelectric properties, ferromagnetic and multiferroic compounds are of great importance in the development of new technologies. In this chapter, a detailed structural analysis of the rare earth orthoferrite $LaFeO_3$ is undertaken with the use of a variable temperature PND study ($25 \leq T \leq 1284$ K) and symmetry mode analysis. Whilst $LaFeO_3$ can be considered a prototypical member of the rare earth orthoferrite series, previous research by Selbach on its structural behaviour as a function of temperature has shown that it undergoes an interesting crossover of the *a* and *c* lattice parameters at $T \sim 725$ K[1], a feature that should not occur if only the tilts of rigid octahedra in the *Pnma* phase ($a^+b^-b^-$) are considered. No rationale for this crossover was offered by Selbach, however that work was based on lab PXRD which only offered poor precision of atomic coordinates. Therefore, this study attempts to elucidate the structural driving force for this crossover in the unit cell metrics.

The rare earth orthoferrites have proven to have many important uses in areas such as fuel cell cathode materials[2], magnetic optics[3], sensors[4] and catalysis[5]. $LaFeO_3$ adopts the *Pnma* $GdFeO_3$-type structure at room temperature that is typical across the series. The *Pnma* space group is the most frequently occurring in perovskites[6] and is usually valid for tolerance factor values of $t < 0.975$[7] (the tolerance factor for $LaFeO_3$ is 0.945). Woodward has shown that for perovskites with large tilt angles (associated with a tolerance factor deviating significantly from 1) the $a^+b^-b^-$ tilt system provides the lowest energy structure as it maximises

the A-site co-ordination whilst simultaneously minimising the repulsive A-X overlap[8]. $LaFeO_3$ undergoes a high temperature transition to a rhombohedral phase with $R\bar{3}c$ symmetry (Glazer notation $a^-a^-a^-$) at $T \sim 1228$ K. This can be rationalised due to the reduction in the octahedral tilting angles at high temperature, which in turn lessens the ion-ion repulsion that initially prevents this phase forming at lower temperatures. This orthorhombic – rhombohedral transition can be seen as a function of A-cation size for the $LnNiO_3$ series and as a function of temperature in $LaGaO_3$ (T_c = 425 K[9]) and $LaCrO_3$ (T_c = 533 K[10]). Work by Zhou and Goodenough[6] concluded that the $c > a$ crossover is a necessary precursor to the orthorhombic – rhombohedral transition. Therefore, this work aims to identify the structural driving force behind this crossover in $LaFeO_3$. The octahedral tilting in the *Pnma* phase gives rise to a distorted unit cell with a cell multiplicity of $\sqrt{2}_{ap} \times 2_{ap} \times \sqrt{2}_{ap}$. In addition to identifying the structural driving force for the $c > a$ crossover, this study is a follow up to previous work in the group which focused on the structural response of multiferroic $Bi_{0.5}La_{0.5}FeO_3$ (BLFO50) as a function of temperature[11]. It was found that BLFO50 displays a number of curious structural anomalies, therefore, in theory a PND study of $LaFeO_3$ allows for comparison to prototypical behavior of the rare earth orthoferrites without the complicating factors of the lone pair on the Bi^{3+} and hence exclusion of the effects due to magnetoelectric coupling.

6.2 Experimental

6.2.1 Synthesis

A ~5 g sample of phase pure $LaFeO_3$ was synthesized by a previous member of the group, Dr. Christopher Kavanagh. Synthesis was based on traditional ceramic methods. Stoichiometric amounts of La_2O_3 (99.9 % Sigma-Aldrich) and Fe_2O_3 (99.9 % (metals basis, Alfa-Aesar) were ball-milled for a period of 1 hour at a rate of 600 rpm. The ball-milled powder was then heated for 5 hours at a temperature of 800 °C in an alumina crucible. Subsequent regrinding and re-annealing at 1100 °C for 10 hours resulted in the product.

6.2.2 Powder Diffraction

Sample purity was confirmed by PXRD analysis. Patterns were obtained on a PANalytical Empyrean diffractometer (Cu $K_{\alpha 1}$ radiation source).

Variable temperature PND experiments were carried out using both the High Resolution Powder Diffractometer (HRPD) instrument (for $25 \leq T \leq 550$ K) and the General Materials Diffractometer (GEM) (for $525 \leq T \leq 1284$ K) instruments at the ISIS facility, Oxfordshire. A sample weighing ~ 3g was loaded into a 13 mm cylindrical vanadium canister and placed in the diffractometer furnace, before being suspended in the neutron beam. Scans were counted for 40 μAh and 50 μAh (corresponding to 50 and 75 mins in collection time) for HRPD and GEM data measurements respectively.

Analysis of the neutron diffraction patterns was carried out *via* Rietveld refinement methods using the GSAS software package[12] and the EXPGUI[12] interface. For HRPD data a consistent refinement strategy was used, consisting of 1, 3, 21 and 5 parameters to model instrumental variables, scale factors, background and peak-shape for data from bank 1 only. For GEM data the same strategy was employed however data from banks 3-6 were used and 2 additional scale factors were refined. The magnetic moment was refined as "black red black" in GSAS convention, corresponding to the Shubnikov symmetry *Pn'ma'* (see Chapter 1 Section 1.8 & 1.9), with the moment constrained along the *c*-axis.

6.3 Results

6.3.1 PND analysis

The first data set measured at 25 K on the HRPD instrument can be successfully modelled in the orthorhombic *Pnma* spacegroup with a $\sqrt{2}a_p \times 2a_p \times \sqrt{2}a_p$ unit cell structure. Peaks arising from the condensation of the M_3^+ "in-phase" tilt, R_4^+ "out of phase" tilt and X_5^+[A] A-site displacement mode which occur at (***k*** = ½, ½, 0), (***k*** = ½, ½, ½) and (***k*** = 0, ½, 0) points respectively, are clearly present at this temperature. With reference to the group-theoretical analysis work carried out by Howard and Stokes[13], three space groups, in addition to *Pnma* ($a^+b^-b^-$), are found to possesses both in-phase and out-of-phase tilts simultaneously; $P2_1/m$ ($a^+b^-c^-$), *Cmcm* ($a^0b^+c^-$), $P4_2/nmc$ ($a^+a^+c^-$). Whilst all three space groups can possess active M_3^+, R_4^+ and X_5^+ distortion modes, the splitting pattern in the observed PND data, namely the splitting of (*hkh*) peaks indicates a $\sqrt{2}$ multiplicity along the *a* and *c* subcell axes, therefore only *Pnma* and $P2_1/m$ are valid. $P2_1/m$ can be discounted as being of too low symmetry, therefore the $a^+b^-b^-$ tilt system with primitive

orthorhombic *Pnma* symmetry is the only congruent model to the observed data. This is in accordance with previous structural studies on $LaFeO_3$, *i.e.* the $GdFeO_3$ structure-type typical of the rare earth orthoferrites. The fit to the PND pattern obtained at a temperature of 275 K on HRPD is shown in Figure 6.1. The structural model obtained from Rietveld refinement of the 300 K PND data is detailed in Table 6.1.

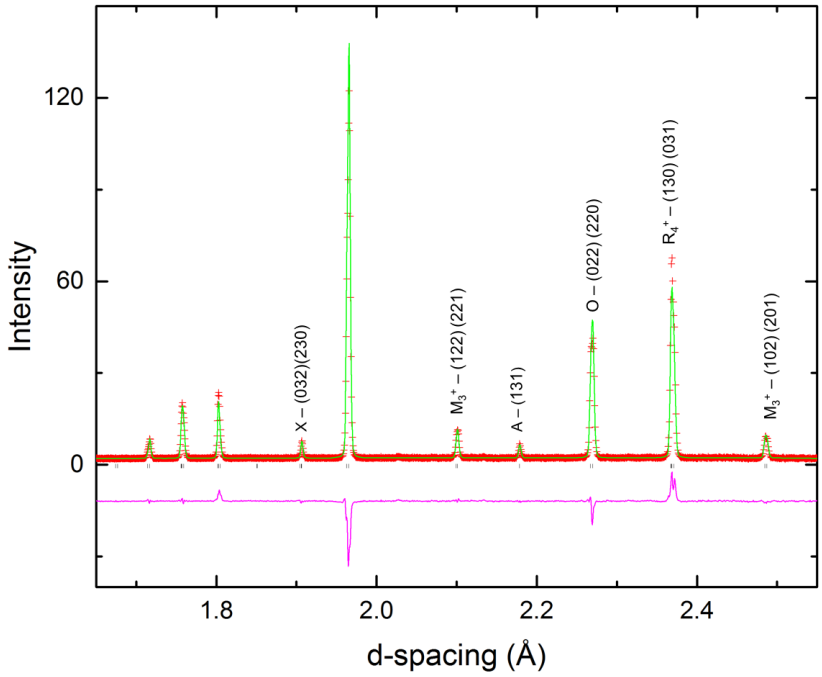

Figure 6.1 Portion of the PND pattern obtained on HRPD at 275 K modelled in the *Pnma* space group for $LaFeO_3$; $\chi^2 = 5.55$, $R_{wp} = 0.0531$. Peaks split due to $\sqrt{2}a_p \times 2a_p \times \sqrt{2}a_p$ unit cell metrics are labelled with an O. M- and R- and X-point peaks also show splitting due to the orthorhombicity of the unit cell. The letter A denotes a peak that would be split if a $2a_p \times 2a_p \times 2a_p$ unit cell were adopted.

Table 6.1. Crystallographic data for $LaFeO_3$ at 300 K modelled in the *Pnma* space group; a = 5.56540(5) Å, b = 7.85426(6) Å, c = 5.55619(4) Å.

Atom	Wyckoff position	x	y	z	100 * U_{iso} (Å^2)
La	4c	0.02842(15)	0.25	-0.0076(3)	0.193(16)
Fe	4b	0	0	0.5	-0.069(12)
O1	4c	0.4858(3)	0.25	0.0745(4)	0.19(3)
O2	8d	0.2824(2)	0.04009(15)	-0.2812(2)	0.13(2)

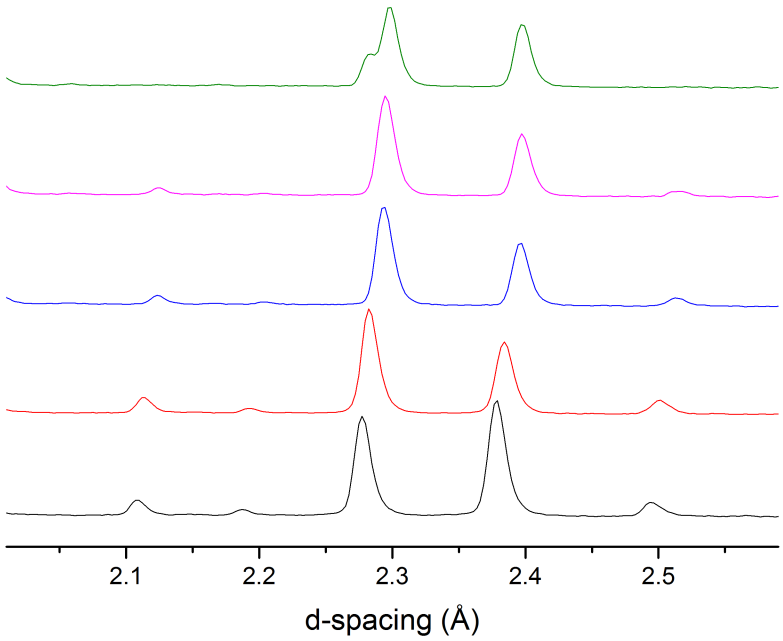

Figure 6.2 Schematic of raw PND data showing the diminishing M_3^+ peaks at a d-spacing of ~ 2.1 and 2.5 Å as the phase transition to the rhombohedral $R\bar{3}c$ phase (Glazer tilt system $a^-a^-a^-$) is approached and finally realized at a temperature of 1270 K. Raw data from bank 5 on the GEM diffractometer is shown at 575 K (black), 775 K (red), 1210 K (blue), 1255 K (pink), 1270 K (green).

The *Pnma* model is fitted as a single phase over the temperature range $25 \leq T \leq 1255$ K. Antiferromagnetic ordering is lost above a temperature of 760 ± 5 K (see section 6.3.2 for further details) Upon elevation of the temperature to 1270 K a phase transition to the rhombohedral $R\bar{3}c$ phase is clearly evidenced in the raw data with the loss of the in-phase M_3^+ tilt, observable in the diffraction data with the disappearance of the peak at $d \sim 2.5$ A (Figure 6.2). This phase progression corresponds to a change in the Glazer tilt system from $a^+b^-b^-$ -> $a^-a^-a^-$. This transition must be 1st order according to Landau theory; however, no phase coexistence is witnessed in the PND data, due to a lack of sufficient data sets in the vicinity of the transition. The centrosymmetric $R\bar{3}c$ phase is fitted to all data sets above and including 1270 K, with anisotropic refinement of the ADPs. The fit to the PND data at 1284 K showing the high temperature $R\bar{3}c$ of $LaFeO_3$ is shown in Figure 6.3. A detailed structural model for this phase is given in Table 6.2.

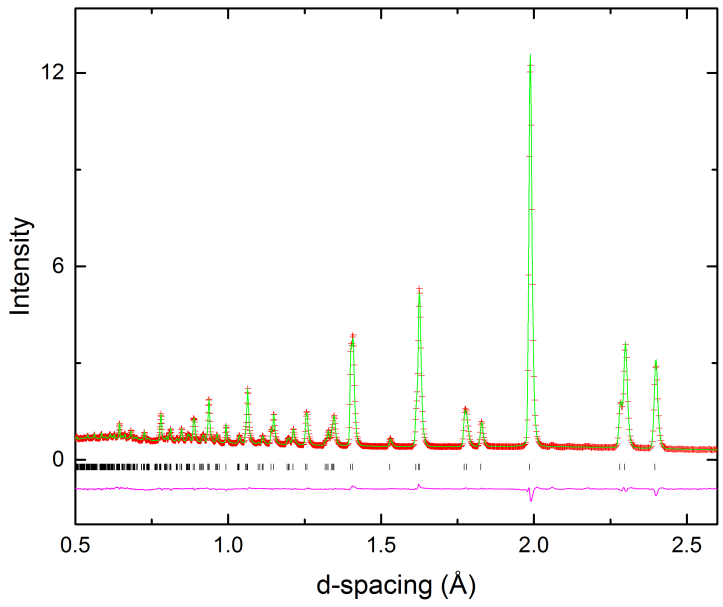

Figure 6.3 Portion of Rietveld refinement on PND data of $LaFeO_3$ recorded at 1284 K modelled in the $R\bar{3}c$ phase; $\chi^2 = 2.65$, $R_{wp} = 0.0225$.

Table 6.2. Crystallographic data for $LaFeO_3$ at 1284 K modelled in the $R\bar{3}c$ space group. a = 5.63043(4) Å, c = 13.68465(14) Å.

Atom	Wyckoff position	x	y	z	100 * U_{11} (Å^2)	100*$U_{22/33}$ (Å^2)
La	6a	0	0	0	2.15(2)	2.61(4)
Fe	6a	0.5	0.5	0.5	1.216(15)	1.28(3)
O	18b	0.22444(7)	0.33	0.0833	3.36(2)	2.49(4)

6.3.2 Magnetic structure of $LaFeO_3$

The magnetic structure adopted by $LaFeO_3$ is that of a G-type antiferromagnet, with Shubnikov symmetry *Pn'm'a* (see Chapter 1, Section 1.8 & 1.9). For G-type antiferromagnetism the adjacent electron spins both *intra*-plane and *inter*-plane are aligned antiparallel[14] (shown in Figure 6.4). This antiferromagnetic ordering is exhibited across the series for the rare earth orthoferrites and in BLFO50.

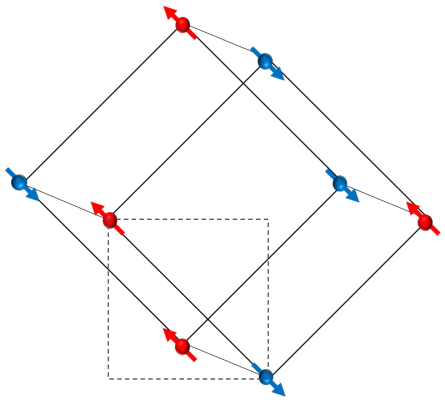

Figure 6.4 Schematic of the magnetic ordering in a G-type antiferromagnet with orthorhombic unit cell. The dashed line represents one face of the cubic parent cell.

The magnetic structure of $LaFeO_3$ was modelled in the GSAS software package[15] using the EXPGUI graphical interface[12] with the magnetic moment constrained along the *c*-axis. The dominant peak corresponding to the magnetic ordering appears in the diffraction data at a d-spacing of ~ 4.55 Å. Rietveld refinement carried out on GEM data at 575 K (Figure 6.5), clearly shows the peak corresponding to the magnetic ordering.

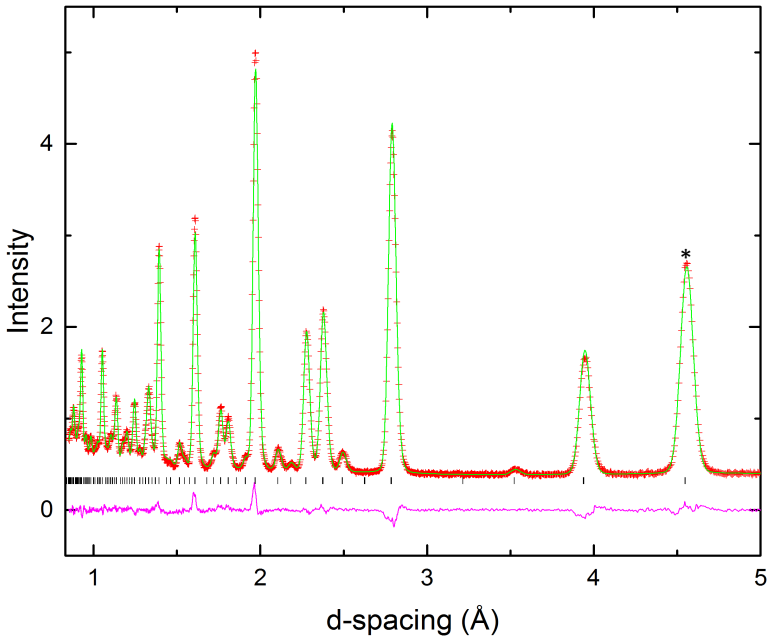

Figure 6.5 Rietveld refinement of PND data on $LaFeO_3$ at 575 K obtained on the GEM instrument; $\chi^2 = 3.27$, $R_{wp} = 0.0314$. Data from bank 5 is shown. The (011/110) peak arising due to the magnetic ordering is annotated with an *.

The magnetic peak at $d \sim 4.55$ Å gradually decreases as a function of temperature corresponding to the loss of magnetic ordering. Figure 6.6 shows the diminishing magnetic peak over the temperature range $25 \leq T \leq 765$ K. A plot of the magnetic moment as a function of temperature is shown in Figure 6.7. The Néel

temperature (T_N) for $LaFeO_3$ is given as 760 ± 5 K. This is slightly higher than previous reports that put T_N in the range of 735 ≤ T_N ≤ 750 K [16, 17], and also higher than that of $BiFeO_3$ (T_N ~653 K[18]).

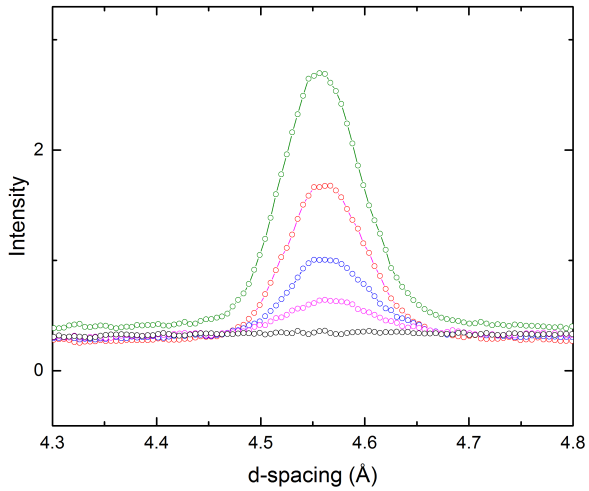

Figure 6.6 Raw data from bank 3 of GEM diffractometer highlighting loss of antiferromagnetic ordering at 765 K. Data recorded at the following temperatures is shown: 575 K (green), 665 K (red), 715 K (blue), 735 K (pink) and 765 K (black).

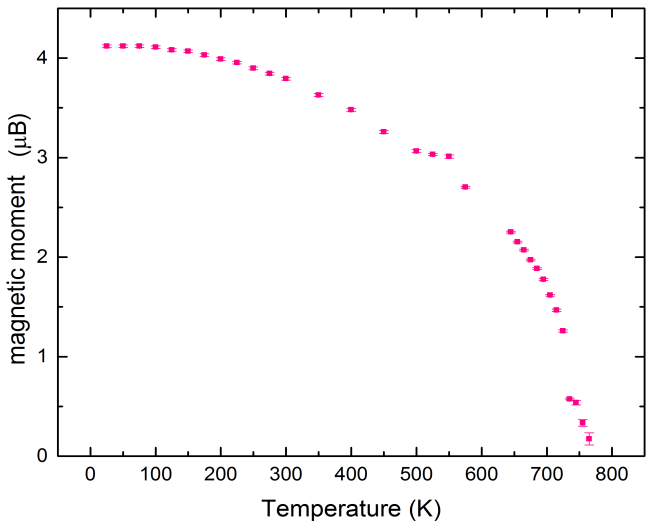

Figure 6.7 Net magnetisation for $LaFeO_3$ plotted as a function of temperature. T_N is given as 760 ± 5 K.

6.3.3 Trends in lattice parameters

A plot of the normalised lattice parameters as a function of temperature for $LaFeO_3$, generated from the results of the Rietveld refinement process, is included in Figure 6.8. The thermal evolution of lattice parameters shows the greatest degree of orthorhombicity at the lowest temperatures, with a gradual merging of the unit cell metrics until pseudocubic lattice parameters are adopted at $T \sim 765$ K (see Figure 6.9). This is coincidental with T_N, but most probably independent of the magnetic ordering. Beyond this, the curious $c > a$ crossover occurs. The lattice parameters subsequently begin to diverge as the orthorhombic – rhombohedral phase transition is approached.

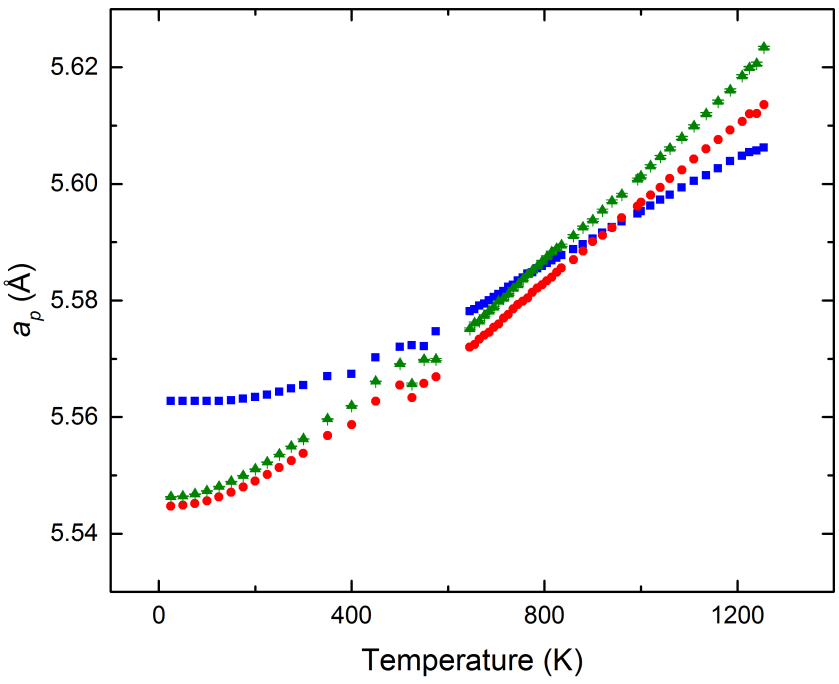

Figure 6.8 Normalised lattice parameters for $LaFeO_3$ sample obtained from Rietveld refinement. The *a* lattice parameter is represented by blue squares, the *b* lattice parameter by red circles and the *c* lattice parameter by green triangles. Note the $c > a$ crossover at $T \sim 770$ K. The discontinuous evolution at 525 K is most likely an artefact due to the different instrument used (switch from HRPD to GEM data is made here).

This phenomenon was also observed by Selbach *et al*. in their PXRD study of $LaFeO_3$. In the study by Selbach, this crossover was also found to approximately coincide with their established T_N (735 K[1]). A structural explanation for this that does not solely consider octahedral tilting is necessary, as in the case for the tilt system $a^+b^-b^-$ in the P*nma* setting, $c < a$ is always valid due to the presence of an out-of-phase tilt around the *a*-axis. This, however, is only strictly true if the octahedral units are perfectly rigid and no further structural distortion other than tilting occurs. Therefore, scrutiny of the structure and in particular, the *intra*-octahedral distortion, is necessary to indicate which structural feature is responsible for this crossover.

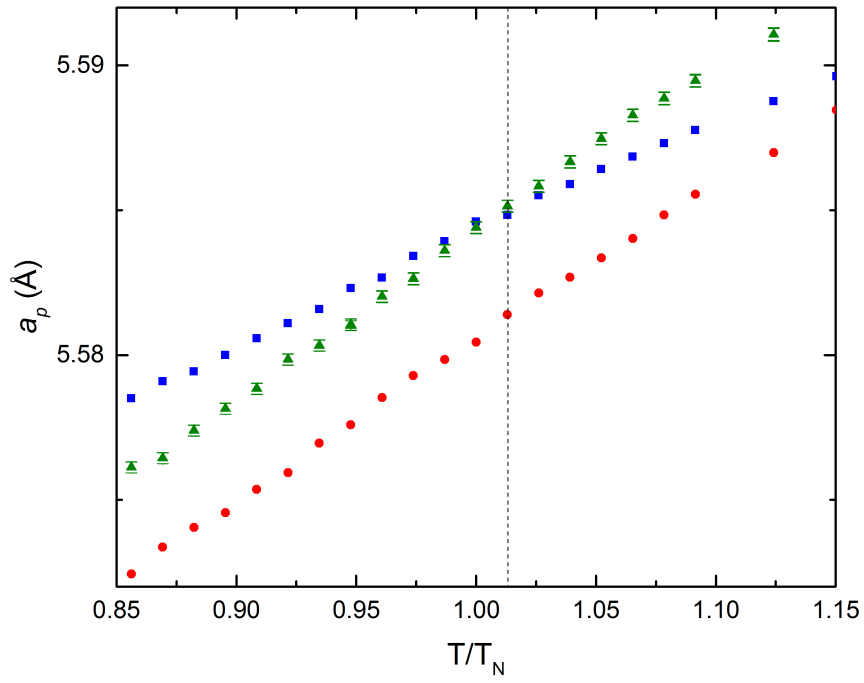

Figure 6.9 Plot of normalised lattice parameters as a function of T/T_N. Note the pseudocubic lattice parameters are assumed at T/T_N, with the crossover realised subsequently at a value of T/T_N = 1.01. The *a* lattice parameter is shown by blue squares, *b* by red circles and *c* by green triangles.

6.3.4 Orthorhombic Distortion

The degree of orthorhombic distortion (D_0) was evaluated using equation 6.1. A plot of D_0 *versus* temperature is shown in Figure 6.10.

$$D_0 = \frac{2|a-c|}{(a+c)} \qquad \text{Equation 6.1}$$

The orthorhombic distortion was found to be at its greatest at low temperatures; typical behavior for a perovskite as the octahedral tilting will be at a maximum here. The distortion then reaches a minimum in the vicinity of T_N at $T \sim 765$ K. This, of course, corresponds with the pseudocubic lattice parameters adopted immediately before the $c > a$ crossover.

The distortion then begins to increase as a function of temperature as the phase transition to the rhombohedral phase is approached and is again at a maximum just preceding the phase transition, indicating an alternative distortion mode is dominant in this temperature region whose influence becomes more significant with increasing tolerance factor. The trend in the orthorhombic distortion is also in agreement with that reported by Selbach[1].

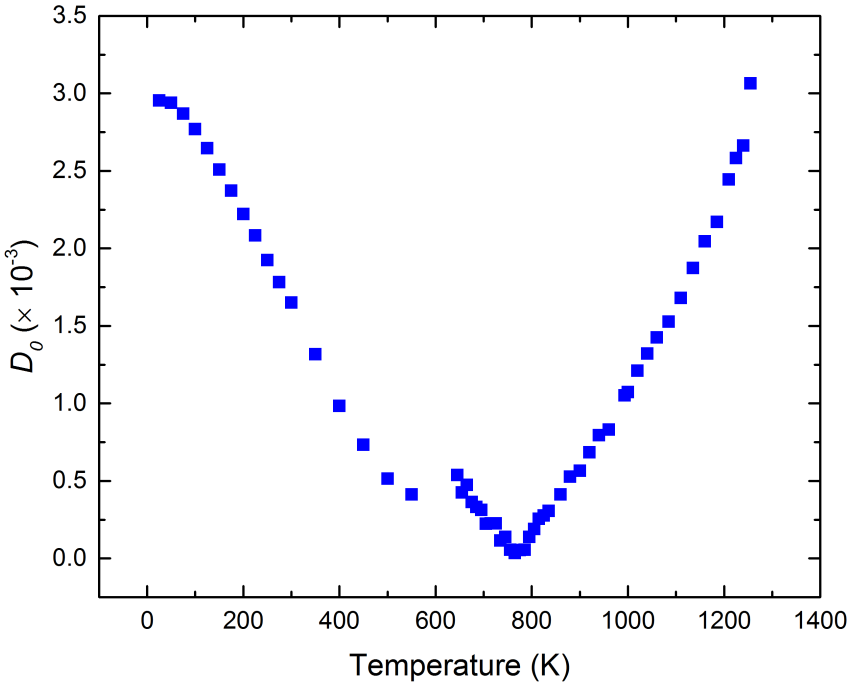

Figure 6.10 Plot of orthorhombic distortion parameter (D_0) as a function of temperature over the temperature regime $25 \leq T \leq 1255$ K. The "blip" is due to the change from HRPD data to GEM data.

6.3.5 Symmetry mode analysis

The ISODISTORT[19] software suite was employed to provide a quantitative appraisal of the decorrelated symmetry modes that act upon the distorted supercell. The seven independent positional parameters are now considered as seven distinct internal symmetry modes which act upon the lattice, with their magnitudes varying as a function of temperature. The seven distinct symmetry modes that act upon a crystal with P*nma* symmetry include two octahedral tilt modes (M_3^+ and R_4^+), three octahedral distortions (M_2^+[O], X_5^+[O] and R_5^+[O]) and two A-site displacement parameters (X_5^+[A] and R_5^+[A]). In the case of perovskites

with *Pnma* symmetry, it is the M_3^+ and R_4^+ tilt modes and the X_5^+[A] A-site distortion modes that have the most profound effect on the structure. Plots of these three significant distortion modes in addition to the R_5^+[A] mode are shown in Figure 6.11.

The M_3^+ mode (in-phase tilt) acts around the *b*-axis whilst the R_4^+ (out-of-phase) tilt mode acts around *a* (both tilts shown in Figure 6.11(a)). The in-phase tilt around *b* does not break four-fold symmetry in itself, which would result in equal *a* and *c* axes if it alone acted upon the structure. However, the out-of-phase tilt around *a* dictates the *a* > *c* relationship in the unit cell metrics. The X_5^+[A] mode corresponds to an anti-polar displacement of the La^{3+} cations in successive *b*-axis layers along *c*.

The trend exhibited by both the M_3^+ and R_4^+ tilt modes is a decrease with increasing temperature, typical behavior for a perovskite structure. However, it is notable that the variation in the M_3^+ tilt mode is much larger that of the R_4^+ tilt mode over the same temperature range. The variation in the M_3^+ tilt mode is 0.22 whereas the variation in R_4^+ is 0.12, significantly lower. This suggests that the in-phase tilt around *b* is the driving force in the subsequent phase transition to the $R\bar{3}c$ space group with rhombohedral symmetry. However, further analysis must be considered before any conclusion can be made. Interestingly, the R_4^+ mode amplitude appears to be saturated at 400 K, and only shows a small increase below this temperature. As the Glazer tilt system undergoes a change from $a^+b^-b^-$ to $a^-a^-a^-$ upon completion of the phase transition, the M_3^+ mode is lost, and whilst it retains some amplitude at 1255 K, it is showing a strong tendency toward zero.

Similarly to the R_4^+ and M_3^+ modes, the X_5^+ mode corresponding to the anti-polar A-site displacements along *a* shows a tendency toward zero over the temperature range for the orthorhombic phase and is indeed almost zero upon the transition.

However, as the transition proceeds *via* a 1st order mechanism this mode is lost in a "step-wise" fashion. The R_5^+[A] mode describes a less significant A-site displacement along *c*, evidenced in the relative changes of the two A-site displacement modes shown in Figure 6.11(b).

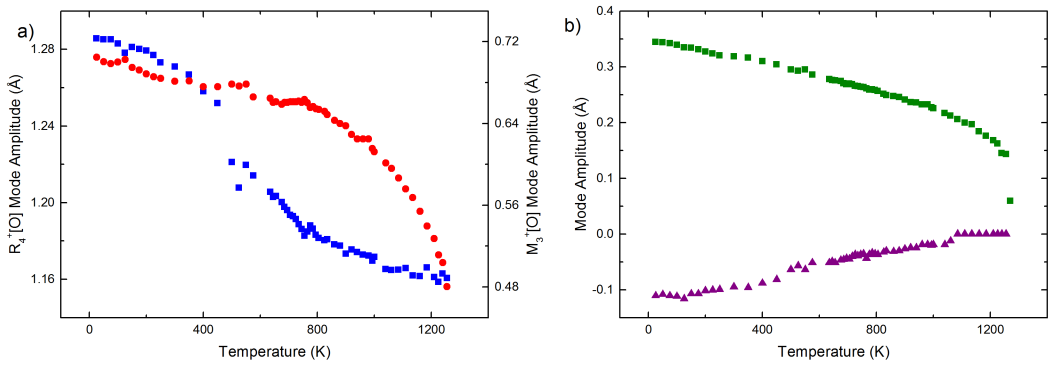

Figure 6.11 Mode amplitudes as a function of temperature for a) the R_4^+ (blue squares), M_3^+ (red circles) modes and b) X_5^+[A] (green squares) and R_5^+[A] A-site displacement modes (purple triangles) over the temperature regime $25 \leq T \leq 1255$ K.

The three symmetry adapted modes relating to the oxygen atoms represent different distortions of the octahedral units. These three octahedral distortion modes are not considered significant in rare earth orthoferrites when in the *Pnma* setting, and indeed the ISODISTORT output shows that these three modes do not vary significantly over the temperature range studied (Figure 6.12). Therefore, it is not anticipated that they play any role in the orthorhombic to rhombohedral phase transition. However, interestingly the R_5^+ distortion mode (which has a scissoring effect on the cross-sectional octahedral angles in the *ab* plane) shows an increase in mode amplitude away from equilibrium at temperature of 525 K and above. This could, therefore, be the driving force in the $c > a$ crossover. However, more analysis, is needed before any conclusion can be drawn.

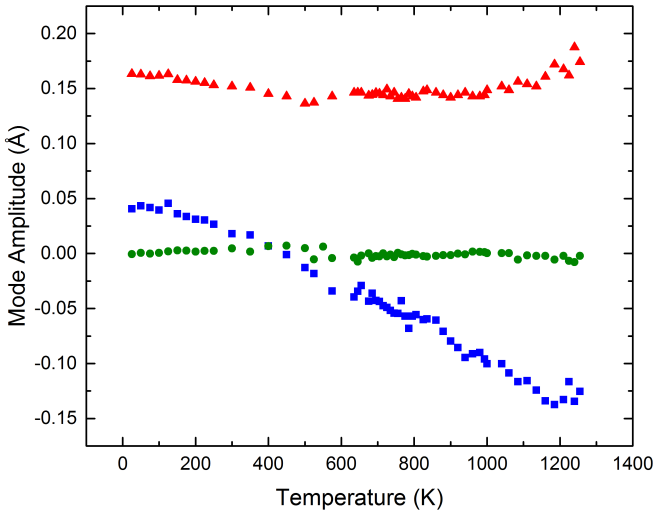

Figure 6.12 Evolution of the octahedral distortion modes over the temperature range $25 \leq T \leq 1255$ K. The X_5^+[O] mode is represented red triangles, M_2^+[O] by green circles and R_5^+[O] mode by blue squares.

6.4 Discussion

6.4.1 *Pnma* and $R\bar{3}c$ phases and the origin of the $c > a$ crossover

The low temperature stabilized *Pnma* ($a^+b^-b^-$) structure of $LaFeO_3$ is the most common phase in which the perovskite structure-type crystallises[6, 20]. Theoretical work by Woodward indicated that this structure is the most stable for perovskites with a Goldschmidt tolerance factor of $t < 0.975$ ($LaFeO_3$ has a tolerance factor of 0.954). For structures with a tolerance factor of $t < 0.975$, the large rotation angles that occur due to the small cation at the A-site result in significantly shortened A-O bond lengths and increased anion-anion repulsive interactions. The $a^+b^-b^-$ tilt system offers the best compromise between maximising the A-X bonding

interactions and minimising the repulsive A-X overlap[21]. For tolerance factors in the range, 0.975 < *t* < 1.01, the $R\bar{3}c$ ($a^-a^-a^-$) structure is stabilised. The transition from *Pnma* - $R\bar{3}c$ occurs as a function of temperature in $LaFeO_3$[1], $LaGaO_3$[9, 10] and $LaCrO_3$[10]. In $LaGaO_3$ and $PrNiO_3$ the orthorhombic to rhombohedral transition has also been shown to be pressure-induced[22, 23]. Schematics of the *Pnma* and $R\bar{3}c$ structure in $LaFeO_3$ are given in Figure 6.13 below.

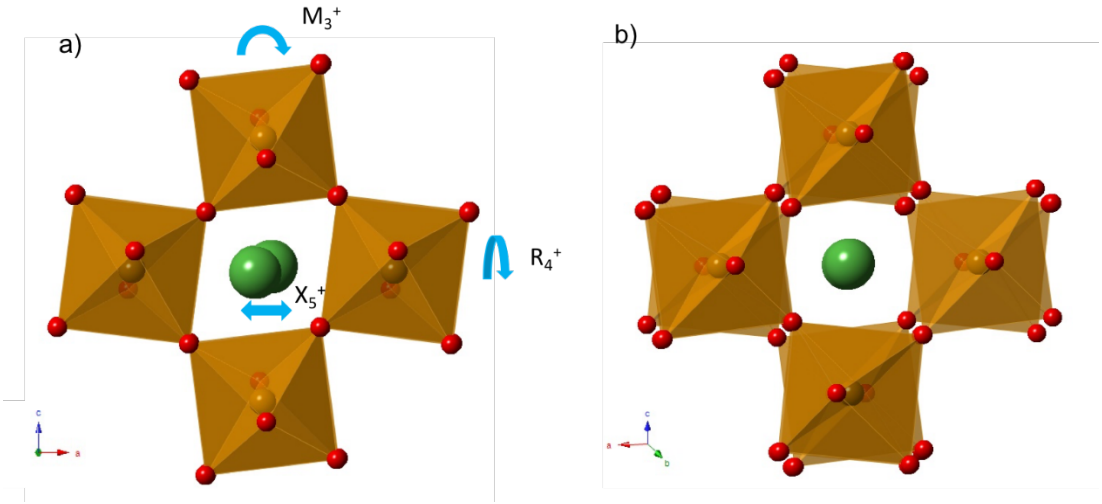

Figure 6.13 Schematic of *Pnma* structure in $LaFeO_3$ at RT (275 K) (a) showing in-phase tilting of octahedra in adjacent layers along the *b*-axis. The actions of the three most significant distortion modes, M_3^+, R_4^+ and X_5^+ are indicated by arrows. The $R\bar{3}c$ crystal structure is shown in (b) highlighting the out-of-phase tilt about [111]. La is shown in green, Fe in orange and O in red.

Work by Zhou and Goodenough on the $RNiO_3$ series (R = La, Pr, …, Gd), concluded that the *c* > *a* crossover is a pre-requisite for the orthorhombic to rhombohedral transition, and that this is found to occur as a function of increasing ionic radius (IR) at the A-site (or by extension increasing tolerance factor as a function of temperature or pressure). Whilst the octahedral tilting distortions in *Pnma* impose *a* > *c*, this is only true under the assumption that the octahedra tilt as rigid bodies. Zhou and Goodenough demonstrated an additional inherent *intra*-octahedral

distortion in the structures of the $RNiO_3$ family that drives the $c > a$ crossover. This distortion away from regular octahedra had a more profound effect on the structure as a function of increasing IR of the A-site cation. At a critical IR (identified as 1.11 Å for the $RNiO_3$ series[6, 23]) this *intra*-octahedral distortion becomes significant enough to overcome the restrictions imposed by the tilt system and the $c > a$ crossover occurs. By extension, a reduction in the octahedral tilting angles as a function of temperature or pressure can result in a similar crossover due to the competition between the conditions imposed by the tilt system ($a > c$) and those associated with the octahedral distortion ($c > a$). $LaFeO_3$ is the only member of the $LnFeO_3$ series that demonstrates this $c > a$ crossover. This is most certainly due to $LaFeO_3$ having a tolerance factor that is sufficiently large to undergo a phase transition to the rhombohedral phase, $R\bar{3}c$, as a function of temperature ($t = 0.954$, where $t = 0.975$[21] stabilises the $R\bar{3}c$ phase).

6.4.1.1 Fe-O bond lengths

To identify the specific lattice distortion that is responsible for this crossover in $LaFeO_3$, it is necessary to look at other structural distortions which are not related to the octahedral tilts; these include the variation in Fe-O bond lengths, *inter*-octahedral (Fe-O-Fe) and *intra*-octahedral (O-Fe-O) bond angles. The Fe-O bond lengths (Figure 6.14) show little variation for Fe-O2 and Fe-O2'. However, a significant expansion can be seen in the magnitude of the Fe-O1 bond length (~ 0.028 Å). When related to the structure (Figure 6.15), it becomes apparent that the Fe-O1 bond lies directly along the *b*-axis, and is in fact responsible for the entire thermal expansion of the *b*-axis (~ 0.087 Å) across the temperature range $25 \leq T \leq 1255$ K for the *Pnma* structure.

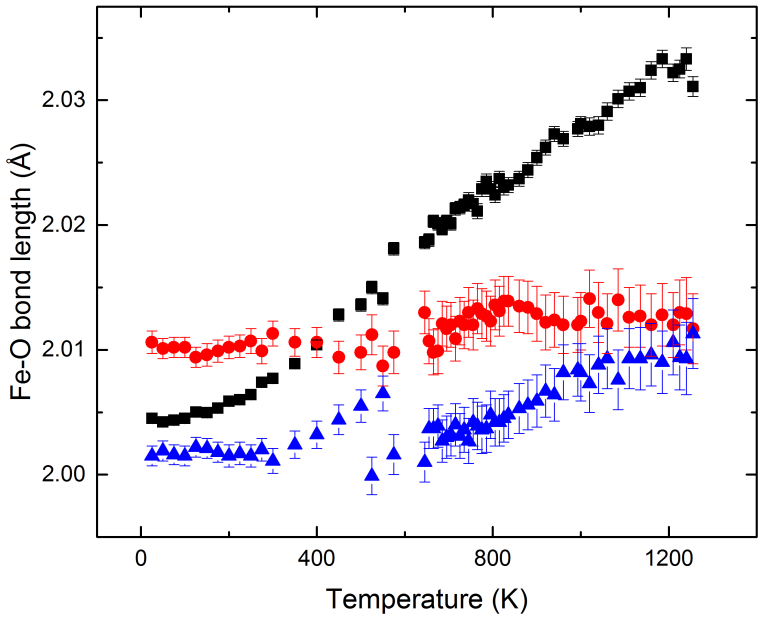

Figure 6.14 Thermal evolution of Fe-O bond lengths for the temperature regime 25 ≤ T ≤ 1255 K. Distances corresponding to the Fe-O1 bond are shown by black squares, Fe-O2 by blue triangles and Fe-O2' by red circles.

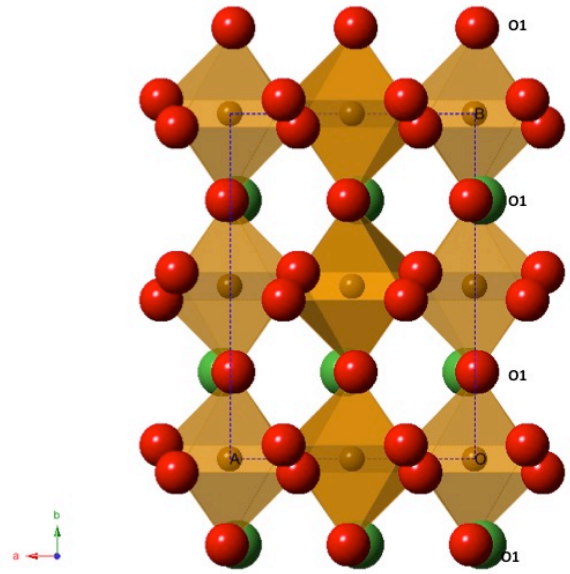

Figure 6.15 Schematic of $LaFeO_3$ structure in *Pnma* setting. La is shown in green, Fe in orange and O in red. The dashed lines represent the unit cell. Note that the Fe-O1 bond lies along the *b*-axis. The unit cell along *b* is effectively 4 × Fe-O1 bond distance, therefore the expansivity of *b* is mostly accounted for by the increase of the Fe-O1 bond length.

6.4.1.2 Fe-O-Fe bond angles

The variation in the Fe-O-Fe *inter*-octahedral bond angles as a function of temperature (Figure 6.16) correspond approximately to the R_4^+ and M_3^+ tilt modes acting about the *a*- and *b*-axes respectively. The Fe-O1-Fe bond angle corresponds to the R_4^+ out-of-phase tilt mode and accordingly, this bond angle does not vary as significantly as the Fe-O2-Fe bond angle that corresponds to the M_3^+ in-phase tilt mode. The relationship between the *inter*-octahedral bond angles and the *a*- and *b*-axes is shown in Figure 6.18. An increasing Fe-O-Fe bond angle indicates a decreasing octahedral tilt. The decrease that is observed in the Fe-O1-Fe bond is therefore likely due to a distortion in the octahedra rather than an increase in the out-of-phase tilt (as discussed in section 6.3.5 the R_4^+ tilt mode varies only slightly with temperature). This seems probable as it appears to become more effective as the $c >$ a crossover temperature of 765 K is approached.

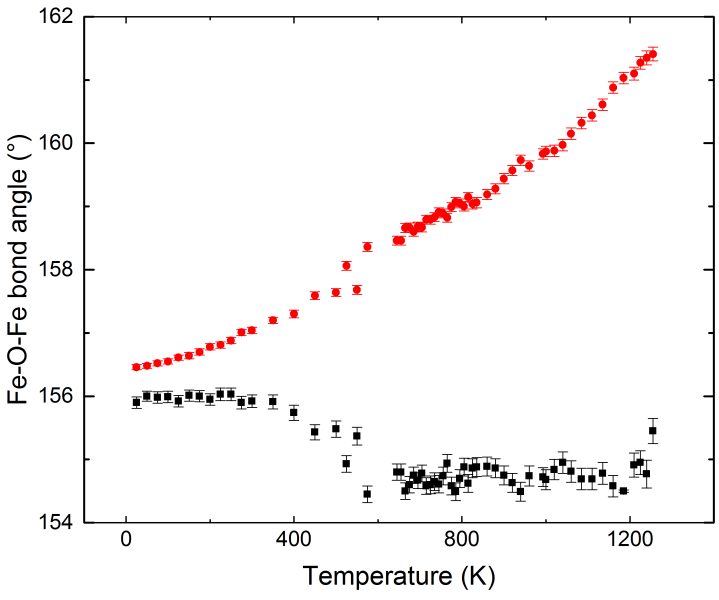

Figure 6.16 Thermal evolution of the Fe-O1-Fe (black squares) and Fe-O2-Fe (red circles) over the temperature range $25 \leq T \leq 1255$ K.

6.4.1.3 O-Fe-O bond angles

Due to the observed trend in the Fe-O1-Fe bond angle, the *inter*-octahedral bond angles (Figure 6.17) were examined, with the aim of rationalising the $c > a$ crossover. Both the O1-Fe-O2, and O1-Fe-O2' bond angles show a significant variation as a function of temperature, with the O1-Fe-O2 decreasing, and the O1-Fe-O2' exhibiting a corresponding increase of ~ 1.5 °. Both bond angles begin to converge to an equilibrium value of 90 ° as the transition to the centrosymmetric $R\bar{3}c$ phase is approached. The most interesting behaviour, however, is observed in the O2-Fe-O2' bond angle which retains a constant value of ~ 91.25 ° throughout the temperature regime $25 \leq T \leq 1255$ K. When related to the structure (Figure 6.18) the significance of this small deviation from 90° becomes apparent as a bond angle for the O2-Fe-O2' bond above 90 ° favours a larger *c*-axis at the expense of *a*. This distortion in the O2-Fe-O2' bond is not related to any of the octahedral distortion modes discussed in the ISODISTORT symmetry mode analysis and can instead be considered as a lattice strain.

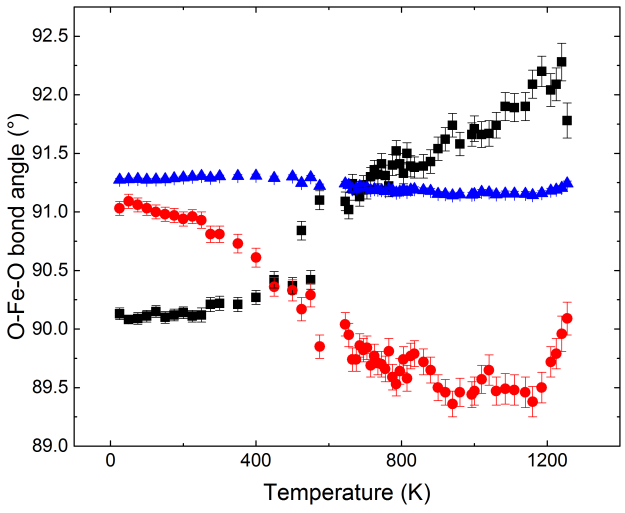

Figure 6.17 Thermal evolution of the *intra*-octahedral bond angle. The O1-Fe-O2 bond angle is depicted by red circles, the O1-Fe-O2' by black squares and the O2-Fe-O2' by blue triangles.

This enhanced bond angle, whilst present throughout the temperature regime for the *Pnma* phase is in direct competition with the R_4^+ tilt mode that favours $a > c$. At low temperatures, when the octahedral tilting is at a maximum, the out-of-phase tilt around *a* "wins out". However, as the amplitude of this tilt continues to diminish, the effect from the O2-Fe-O2' bond angle becomes increasingly significant, until eventually $c > a$ metrics are realised at a temperature above 765 K. The relative values for the *c* and *a* unit cell edges continue to diverge as the R_4^+ mode amplitude decreases as a function of temperature beyond the crossover point. The deviation of 1.5 ° may initially seem rather diminutive to exact such a large influence on the structure. However, previous work by Woodward has shown that an increase of as little as 1 ° in the O-B-O bond angle is sufficient to overcome modest tilts about the *a*-axis[24].

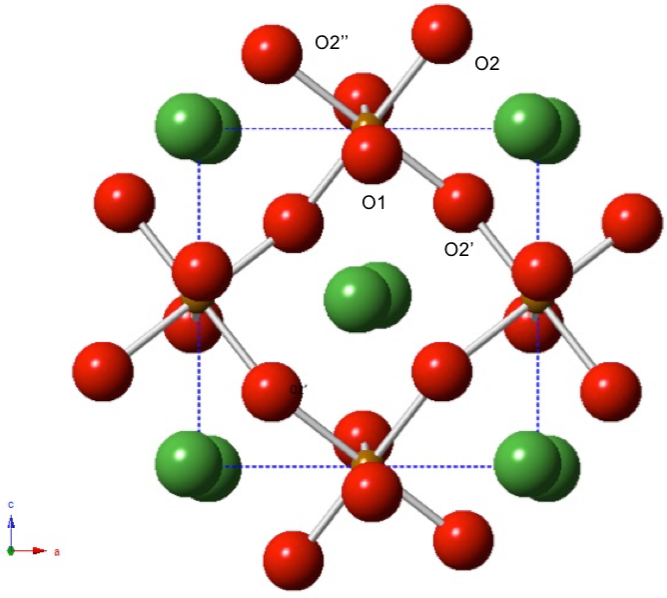

Figure 6.18 Ball and stick representation of $LaFeO_3$ looking down the *b*-axis, highlighting the effect a O2-Fe-O2' bond angle > 90 ° has on both the *c*- and *a*-axes. The relationship between Fe-O1-Fe and Fe-O2-Fe bond angle and the M_3^+ and R_4^+ tilt modes is also apparent. La is shown in green, Fe in orange and O in red. The dashed line indicates the unit cell.

6.4.2 Evolution of lattice metrics and BVS arguments

With further note to the evolution of the lattice cell metrics, the continued divergence of the *a* and *c* lattice parameters at low temperature occurs as a consequence of the increasing anti-polar A-site displacements along *c* (*i.e.* the X_5^+[A] distortion mode) as opposed to the out of phase tilt (R_4^+) mode that is relatively invariant below 400 K. Typically, for *Pnma* perovskites the octahedral tilting and A-site displacements are co-operative; therefore, the variation in the X_5^+ mode at low temperature, at which point the R_4^+ mode is largely unchanged, indicates that it is in fact the M_3^+ mode that permits the A-site displacement. As the M_3^+ mode does not impact the *c*/*a* ratio, this allows increased A-site displacements with a correspondingly small variation in the *a* lattice metric below 400 K. BVS calculations carried out on $LaFeO_3$, indicate that the BVS of La^{3+} increases due to enhanced A-site displacement at lower temperatures (Figure 6.19). BVS arguments have shown that the large distribution in the A-O bond lengths for *c* relative to *a* should allow for expansion of the *a*-axis as the temperature is decreased[25, 26]. This effect, however, is clearly not sufficient to impact on the previous argument, in which a co-operation of the in-phase tilt over the out-of-phase tilt results in relatively low thermal expansivity of the *a*-axis. The continued trend in the normalised *b* lattice parameter whereby it is smaller than *a* and *c* throughout the temperature regime is suggestive of orbital ordering[24].

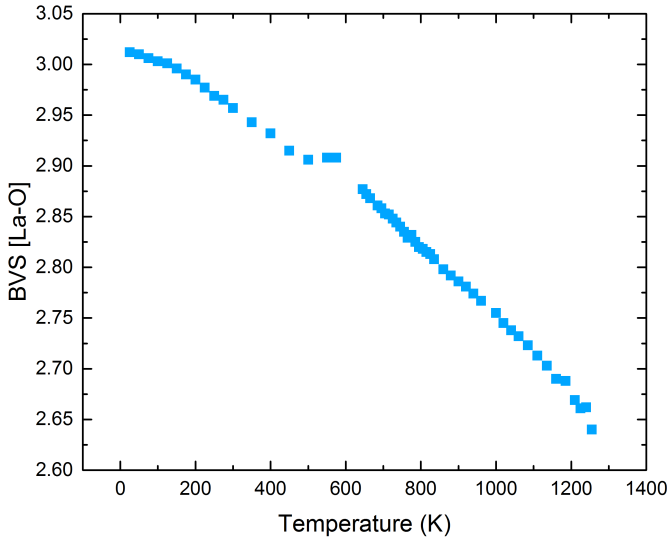

Figure 6.19 Thermal evolution of the bond valence sum for the La site (calculated as 12 coordinate LaO_{12}). The plateau at $T \sim 575$ K is due to switching of the PND instruments from which the data were obtained rather than any real structural effect.

6.4.3 Comparison to BLFO50

The original aim of this work was to provide a "simple" comparative model to BLFO50; isolating any structural anomalies attributable to magnetoelectric coupling effects. BLFO50 exhibits some unusual structural responses as a function of temperature, with both the M_3^+ and X_5^+[A] distortion modes decreasing with the onset of anti-ferromagnetic ordering. This leads to a plateauing of the *c*-axis rather than *a* as seen in $LaFeO_3$ below T_N (~ 700 K[11]). This anomalous behavior for both the in-phase tilt and A-site displacement is not echoed in $LaFeO_3$, which demonstrates "typical" behavior for a perovskite with an increase in the mode amplitudes as a function of decreasing temperature. Additionally, the orthorhombic distortion in BLF050 shows a broad maximum around T_N. This is in

complete contrast to $LaFeO_3$ which adopts pseudocubic lattice parameters in the vicinity of T_N, corresponding to a minimum in the orthorhombic distortion. The *c* > *a* crossover is not observed in BLFO50, despite the similar tolerance factor to $LaFeO_3$ (Bi^{3+} and La^{3+} possess very similar IRs of 1.17 and 1.16 Å respectively[26]). This is most likely due to the introduction of Bi^{3+} at the perovskite A-site, with Zhou and Goodenough predicting that changes in electronic structure may alter the effect of the octahedral distortion that drives the *c* > *a* crossover.

Owing to the nominally similar IR of Bi^{3+} compared to La^{3+}, the effect of the stereochemically active lone pair on bismuth is evidenced in the contrasting thermal evolution of the mode amplitudes and by extension, unit cell parameters, whilst cell volumes of $LaFeO_3$ and BLFO50 remain comparable throughout the temperature regime. At room temperature, the *Pnma* structures in both are similar, with similar mode amplitudes for the three significant distortion modes (mode amplitudes for the M_3^+, R_4^+ and X_5^+[A] are 0.719, 1.206, 0.321 and 0.744, 1.225 and 0.259 for $LaFeO_3$ and BLFO50 respectively). At 700 K, the anomalies in M_3^+ and X_5^+[A] mode evolution are evident from their corresponding mode amplitudes (0.658, 1.196, 0.268 for $LaFeO_3$ and 0.837, 1.167 and 0.313 and BLFO50). Unit cell volumes at 300 K and 700 K are 242.8 and 245.5 $Å^3$ for both $LaFeO_3$ and BLFO50 respectively.

6.5 Conclusions and Further Work

The thermal evolution of $LaFeO_3$ has been investigated with the use of variable temperature PND experiments over the temperature range $25 \leq T \leq 1284$ K. A detailed structural analysis using symmetry mode arguments and both bond length and bond angle analysis was detailed. This allowed for rationalisation of the $c > a$ crossover in the unit cell metrics of the orthorhombic phase; found to occur as a result of an inherent distortion in the equilibrium O-Fe-O bond angle that favours a larger *c*-axis relative to *a*. Whilst constant, this octahedral distortion is found to have a more profound effect on the structure as $t < 1$ approaches unity *i.e.* as tilt angle is reduced. This is in agreement with previous work by Zhou and Goodenough (on members of the $LnNiO_3$ series) and Woodward, who first demonstrated that a deviation of as little as 1 ° in the equilibrium O-Fe-O bond angle can overcome moderate octahedral tilts[24]. The antiferromagnetic – paraelectric transition was identified at 760 ± 5 K; slightly higher than in previous studies (T_N 735 -750 K [16,17]). When compared to the evolution of the unit cell metrics, the Néel temperature and the crossover of the *a* and *c* unit cell axes coincide, however this seems to be purely coincidental as the $c > a$ crossover can be fully rationalised in terms of octahedral distortion and is not a consequence of the antiferromagnetic ordering. Additionally, the *Pnma* – *R*3*c* phase transition was observed at 1260 ± 7K. Trends in the lattice parameters at low temperature were rationalised using symmetry mode arguments. The anomalous behavior exhibited in the thermal evolution of the M_3^+ and X_5^+[A] modes with the onset of the magnetic ordering in BLFO50 was not echoed in $LaFeO_3$, confirming that this peculiar structural behavior must be a magnetostrictive effect brought about by magnetoelectric coupling owing to the presence of the Bi^{3+} lone pair at the A-site.

6.6 References

1. Selbach, S. M.; Tolchard, J. R.; Fossdal, A.; Grande, T., Non-linear thermal evolution of the crystal structure and phase transitions of $LaFeO_3$ investigated by high temperature X-ray diffraction. *Journal of Solid State Chemistry* **2012,** *196*, 249-254.
2. Kuscer, D.; Hrovat, M.; Holc, J.; Bernik, S.; Kolar, D., Some characteristics of Al_2O_3- and CaO-modified $LaFeO_3$-based cathode materials for solid oxide fuel cells. *Journal of Power Sources* **1996,** *61*, 161-165.
3. Mikhaylovskiy, R. V.; Hendry, E.; Secchi, A.; Mentink, J. H.; Eckstein, M.; Wu, A.; Pisarev, R. V.; Kruglyak, V. V.; Katsnelson, M. I.; Rasing, T.; Kimel, A. V., Ultrafast optical modification of exchange interactions in iron oxides. *Nature Communications* **2015,** *6*.
4. Traversa, E.; Matsushima, S.; Okada, G.; Sadaoka, Y.; Sakai, Y.; Watanabe, K., NO_2 sensitive $LaFeO_3$ thin films prepared by r.f sputtering. *Sensors and Actuators B-Chemical* **1995,** *25*, 661-664.
5. Meng, X. X.; He, F. L.; Shen, X. Q.; Xiang, J.; Wang, P., Nanocrystalline $La_{1-x}K_xFeO_3$ (x = 0 - 0.4) Oxides for Catalytic Removal of Soot from Practical Diesel Exhaust Emission. *Industrial & Engineering Chemistry Research* **2011,** *50*, 11037-11042.
6. Zhou, J. S.; Goodenough, J. B., Universal Octahedral-Site Distortion in Orthorhombic Perovskite Oxides. *Physical Review Letters* **2005,** *94*, 065501.
7. Goldschmidt, V. M., Die Gesetze der Krystallochemie. *Naturwissenschaften* **1926,** *14*, 477-485.
8. Woodward, D. I.; Reaney, I. M., Electron diffraction of tilted perovskites. *Acta Crystallographica Section B* **2005,** *61*, 387-399.
9. Marti, W.; Fischer, P.; Altorfer, F.; Scheel, H. J.; Tadin, M., Crystal structures and phase transitions of orthorhombic and rhombohedral $RGaO_3$ (R = La, Pr, Nd) investigated by neutron powder diffraction. *Journal of Physics-Condensed Matter* **1994,** *6*, 127-135.
10. Oikawa, K.; Kamiyama, T.; Hashimoto, T.; Shimojyo, Y.; Morii, Y., Structural phase transition of orthorhombic $LaCrO_3$ studied by neutron powder diffraction. *Journal of Solid State Chemistry* **2000,** *154*, 524-529.
11. Kavanagh, C. M.; Goff, R. J.; Daoud-Aladine, A.; Lightfoot, P.; Morrison, F. D., Magnetically Driven Dielectric and Structural Behavior in $Bi_{0.5}La_{0.5}FeO_3$. *Chemistry of Materials* **2012,** *24*, 4563-4571.
12. Toby, B. H., EXPGUI, a graphical user interface for GSAS. *Journal of Applied Crystallography* **2001,** *34*, 210-213.
13. Howard, C. J.; Stokes, H. T., Group-theoretical analysis of octahedral tilting in perovskites. *Acta Crystallographica Section B* **1998,** *54*, 782-789.
14. Mochizuki, M.; Imada, M., G-type antiferromagnetism and orbital ordering due to the crystal field from the rare-earth ions induced by the $GdFeO_3$-type

distortion in $RTiO_3$ where R = La, Pr, Nd and Sm. *Journal of the Physical Society of Japan* **2004,** *73*, 1833-1850.
15. Larson, A. C.; Von Dreele, R. B., Los Alamos Natl. Lab: 1994.
16. Stolen, S.; Gronvold, F.; Brinks, H.; Atake, T.; Mori, H., Heat capacity and thermodynamic properties of $LaFeO_3$ and $LaCoO_3$ from T = 13 K to T = 1000 K. *Journal of Chemical Thermodynamics* **1998,** *30*, 365-377.
17. Koehler, W. C.; Wollan, E. O., Neutron-diffraction study of the magnetic properties of perovskite-like compounds $LaBO_3$. *Journal of Physics and Chemistry of Solids* **1957,** *2*, 100-106.
18. Palkar, V. R.; John, J.; Pinto, R., Observation of saturated polarization and dielectric anomaly in magnetoelectric $BiFeO_3$ thin films. *Applied Physics Letters* **2002,** *80*, 1628-1630.
19. Campbell, B. J.; Stokes, H. T.; Tanner, D. E.; Hatch, D. M., ISODISPLACE: a web-based tool for exploring structural distortions. *Journal of Applied Crystallography* **2006,** *39*, 607-614.
20. Lufaso, M. W.; Woodward, P. M., Prediction of the crystal structures of perovskites using the software program SPuDS. *Acta Crystallographica Section B* **2001,** *57*, 725-738.
21. Woodward, P. M., Octahedral tilting in perovskites. II. Structure stabilizing forces. *Acta Crystallographica Section B* **1997,** *53*, 44-66.
22. Kennedy, B. J.; Vogt, T.; Martin, C. D.; Parise, J. B.; Hriljac, J. A., Pressure-induced orthorhombic to rhombohedral phase transition in $LaGaO_3$. *Journal of Physics-Condensed Matter* **2001,** *13*, L925-L930.
23. Zhou, J. S.; Goodenough, J. B.; Dabrowski, B., Structure anomaly and electronic transition in $RNiO_3$ (R = La,Pr,...,Gd). *Physical Review B* **2004,** *70*, 081102.
24. Woodward, P. M.; Vogt, T.; Cox, D. E.; Arulraj, A.; Rao, C. N. R.; Karen, P.; Cheetham, A. K., Influence of cation size on the structural features of $Lu_{1/2}A_{1/2}MuO_3$ perovskites at room temperature. *Chemistry of Materials* **1998,** *10*, 3652-3665.
25. Brown, I. D., Chemical and steric constraints in inorganic solids. *Acta Crystallographica Section B* **1992,** *48*, 553-572.
26. Shannon, R. D., Revised Effective Ionic-Radii and Systematic Studies of Interatomic Distances in Halides and Chalcogenides. *Acta Crystallographica Section A* **1976,** *32*, 751-767.

7 $CsBi_{0.6}La_{0.4}Nb_2O_7$: A Hybrid-Improper Ferroelectric

7.1 Introduction

Recent theoretical and experimental work has revealed a novel mechanism through which new polar and, in some cases, ferroelectric structures have been isolated in several families of layered perovskites[1, 2]. Whilst traditional ABO_3 perovskites have been studied, in depth, for their wide range of physical properties and extensive chemical tunability, relatively few of these structures are polar, with even fewer displaying ferroelectric properties. In the case of the layered perovskite structures, the paraelectric – ferroelectric transition may involve the condensation of two non-polar zone-boundary lattice distortions (typically tilting of the BO_6 octahedra). The two zone boundary order parameters then couple to a polar lattice distortion in a so-called "tri-linear coupling" mechanism[3]. This is in contrast to the SOJT mechanism observed for traditional ABO_3 perovskites whereby the ferroelectricity is driven by the freezing of a zone-centre polar lattice distortion[4]. The origin of the polarity in these tri-linear coupling systems can therefore be thought of as a geometric effect (specifically octahedral tilting and A-site displacements) rather than a chemical one (charge transfer in d^0 transition metals)[5]. Owing to the similarity with improper ferroelectrics such as hexagonal $YMnO_3$, in which a zone-boundary lattice distortion is the primary order parameter that drives the ferroelectric transition, these systems are known as "Hybrid Improper Ferroelectrics"[6-8]. Similarly to improper ferroelectrics it is typically an ionic size mismatch and the associated octahedral tilting that indirectly result in distorted ferroelectric structures, thus allowing for novel design approaches and the potential discovery of many new polar or ferroelectric materials in these layered perovskite phases by targeted tuning of the chemical composition. Three families of layered perovskites, which have been highlighted

in theoretical studies and in many cases shown experimentally to be good candidates for new polar structures, are the Aurivillius phases ($Bi_2O_2[A_{n-1}B_nO_{3n+1}]$) (e.g. $SrBi_2Ta_2O_9$[9]), Ruddlesden-Popper phases ($A_{n+1}B_nO_{3n+1}$) (e.g. $Ca_3Mn_2O_7$[10], $Ca_3Ti_2O_7$[11]) and more recently the Dion-Jacobson phases ($A'[A_{n-1}B_nO_{3n+1}]$) (e.g. $RbBiNb_2O_7$). Whilst non-centrosymmetric structures have proven abundant in the Aurivillius family[12-14] they have been thus far less prevalent in the Ruddlesden-Popper and Dion-Jacobson families. However, this is changing with the recent work by Strayer *et al*., predicting, with the use of *ab initio* density functional theory calculations[2], that $CsLaNb_2O_7$, $CsLaTa_2O_7$ and their rubidium analogues each adopt polar ground state structures. Furthermore, a recent publication by Li *et al*. confirmed ferroelectricity in the Dion-Jacobson phase $RbBiNb_2O_7$[15]. This was the first instance that ferroelectricity had been shown experimentally in any Dion-Jacobson phases. The related compound, $CsBiNb_2O_7$, is of interest due to the observation by Snedden *et al*. that its room temperature structure ($P2_1am$ symmetry) possesses the same Glazer tilt system, $a^-a^-c^+$[16], as the ferroelectric Aurivillius phase ($A2_1am$ symmetry) and by extension could be expected to exhibit ferroelectric behaviour[17]. However, observing polarisation-field hysteresis had, until recently, proved difficult due to the hygroscopic nature of $CsBiNb_2O_7$, with water uptake believed to promote a high degree of proton conductivity[18]. A renewed interest in the system was sparked by the recent work published by Chen *et al*. in which they were able to successfully demonstrate ferroelectricity in $CsBiNb_2O_7$ for the first time experimentally [19]. Impedance measurements gave the T_c of $CsBiNb_2O_7$ to be 1033 ± 5 °C with a calculated spontaneous polarisation of 43 $\mu C\ cm^{-2}$, in good agreement with previous theoretical studies based on first-principles calculations[20, 21]. This result was further confirmed by thermal depoling measurements. Whilst the temperature dependence of the transition has been established, this does not offer information with regards to the crystallographic nature of the structural transition. First-principles calculations carried out by Fennie and Rabe highlighted the importance of octahedral rotations in the

resulting polar structure, however their calculations did not shed light on the mechanism by which the distorted polar phase arises from the *P*4/*mmm* parent[20]. A subsequent study by Benedek found that the tetragonal structure of $CsBiNb_2O_7$ was unstable to the Γ_5^-, M_2^+ and M_5^- modes with the polar $P2_1am$ structure found to be more stable when compared to *P*4/*mmm*, *Pmam*, *P*4/*mbm* and *C*2*mm* structures[21] (*i.e.* a structure that contained all three distortions was lower in energy than those which only contained one). However once again, the mechanism involved in the transition was not clarified. For these reasons, a detailed crystallographic analysis of the transition is necessary, specifically, with the purpose of establishing whether the proposed *P*4/*mmm* – $P2_1am$ transition proceeds as a 1st order "avalanche" transition, in which both primary order parameters (M_2^+ and M_5^-) condense simultaneously, or as a second order continuous transition *via* an intermediary phase with, for example, *Pmam* symmetry. Such an intermediary phase occurs in the case that one zone boundary distortion shows greater instability over the other, thus condensing at a higher temperature. It was originally believed that "even-layer" (*i.e. n* even in the generic formula) materials underwent a two-phase continuous transition and "odd-layer" materials a single-step discontinuous transition, however a detailed PND study by Lightfoot *et al*. on the temperature-dependent phase diagram of $SrBi_2Nb_2O_9$ (a double-layer Aurivillius phase) showed that this system undergoes a 1st order discontinuous transition, *I*4/*mmm* – $A2_1am$, disproving this initial theory[14]. Interestingly, the isostructural compound $SrBi_2Ta_2O_9$, behaves differently, with the *I*4/*mmm* – $A2_1am$ transition proceeding through an intermediary phase with *Amam* symmetry[9, 22]. Owing to this inability to predict the nature of the transition associated with the tri-linear coupling mechanism based on composition, theoretical and experimental studies on these systems are vital.

Previous PND studies have shown that decomposition of the $CsBiNb_2O_7$ starts to occur at a temperature of ~960 °C[18]. As this falls well below the reported Curie

temperature (T_C) of 1033 $\pm$ 5 °C, chemical doping with the rare earth metal La^{3+} was undertaken to lower T_C (by decreasing the degree of orthorhombic distortion) and allow for the structural changes in the region of the paraelectric - ferroelectric phase transition to be tracked using high resolution PND techniques. The composition $CsBi_{0.6}La_{0.4}Nb_2O_7$ was chosen as preliminary work on the $CsBi_{1-x}La_xNb_2O_7$ solid solution identified it as being close to the transition to *P*4/*mmm* but still lying within the phase region with $P2_1am$ symmetry.

7.2 Experimental

7.2.1 Synthesis

A phase pure sample of $CsBi_{0.6}La_{0.4}Nb_2O_7$ was prepared *via* traditional ceramic methods. Stoichiometric amounts of La_2O_3 (99.9 % Sigma-Aldrich), Nb_2O_5 (99.9 % Alfa Aesar) and, due to its volatility, a 20 % excess of Cs_2CO_3 (99 % Alfa Aesar) were dried at 100 °C for a period of 24 hours. The dried, loose powders were then ground using a pestle and mortar for a period of 30 minutes before being pressed into a pellet of approximately 10 mm diameter and 5 mm thickness. The pellet was annealed at 1000 °C for a period of 24 hours with a cooling rate of 10 $°min^{-1}$.

7.2.2 PXRD analysis

Diffraction patterns to confirm sample purity of the neutron sample and on the preliminary work to establish the solid solution $CsBi_{1-x}La_xNb_2O_7$ were obtained on a PANalytical Empyrean diffractometer (Cu $K_{\alpha 1}$ radiation source). Analysis of the PXRD patterns was carried out *via* Rietveld refinement methods using the GSAS software package[23] and the EXPGUI interface[24]. A self-consistent refinement

strategy was employed with refinement of 9 background terms, zero point, 2/3 lattice parameters for tetragonal and orthorhombic models respectively, 2 profile parameters and finally, refinement of fractional atomic coordinates for the three cationic species. Doping with lanthanum was accounted for in the refinement model by modifying the occupancy values of the Bi to reflect the decreased electron density at the A-site. A March-Dollase function was employed to refine for preferred orientation along the (00l) peaks. This preferential orientation has been found to be common in $CsBiNb_2O_7$ and other layered perovskites with crystallites orientated along the layered axis (axis containing the layers)[17, 25].

7.2.3 PND analysis

Variable temperature PND experiments were carried out using the High Resolution Powder Diffractometer (HRPD) instrument at the ISIS facility, Oxfordshire. A sample weighing ~5g was loaded into an 8 mm cylindrical vanadium canister and placed in the diffractometer furnace, before being suspended in the neutron beam. Data collection was made at room temperature and then at intervals of 100 °C between 200 and 800 °C with an additional, final pattern collected at 850 °C. With the exception of the data collection at 600 and 700 °C, which were collected over a duration of approximately 2 hours, all patterns were measured for 3.5 hours. Intermediate patterns were collected in intervals of 10 ° between 810 and 840 °C, and then in intervals of 25 ° between 725 and 775 °C, with each data collection lasting for approximately 25 minutes. Measurements were carried out with the assistance of Dr. Kevin Knight and Dr. Alexandra Gibbs.

Analysis of the neutron diffraction patterns was carried out *via* Rietveld refinement methods using the GSAS software package and the EXPGUI interface. A consistent refinement strategy was used, consisting of 3, 3, 21 and 5 parameters

to model instrumental variables, scale factors, background and peak-shape for each data set in the temperature region $25 \leq T \leq 700$ °C. For the remaining data sets in the temperature regime $725 \leq T \leq 850$ °C, the same strategy was employed differing only in a reduction of the number of background terms from 21 to 18. Site occupancies of Bi and La were refined at RT to ensure the 0.6:0.4 ratio was accurate. The site occupancies were then fixed at this ratio over the temperature regime recorded. Peaks originating from the vanadium sample canister are seen clearly in all the recorded data sets, therefore vanadium was fitted as a secondary phase.

7.2.4 Dielectric measurements

A phase-pure pellet was electroded with sputtered Au. Due to the temperature demands of the experiment the electrode was then coated in Ag paste (RS components) to protect the Au and prevent electrode failure at high temperatures. Dielectric measurements were carried out using a Wayne Kerr 6500B impedance analyser with the sample mounted in a tube furnace. Loss and capacitance data were recorded in the frequency range 100 Hz – 10 MHz on both heating and cooling cycles at a rate of 2 $Kmin^{-1}$ over the temperature range $50 \leq T \leq 750$ °C. The data collected on cooling was selected for presentation as heating data showed a broad dielectric event at ~ 450 °C. This is due to failure of the sacrificial silver Ag paste as opposed to any structural event and as such was not replicated in the cooling data. Measurements were carried out with the assistance of Dr. Finlay Morrison and Mr. Jason McNulty.

7.3 Results

7.3.1 $CsBi_{1-x}La_xNb_2O_7$ solid solution

The solid solution $CsBi_{1-x}La_xNb_2O_7$ was investigated in order to establish the doping dependency of the ferroelectric – paraelectric transition. The end-member $CsBiNb_2O_7$ is reported in the literature as adopting the polar orthorhombic space group $P2_1am$ at room temperature[17]. Despite the recent discovery by Strayer *et al.*[2] detailing the polar nature of $CsLaNb_2O_7$ (*Amm*2 symmetry at RT), Rietveld refinements for the $CsLaNb_2O_7$ structure-type were carried out in the higher symmetry tetragonal space group, *P*4/*mmm*[26], as this proved satisfactory within the remit of this investigation. As previously detailed, La doping was carried out to decrease the degree of orthorhombic distortion and determine a composition of *x* that lies close to the orthorhombic-tetragonal phase boundary that would then be suitable for the variable temperature PND study. The samples used in this analysis were synthesised by Mr. William Skinner and Mr. Adam Smyth.

7.3.2 PXRD analysis

Initial observation of the raw data obtained by laboratory PXRD analysis shows a merging of certain peaks upon going from the x = 0.5 to x = 0.6 compositions

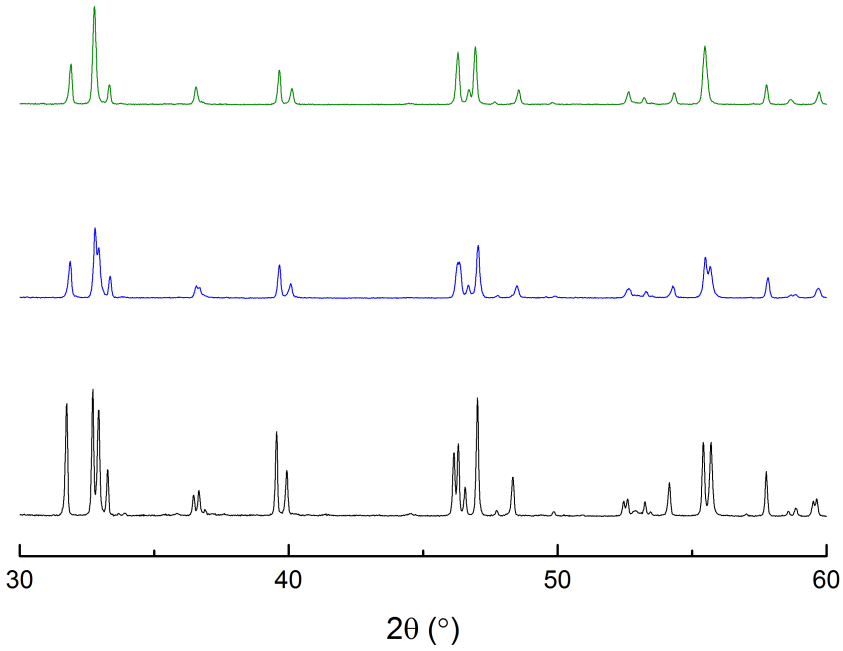

Figure 7.1 X-ray diffraction patterns for $CsBi_{1-x}La_xNb_2O_7$ at x values of 0.4 (shown in black), 0.5 (blue) and 0.6 (green). The gradual merging of several peaks indicates a phase transition to the $CsLaNb_2O_7$-type structure, which is completed at a composition of x = 0.6.

Rietveld refinement on compositions in the range $0 \leq x \leq 0.4$ were performed in the orthorhombic space group $P2_1am$, isostructural to the end-member $CsBiNb_2O_7$. As shown in Figure 7.1, a gradual merging of peaks is visible at a composition of x = 0.5, therefore the diffraction data were refined in both the $P2_1am$, $CsBiNb_2O_7$-type and $P4/mmm$, $CsLaNb_2O_7$-type structures. The orthorhombic model gave a significantly superior fit (χ^2=14.58 and χ^2 = 5.39 for

tetragonal and orthorhombic models respectively). Orthorhombic splitting is still clearly visible at a composition of x = 0.5, therefore it can be concluded that the structure is still $CsBiNb_2O_7$ – type at this value of x. Whilst difficult to observe orthorhombic splitting at a composition where x = 0.6 with raw data alone, upon closer inspection some splitting of the (*hhl*) peaks remains, with Rietveld refinement in both $P2_1am$ and $P4/mmm$ models, whilst more comparable than at x = 0.5, showing orthorhombic $P2_1am$ still provides a better model to the data at this composition (χ^2= 5.95 and χ^2 = 3.99 for tetragonal and orthorhombic models respectively). A self-consistent refinement in the orthorhombic space group at a composition of x = 0.7 was not possible as the model was unstable to refinement of the atomic coordinates of the three cations. Employing a damping strategy did eventually allow for convergence. Goodness of fit values for the two models still suggest that the orthorhombic model is superior at x = 0.7 (χ^2 = 8.51 and χ^2 = 7.74 for tetragonal and orthorhombic models respectively), however this is most likely an artefact of the increased degree of freedom allowed for in the $P2_1am$ setting meaning other factors must be considered when evaluating the validity of such a result. In addition to the increased instability of the refinement in the orthorhombic model, no splitting of the (*hhl*) peaks remains (suggestive of tetragonal unit cell metrics of $a = b$), therefore it can be concluded that at a composition of x = 0.7 the $CsLaNb_2O_7$ - type structure is adopted. Due to the limitations in the resolution of the PXRD instrument, the final composition where orthorhombic splitting was clearly defined (*i.e.* x = 0.4, before any merging of peaks can be observed) was chosen for further analysis. This ensures that a ground state isostructural with $CsBiNb_2O_7$ is the starting point for the variable temperature PND experiment, as it is not possible to rule out that a composition where x = 0.5 is not in fact an intermediary phase in any associated ferroelectric-paraelectric transition (should it occur as a two-step transition).

Plots of the lattice parameters for the normalised unit cell as a function of composition (x) appear to indicate a continuous transition between $0.5 < x < 0.6$ (Figure 7.2).

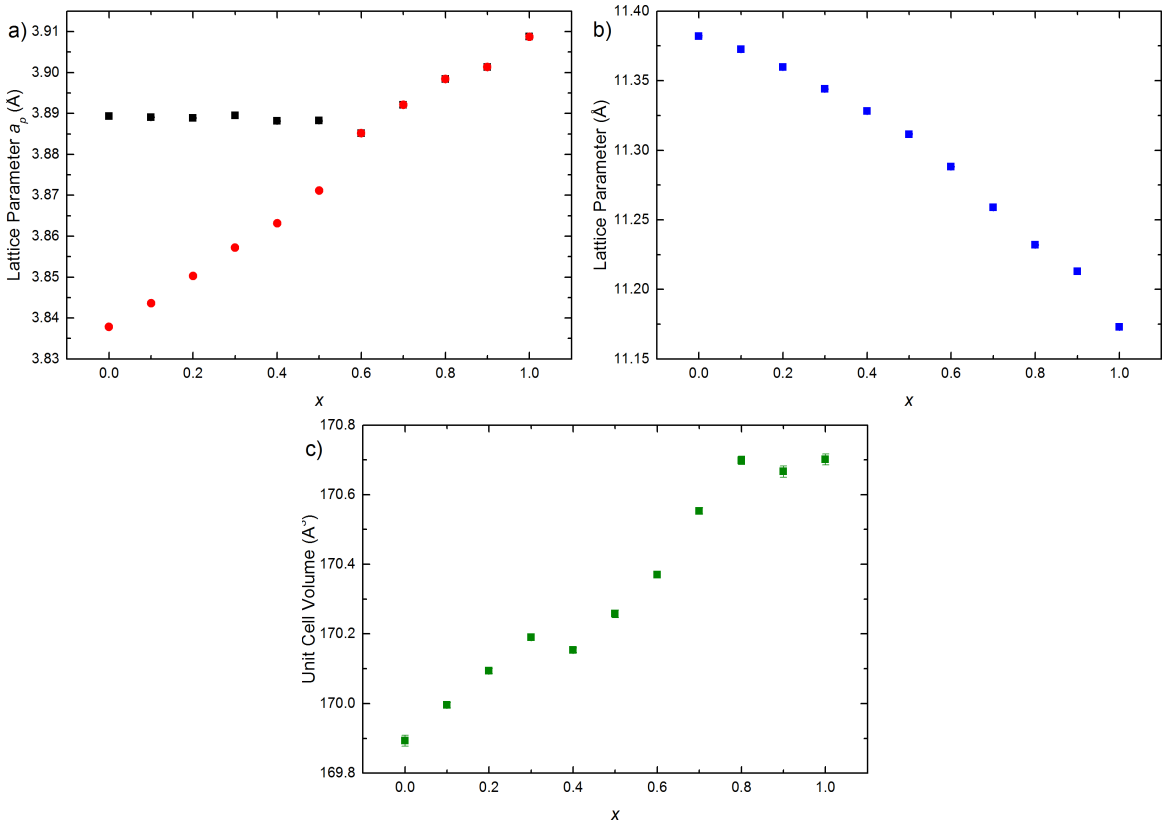

Figure 7.2 Thermal evolution of lattice parameters for the $CsBi_{1-x}La_xNb_2O_7$ solid solution showing, a) normalised a (black squares) and b (red circles) lattice parameters obtained for varying values of x across the solid solution $CsBi_{1-x}La_xNb_2O_7$, b) c lattice parameter for varying values of x and c) unit cell volume for varying values of x. Rietveld refinement for compositions where $x \geq 0.7$ were carried out in the tetragonal $P4/mmm$ setting.

7.3.3 PND analysis

7.3.3.1 Room temperature structure determination

Rietveld refinement of the RT (20 °C) PND data on $CsBi_{0.6}La_{0.4}Nb_2O_7$ is in agreement with previous literature reports for the room temperature structure of the parent, $CsBiNb_2O_7$[17], resulting in a good fit to the orthorhombic $P2_1am$ phase. However, to determine this unambiguously, other options must necessarily be considered. When considering other viable space group symmetries, both the multiplicity of the unit cell and the various octahedral tilts that generate the characteristic supercell peaks must be identified. The multiplicity of the supercell along the *a* and *b* axes (the *c* axis corresponds directly to c_t) can be determined from observation of the peak splittings. Splitting of (0*hl*) and (*h*0*l*) peaks indicate a unit cell with multiplicity $2_{at} \times 2_{at} \times c_t$, whilst splitting of (*hhl*) peaks is indicative of a unit cell with a $\sqrt{2}a_t \times \sqrt{2}a_t \times c_t$ cell metric relative to the tetragonal parent phase (*P*4/*mmm*). The PND data measured at RT indicates the highest symmetry cell applicable is a $\sqrt{2}a_t \times \sqrt{2}a_t \times c_t$ orthorhombic supercell. Work by Strayer *et al*. helpfully outlines all possible space group symmetries arising from a combination of in-phase and out-of-phase tilts for Dion-Jacobson type structures, therefore this is used to assist evaluation of all potential structures at room temperature[2]. Using the ISODISTORT software suite[27] it is first important to establish which tilt mode is a requirement for generating specific superlattice peaks in the observed PND pattern. There are four individual tilt modes that must be considered, in-phase and out-of-phase tilts in either the *a*- (or *b*-) and *c*-axes of the parent aristotype and vice versa with corresponding Glazer-type notation a^+ (or b^+) and c^+ to describe in-phase tilts and a^- (or b^-) and c^- used to describe out-of-phase tilts. This equates to four different tilt systems in 3D space of $a^+a^+c^-$, $a^+b^+c^-$, $a^-a^-c^+$ and $a^-b^-c^+$. The two important types of distortion mode to be considered are M-point and X-point modes, occurring at (***k*** = ½, ½, 0) and (***k*** = 0, ½, 0) points respectively along

the zone boundary in the tetragonal parent Brillouin zone. The four distinct symmetry modes corresponding to the four possible tilts are X_1^+ (a^+), M_5^- (a^-), M_2^+ (c^+) and M_4^- (c^-). A table listing the space group symmetries of the various tilt combinations that must be considered and the active modes associated with each of these is included in Table 7.1. Using ISODISTORT to simulate the PND patterns when each of these modes is "turned on" shows that the X_1^+ mode can be eliminated as the resulting peaks (several at a d-spacing centred at $d \sim 2.15$ Å) do not "fit" with those observed in the experimental data. Identification of the required modes becomes quite confusing as all three M-point modes generate a number of the same superlattice peaks. However, a peak at $d \sim 2.5$ Å as seen in the PND data can only be generated by the M_5^- mode, conclusive evidence that this is a required active mode when considering the distorted supercell at room temperature. The M_4^- mode could account for the peak at $d \sim 2.09$ Å, however no example can be found of a simultaneous M_4^- and M_5^- tilt mode condensing in the various viable tilt systems and it can therefore be discounted. Finally, analysis of the effect of the M_2^+ mode on the resulting PND pattern does show the presence of several of the same superlattice peaks as those observed experimentally (for example the peak at $d \sim 2.09$ Å), however, these can all be accounted for when the M_5^- mode alone is considered (none of these are specific to the M_2^- mode over the M_5^- mode). Therefore, models which involve condensation of at least the M_5^- mode and possibly the M_2^+ mode can be considered as alternatives to the current $P2_1am$ model. Considering both the active modes and the required multiplicity of the unit cell, as suggested by the diffraction data, the only alternative offered to the $P2_1am$ structure ($a^-a^-c^+$) at RT is one with *Pmam* symmetry ($a^-a^-c^0$), therefore a comparative fit to both models must be made. The *Amm*2 model, which is the suggested RT phase of $CsLaNb_2O_7$[2], can be discounted here as a quadrupling in the unit cell is not evidenced in the peak splitting pattern of the PND data.

Table 7.1 Details of the various possible tilt combinations that arise from the 4 distinct tilt modes. Adapted from Strayer et al.[2] The ISODISTORT software tool was used to identify the active modes for each setting.

Spacegroup	Glazer tilt system	Unit cell metrics	Tilt modes active	Polar?
*P*4/*mmm*	$a^0\,a^0\,a^0$	$a_t \times a_t \times c_t$	none	CS
*P*4/*mbm*	$a^0\,a^0\,c^+$	$\sqrt{2}a_t \times \sqrt{2}a_t \times c_t$	M_2^+	CS
*P*4/*nmb*	$a^0\,a^0\,c^-$	$\sqrt{2}a_t \times \sqrt{2}a_t \times c_t$	M_4^-	CS
*P*4/*mmm*	$a^+\,a^+\,c^0$	$2a_t \times 2a_t \times c_t$	X_1^+	CS
Pmam	$a^-\,a^-\,c^0$	$\sqrt{2}a_t \times \sqrt{2}a_t \times c_t$	M_5^-	CS
*P*2$_1$*am*	$a^-\,a^-\,c^+$	$\sqrt{2}a_t \times \sqrt{2}a_t \times c_t$	$M_2^+ \times M_5^-$	polar
Cmmm	$a^-\,b^0\,c^0$	$2a_t \times 2a_t \times c_t$	M_5^-	CS
**Amm*2	$a^-b^0c^+$	$c_t \times 2a_t \times 2a_t$	$M_2^+ \times M_5^-$	polar
*P*2/*m*	$a^-b^-c^0$	$\sqrt{2}a_t \times c_t \times \sqrt{2}a_t$	M_5^-	CS
Pm	$a^-\,b^-c^+$	$\sqrt{2}a_t \times c_t \times \sqrt{2}a_t$	$M_2^+ \times M_5^-$	polar

*C2*mm* setting for *c* corresponding to c_t. CS denotes a centrosymmetric space group.

Rietveld refinement the RT PND data using a *Pmam* model gives a χ^2 value of 9.08 compared to 5.87 for the same data set in the *P*2$_1$*am* setting, providing good evidence that the phase stabilised at room temperature has *P*2$_1$*am* symmetry as previously reported by Snedden *et al*[17]. Furthermore, a space group with *P*2$_1$*am* symmetry is concordant with work carried out on pure $CsBiNb_2O_7$ that confirms the non-centrosymmetricity of the phase at room temperature with the use of SHG analysis[28]. Mode analysis of the distorted RT supercell carried out with ISODISTORT[27] shows that both the M_5^- and M_2^+ modes have significant amplitude in this structure in addition to the Γ_5^- mode (a much weaker M_3^+ mode is also symmetry-allowed). The fit to *P*2$_1$*am* at RT is shown in Figure 7.3. Details on the refined structural model in *P*2$_1$*am* plus selected bond lengths are included in Tables 7.2 and 7.3.

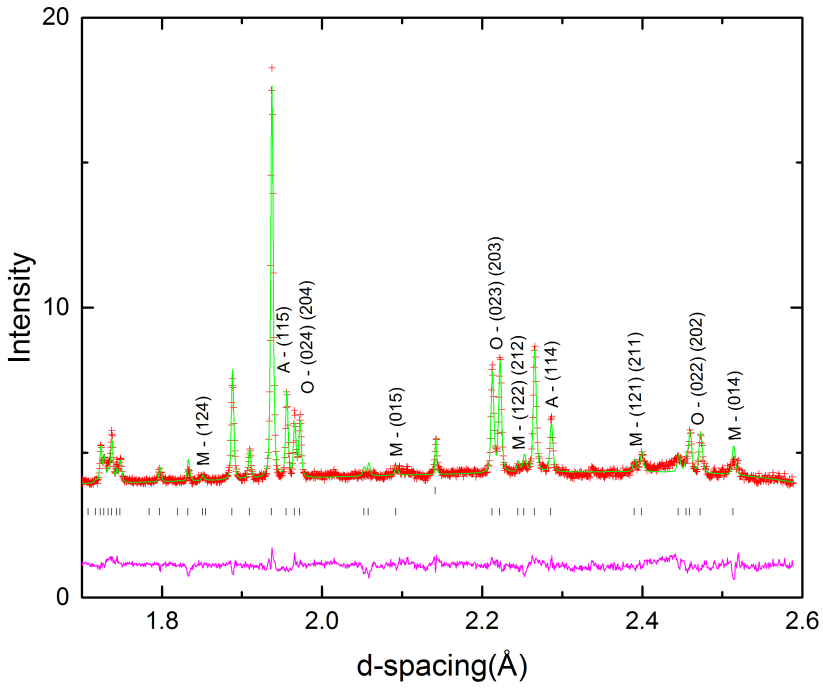

Figure 7.3 Portion of the Rietveld refinement carried out on RT PND data on a sample of $CsBi_{0.6}La_{0.4}NbO_7$ in the $P2_1am$ space group. Peaks arising from a combination of M_2^+ and M_5^- modes are labelled M, with the peak arising from the M_5^- only labelled accordingly. Orthorhombic splitting due to a unit cell metric ($a \sim b \sim \sqrt{2}a_t$) is indicated by O, whilst A identifies a subcell peak that would be split were a phase with ($a \sim b \sim 2a_t$) metrics adopted.

Table 7.2 Refined structural model for $CsBi_{0.6}La_{0.4}Nb_2O_7$ at 20°C. Space group $P2_1am$; a = 5.49618(14), b = 5.46012(14), c = 11.3254(3) Å.

Atom	Wyckoff position	x	y	z	100 * U_{iso} (Å^2)
Cs1	2b	0.3349(17)	0.2579(12)	0.5	2.08(10)
Bi*	2a	0.367	0.2692(8)	0.0	2.91(11)
Nb	4c	0.3334(10)	0.7540(6)	0.20533(14)	0.56(7)
O1	2a	0.321(2)	0.6892(9)	0.0	2.83(15)
O2	4c	0.3272(12)	0.7812(7)	0.3574(2)	1.66(9)
O3	4c	0.0869(15)	0.0104(12)	0.1589(3)	3.10(13)
O4	4c	0.5290(11)	0.4590(8)	0.1840(3)	2.25(13)

* fixed occupancy $Bi_{0.6}La_{0.4}$

Table 7.3 Selection of bond lengths for $CsBi_{0.6}La_{0.4}Nb_2O_7$ at 20°C in the $P2_1am$ model at 20 °C.

Cs-O	Bond Length (Å)	Bi/La-O	Bond Length (Å)	Nb-O	Bond Length (Å)
Cs1-O2 × 2	3.063(7)	Bi1-O1	2.307(7)	Nb1-O1	2.3531(19)
Cs1-O2 × 2	3.158(10)	Bi1-O1	2.508(12)	Nb1-O2	1.730(3)
Cs1-O2 × 2	3.231(10)	Bi1-O3 × 2	2.651(6)	Nb1-O3	1.968(9)
Cs1-O2 × 2	3.282(7)	Bi1-O3 × 2	2.758(6)	Nb1-O3	2.018(8)
		Bi1-O4 × 2	2.492(4)	Nb1-O4	1.952(6)
				Nb1-O4	2.052(6)

7.3.4 Thermal evolution of $CsBi_{0.6}La_{0.4}Nb_2O_7$

Following confirmation that the RT structure adopts $P2_1am$ symmetry, this phase is fitted to the data in the temperature range RT $\leq T \leq$ 700 °C. Peaks that are split due to orthorhombicity of the unit cell are tracked as merging of these peaks signifies a shift to a unit cell that is metrically tetragonal (a = b). Ideally the intensity of the M-point peaks would be tracked to give an indication of the presence of an intermediate phase (*i.e.* a phase with *Pmam* symmetry, upon loss of a peak associated with the M_2^+ mode). However, due to the weak intensity of these superlattice peaks at room temperature and the fact that no reflection is contributed to solely by the M_2^+ mode, this is not a viable approach here. Mode analysis performed with the ISODISTORT tool is used to track the magnitudes of the various M-point distortion modes throughout the temperature regime in which the orthorhombic $P2_1am$ phase is present, with the outcomes of this discussed in section 7.3.7. Due to the inability to closely monitor the evolution of the M-point peaks in the raw data, comparative fits, using a self-consistent refinement strategy as detailed in the experimental section, of $P2_1am$ and *Pmam* are made for the data measured over the temperature range $20 \leq T \leq 700$ °C. The resulting χ^2 values denoting the 'goodness of fit' are given in Figure 7.4. It is clearly apparent that throughout the temperature range of the orthorhombic phase $P2_1am$ proves consistently to be a better model to the data than the *Pmam* alternative, indicating that no intermediary phase forms in this temperature region. The gradual convergence in the χ^2 values for the two models with increasing temperature can be expected as contributions from the M-point modes lessen and the two models become increasingly less distinguishable. The decrease in χ^2 values upon going from a temperature of 500 °C to 600 °C occurs as a result of fitting to the inferior quality data obtained using shorter collection times (as detailed in the experimental section (7.2.3)) as opposed to any real statistical improvement.

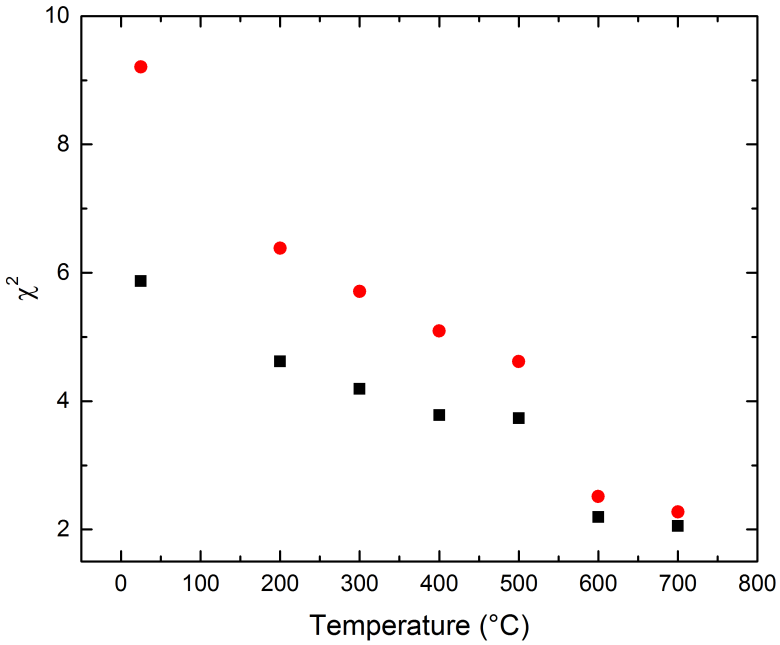

Figure 7.4 Comparison of Rietveld goodness-of-fit parameters (χ^2) for the $P2_1am$ and *Pmam* models in the temperature range $20 \leq T \leq 700$ °C.

A merging of the peaks with orthorhombic splittings (*e.g*. the 024 and 204 *hkl* peaks) upon elevating the temperature from 700 °C to 725 °C suggests that a tetragonal phase is adopted at this temperature. In addition to this, the raw data shows no visible evidence that the M-point peaks persist at 725 °C. The data at 725 °C is fitted to a model isostructural to that of the high temperature *P*4/*mmm* tetragonal phase in $CsLaNb_2O_7$. The fit to *P*4/*mmm* at 725 °C is both statistically and graphically excellent (Figure 7.5).

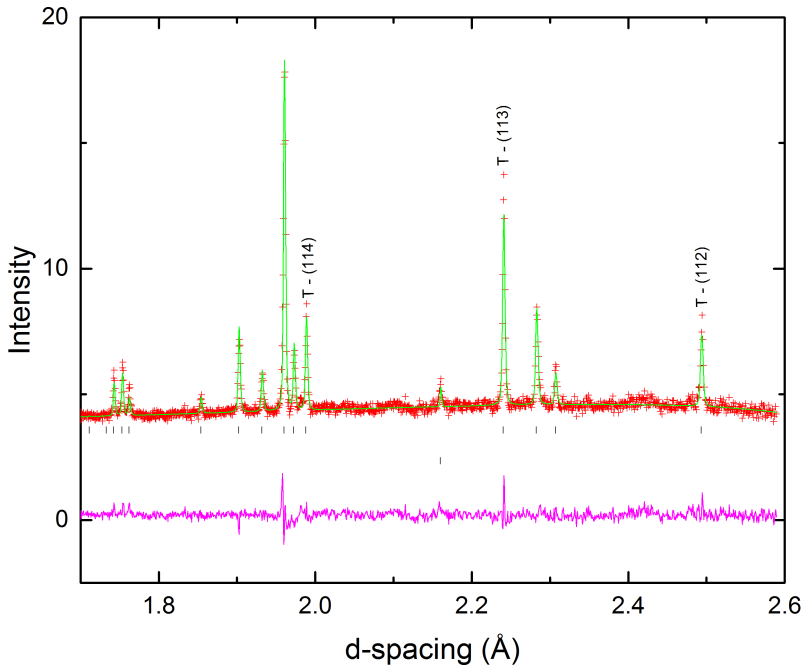

Figure 7.5 Portion of Rietveld refinement on PND data at 725 °C on a sample of $CsBi_{0.6}La_{0.4}Nb_2O_7$ modelled in the tetragonal *P*4/*mmm* setting. Peaks that have coalesced upon adoption of the tetragonal phase are annotated with the letter T. Note the disappearance of all superlattice peaks attributable to M-point condensation.

However, it is again necessary to trial this model against all other viable options. Details of the comparative fits of all viable models to the PND data at 725 °C are given in Table 7.4. The pathways through which the $P2_1am$ – *P*4/*mmm* transition can occur and the symmetry adapted modes that facilitate these are illustrated in Figure 7.6.

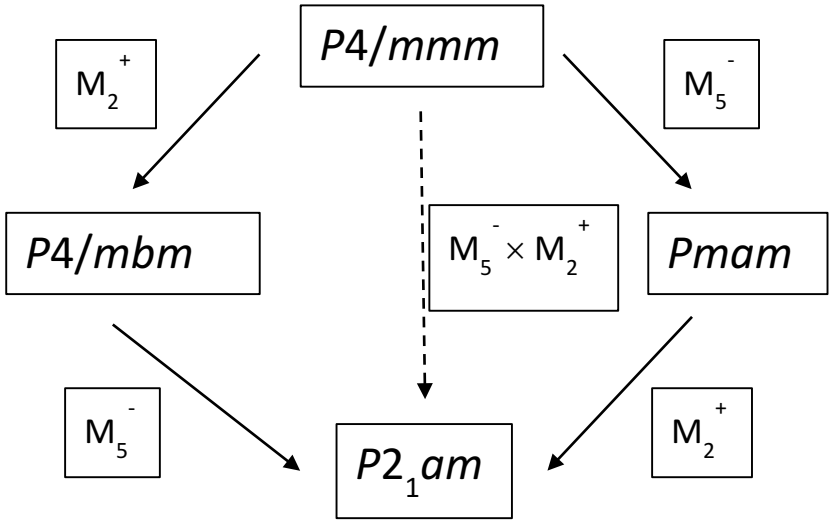

Figure 7.6 Symmetry descent diagram showing available pathways from parent *P*4/*mmm* structure to the lower temperature distorted $P2_1am$ structure. Solid lines indicate a continuous 2nd order phase transition by Landau theory. A dashed line represents a forbidden transition that must therefore be of 1st order.

Rietveld refinement using a model with *Pmam* symmetry gives a slightly better result statistically but the improvement is not significant enough to suggest that the phase transition in $CsBi_{0.6}La_{0.4}Nb_2O_7$ proceeds *via* a two-step mechanism. One additional model that must be considered at this temperature is the $a^0a^0c^+$ tilt system in the *P*4/*mbm* setting. A phase with *P*4/*mbm* symmetry could occur in the event the M_2^+ mode has a greater instability than the M_5^-, resulting in its primary condensation. The 'goodness of fit' upon Rietveld refinement in the *P*4/*mbm* model again offers a very slight improvement on the *P*4/*mmm* model, but not significantly. Finally, the data at 725 °C was modelled in the orthorhombic $P2_1am$ phase for completeness. The χ^2 for the $P2_1am$ model is considerably lower than the other models trialled at 725 °C. However, this is to be expected due to the increased degree of freedom allowed for in a lower symmetry space group.

Table 7.4 Comparison of the Rietveld refinements for the various possible space group symmetries for the phase at 725 °C. N_{ref} defines the total number of variable parameters refined, N_{xyz} is the number of fractional atomic coordinates refined and N_{Uiso} is the number of isotropic atomic displacement parameters (ADPs) refined in each case. Occupancies at the A-site were fixed as Bi:La 0.6:0.4, with Bi/La at each site constrained to have equal ADPs.

Space group	χ^2	N_{ref}	N_{xyz}	N_{Uiso}
*P*4/*mmm*	2.065	44	3	6
$P2_1am$	1.888	55	17	7
Pmam	2.041	51	9	7
*P*4/*mbm*	2.054	44	5	6

Graphically the fit to $P2_1am$ is less convincing than the fit to the tetragonal *P*4/*mmm* parent phase. Therefore, with all models thoroughly considered, refinement in the *P*4/*mmm* setting is carried out for the data sets in the temperature region $725 \leq T \leq 850$ °C. A refined structural model and selected bond lengths and bond angles for the *P*4/*mmm* phase at 750 °C are detailed in Tables 7.5 and 7.6.

Table 7.5 Refined structural model for $CsBi_{0.6}La_{0.4}Nb_2O_7$ at 750 °C. Space group *P*4/*mmm*; *a* = 3.92282(16), *c* = 11.4138(5) Å.

Atom	Wyckoff position	*x*	*y*	*z*	100 * U_{iso} (Å^2)
Cs	1b	0.0	0.0	0.5	7.09(13)
Bi*	1a	0.0	0.0	0.0	7.17(16)
Nb	2h	0.5	0.5	0.20414(16)	2.13(9)
O1	4i	0.0	0.5	0.17054(17)	5.56(10)
O2	2h	0.5	0.5	0.3555(3)	6.44(13)
O3	1c	0.5	0.5	0.0	7.20(17)

* fixed occupancy $Bi_{0.6}La_{0.4}$

Table 7.6 Selected bond lengths for $CsBi_{0.6}La_{0.4}Nb_2O_7$ at 750 °C in the *P*4/*mmm* model.

Cs-O	Bond length (Å)	Bi/La-O	Bond length (Å)	Nb-O	Bond length (Å)
Cs-O2 × 8	3.2273(14)	Bi-O1 × 8	2.7634(14)	Nb-O1 × 4	1.9985(5)
		Bi-O3 × 4	2.77385(11)	Nb-O2	1.727(4)
				Nb-O3	2.3300(18)

7.3.5 Thermal evolution of lattice metrics in $CsBi_{0.6}La_{0.4}Nb_2O_7$

As previously indicated in the PND data, a plot of the refined lattice parameters as a function of temperature demonstrates a gradual merging of the *a* and *b* unit cell axes before tetragonal unit cell metrics are finally adopted at a temperature of

725 °C (Figure 7.7). The discontinuous evolution of the *c* unit cell metric could be suggestive of a 1st order phase transition somewhere in the region 700 < *T* < 725 °C. This discontinuity is not echoed however in the unit cell volume, which would provide a more valid argument since volume is the relevant thermodynamic variable. ISODISTORT analysis using group theory shows that the direct *P*4/*mmm* to $P2_1am$ phase transition cannot be continuous. However, a two-step transition involving an intermediary *Pmam* phase, is permitted to be continuous. Therefore, it is necessary to evaluate any available evidence for the latter, with further scrutiny of the available data.

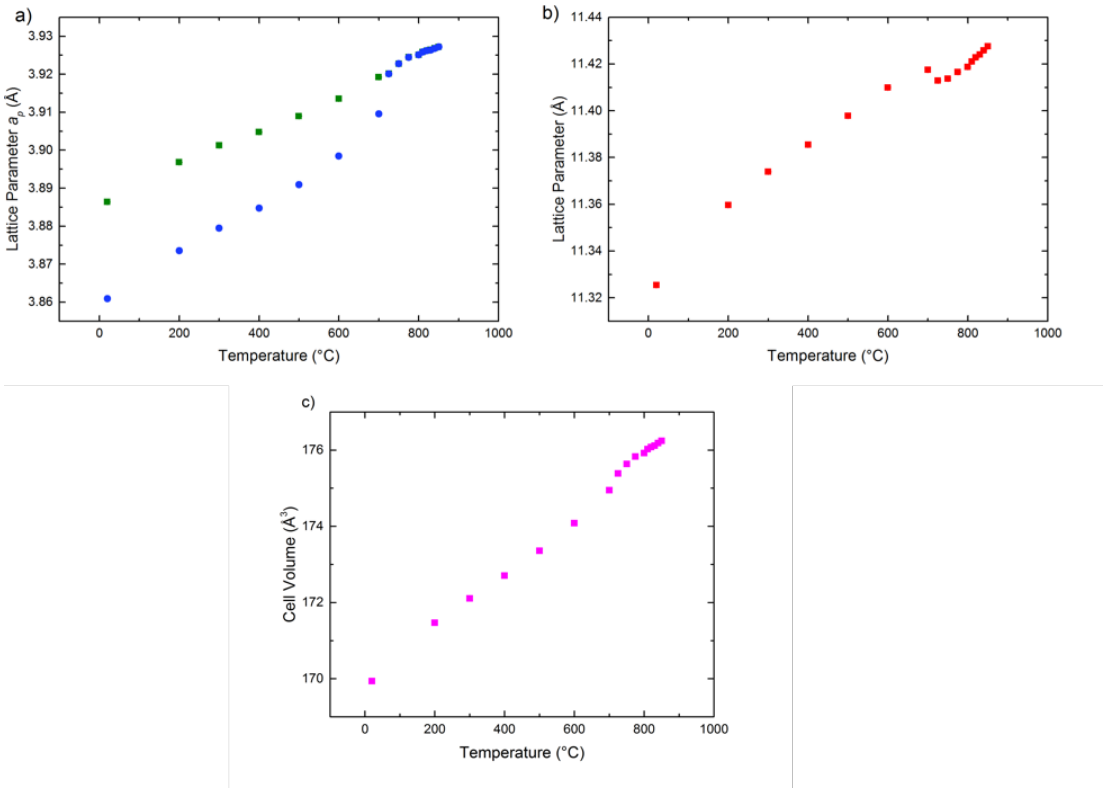

Figure 7.7 Unit cell metrics as a function of temperature throughout the temperature regime 25 ≤ *T* ≤ 850 °C. Merging of the *a* and *b* lattice parameters (part (a), with the *a* lattice parameter shown as green squares and *b* as blue circles) is visible as the orthorhombic – tetragonal phase transition is approached. A kink observable in the *c* lattice parameter (part (b)) between 700 and 725 °C supports the temperature range in which the transition is believed.

7.3.6 Orthorhombic distortion

A measure of the orthorhombic distortion present in the $P2_1am$ phase over the temperature region $20 \leq T \leq 700$ °C is shown in Figure 7.8. The distortion parameter, D_0, is calculated as $D_0 = 2(a - b)/(a + b)$. Following the expected trend for perovskites, the maximum orthorhombic distortion is present in the RT structure. This tends toward zero as the $P2_1am$ – $P4mmm$ phase transition is approached. Using a weighted power law of the form; $D_0 = A(T_c\text{-}T)^{\beta}$, the critical temperature (T_c), was evaluated as a function of the orthorhombic distortion. The variables derived from the fit are given as A = 0.00041 $K^{-\beta}$, T_c = 731 °C and β = 0.315. The T_c of 731 °C, is in agreement with both crystallographic data and mode amplitude analysis (discussed, in detail, in the following section) that place the phase transition in the temperature region $700 < T < 750$ °C.

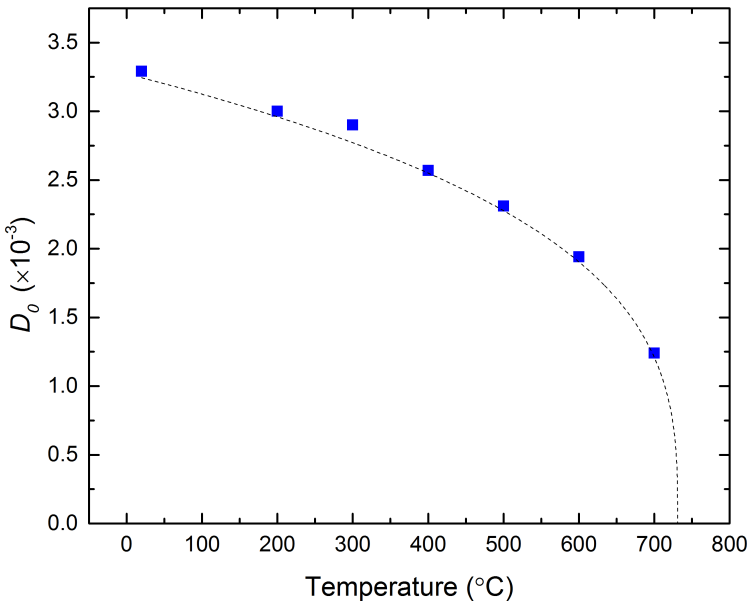

Figure 7.8 Orthorhombic distortion (D_0) for $P2_1am$ phase of $CsBi_{0.6}La_{0.4}Nb_2O_7$. The dashed line gives the fit to a weighted power law of the form $d_0 = A(T_c\text{-}T)^{\beta}$.

7.3.7 Symmetry mode analysis

Mode amplitudes for the active modes in the orthorhombic phase were obtained using the ISODISTORT tool (Figure 7.9) with the purpose of elucidating their influence on the structure. The M_3^+ mode describes a minor octahedral distortion involving the simultaneous expansion and contraction of opposing oxygen atoms in the *ab* plane (note the small and constant amplitude for the M_3^+ mode indicates it is not the driving force behind any phase transition). The M_2^+ mode describes an in-phase octahedral rotation around the *c*-axis. The M_5^- mode is made up of contributions from different distortions; the majority of which are from the out-of-phase tilt around the *ab* plane, with further contributions from an antiferrodistortive cation displacement along the *b*-axis. Both the M_2^+ and M_5^- modes would be considered primary order parameters in a direct $P2_1am$ – $P4/mmm$ phase transition, as both possess a significant amplitude below T_c, therefore their tendency toward zero exacts the largest influence on the structure. The Γ_5^- mode, the polar mode, describes all polar displacements of atoms along *a*. This would be considered a secondary order parameter with regard to an avalanche transition resulting from the simultaneous or successive condensation of the M_5^- and M_2^+ modes. With reference to Figure 7.9, the mode amplitude of the M_3^+ octahedral distortion mode is relatively small even at room temperature and diminishes to zero near the phase boundary, but does not play any significant role in the paraelectric - ferroelectric transition. The M_2^+ in-phase tilt mode, conversely, has a significant amplitude at RT and can be seen to diminish toward zero upon approaching the phase transition. On first intuition, it appears that the M_2^+ mode is decreasing fairly smoothly, suggesting a second-order relationship with temperature. Comparatively, the M_5^- mode amplitude appears to diminish at a slower rate up to 700 °C, but then much more abruptly, suggesting a more 1^{st} order nature. With the absence of additional data in the vicinity of the phase transition it is not possible to conclude whether the M_5^- mode retains a degree of

tilting upon loss of the M_2^+ mode, resulting in an intermediary phase with *Pmam* symmetry, or does in fact undergo a rapid reduction to zero coincidental with the critical temperature of the M_2^- mode. However, it seems that the alternative scenario, whereby the M_2^+ mode is retained in the absence of the M_5^- mode, facilitating an intermediary phase with *P*4/*mbm* symmetry, can be discounted. To clarify the temperature dependency of the critical temperatures (note: T_c is used as opposed to T_C as it has not been established whether one or both modes are primary order parameters in the paraelectric – ferroelectric phase transition) of both the M_5^- and M_2^+ active modes, a fit to a weighted power law (mode amplitude = $A(T_c-T)^{\beta}$) was carried out. The critical exponents obtained were β = 0.401 and 0.127, with a fit constant A = 0.0292 $Å.K^{-\beta}$ and 0.227 $Å.K^{-\beta}$, for the M_2^+ and M_5^- modes respectively. Critically, the values for T_c were calculated as 749 and 742 °C for the M_2^+ and M_5^- modes, respectively. The similarity in T_c values (whilst slightly higher than the T_c of 725 °C suggested by the crystallographic data) inclines to suggest that both modes condense simultaneously and the phase transition is a so-called 'avalanche' transition from *P*4/*mmm* to *P*2_1*am* directly, similar to that seen in $SrBi_2Nb_2O_9$[14]. The similarity in the χ^2 values obtained upon Rietveld refinement of the data at 725 °C (χ^2 values of 2.065, 2.054, 2.041 and 1.888 for *Pmam*, *P*4/*mbm*, *P*4/*mmm* and *P*2_1*am* models respectively) suggests that upon the phase transition no octahedral tilting remains, further supporting the theory of an avalanche transition.

The Γ_5^- mode still has a significant amplitude at 700 °C (mode amplitude = 0.356 Å) which appears to have plateaued upon reaching a temperature of 600 °C. This seems rather curious, and might suggest that the polarisation itself could be involved in the driving force for the transition. Although this cannot be completely ruled out from the present study, it seems unlikely given the behaviour of the M_5^- and M_2^- modes and observations from the crystallographic data. Crystal-chemical intuition suggests that geometric effects and octahedral tilting drive the

transitions and the combination of the two distinct tilt modes allows tri-linear coupling with the polar mode, to induce a hybrid-improper mechanism. First-principles calculations would be helpful in confirming this hypothesis.

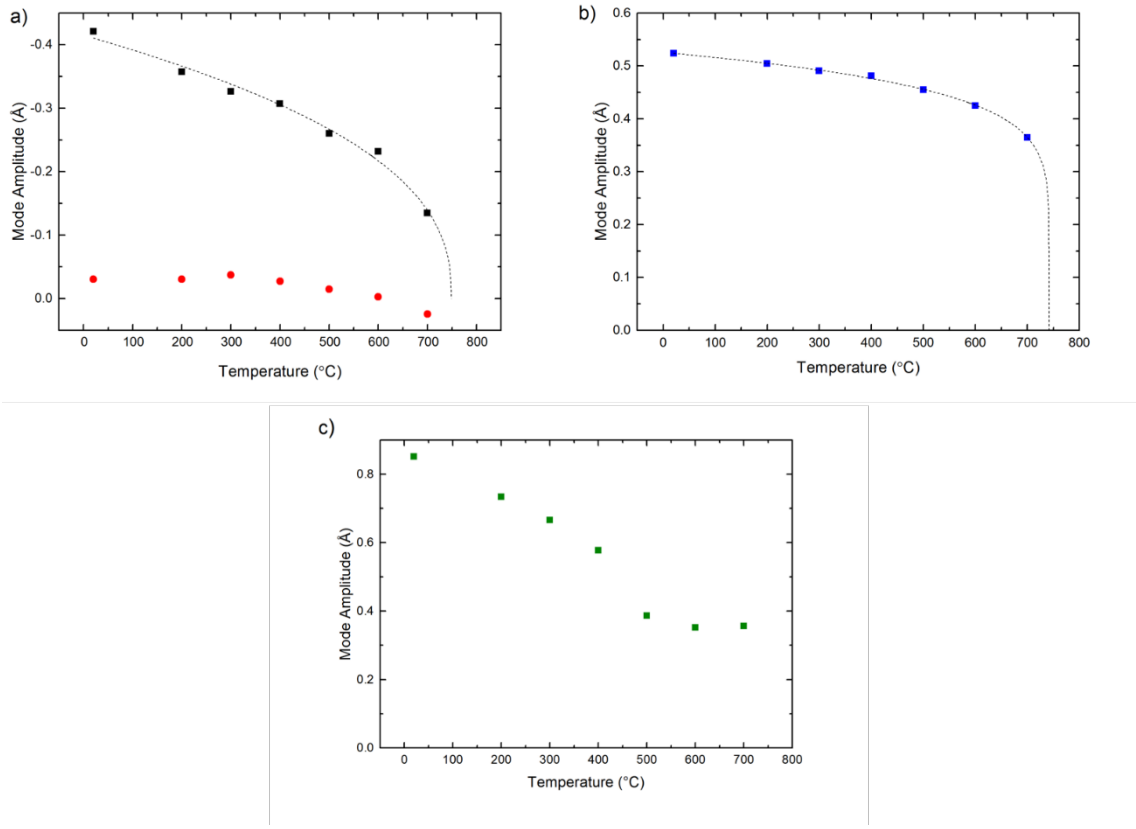

Figure 7.9 Thermal evolution of various symmetry-adapted modes throughout the temperature regime $20 \leq T \leq 700$ °C. a) shows the M_2^+ (black squares) and M_3^+ modes (red circles), b) shows the overall M_5^- mode and c) shows the Γ_5^- mode indicating the polar distortion along *a*. The M_2^+ and M_5^- modes have been fit to the expression; mode amplitude = $A(T_c\text{-}T)^{\beta}$. The fits are shown as dashed lines.

7.3.8 Relative permittivity measurements

Relative permittivity measurements were performed on a phase pure sample of $CsBi_{0.6}La_{0.4}Nb_2O_7$. Whilst the results of the permittivity measurements are of

interest to this study in order to identify the T_C of the paraelectric – ferroelectric transition, they are of further value as the presence of two dielectric events could indicate a two-step transition occurs and *vice versa*, a single dielectric event offers evidence for a direct avalanche-type transition.

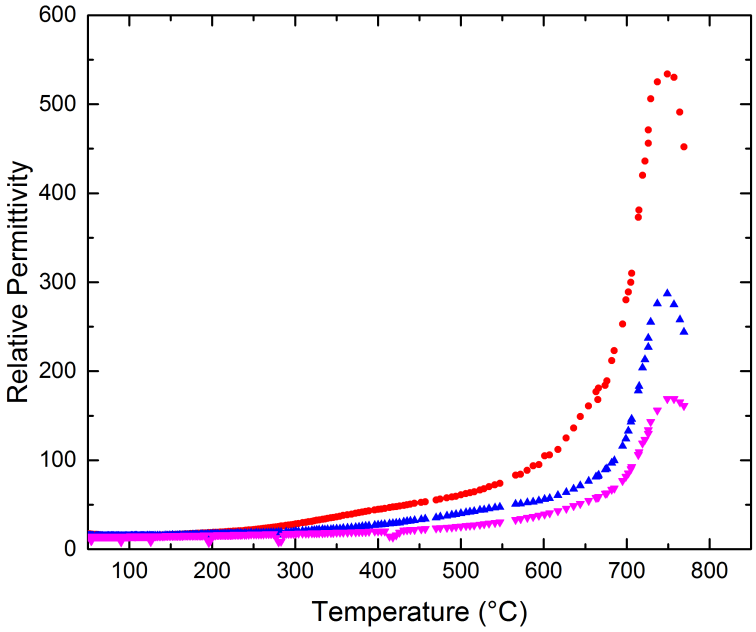

Figure 7.10 Relative permittivity data collected on cooling obtained on a sample of $CsBi_{0.6}La_{0.4}Nb_2O_7$ at selected frequencies. Red circles represent the data collected at a frequency of 10 Hz, blue triangles show the 100 kHz data with pink triangles showing the 1 MHz data.

The apex of the dielectric event occurs at a temperature of $T \sim 748$ °C, as shown in Figure 7.10. There is a slight discrepancy between this and the T_C deduced from the analysis of the crystallographic data ($T_C = 700 < T < 725$ °C), however this higher T_C is also in agreement with the average T_C obtained from analysis of the M_2^+ and M_5^- mode amplitudes. No definitive evidence can be seen for a second transition closely following or preceding the one at 748 °C. However, the presence of a shoulder in the temperature region $700 < T < 750$ °C cannot be definitively ruled

out. This ambiguity in the interpretation of the data makes it impossible to make any firm deduction on the nature of the phase transition. However, the presence of a singular peak in the permittivity values is suggestive of a direct 1st order transition.

7.4 Discussion

The desired outcome of this study is to establish the nature of the paraelectric – ferroelectric transition for the $CsBiNb_2O_7$-type structure type, including the presence of any intermediary phases. To realise a direct (avalanche) transition from the parent $a^0a^0a^0$ (*P*4/*mmm*) structure to the $a^-a^-c^+$ ($P2_1am$) structure simultaneous freezing of zone boundary M_2^+ and M_5^- modes must occur. When considering the neutron powder diffraction data, ISODISTORT mode amplitude outputs and relative permittivity measurements, it is appropriate to conclude, given the available evidence, that the phase transition in $CsBi_{0.6}La_{0.4}Nb_2O_7$ is a so-called 'avalanche' transition, whereby two primary structural order parameters (octahedral rotations) simultaneously condense and induce a polar lattice instability. The nature of such a transition is intriguing as intuitively it seems remarkable that two separate order parameters should have the same temperature dependency. However, this is known to occur in systems in which a sufficiently strong trilinear coupling mechanism is present, such as $SrBi_2Nb_2O_9$ and $Bi_4Ti_3O_{12}$[14, 22, 29]. Trends in the lattice parameters, specifically the discontinuity in the *c* unit cell metric between 700 and 725 °C, suggest the ferroelectric - paraelectric transition is of a 1st order nature. Similarly, the consistent superiority of the $P2_1am$ model over the *Pmam* model in terms of their respective χ^2 values up to and including a temperature of 700 °C suggests that no intermediate phase is involved in the transition. Further evidence in the crystallographic data is given

by the comparable nature of the χ^2 values for the various models trialled at 725 °C, indicating that no octahedral tilting remains at this temperature (the $P2_1am$ tilt system is clearly still adopted at 700 °C). Whilst the possibility of an intermediate phase with *Pmam* symmetry between 700 and 725 °C cannot be definitively ruled out, mode amplitude analysis reveals the M_2^+ (in-phase) tilt mode still retains a fairly large amplitude at 700 °C. Similarly, the large amplitude of the M_5^- mode at 700 °C discounts the possibility of an intermediary *P*4/*mbm* phase. Both the dielectric data and the fits to a weighted power law for the M_2^+ and M_5^- modes suggest a higher T_C just below 750 °C (T_C obtained from dielectric data = 748 °C, whilst M_2^+ and M_5^- modes indicated critical temperatures (T_c) of 749 and 742 °C, respectively). The disparity between the T_C indicated by the crystallographic data and those obtained from analysis of both the dielectric data and mode amplitudes makes it difficult to pinpoint the temperature region for the transition to a temperature interval narrower than $700 < T_C < 750$ °C. This is unfortunate and this study could, of course, be greatly benefited with hindsight, however the similarity in the transition temperatures obtained from the fits to the two mode amplitudes and the presence of a sole dielectric event in the permittivity measurements is in agreement with the crystallographic data in so far as all the evidence points toward a "so-called" avalanche transition. This in turn suggests a strong tri-linear coupling mechanism is present in $CsBi_{0.6}La_{0.4}Nb_2O_7$ and by extension the parent phase $CsBiNb_2O_7$.

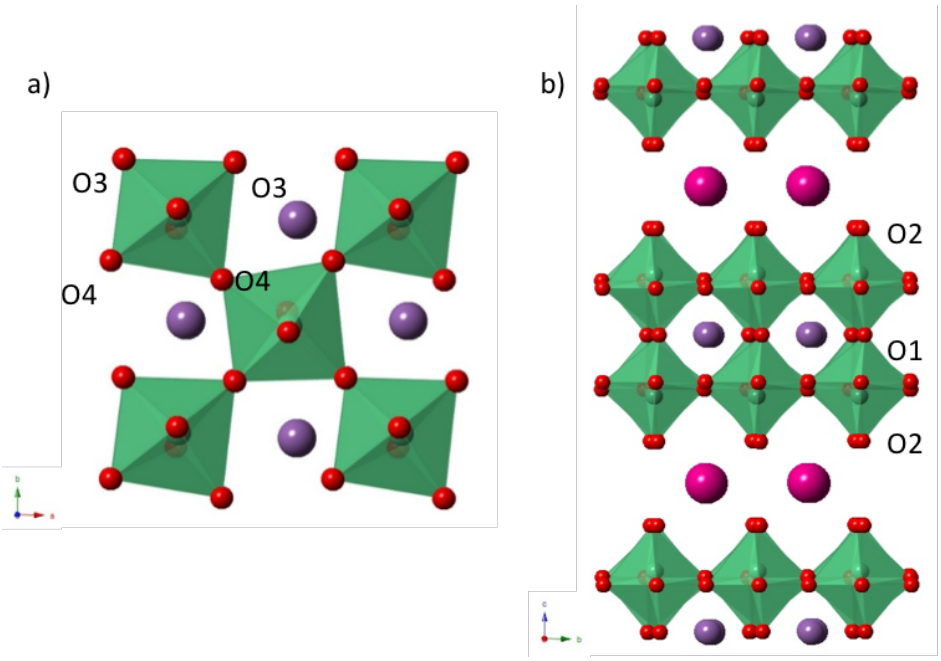

Figure 7.11 Crystal structure of $CsBi_{0.6}La_{0.4}Nb_2O_7$ at RT viewed as (a) down the *c*-axis, showing the in-phase (M_2^+) tilt and (b) perpendicular view, showing the out-of-phase (M_5^-) tilt.

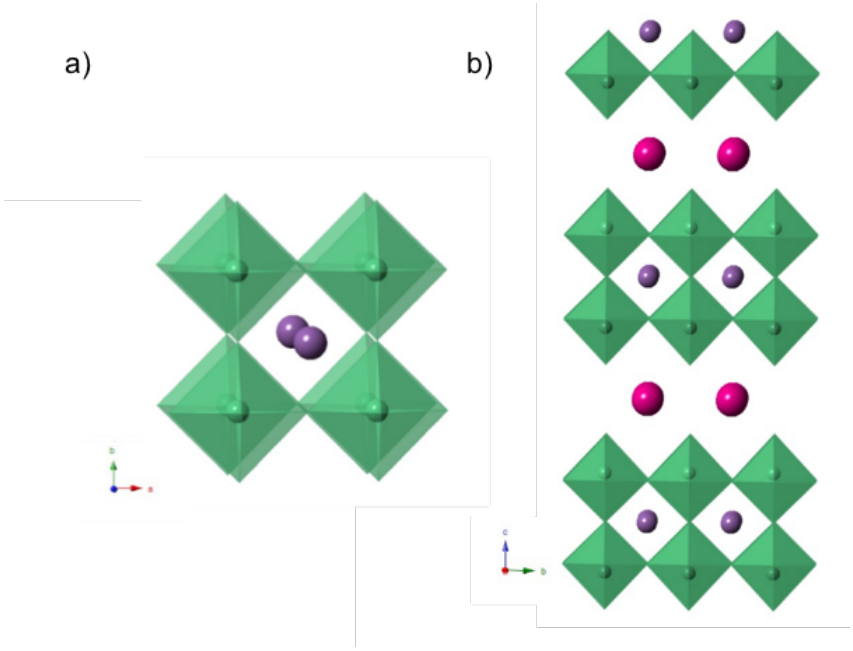

Figure 7.12 Crystal structure of $CsBi_{0.6}La_{0.4}Nb_2O_7$ at 725 °C showing tetragonal polymorph *P*4/*mmm* viewed a) down the *c*-axis now with zero tilting and b) perpendicular view highlighting loss of the out-of-phase tilt around the *a*-axis.

Schematics of the orthorhombic and tetragonal structures are given in Figures 7.11 and 7.12 respectively. The room temperature crystal structure of the $P2_1am$ phase consists of eclipsed blocks of perovskite (of the formula "$BiNb_2O_7$") in the *ab* plane interspersed with layers of Cs^+ cations. Condensation of the M_2^+ (in-phase) and M_5^- (out-of-phase) symmetry-adapted modes (which occur to maximise A-O bonding interactions) result in a doubling of the unit cell in the *ab* plane relative to the tetragonal parent structure, and a tilt pattern analogous to $a^-a^-c^+$ found in bulk perovskites. The Dion-Jacobson family is structurally similar to the Aurivillius phases (e.g. $SrBi_2Ta_2O_9$), differing only in the composition of the intergrowth layers. In the Aurivillius phases, fluorite-like Bi_2O_2 populate the layers between the perovskite blocks whilst in the Dion-Jacobson phases the interlayers are solely made up of individual cations. The nature of the interlayer dictates the degree of displacement at the B-site, which occurs to compensate for the underbonding at the apical oxygen site.

In the view shown in Figure 7.11 b) this B-site displacement is clearly demonstrated. Such off-centring is typical of a d^0 cation at the perovskite B-site, however this 'ferroelectric-like' displacement, which would normally be the origin of ferroelectricity in prototypical ferroelectric structures of the formula ABO_3, does not result in an overall polarisation in these layered systems. The presence of the mirror plane symmetry perpendicular to the *c*-axis results in equal and opposite Nb displacements within the perovskite blocks, and as such the net polarisation is equal to zero. The degree of off-centring of the Nb^{5+} cation towards the apical oxygen is greater in the Dion-Jacobson phases compared to the Aurivillius. This is due to the greater need to compensate for the larger degree of underbonding at the apical oxygen site due to the cationic interlayer ($Nb\text{-}O_{apical}$ = 1.730(3) Å for $CsBi_{0.6}La_{0.4}Nb_2O_7$ as opposed to 1.832(5) Å for $SrBi_2Nb_2O_9$ and 1.839(4) Å in $BaBi_2Nb_2O_9$)[30]. A schematic of the distorted NbO_6 octahedron is shown in Figure 7.13.

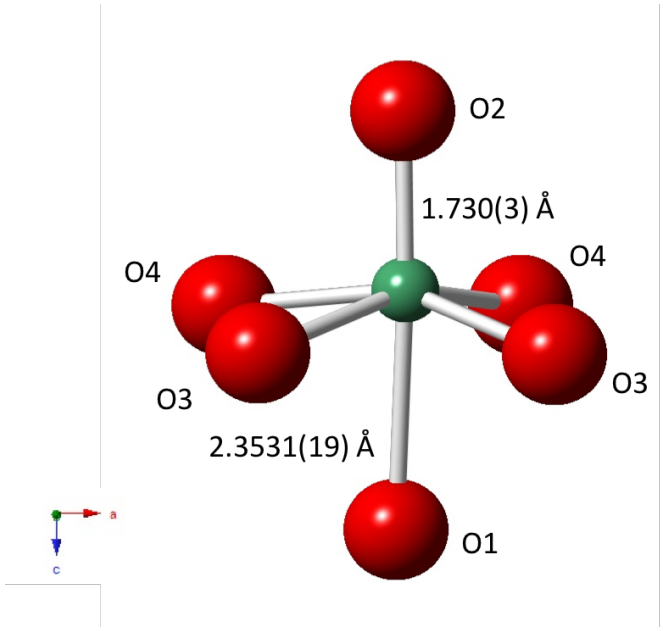

Figure 7.13 Ball and stick representation of NbO_6 octahedra in $CsBi_{0.6}La_{0.4}Nb_2O_7$ showing displacement of Nb^{5+} B-site cation toward apical oxygen.

In contrast to traditional ABO_3 perovskites, the origin of polarity and in some instances ferroelectricity in layered systems such as the Aurivillius, Ruddlesden-Popper and Dion-Jacobson phases is located at the perovskite A-site. The ion-size mismatch between the interlayer A cation and A' or B cations dictate the distortions in the perovskite blocks in a similar manner to those distortions which arise as a function of the tolerance factor in traditional ABO_3 perovskites. The A-site displacements and the co-operative octahedral tilts in $CsBiNb_2O_7$ and the related compound $CsBi_{0.6}La_{0.4}Nb_2O_7$ result in a distorted structure with orthorhombic $P2_1am$ symmetry and $a^-a^-c^+$ tilt pattern analogous with the well-known *Pbnm* three-dimensional perovskites. The antiferroelectric displacements of the A-site cations in traditional *Pbnm* perovskites negate one another as they are related *via* inversion symmetry through the B-site. However, in these cation-ordered layered phases such as the Dion-Jacobson series (with layered ordering of inequivalent interlayer A and perovskite A' cations), the inversion symmetry is now broken due to the presence of two different cations at the A-sites that

displace by different amounts. As the anti-ferroelectric A-site displacements are no longer equal they do not completely cancel out, generating a macroscopic polarisation in the A-O layers[31]. In addition to this, the presence of Bi^{3+} at the A-site enhances the ferroelectric properties due to the polarisability of the bismuth lone pair, known as the "inert-pair effect".

As the octahedral tilt are driven by A-O bonding considerations, bond valence sum calculations were carried out on both the distorted ($P2_1am$) and aristotype structures ($P4/mmm$). The A-site cation is 8 coordinate to oxygen in the RT $P2_1am$ structure [32] giving a bond valence of v_{ij} = 2.54. This clearly demonstrates that a degree of underbonding at the A-site remains even in the distorted ground state. The A-site displacements and octahedral tilting rotations associated with the orthorhombic phase do, however, offer a significant improvement on co-ordination of the A-site in the tetragonal parent structure (v_{ij} = 1.928 at 800 °C). The thermal evolution of the BVS calculations is shown in Figure 7.14. A schematic highlighting the displacement of the Bi cations along *a* is given in Figure 7.15.

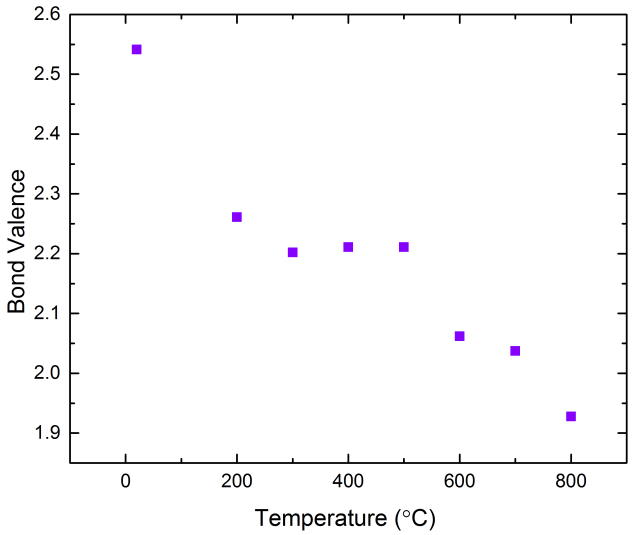

Figure 7.14 Results from bond valence sum calculations plotted as a function of temperature showing the how the loss of the out-of-phase tilt with increasing temperature leads to increased underbonding at the perovskite A-site.

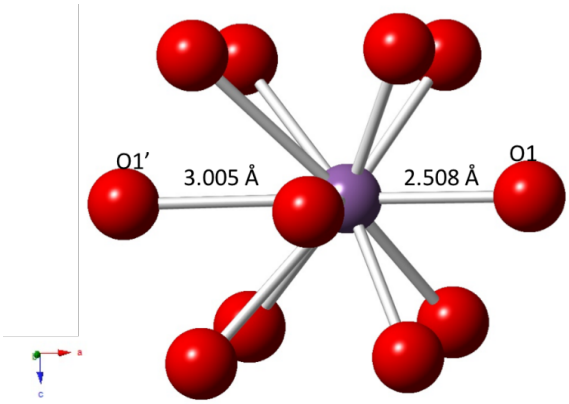

Figure 7.15 Co-ordination of the Bi^{3+} cation at the perovskite A-site showing displacement of Bi along the *a*-axis.

7.5 Conclusions and Further Work

A detailed PND study has evaluated the thermal evolution of the structure of the Dion-Jacobson phase $CsBi_{0.6}La_{0.4}Nb_2O_7$, shedding light on the nature of the paraelectric- ferroelectric transition present in the parent structure $CsBiNb_2O_7$.

Collectively, the available evidence points toward a discontinuous "avalanche" transition for the system $CsBi_{0.6}La_{0.4}Nb_2O_7$ akin to the paraelectric-ferroelectric transition previously exemplified in the Aurivillius phase $SrBi_2Nb_2O_9$[14]. PND data shows a gradual merging of several of the (*hhl*) peaks attributed to the orthorhombic distortion, with complete convergence observed in temperature region 700 < *T* < 725 °C. No evidence for an intermediary phase can be seen in the crystallographic data. However, it must be noted that due the paucity of the data measured in the vicinity of the phase transition an intermediary phase cannot be definitively ruled out at present. Similarly, the dielectric data appears to show a singular dielectric event, however, the possibility of a second event undetectable by eye (due to its close proximity to the first) cannot be entirely discounted. The most convincing evidence, arguably, is the similarity in T_c values obtained from the fits of the M_2^+ and M_5^- mode evolution; 749 and 742 °C respectively. The coincidental condensation of the two active modes would result in a direct *P*4/*mmm* to $P2_1am$ transition and stabilise the polar A-site lattice distortion.

The critical temperature of the structural transition was evaluated in numerous ways. From the crystallographic data alone the interval appears to be much narrower 700 < T_C < 725 °C, however both the mode amplitude analysis and dielectric data suggest a higher T_C approximately in the region 741 < T_C < 749 °C. Finally, a fit to the orthorhombic distortion gave T_C to be 732 °C. Therefore, with all the available analysis the ferroelectric-paraelectric transition can be narrowed down to a temperature interval of 700 < T_C < 750 °C.

Due to the limitations of the temperature resolution in the data sets, only realised with the benefit of hindsight, a second PND study consisting of an enhanced number of data sets collected over a longer period of time in the vicinity of the phase transition would be warranted. This should definitively rule out the possibility of a continuous transition through a phase with *Pmam* symmetry, thus confirming the avalanche-like nature of the transition in $CsBi_{0.6}La_{0.4}Nb_2O_7$ hypothesised here.

7.6 References

1. Bousquet, E.; Dawber, M.; Stucki, N.; Lichtensteiger, C.; Hermet, P.; Gariglio, S.; Triscone, J. M.; Ghosez, P., Improper ferroelectricity in perovskite oxide artificial superlattices. *Nature* **2008,** *452*, 732-736.
2. Strayer, M. E.; Gupta, A. S.; Akamatsu, H.; Lei, S.; Benedek, N. A.; Gopalan, V.; Mallouk, T. E., Emergent Noncentrosymmetry and Piezoelectricity Driven by Oxygen Octahedral Rotations in *n* = 2 Dion–Jacobson Phase Layer Perovskites. *Advanced Functional Materials* **2016,** *26*, 1930-1937.
3. Benedek, N. A.; Fennie, C. J., Hybrid Improper Ferroelectricity: A Mechanism for Controllable Polarization-Magnetization Coupling. *Physical Review Letters* **2011,** *106*, 107204.
4. Lalena, J. N.; Cleary, D. A., *Principles of Inorganic Materials Design*. Wiley: 2005.
5. Benedek, N. A.; Fennie, C. J., Why Are There So Few Perovskite Ferroelectrics? *Journal of Physical Chemistry C* **2013,** *117*, 13339-13349.
6. Gibbs, A. S.; Knight, K. S.; Lightfoot, P., High-temperature phase transitions of hexagonal $YMnO_3$. *Physical Review B* **2011,** *83*, 094111.
7. Benedek, N. A.; Rondinelli, J. M.; Djani, H.; Ghosez, P.; Lightfoot, P., Understanding ferroelectricity in layered perovskites: new ideas and insights from theory and experiments. *Dalton Transactions* **2015,** *44*, 10543-10558.
8. Fennie, C. J.; Rabe, K. M., Ferroelectric transition in $YMnO_3$ from first principles. *Physical Review B* **2005,** *72*, 100103.
9. Boullay, P.; Tellier, J.; Mercurio, D.; Manier, M.; Zuniga, F. J.; Perez-Mato, J. M., Phase transition sequence in ferroelectric Aurivillius compounds investigated by single crystal X-ray diffraction. *Solid State Sciences* **2012,** *14*, 1367-1371.
10. Harris, A. B., Symmetry analysis for the Ruddlesden-Popper systems $Ca_3Mn_2O_7$ and $Ca_3Ti_2O_7$. *Physical Review B* **2011,** *84*, 064116.
11. Oh, Y. S.; Luo, X.; Huang, F. T.; Wang, Y. Z.; Cheong, S. W., Experimental demonstration of hybrid improper ferroelectricity and the presence of abundant charged walls in $(Ca, Sr)_3Ti_2O_7$ crystals. *Nature Materials* **2015,** *14*, 407-413.
12. Etxebarria, I.; Perez-Mato, J. M.; Boullay, P., The Role of Trilinear Couplings in the Phase Transitions of Aurivillius Compounds. *Ferroelectrics* **2010,** *401*, 17-23.
13. Perez-Mato, J. M.; Blaha, P.; Schwarz, K.; Aroyo, M.; Orobengoa, D.; Etxebarria, I.; Garcia, A., Multiple instabilities in $Bi_4Ti_3O_{12}$: A ferroelectric beyond the soft-mode paradigm. *Physical Review B* **2008,** *77*, 184104.
14. Snedden, A.; Hervoches, C. H.; Lightfoot, P., Ferroelectric phase transitions in $SrBi_2Nb_2O_9$ and $Bi_5Ti_3FeO_{15}$: A powder neutron diffraction study. *Physical Review B* **2003,** *67*, 092102.
15. Li, B. W.; Osada, M.; Ozawa, T. C.; Sasaki, T., $RbBiNb_2O_7$: A New Lead-Free High-T_c Ferroelectric. *Chemistry of Materials* **2012,** *24*, 3111-3113.

16. Glazer, A., The classification of tilted octahedra in perovskites. *Acta Crystallographica Section B* **1972,** *28*, 3384-3392.
17. Snedden, A.; Knight, K. S.; Lightfoot, P., Structural distortions in the layered perovskites $CsANb_2O_7$ (A = Nd, Bi). *Journal of Solid State Chemistry* **2003,** *173*, 309-313.
18. Goff, R. J.; Keeble, D.; Thomas, P. A.; Ritter, C.; Morrison, F. D.; Lightfoot, P., Leakage and Proton Conductivity in the Predicted Ferroelectric $CsBiNb_2O_7$. *Chemistry of Materials* **2009,** *21*, 1296-1302.
19. Chen, C.; Ning, H. P.; Lepadatu, S.; Cain, M.; Yan, H. X.; Reece, M. J., Ferroelectricity in Dion-Jacobson $ABiNb_2O_7$ (A = Rb, Cs) compounds. *Journal of Materials Chemistry C* **2015,** *3*, 19-22.
20. Fennie, C. J.; Rabe, K. M., Ferroelectricity in the Dion-Jacobson $CsBiNb_2O_7$ from first principles. *Applied Physics Letters* **2006,** *88*, 262902.
21. Benedek, N. A., Origin of Ferroelectricity in a Family of Polar Oxides: The Dion-Jacobson Phases. *Inorganic Chemistry* **2014,** *53*, 3769-3777.
22. Petralanda, U.; Etxebarria, I., Structural instabilities and sequence of phase transitions in $SrBi_2Nb_2O_9$ and $SrBi_2Ta_2O_9$ from first principles and Monte Carlo simulations. *Physical Review B* **2015,** *91*, 184106.
23. Larson, A. C.; Von Dreele, R. B., Los Alamos Natl. Lab: 1994.
24. Toby, B. H., EXPGUI, a graphical user interface for GSAS. *Journal of Applied Crystallography* **2001,** *34*, 210-213.
25. Wu, Y. Y.; Zhang, D. M.; Yu, J.; Wang, Y. B., Effect of Bi_2O_3 seed layer on crystalline orientation and ferroelectric properties of $Bi_{3.25}La_{0.75}Ti_3O_{12}$ thin films prepared by rf-magnetron sputtering method. *Journal of Applied Physics* **2009,** *105*, 061613.
26. Kumada, N.; Kinomura, N.; Sleight, A. W., $CsLaNb_2O_7$. *Acta Crystallographica Section C* **1996,** *52*, 1063-1065.
27. Campbell, B. J.; Stokes, H. T.; Tanner, D. E.; Hatch, D. M., ISODISPLACE: a web-based tool for exploring structural distortions. *Journal of Applied Crystallography* **2006,** *39*, 607-614.
28. Kim, H. G.; Yoo, J. S.; Ok, K. M., Second-harmonic generation (SHG) and photoluminescence properties of noncentrosymmetric (NCS) layered perovskite solid solutions, $CsBi_{1-x}Eu_xNb_2O_7$ (x = 0, 0.1, and 0.2). *Journal of Materials Chemistry C* **2015,** *3*, 5625-5630.
29. Hervoches, C. H.; Lightfoot, P., A variable-temperature powder neutron diffraction study of ferroelectric $Bi_4Ti_3O_{12}$. *Chemistry of Materials* **1999,** *11*, 3359-3364.
30. Blake, S. M.; Falconer, M. J.; McCreedy, M.; Lightfoot, P., Cation disorder in ferroelectric Aurivillius phases of the type $Bi_2ANb_2O_9$ (A = Ba, Sr, Ca). *Journal of Materials Chemistry* **1997,** *7*, 1609-1613.
31. Mulder, A. T.; Benedek, N. A.; Rondinelli, J. M.; Fennie, C. J., Turning ABO_3 Antiferroelectrics into Ferroelectrics: Design Rules for Practical Rotation-Driven

Ferroelectricity in Double Perovskites and $A_3B_2O_7$ Ruddlesden-Popper Compounds. *Advanced Functional Materials* **2013,** *23*, 4810-4820.
32. Brese, N. E.; O'Keeffe, M., Bond-valence parameters for solids. *Acta Crystallographica Section B* **1991,** *47*, 192-197.

8. Summary, Conclusions and Further Work

8.1 Summary

The thermal evolution of several perovskite structures with various functional properties have been studied, primarily with PND analysis. Phase pure samples have been synthesised *via* a solid-state synthesis approach, typically using temperatures of ~ 1000 °C. In addition to PND methods, symmetry mode analysis, relative permittivity and SHG measurements were employed where appropriate for assistance in the structural characterisation and determination of the temperature-dependent phase diagrams.

8.2 Conclusions

Chapter 4 detailed the phase diagrams of three compositions of the LNN-*X* solid solution at values of x = 0.03, 0.08 and 0.12. None of these compositions were found to adopt phases R and S as observed in $NaNbO_3$, however, all three systems show susceptibility to condensation of the T_4 complex octahedral tilt mode. From the PND data it was clear the point along the generic T-line at which the T_4 mode was located varied for each composition, resulting in structures with novel tilt systems that cannot be described using conventional Glazer notation. Whilst the precise nature of the S-like phases of LNN-3 and LNN-8 could not be determined due to the inability to identify all potential models (owing to the large proposed sizes of the respective unit cells), the long-range tilt system adopted in LNN-12 (phase S') was successfully characterised to a high degree of detail. This new phase in LNN-12 was similar to Phase S in $NaNbO_3$ (with the T_4 mode located at ($\boldsymbol{k}$ = ½,

½, ¼) in the parent cubic Brillouin zone) but different, as in phase S' each *irrep.* acts about an individual axis, with no evidence for the compound tilt along *c* as observed in Phase S. Due to the limitations of PND, no meaningful distinction could be made between two similar models (each with the T_4 mode in a different configuration). However, the ability to assign specific symmetry modes along specific unit cell axes highlights the power of current PND instruments. The characterisation of phase S' in LNN-12 offers a correction to the previous phase diagram reported by Mishra[1]. The high temperature behaviour of all three compositions was found to echo that of pure $NaNbO_3$.

Chapter 5 reports the thermal evolution of the related compound $Li_{0.2}Na_{0.8}NbO_3$ (LNN-20). The increased degree of doping was found to have an interesting effect on the structural behaviour with a previously unexampled phase sequence of *R*3*c* – $P4_2mc$ – $P4_2/nmc$ – *P*4/*mbm* - $Pm\bar{3}m$. The presence of two variants of the rare $a^+a^+c^-$ tilt system is particularly interesting, with previous examples being A-site ordered[2-4] (and in one case A- and B-site ordered[5]) double perovskites with unusually small A-site cations, synthesised under conditions of high pressure. Indeed, the isolation of the polar form of the $a^+a^+c^-$ tilt system is intriguing as the only other example of this space group adopted in a perovskite structure exhibited polarisation-field hysteresis (*i.e.* ferroelectricity)[3]. Again, the high temperature structural evolution of LNN-20 was identical to that of $NaNbO_3$ and the x = 0.03, 0.08 and 0.12 compositions.

Chapter 6 describes a detailed structural analysis of the rare earth orthoferrite, $LaFeO_3$. With the high resolution obtainable on the HRPD instrument at ISIS, a systematic survey of the trends in bond angles and bond lengths was achievable. This lead to the identification of the structural driving force behind the $c > a$ crossover observed in the orthorhombic phase at $T \sim 770$ K. Interestingly this was found to be as a result of a small and constant deviation (~ 1.25 °) from 90 ° in the

O1-Fe-O2' bond angle. This octahedral distortion, which favours the *c*-axis over *a*, is overpowered by the R_4^+ out-of-phase tilt mode at lower temperatures, but becomes increasingly dominant, until the $c > a$ crossover is realised as the temperature is increased and *t* approaches unity. Additionally, a structural comparison between $LaFeO_3$ and the multiferroic compound, $Bi_{0.6}La_{0.4}FeO_3$ was detailed, identifying the anomalous structural behaviour due to magnetoelectric coupling effects with corresponding trends in the lattice parameters for both compounds rationalised.

Finally, Chapter 7 evaluates the nature of the paraelectric – ferroelectric transition in the Dion-Jacobson phase $CsBi_{0.6}La_{0.4}Nb_2O_7$, an example of a hybrid improper ferroelectric. Using PND analysis, symmetry mode arguments and relative permittivity measurements, it was concluded that the transition proceeds *via* a direct "avalanche" type transition, in which two primary order parameters (zone boundary modes, M_2^+ and M_5^-) condense simultaneously, generating a polarisation (zone centre mode, Γ_4^-). This direct nature of the transition was rationalised as PND data did not indicate the presence of an intermediary phase associated with the primary condensation of either one of the zone boundary modes. Similarly, symmetry mode analysis on the M_2^+ and M_5^- modes indicated that both had very similar temperature dependencies, suggestive of a direct transition.

Overall, this work highlights the power of PND techniques using the highest resolution instrument (HRPD) available today, with the ability to observe low frequency or soft modes such as the T_4 octahedral tilt mode described in Chapter 4. Certain limitations associated with PND data have also been highlighted, such the inability to discern between two very similar models, for phase S', as discussed above.

The extensive use of symmetry mode arguments, with the help of the ISODISTORT online software, highlights a different approach (as opposed to bond angle/length analysis for example) to describe the symmetry lowering distortions in crystalline systems, with the structural degrees of freedom recast as symmetry adapted modes. The extensive functionality and user-friendly interface of the ISODISTORT software provided a qualitative and quantitative analysis; identifying the various symmetry lowering distortions in addition to their relative magnitudes and "role", if any, in the various phase transitions observed for the crystal systems described throughout this work. The capability to derive "isotropy" subgroups for any **k**-point value has expanded the capability of structural determination from powder techniques, enabling the previous identification of Phases R and S of $NaNbO_3$[6] and, within the scope of this work, characterisation of phase S' of LNN-12. A symmetry mode analysis approach is also highly useful, with regard to the layered-like perovskite phases like the $CsBi_{0.6}La_{0.4}Nb_2O_7$ system, as the critical behaviour of the symmetry modes involved in the paraelectric – ferroelectric phase transition has relevance when establishing the nature of the transition mechanism. Indeed, it appears that the "symmetry mode approach" is becoming increasingly prevalent in the field of materials chemistry and crystallography.

8.3 Further Work

With regard to the LNN-*X* solid solution, it would be interesting to elucidate the exact nature of the two unique long-range structures adopted in the LNN-3 and LNN-8 systems. Possibly with the assistance of DFT calculations to conclusively identify the location at which the T_4 shows the greatest instability in the cubic Brillouin zone for each composition. Additionally, further PND studies on additional compositions in the region $0.05 < x < 0.20$, would likely yield additional phases with unique tilt systems. As softening of the T_4 mode is no longer witnessed

at a composition of x = 0.20, further experimental work could be carried out to identify the doping limit associated with the long-range tilt systems.

Owing to the interesting behaviour observed fin LNN-20, whereby two polymorphs of the rare $a^+a^+c^-$ tilt system are adopted within one system, further compositions at $x > 0.20$ could be of potential structural interest. Specifically, with regard to the polar form, which has the potential to display ferroelectricity.

With regard to $LaFeO_3$, two further PND studies not included in this thesis, on $YFeO_3$ and $LuFeO_3$, were carried out. Analysis of this data will allow for a comparison of the thermal evolution across the rare earth orthoferrite series, specifically with the aim of highlighting the structural evolution and thermal behaviour purely as a function of A-cation size (all three structures adopt G-type antiferromagnetic structures therefore effects due to magnetostriction would be minimised).

Finally, as the value for T_C of $CsBi_{0.6}La_{0.4}Nb_2O_7$ could not be specified to a more narrow temperature range than $700 \leq T_C \leq 750$ °C, owing to insufficient data in the vicinity of the phase transition, a further PND study is warranted with additional data collection in this region. This would clarify the transition temperature and hopefully erase any ambiguity over the nature of the trilinear coupling mechanism (*i.e.* confirmation of the direct transition or alternatively, identification of an intermediary phase). Secondly, with the ferroelectricity of $CsBiNb_2O_7$ recently confirmed, the introduction of magnetic cations into the structure could offer an interesting pathway to multiferrocity. Ion-exchange reactions where the intergrowth layers are replaced by magnetically active transition metal cations have already been shown to possible[7-9]. Using this approach, magnetic properties could potentially be introduced to $CsBiNb_2O_7$, with the exchange of Cs^+ for TM^{2+}-Cl^- linkages for example.

8.4 References

1. Mishra, S. K.; Krishna, P. S. R.; Shinde, A. B.; Jayakrishnan, V. B.; Mittal, R.; Sastry, P. U.; Chaplot, S. L., High temperature phase stability in $Li_{0.12}Na_{0.88}NbO_3$: A combined powder X-ray and neutron diffraction study. *Journal of Applied Physics* **2015,** *118*, 7.
2. Leinenweber, K.; Parise, J., High-Pressure Synthesis and Crystal-Structure of $CaFeTi_2O_6$, a New Perovskite Structure Type. *Journal of Solid State Chemistry* **1995,** *114*, 277-281.
3. Aimi, A.; Mori, D.; Hiraki, K.; Takahashi, T.; Shan, Y. J.; Shirako, Y.; Zhou, J. S.; Inaguma, Y., High-Pressure Synthesis of A-Site Ordered Double Perovskite $CaMnTi_2O_6$ and Ferroelectricity Driven by Coupling of A-Site Ordering and the Second-Order Jahn-Teller Effect. *Chemistry of Materials* **2014,** *26*, 2601-2608.
4. Hazen, R.M.; Burnham, C.W., The crystal structures of gillespite I and II: A structure determination at high pressure. *American Mineralogist* **1974,** *59*, 1166 - 1176.
5. Solana-Madruga, E.; Arevalo-Lopez, A. M.; Dos Santos-Garcia, A. J.; Urones-Garrote, E.; Avila-Brande, D.; Saez-Puche, R.; Attfield, J. P., Double Double Cation Order in the High-Pressure Perovskites $MnRMnSbO_6$. *Angewandte Chemie-International Edition* **2016,** *55*, 9340-9344.
6. Peel, M. D.; Thompson, S. P.; Daoud-Aladine, A.; Ashbrook, S. E.; Lightfoot, P., New Twists on the Perovskite Theme: Crystal Structures of the Elusive Phases R and S of $NaNbO_3$. *Inorganic Chemistry* **2012,** *51*, 6876-6889.
7. Kageyama, H.; Viciu, L.; Caruntu, G.; Ueda, Y.; Wiley, J. B., New magnetic materials obtained by ion-exchange reactions from non-magnetic layered perovskites. *Journal of Physics-Condensed Matter* **2004,** *16*, S585-S590.
8. Schaak, R. E.; Mallouk, T. E., Perovskites by design: A toolbox of solid-state reactions. *Chemistry of Materials* **2002,** *14*, 1455-1471.
9. Viciu, L.; Caruntu, G.; Royant, N.; Koenig, J.; Zhou, W. L. L.; Kodenkandath, T. A.; Wiley, J. B., Formation of metal-anion arrays within layered perovskite hosts. Preparation of a series of new metastable transition-metal oxyhalides, $(MCl)LaNb_2O_7$ (M = Cr, Mn, Fe, Co). *Inorganic Chemistry* **2002,** *41*, 3385-3388.

Appendix

List of Publications

Within the scope of this thesis:

1. Dixon, C. A. L.; Kavanagh, C. M.; Knight, K. S.; Kockelmann, W.; Morrison, F. D.; Lightfoot, P., Thermal evolution of the crystal structure of the orthorhombic perovskite $LaFeO_3$. *Journal of Solid State Chemistry* **2015,** *230*, 337-342.
2. Dixon, C. A. L.; McNulty, J. A.; Huband, S.; Thomas, P. A.; Lightfoot, P., Unprecedented phase transition sequence in the perovskite $Li_{0.2}Na_{0.8}NbO_3$. *IUCrJ* **2017,** *4*, 215-222.
3. Dixon, C. A. L.; McNulty, J. A.; Knight, K. S.; Gibbs, A. S.; Lightfoot, P., Phase Transition Behavior of the Layered Perovskite $CsBi_{0.6}La_{0.4}Nb_2O_7$: A Hybrid Improper Ferroelectric. *Crystals* **2017,** *7*.

Other publications:

4. Cordrey, K. J.; Stanczyk, M.; Dixon, C. A. L.; Knight, K. S.; Gardner, J.; Morrison, F. D.; Lightfoot, P., Structural and dielectric studies of the phase behaviour of the topological ferroelectric $La_{1-x}Nd_xTaO_4$. *Dalton Transactions* **2015,** *44*, 10673-10680.
5. Cochrane, A. K.; Telfer, M.; Dixon, C. A. L.; Zhang, W. G.; Halasyamani, P. S.; Bousquet, E.; Lightfoot, P., $NdBaScO_4$: aristotype of a new family of geometric ferroelectrics? *Chemical Communications* **2016,** *52*, 10980-10983.

Manuscripts in preparation:

Complex Octahedral Tilt Phases in the Perovskite System $Li_xNa_{1-x}NbO_3$, Journal TBC.

All raw data and select crystallographic information files related to the work presented in this thesis are (or will be, upon completion) published online in connection with each manuscript.